# Immuno-therapeutics Modulating B Immunity Against Cancer

By

**Chengyi Li**

A dissertation submitted in partial fulfillment
of the requirements for the degree of
Doctor of Philosophy
(Pharmaceutical Sciences)
in The University of Michigan
2024

Doctoral Committee:

Professor Duxin Sun, Chair
Associate Professor Wei Cheng
Associate Professor Yu Lei
Professor James Moon

Chengyi Li

chengyil@med.umich.edu

ORCID iD: 0000-0003-2378-6408

*For my grandpa, mom, and dad -*

*You laid the foundation for me to pursue any endeavor.*

*You demonstrated to me how brightness can radiate from a no one.*

# Acknowledgements

Firstly, I would like to express my sincere gratitude to my Ph.D. advisor, Dr. Duxin Sun, for his invaluable support and mentorship throughout my academic journey. His guidance not only helped me navigate academia but also exemplified essential principles of cooperation and communication in everyday life.

Besides, I also want to recognize my dissertation committee members including Dr. James Moon, Dr. Wei Cheng and Dr. Yu Lei. Your professional insights, knowledge, and experiences have offered invaluable guidance and suggestions, enriching my understanding, critical thinking, and research capabilities.

Next, I would like to acknowledge my lab members for their great support academically and emotionally. I would like to thank Dr. Hongxiang Hu, Dr. Wei Gao, Dr. Yudong Song, Zucal Erika, Hanning Wen, Zhixin Yu, Dr. Yingzi Bu, Luchen Zhang, Dr. Bo Wen, Dr. Djibo Mahamadou, Farzad Sarkari, and other lab members.

I would also like to acknowledge my friendships outside of research. Though time and distance may physically separate us, your support has been crucial in helping me navigate through the pandemic and periods of loneliness.

Lastly, I want to express my heartfelt gratitude to my family. You have shaped my character, and I know that no matter what decisions I make, your unwavering support will always be by my side.

# Table of Contents

# List of Figures

# List of Tables

# List of Appendices

# Abstract

Vaccines activating B cell to mount robust antigen specific humoral immunity against foreign pathogens, like SARS-CoV-2 virus, influenza virus, human papillomavirus., have achieved tremendous clinical success. However, the roles of B cell immunity in cancer and cancer immunotherapy have been a subject of debate for several decades. B cell immunity showed anti-tumor and pro-tumor roles under different cancers and therapeutical scenarios. In this research, we focus on two aspects of B cell immunity, a) amplification of the antigen presenting function of B cell immunity to promote B/CD4 T cell crosstalk by cancer vaccine for enhanced anti-tumor immunity, and b) elimination of B regulatory cells from tumor immune microenvironment to overcome STING agonist resistance for pancreatic tumor immunotherapy.

Neoantigen cancer vaccines using peptide or mRNA have shown promising anticancer efficacy in melanoma, colon and pancreatic cancer patients. Their efficacy is achieved through dendritic cell-mediated antigen presentation to activate CD4/CD8 T cell antitumor immunity. Most recent studies discovered that tumor infiltrating B cells are positively associated with better responses to anti-PD-1 immunotherapy in patients with various cancer types. However, it is unclear whether traditional B cell immunity or other B cell functions are crucial for its beneficial anticancer efficacy, while B/CD4 T cell crosstalk is essential for CD4/CD8 T cell antitumor immunity. Yet, current neoantigen vaccines using CD4/CD8 T epitopes are unable to promote B/CD4 T cell crosstalk. We designed SARS-CoV-2 B epitope-guided neoantigen cancer vaccines using peptide or mRNA to promote the crosstalk between SARS-CoV-2 B cells and tumor CD4 T cells, through B cell-mediated antigen presentation, for improving cancer immunotherapy.

In addition, the immune suppression in tumors and lymph nodes, regulated by suppressive myeloid cells and regulatory B (Breg) cells, hinders the effectiveness of immunotherapy. Although STING agonists activate myeloid cells to overcome immune suppression, it expands Breg cells, conferring STING resistance in PDAC. In the second project, we discovered that blocking PI3Kγ during STING activation abolished IRF3 phosphorylation to eliminate Breg cells, while PI3Kγ inhibition sustained STING-induced IRF3 phosphorylation to preserve STING function in myeloid cells. Therefore, we developed a dual functional compound SH-273 and its albumin

nanoformulation Nano-273, which stimulates STING to activate myeloid cells and inhibits PI3Kγ to eliminates Breg cells overcoming STING resistance. Nano-273 achieved systemic antitumor immunity through intravenous administration and preferential delivery to tumors and lymph nodes, which decreases Breg cells and remodels microenvironment. Nano-273, combined with anti-PD-1, extended median survival of 200 days in transgenic KPC PDAC mice (KrasG12D-P53R172H-Cre), offering potential for PDAC treatment.

# Chapter 1

# Introduction: B cell immunity and Cancer

B cells as the major component of the adaptive immune system are abundant in many tumors. Recent clinical studies suggest that B cell immunity is essential for achieving long-term anticancer efficacy in immunotherapy. High densities of B cells in tumors have been shown to be strongly associated with better clinical responses to immune checkpoint blockade. While B cells are associated with the antitumor immunity and efficacy of immunotherapy, studies have revealed that regulatory B cells (Bregs) may have negative antitumor immune responses, through cytokines that directly or indirectly affect antitumor immunity and tumor progression. Besides the humoral immune responses, B cell immunity has broad and differential functions for anti-tumor activity including antigen presentation, cytokine production, neogenesis of tertiary lymphoid structures.

In this thesis, we will develop cancer vaccine strategies to leverage the antigen presenting function of B cells to promote B/CD4 T cells crosstalk for amplified antitumor immune responses and efficacy. We will also investigate the immune suppressive function of B cell immunity through Bregs and develop strategies to overcome suppressive immune microenvironment and STING agonist resistance in pancreatic cancer.

**B cell antigen presentation mediated B/CD4 T cell crosstalk**

In general, dendritic cells (DCs) serve as the professional antigen presenting cells, present antigens to activate CD4 T cells. However, hampered both by physical barrier and decreased secretion of chemotaxis chemokines, the number of DCs in tumors decreased dramatically. Theoretically, due to the capacity of endocytic, low dose antigen concentrating, antigen processing and close spatial proximity with T cells in lymphoid organs and tumors, B cells could be more efficient in presenting the antigens. In order for B cell to present antigen, antigen binding to the B cell receptor needs to be endocytosed, processed, and presented onto MHC-II complex to CD4 T cells. Different from DCs, antigen presenting by B cells should be recognized specifically

both by B cells and T cells. Studies showed that long-term survival under immunotherapy is associated with increased infiltration of B cells, that is colocalized with CD8 T and CD4 T cells within solid tumor nidus, while the presence of CD8 T cells alone is not predictive for durable efficacy of immunotherapy in different cancer types. Interestingly, previous study showed when anti-CD20 antibody was used to remove CD20 B cells in murine model, the activation, clonal expansion of CD4 T cells and anti-tumor immune responses are all severely impaired[1-3].

In addition, B and CD4 T cell crosstalk is critical to drive anticancer immunity and is correlated with the clinical response of ICB.[4-14] B and CD4 T cell crosstalk is mediated through B cell-mediated antigen presentation rather than through DCs or macrophages. In this process, B cells recognize B cell epitopes through the B cell receptor (BCR), triggering BCR crosslinking and uptake of the antigen into B cells. Subsequently, B cells process CD4 epitopes to form MHC II complexes, which presents the CD4 epitopes to antigen-specific CD4 T cells for B/CD4 T cell crosstalk. Studies have shown that blocking B cell-mediated antigen presentation or B/CD4 T cell interaction (such as ICOS-ICOSL and CD40-CD40L interaction) impairs the anticancer efficacy of immunotherapy.[4, 5]

Further, the B cell and CD4 T cell crosstalk typically drives a T follicular helper (Tfh) cell-dependent germinal center (GC) response, which promotes B cell affinity maturation, differentiation into antigen-specific memory B cells, as well as differentiation and expansion of antigen-specific Tfh cells. Recent finding demonstrated that Tfh cell and GC B cell activation is critical to facilitate the antitumor response of ICB in breast cancer model.[6]

Finally, B/CD4 crosstalk induced Tfh cells may enhance CD8 effector T cell functions and driving intratumor TLS formation to improve anti-cancer immunity.[5, 13, 14] Tumor TLS is composed of many B cells in the center surrounded by CD4 T cells, and it is enriched with GC B cells, Tfh cells, and follicular DCs.[7-11] The B/CD4 T cell crosstalk in situ present in tumor TLS is also associated with better anticancer efficacy of anti-PD-1 immunotherapy in cancer patients.[7-12]

**Regulatory B cells**

Besides antitumorigenic effects, research has also showed suppressive effects of B cells upon host immunity that facilitate the progression of tumor. The regulatory role of B cells was first discovered in autoimmune diseases, where suppression of inflammation was observed and modulated by IL-10 secreting B cells[15, 16]. Gordon et. al. first introduced the suppressive effect of B cells through depleting B-cells and subsequently observed better anti-tumor response[17]. Later, research further confirmed the regulatory role of B cells in cancer, autoimmune diseases and transplantation. Bregs regulates T cells and innate immune immunity through secreting

suppressive cytokines (like, IL-10, TGF-β and IL-35) or direct contacting with cellular surface motifs (like, BCR, CD 80/86, PD L1, CD 40L, OX 40L and LAP)[18-21]. By expressing IL-10, Bregs can decrease the pro-inflammatory cytokines secretion of DC. Thus Treg induction would be increased, while the differentiation of Th1 and Th17 cells be impaired. Bregs can enhance the apoptosis of CD4 effector T cells and cause anergy of CD8 cytotoxic T cells through TGF-β. Recently, IL-35 was proved to be the third cytokine through which Bregs could reduce the immune responses of Th1 and decrease macrophages in spleen. Through lipid-antigen presenting, CD1d+ Bregs could maintain the balance of invariant natural killer cells, in avoid of the autoimmune responses. Notably, Bregs could constitutively express phosphorylated Stat3 that associate with promotion of tumor angiogenesis, growth, metastasis, and worse survival rate[22, 23].

However, research on the phenotypic identification and ontogeny of Bregs is far less clear. B cells that can secrete IL-10 to regulate immune responses are recognized as Bregs. Yet, IL-10 is not an ideal marker to define Bregs, especially with copious phenotypes of Bregs discovered within different subsets of B cells across all developmental stages[6, 18, 24-32]. Nevertheless, less than 20% of B cells with these phenotypes exhibit capacity to suppress immune responses. Hence, more efforts are needed to identify precise markers for Bregs. As for the ontogeny of Bregs, several pathways play an important role in leading the differentiation of Bregs, such as toll like receptor-9 (TLR-9), IL-1β, IL-6 and IL-21[33]. Two main models are postulated for elucidation of Bregs ontogeny. First, similar as fork head transcription factor p3+ (FoxP3+) for regulatory T cells (Treg), researcher investigated on specific markers that can identify Bregs as an independent lineage. Another model describes that B cells have much plasticity and should be investigated in a dynamic way where any B cells can differentiate into Bregs under certain environmental stimuli. The plasticity model is supported by the facts that no clear lineage identification marker has been found, where Bregs with distinct phenotypes are distributed among different subsets of B cells and multiple inflammatory cytokines are involved in the induction of Bregs[18, 24, 34, 35]. Many types of cancer including non-small cell lung cancer, pancreatic cancer, ovarian cancer, gastric cancer, esophageal cancer, head cancer, neck cancer, liver cancer, have been observed with infiltrating of Bregs in tumor immune microenvironment, suppress the function of anti-tumor immunity and promote tumorigenesis[36-38]. Li et. al. recently found that Bregs secreted IL35 compromised natural killer cell function led to STING agonist resistance, impaired antitumor immunity and efficacy in pancreatic cancer[39].

To promote the B cell antigen presentation mediated B/CD4 T cell crosstalk in the first and second projects, we have developed the SARS-CoV-2 B epitope-guided tumor neoantigen nanovaccine

(ACNVax). ACNVax with viral antigen cluster structures can efficiently crosslink with B cell receptors, facilitates B cell internalization and subsequently presentation by MHC-II complex to CD4 T cells, promotes robust B/CD4 T cell crosstalk with amplified downstream antitumor immune responses. Efficacy studies have shown that ACNVax achieved long-term tumor remission in mouse HER2+ breast cancer. In the second project, ACNVax uniquely combines viral (SARS-CoV-2) B antigens and tumor-specific T neoantigens. This nanovaccine features SARS-CoV-2 B epitope-cluster configuration on its surface, crosslink with the BCR of SARS-CoV-2 B antigen specific B cells, subsequently present tumor T cell neoantigen to CD4 T cells, which fosters cross-talk between virus-specific B cells and tumor-specific CD4 T cells. The ACNVax combined with anti-PD-1 showed significant anticancer efficacy in various cancer models. The results suggest SARS-CoV-2 B epitope and viral mimicry nanocarrier strategies can be applied to cancer vaccine design to improve anticancer efficacy.

In the third project, we also studied a strategy to eliminate Breg cells to overcome immune suppression in the microenvironment in tumors and lymph nodes for pancreatic cancer immunotherapy. We developed a novel dual functional compound that can eliminate Bregs while preserve the activation of myeloid cells. We found that blocking PI3Kγ pathway in B cells, can abolish the phosphorylation of IRF3 by STING activation, and hence eliminates the induction of Bregs. In the meantime, blocking PI3Kγ pathway in myeloid cells, like dendritic cells or macrophages, does not suppress the phosphorylation of IRF3 by STING activation, and hence preserve the activation of myeloid cells. Therefore, we designed a dual functional compound SH-273 to stimulate STING to activate myeloid cells and to inhibit PI3Kγ to eliminate Bregs. We have also generated an albumin nanoformulation of SH-273 (Nano-273), which can be preferentially delivered to lymph nodes and tumors, to better remodel tumor immune suppressive microenvironment and lower the toxicity. Nano-273 significantly reduced Bregs and stimulated myeloid cells, improved the median survival date of KPC transgenic mice to 200 days, provided potential treatment option for pancreatic cancer patients.

## Bibliography

1. Shi, J. Y.; Gao, Q.; Wang, Z. C.; Zhou, J.; Wang, X. Y.; Min, Z. H.; Shi, Y. H.; Shi, G. M.; Ding, Z. B.; Ke, A. W.; Dai, Z.; Qiu, S. J.; Song, K.; Fan, J., Margin-infiltrating CD20(+) B cells display an atypical memory phenotype and correlate with favorable prognosis in hepatocellular carcinoma. *Clinical cancer research : an official journal of the American Association for Cancer Research* **2013,** *19* (21), 5994-6005.

2. Nielsen, J. S.; Sahota, R. A.; Milne, K.; Kost, S. E.; Nesslinger, N. J.; Watson, P. H.; Nelson, B. H., CD20+ tumor-infiltrating lymphocytes have an atypical CD27- memory phenotype and together with CD8+ T cells promote favorable prognosis in ovarian cancer. *Clinical cancer research : an official journal of the American Association for Cancer Research* **2012,** *18* (12), 3281-92.
3. Bodogai, M.; Lee Chang, C.; Wejksza, K.; Lai, J.; Merino, M.; Wersto, R. P.; Gress, R. E.; Chan, A. C.; Hesdorffer, C.; Biragyn, A., Anti-CD20 antibody promotes cancer escape via enrichment of tumor-evoked regulatory B cells expressing low levels of CD20 and CD137L. *Cancer research* **2013,** *73* (7), 2127-38.
4. Sagiv-Barfi, I.; Czerwinski, D. K.; Shree, T.; Lohmeyer, J. J. K.; Levy, R., Intratumoral immunotherapy relies on B and T cell collaboration. *Sci Immunol* **2022,** *7* (71), eabn5859.
5. Cui, C.; Wang, J.; Fagerberg, E.; Chen, P. M.; Connolly, K. A.; Damo, M.; Cheung, J. F.; Mao, T.; Askari, A. S.; Chen, S.; Fitzgerald, B.; Foster, G. G.; Eisenbarth, S. C.; Zhao, H.; Craft, J.; Joshi, N. S., Neoantigen-driven B cell and CD4 T follicular helper cell collaboration promotes anti-tumor CD8 T cell responses. *Cell* **2021,** *184* (25), 6101-6118 e13.
6. Hollern, D. P.; Xu, N.; Thennavan, A.; Glodowski, C.; Garcia-Recio, S.; Mott, K. R.; He, X.; Garay, J. P.; Carey-Ewend, K.; Marron, D.; Ford, J.; Liu, S.; Vick, S. C.; Martin, M.; Parker, J. S.; Vincent, B. G.; Serody, J. S.; Perou, C. M., B Cells and T Follicular Helper Cells Mediate Response to Checkpoint Inhibitors in High Mutation Burden Mouse Models of Breast Cancer. *Cell* **2019,** *179* (5), 1191-1206.e21.
7. Helmink, B. A.; Reddy, S. M.; Gao, J.; Zhang, S.; Basar, R.; Thakur, R.; Yizhak, K.; Sade-Feldman, M.; Blando, J.; Han, G.; Gopalakrishnan, V.; Xi, Y.; Zhao, H.; Amaria, R. N.; Tawbi, H. A.; Cogdill, A. P.; Liu, W.; LeBleu, V. S.; Kugeratski, F. G.; Patel, S.; Davies, M. A.; Hwu, P.; Lee, J. E.; Gershenwald, J. E.; Lucci, A.; Arora, R.; Woodman, S.; Keung, E. Z.; Gaudreau, P. O.; Reuben, A.; Spencer, C. N.; Burton, E. M.; Haydu, L. E.; Lazar, A. J.; Zapassodi, R.; Hudgens, C. W.; Ledesma, D. A.; Ong, S.; Bailey, M.; Warren, S.; Rao, D.; Krijgsman, O.; Rozeman, E. A.; Peeper, D.; Blank, C. U.; Schumacher, T. N.; Butterfield, L. H.; Zelazowska, M. A.; McBride, K. M.; Kalluri, R.; Allison, J.; Petitprez, F.; Fridman, W. H.; Sautès-Fridman, C.; Hacohen, N.; Rezvani, K.; Sharma, P.; Tetzlaff, M. T.; Wang, L.; Wargo, J. A., B cells and tertiary lymphoid structures promote immunotherapy response. *Nature* **2020,** *577* (7791), 549-555.
8. Cabrita, R.; Lauss, M.; Sanna, A.; Donia, M.; Skaarup Larsen, M.; Mitra, S.; Johansson, I.; Phung, B.; Harbst, K.; Vallon-Christersson, J.; van Schoiack, A.; Lövgren, K.; Warren, S.; Jirström, K.; Olsson, H.; Pietras, K.; Ingvar, C.; Isaksson, K.; Schadendorf, D.; Schmidt, H.; Bastholt, L.; Carneiro, A.; Wargo, J. A.; Svane, I. M.; Jönsson, G., Tertiary lymphoid structures improve immunotherapy and survival in melanoma. *Nature* **2020,** *577* (7791), 561-565.
9. Petitprez, F.; de Reyniès, A.; Keung, E. Z.; Chen, T. W.; Sun, C. M.; Calderaro, J.; Jeng, Y. M.; Hsiao, L. P.; Lacroix, L.; Bougoüin, A.; Moreira, M.; Lacroix, G.; Natario, I.; Adam, J.; Lucchesi, C.; Laizet, Y. H.; Toulmonde, M.; Burgess, M. A.; Bolejack, V.; Reinke, D.; Wani, K. M.; Wang, W. L.; Lazar, A. J.; Roland, C. L.; Wargo, J. A.; Italiano, A.; Sautès-Fridman, C.; Tawbi, H. A.; Fridman, W. H., B cells are associated with survival and immunotherapy response in sarcoma. *Nature* **2020,** *577* (7791), 556-560.
10. Kroeger, D. R.; Milne, K.; Nelson, B. H., Tumor-Infiltrating Plasma Cells Are Associated with Tertiary Lymphoid Structures, Cytolytic T-Cell Responses, and Superior Prognosis in Ovarian Cancer. *Clinical cancer research : an official journal of the American Association for Cancer Research* **2016,** *22* (12), 3005-15.
11. Garaud, S.; Buisseret, L.; Solinas, C.; Gu-Trantien, C.; de Wind, A.; Van den Eynden, G.; Naveaux, C.; Lodewyckx, J. N.; Boisson, A.; Duvillier, H.; Craciun, L.; Ameye, L.; Veys, I.; Paesmans, M.; Larsimont, D.; Piccart-Gebhart, M.; Willard-Gallo, K., Tumor infiltrating B-cells signal functional humoral immune responses in breast cancer. *JCI Insight* **2019,** *5*.

12. Wieland, A.; Patel, M. R.; Cardenas, M. A.; Eberhardt, C. S.; Hudson, W. H.; Obeng, R. C.; Griffith, C. C.; Wang, X.; Chen, Z. G.; Kissick, H. T.; Saba, N. F.; Ahmed, R., Defining HPV-specific B cell responses in patients with head and neck cancer. *Nature* **2020**.
13. Chaurio, R. A.; Anadon, C. M.; Lee Costich, T.; Payne, K. K.; Biswas, S.; Harro, C. M.; Moran, C.; Ortiz, A. C.; Cortina, C.; Rigolizzo, K. E.; Sprenger, K. B.; Mine, J. A.; Innamarato, P.; Mandal, G.; Powers, J. J.; Martin, A.; Wang, Z.; Mehta, S.; Perez, B. A.; Li, R.; Robinson, J.; Kroeger, J. L.; Curiel, T. J.; Yu, X.; Rodriguez, P. C.; Conejo-Garcia, J. R., TGF-β-mediated silencing of genomic organizer SATB1 promotes Tfh cell differentiation and formation of intra-tumoral tertiary lymphoid structures. *Immunity* **2022,** *55* (1), 115-128.e9.
14. Overacre-Delgoffe, A. E.; Bumgarner, H. J.; Cillo, A. R.; Burr, A. H. P.; Tometich, J. T.; Bhattacharjee, A.; Bruno, T. C.; Vignali, D. A. A.; Hand, T. W., Microbiota-specific T follicular helper cells drive tertiary lymphoid structures and anti-tumor immunity against colorectal cancer. *Immunity* **2021,** *54* (12), 2812-2824.e4.
15. Mizoguchi, A.; Mizoguchi, E.; Takedatsu, H.; Blumberg, R. S.; Bhan, A. K., Chronic intestinal inflammatory condition generates IL-10-producing regulatory B cell subset characterized by CD1d upregulation. *Immunity* **2002,** *16* (2), 219-30.
16. Fillatreau, S.; Sweenie, C. H.; McGeachy, M. J.; Gray, D.; Anderton, S. M., B cells regulate autoimmunity by provision of IL-10. *Nat Immunol* **2002,** *3* (10), 944-50.
17. Brodt, P.; Gordon, J., Antitumor immunity in B-lymphocyte-deprived mice. II. In vitro studies. *Cellular immunology* **1981,** *65* (1), 20-32.
18. Matsumoto, M.; Baba, A.; Yokota, T.; Nishikawa, H.; Ohkawa, Y.; Kayama, H.; Kallies, A.; Nutt, S. L.; Sakaguchi, S.; Takeda, K.; Kurosaki, T.; Baba, Y., Interleukin-10-producing plasmablasts exert regulatory function in autoimmune inflammation. *Immunity* **2014,** *41* (6), 1040-51.
19. Shen, P.; Roch, T.; Lampropoulou, V.; O'Connor, R. A.; Stervbo, U.; Hilgenberg, E.; Ries, S.; Dang, V. D.; Jaimes, Y.; Daridon, C.; Li, R.; Jouneau, L.; Boudinot, P.; Wilantri, S.; Sakwa, I.; Miyazaki, Y.; Leech, M. D.; McPherson, R. C.; Wirtz, S.; Neurath, M.; Hoehlig, K.; Meinl, E.; Grützkau, A.; Grün, J. R.; Horn, K.; Kühl, A. A.; Dörner, T.; Bar-Or, A.; Kaufmann, S. H. E.; Anderton, S. M.; Fillatreau, S., IL-35-producing B cells are critical regulators of immunity during autoimmune and infectious diseases. *Nature* **2014,** *507* (7492), 366-370.
20. Komai, T.; Inoue, M.; Okamura, T.; Morita, K.; Iwasaki, Y.; Sumitomo, S.; Shoda, H.; Yamamoto, K.; Fujio, K., Transforming Growth Factor-β and Interleukin-10 Synergistically Regulate Humoral Immunity via Modulating Metabolic Signals. *Frontiers in immunology* **2018,** *9*, 1364.
21. Mauri, C.; Menon, M., Human regulatory B cells in health and disease: therapeutic potential. *The Journal of clinical investigation* **2017,** *127* (3), 772-779.
22. Olkhanud, P. B.; Damdinsuren, B.; Bodogai, M.; Gress, R. E.; Sen, R.; Wejksza, K.; Malchinkhuu, E.; Wersto, R. P.; Biragyn, A., Tumor-evoked regulatory B cells promote breast cancer metastasis by converting resting $CD4^+$ T cells to T-regulatory cells. *Cancer research* **2011,** *71* (10), 3505-15.
23. Yang, C.; Lee, H.; Pal, S.; Jove, V.; Deng, J.; Zhang, W.; Hoon, D. S.; Wakabayashi, M.; Forman, S.; Yu, H., B cells promote tumor progression via STAT3 regulated-angiogenesis. *PloS one* **2013,** *8* (5), e64159.
24. Blair, P. A.; Noreña, L. Y.; Flores-Borja, F.; Rawlings, D. J.; Isenberg, D. A.; Ehrenstein, M. R.; Mauri, C., CD19(+)CD24(hi)CD38(hi) B cells exhibit regulatory capacity in healthy individuals but are functionally impaired in systemic Lupus Erythematosus patients. *Immunity* **2010,** *32* (1), 129-40.

25. Menon, M.; Blair, P. A.; Isenberg, D. A.; Mauri, C., A Regulatory Feedback between Plasmacytoid Dendritic Cells and Regulatory B Cells Is Aberrant in Systemic Lupus Erythematosus. *Immunity* **2016,** *44* (3), 683-697.
26. Iwata, Y.; Matsushita, T.; Horikawa, M.; Dilillo, D. J.; Yanaba, K.; Venturi, G. M.; Szabolcs, P. M.; Bernstein, S. H.; Magro, C. M.; Williams, A. D.; Hall, R. P.; St Clair, E. W.; Tedder, T. F., Characterization of a rare IL-10-competent B-cell subset in humans that parallels mouse regulatory B10 cells. *Blood* **2011,** *117* (2), 530-41.
27. Horikawa, M.; Weimer, E. T.; DiLillo, D. J.; Venturi, G. M.; Spolski, R.; Leonard, W. J.; Heise, M. T.; Tedder, T. F., Regulatory B cell (B10 Cell) expansion during Listeria infection governs innate and cellular immune responses in mice. *J Immunol* **2013,** *190* (3), 1158-68.
28. Lindner, S.; Dahlke, K.; Sontheimer, K.; Hagn, M.; Kaltenmeier, C.; Barth, T. F.; Beyer, T.; Reister, F.; Fabricius, D.; Lotfi, R.; Lunov, O.; Nienhaus, G. U.; Simmet, T.; Kreienberg, R.; Möller, P.; Schrezenmeier, H.; Jahrsdörfer, B., Interleukin 21-induced granzyme B-expressing B cells infiltrate tumors and regulate T cells. *Cancer research* **2013,** *73* (8), 2468-79.
29. Chesneau, M.; Michel, L.; Dugast, E.; Chenouard, A.; Baron, D.; Pallier, A.; Durand, J.; Braza, F.; Guerif, P.; Laplaud, D. A.; Soulillou, J. P.; Giral, M.; Degauque, N.; Chiffoleau, E.; Brouard, S., Tolerant Kidney Transplant Patients Produce B Cells with Regulatory Properties. *Journal of the American Society of Nephrology : JASN* **2015,** *26* (10), 2588-98.
30. van de Veen, W.; Stanic, B.; Yaman, G.; Wawrzyniak, M.; Söllner, S.; Akdis, D. G.; Rückert, B.; Akdis, C. A.; Akdis, M., IgG4 production is confined to human IL-10-producing regulatory B cells that suppress antigen-specific immune responses. *The Journal of allergy and clinical immunology* **2013,** *131* (4), 1204-12.
31. Saze, Z.; Schuler, P. J.; Hong, C. S.; Cheng, D.; Jackson, E. K.; Whiteside, T. L., Adenosine production by human B cells and B cell-mediated suppression of activated T cells. *Blood* **2013,** *122* (1), 9-18.
32. Liu, J.; Zhan, W.; Kim, C. J.; Clayton, K.; Zhao, H.; Lee, E.; Cao, J. C.; Ziegler, B.; Gregor, A.; Yue, F. Y.; Huibner, S.; MacParland, S.; Schwartz, J.; Song, H. H.; Benko, E.; Gyenes, G.; Kovacs, C.; Kaul, R.; Ostrowski, M., IL-10-producing B cells are induced early in HIV-1 infection and suppress HIV-1-specific T cell responses. *PloS one* **2014,** *9* (2), e89236.
33. Baba, Y.; Matsumoto, M.; Kurosaki, T., Signals controlling the development and activity of regulatory B-lineage cells. *International immunology* **2015,** *27* (10), 487-93.
34. Rosser, E. C.; Mauri, C., Regulatory B cells: origin, phenotype, and function. *Immunity* **2015,** *42* (4), 607-12.
35. Wang, R. X.; Yu, C. R.; Dambuza, I. M.; Mahdi, R. M.; Dolinska, M. B.; Sergeev, Y. V.; Wingfield, P. T.; Kim, S. H.; Egwuagu, C. E., Interleukin-35 induces regulatory B cells that suppress autoimmune disease. *Nat Med* **2014,** *20* (6), 633-41.
36. Shen, M.; Wang, J.; Ren, X., New Insights into Tumor-Infiltrating B Lymphocytes in Breast Cancer: Clinical Impacts and Regulatory Mechanisms. *Frontiers in immunology* **2018,** *9*, 470.
37. Patel, A. J.; Richter, A.; Drayson, M. T.; Middleton, G. W., The role of B lymphocytes in the immuno-biology of non-small-cell lung cancer. *Cancer Immunol Immunother* **2020,** *69* (3), 325-342.
38. Tokunaga, R.; Naseem, M.; Lo, J. H.; Battaglin, F.; Soni, S.; Puccini, A.; Berger, M. D.; Zhang, W.; Baba, H.; Lenz, H. J., B cell and B cell-related pathways for novel cancer treatments. *Cancer treatment reviews* **2019,** *73*, 10-19.
39. Li, S.; Mirlekar, B.; Johnson, B. M.; Brickey, W. J.; Wrobel, J. A.; Yang, N.; Song, D.; Entwistle, S.; Tan, X.; Deng, M.; Cui, Y.; Li, W.; Vincent, B. G.; Gale, M., Jr.; Pylayeva-Gupta, Y.; Ting, J. P., STING-induced regulatory B cells compromise NK function in cancer immunity. *Nature* **2022,** *610* (7931), 373-380.

# Chapter 2

# Antigen-Clustered Nanovaccine Achieves Long-Term Tumor Remission by Promoting B/CD4 T Cells Crosstalk

## 2.1 Abstract

Current cancer vaccines using T cell epitopes activate antitumor T cell immunity through dendritic cell/macrophage-mediated antigen presentation, but lack the ability to promote B/CD4 T cells crosstalk, limiting their anticancer efficacy. We developed antigen-clustered nanovaccine (ACNVax) to achieve long-term tumor remission by promoting B/CD4 T Cells Crosstalk. The topographic features of ACNVax were achieved using a core of iron nanoparticle attached with optimal number of gold nanoparticles, where the clusters of HER2 B/CD4 T cell epitopes were conjugated on the gold surface with an optimal inter-cluster distance of 5-10 nm. ACNVax effectively trafficked to lymph nodes and crosslinked with BCR, which are essential for stimulating B cell antigen presentation-mediated B/CD4 T cell crosstalk *in vitro* and *in vivo*. ACNVax, combined with anti-PD-1, achieved long-term tumor remission (>200 days) with 80% complete response in mice with $HER2^+$ breast cancer. ACNVax not only remodeled the tumor immune microenvironment but also induced a long-term immune memory, as evidenced by complete rejection of tumor rechallenge and a high level of antigen-specific memory B, CD4, and CD8 cells in mice (> 200 days). This study provides a novel cancer vaccine design strategy, using B/CD4 T cell epitopes in an antigen clustered topography, to achieve long-term durable anticancer efficacy through promoting B/CD4 T cell crosstalk.

## 2.2 Introduction

Current anticancer vaccines are designed to activate T cell immunity against tumor-associated antigens (TAAs) or neoantigens[1-3], which have achieved promising clinical anticancer efficacy in patients with certain cancer type such as melanoma[4-12]. However, these vaccines have only

shown limited efficacy in improving overall survival in patients with various other cancer types although they successfully activated T cell immunity[1-3, 5, 6, 13-19].

Typically, a vaccine against infectious diseases needs to stimulate both B cell and T cell immunity in a healthy body to generate long-lasting efficacy[20-24]. However, current cancer therapeutic vaccines using T cell epitopes are not designed to activate B cell immunity because the role of B cell immunity in cancer vaccines has been a subject of debate for several decades[25-33]. In fact, if the purpose of a cancer vaccine is solely to activate B cell immunity for antibody secretion[34], it will neither generate durable anticancer efficacy nor have a clinical need, since monoclonal antibody therapy is readily available for cancer treatment. In addition, there is controversy over whether activation of B cell immunity may have pro-tumor activity, although recent studies suggest this may be related to regulatory B cells rather than other forms of B cell activations[25-33].

However, Latest clinical studies suggest B cell activation are critical for achieving durable anticancer efficacy in patients using immune checkpoint blockade (ICB) therapy[35-39]. B/CD4 T cell crosstalk, especially B cell and follicular T cells (Tfh) crosstalk, is critical to drive anticancer immunity and is associated with the clinical response to ICB therapy.[35-45] B cell activation in tumor improves antigen presentation, driving the expansion of tumor-specific T cells for anticancer efficacy. Activated B cells in tumors also secrete inflammatory cytokines (including TNF, IL-2, IL-6 and IFNγ) to activate and recruit other immune effector cells (eg. CD 4 and CD 8 T cells) to promote antitumor immunity[35, 37, 41, 42]. More importantly, B cell activation may be required to achieve long-term T cell memory during immunotherapy[46-49]. Furthermore, when B cell tumor infiltration are presented in a tertiary lymphoid structure (TLS) structure, which are organized lymphoid aggregates consisting of mainly B cells and CD4 T cells, tends to show favorable clinical response to ICB therapy[35-45].

Since presence of B cell immunity is correlated with enhanced long-term survival rates in patients treated with anti-PD-1 therapy[35-39], it is imperative to investigate whether incorporating B cell immunity to enhance B cell antigen presentation-mediated B/CD4 T cell crosstalk in current cancer vaccine designs can improve long-term efficacy. However, current cancer vaccines using T cell epitopes (without B cell epitopes) only activate T cell immunity through dendritic cell/macrophage-mediated antigen presentation[19, 50]. Furthermore, current vaccine delivery systems using nanoparticle encapsulated antigen inside or simply mixing antigen with adjuvant are unable to bind and crosslink with B cell receptor (BCR), and thus they are unable to activate B cell receptor-mediated antigen uptake, processing, and presentation to CD4 T cells[51].

To design a nanovaccine for promoting B cell antigen presentation-mediated B/CD4 T cell crosstalk[52, 53], three critical challenges must be addressed[52, 53]. Firstly, the vaccine needs to efficiently penetrate the lymph nodes and directly engage with B cells. While nanoparticles smaller than 200 nm can enter the lymph nodes, they tend to accumulate in the subcapsular sinus macrophages positioned above the B-cell follicles, rather than reaching the follicles themselves[54]. Secondly, the antigens must be displayed on the nanoparticle surface with a high antigen density comparable to immunogenic viruses in order to induce robust B cell activation[55]. Thirdly, repetitive antigens in a cluster with an optimal distance between clusters is crucial for efficient crosslinking with the BCR[56-58]. This crosslinking likely triggers effective internalization of the antigen, and may overcomes tolerance in antitumor B cell immunity[59-61]. Unfortunately, the commonly used nanoplatforms (< 200 nm) with peptide epitopes uniformly distributed on the surface cannot achieve the optimal distance of 5-10 nm[62] required for effective BCR crosslinking while maintaining a high antigen density simultaneously.[63] Several studies have demonstrated that antigen cluster structures, such as a glycoprotein on virus like nanoparticles[62, 64], with an ideal spacing between antigen clusters, can induce a high level of BCR crosslinking while preserving a high surface antigen density. However, such nanoplatforms with antigen cluster structure have not yet been realized in peptide nanovaccine design.

In this study, we designed a nanovaccine using HER2 B/CD4 T cell epitopes in an antigen-cluster topography (ACNVax) to achieve long-term tumor remission by promoting B cell antigen presentation-mediated B/CD4 T cell crosstalk. We engineered the ACNVax with an antigen-cluster topography on its surface, including a high density of HER2 B/CD4 cell epitopes and optimal distance (5-10 nm) between two antigen clusters. These topographic features of ACNVax promote lymph node trafficking and crosslinking with BCR[65], which are essential for stimulating B cell antigen presentation-mediated B/CD4 T cell crosstalk *in vitro* and *in vivo*[50, 66]. To further stimulate TLS formation in tumors, we also generated ACNVax with LIGHT, a member of the tumor necrosis factor (TNF) ligand family previously reported to promote TLS formation[67, 68]. We tested that ACNVax/LIGHT in combination with anti-PD-1 antibody, to achieve long-term tumor remission (>200 days) with a complete response (CR) rate of 80% in mice with HER2 breast cancer. We used CyTOF and single cell RNA-seq to evaluate how ACNVax/LIGHT remodeled the tumor immune microenvironment. Finally, we monitored how ACNVax/LIGHT generates long-term antigen specific B/CD4/CD8 T cell immune memory for its long-term efficacy. Our data provide a novel cancer vaccine design strategy, using B/CD4 T cell epitopes in an antigen clustered topography, to achieve long-term durable anticancer efficacy through promoting B cell

antigen presentation-mediated B/CD4 T cell crosstalk, and remodeling tumor immune microenvironment. (**Figure 2.1**).

## 2.3 Results

### Engineer ACNVax with clustered-antigen topography to effectively bind/crosslink with B cell receptor (BCR).

To prepare a nanoparticle with clustered antigen topography for efficient BCR crosslinking, we first prepared the iron nanoparticle core coated with poly(siloxane)- and poly (ethylene glycol)-containing di-block copolymer (IONP-Polymer, 15 nm) as we reported previously[69-71] (**Figure S1a**). Ultra-small gold nanoparticles (AuNPs) (2 nm) were then attached to the surface of IONP-Polymer, which is used to form an antigen-clustered nanoparticle (ACN) (**Figure S1b**). The antigen-cluster topography of ACNVax was achieved by conjugating antigen peptides with cysteine to the surface AuNPs of the ACN through a thiol-Au reaction (**Figure 2.2a, 2.2b)**[69-71]. The human HER2 CD4 T cell and B cell epitope (CDDD-PESFDGDPASNTAPLQPEQLQ-GGK) was used as the antigen to promote T cell-dependent B cell activation[72-74].

To control the optimal distance between antigen clusters on ACNVax at 5-10 nm, which is an ideal distance for BCR crosslinking[56, 57], we adjusted the ratio of AuNP to IONP-Polymer and calculated the distances between AuNPs on the ACNVax surface based on two methodologies (the arc length equation for a circle and the triangulation equation). The weight ratios of AuNP to IONP-Polymer at 0-30% generated ACNVax with 0-12 AuNP on each IONP-Polymer surface which correlated to 5 - 20 nm distances between antigen clusters on ACN (**Figure 2.2b-2.2d**, **S1c-1e, Table S1-S4**).

To achieve a high antigen density, we adjusted the peptide to ACN (calculated by Fe) weight ratio. The maximum peptide loadings were 232 ± 73 (0 AuNPs), 888 ± 42 (4 AuNPs), and 1954 ± 157 (12 AuNPs) peptides per ACNVax (**Figure 2.2e, 2.2f**). The nonspecific peptide binding to IONP-Polymer surface (without AuNP) was ~12% (**Figure 2.2e, 2.2f**), suggesting that most peptides were conjugated on the AuNPs of ACNVax but not on the IONP-Polymer core, which provided the antigen cluster topography.

The ACNVax was optimized with overall antigen density (~2000 peptides/ACN) and distance (~5 nm) between antigen clusters (12 AuNPs per ACN), which equates to a peptide density of 20,000–25,000 per $\mu m^2$ (**Figure S1f**), comparable to the antigen density reported for virus-like particles (e.g., hepatitis B virus, ~20,000 antigens)[55]. ACNVax with conjugated antigen was 44 ±

2 nm by dynamic light scattering (DLS) (**Figure 2.2a**) with a polydispersity index (PDI) of 0.087 ± 0.03 and a zeta potential of -16 mV ± 4 (**Table S5**). This size and surface charge are optimal for efficiently lymph node draining and penetration[53]. ACNVax was stable under *in vivo* relevant serum conditions (**Figure S2a**).

The high density of B cell epitopes crosslinks BCRs to trigger strong B cell-mediated antigen uptake[59-61]. To test if ACNVax facilitates BCR crosslinking, we used hapten-specific B cells from the spleen of QM transgenic mice to incubate with Cy3- and hapten-labeled ACNVax where hapten was conjugated at the end of HER2 B cell epitope[75]. The results showed that hapten-labeled ACNVax (red) efficiently bound to BCRs (stained with FITC-labeled antibody, green) on the hapten-specific B cells from 1-5 mins to generate cross-linked BCR clusters on the B cell surface (**Figure 2.2g, S3**)[76].

To investigate if the antigen-clustered topography of ACNVax is indeed critical for BCR crosslinking, we prepared different control groups using the same HER2 B/CD4 antigen and labeled with hapten and Cy3: (a) IONPVax using the same IONP core and surface conjugation with similar overall density of B/CD4 antigen and similar overall size, but without antigen cluster mimicry (2323 ± 394 peptides per IONPVax, 48 ± 5 nm, PDI: 0.074 ± 0.02) (**Figure S2b-S2d, Table S6**); (b) AuNPVax using the same surface AuNPs (2 nm) and same B/CD4 antigen, but without antigen cluster mimicry; (c) ACNVax-LC with longer antigen cluster distance (~20 nm between antigen cluster); (d) ACNVax-LD with lower peptide density (2% of peptide loading); (e) Soluble peptide (PepVax); (f) lipoVax (The liposome, prepared according to previous reports[63], was modified to have the same antigen uniformly conjugated on its surface with a similar overall density, but without antigen cluster topography). The image and quantification data showed that all these control groups had significantly less BCR crosslink compared to ACNVax (**Figure 2.2h, 2.2i, S3**). Specifically, ACNVax with longer antigen cluster distance and lower peptide density reduced BCR crosslink significantly compared to ACNVax with antigen density (150 peptides per AuNP, 2000 peptides/ACN) and distance (~ 5 nm) between antigen clusters (12 AuNPs per ACN). These data suggest that antigen clusters topography is critical to achieving highly efficient BCR crosslink. In addition, we also showed that longer distance between antigen clusters and/or low peptide density of ACNVax particles decreased the production of HER2 specific IgG, indicating a lower level of B cell activation (**Figure S1g**).

**ACNVax promoted B cell antigen presentation-mediated B/CD4 T cell crosstalk**

To test if BCR crosslinking by ACNVax promotes B cell antigen presentation, we compared the *in vitro* B cell uptake of antigen following incubation of hapten-specific B cells with ACNVax (hapten), IONPVax (hapten), or with PepVax (hapten) for 15 mins, 30 min, 60 mins (**Figure S4**). Results showed that more ACNVax was internalized by B cells than IONPVax and PepVax, which suggests that antigen-clustered topography of ACNVax increases uptake.

To study if ACNVax could promote B cell antigen presentation mediated B/CD4 T cell crosstalk, we engineered ACNVax with HER2-CD4/B epitope-hapten and OT-II CD4 epitope (chicken ovalbumin$_{323-339}$), incubated with hapten-specific B cells from the splenocytes of QM mice[75] (B cells labeled with CFSE tracker), then mixed with OT-II specific CD4 T cells from the spleen of OT-II transgenic mice (labeled with CFSE tracker)[77] for 24-96 h (**Figure 2.3a, S5**). IONPVax and PepVax with the same antigens were used as comparison.

To test if ACNVax could activate antigen-specific B cells, we monitored the activation and proliferation of hapten-specific B cells. The results showed that ACNVax (with HER2-CD4/B antigen-hapten and OT-II CD4 epitope) increased the activation of hapten-specific B cell by 3.5-fold (as monitored by CD86 and CD69 intensity in hapten-specific B cell, **Figure 2.3b**, **S6**) and proliferation of hapten-specific B cell by 32.7-fold (as monitored by CFSE staining) after 96 h (**Figure 2.3c, S7**) compared to other control groups with the same antigens. These data suggest ACNVax could effectively activate antigen-specific B cells.

To test if these B cells activated by ACNVax could present CD4 T cell epitope to activate antigen-specific CD4 T cells, we monitored the activation and proliferation of OT-II specific CD4 T cells. The results showed that ACNVax (with HER2-CD4/B antigen-hapten and OT-II CD4 epitope) increased activation of OT-II-specific CD4 T cell by 28-fold (as monitored by CD69 and CD25 after 96 h) and proliferation by 90-fold after 96 h compared to other control groups with the same antigens (**Figure 2.3d, 2.3e, S8, S9**). To confirm that ACNVax did not enhance non-specific CD4 T cell activation, we also monitored CD4 T cell activation from splenocytes of QM mice (not specific to OT-II CD4 epitope). The data showed that ACN (with HER2-CD4/B antigen-hapten and OT-II CD4 epitope) did not activate nonspecific CD4 T cells from QM mice (**Figure S10**). These data suggested that the T cell epitope on ACNVax was efficiently processed by B cells and presented to activate antigen specific CD4 T cells.

Furthermore, to confirm if ACNVax induced B/CD4 T cell crosstalk owing to B cell antigen presentation but not owing to other antigen presenting cells such as dendritic cells or macrophages, we depleted B cells from splenocytes of QM using CD19 positive selection kit and then co-incubated with OT-II-specific CD4 T cells from OT-II transgenic mice (**Figure S5**). The results showed that depletion of B cells impaired ACNVax activation of OT-II-specific CD4 T cells

(**Figure 2.3f, 2.3g, S11-S13**). These suggest that B cell and CD4 T cell crosstalk by ACNVax is indeed mediated by B cell antigen presentation.

**ACNVax efficiently penetrated into lymph node and induced a robust Tfh-dependent B cell response.**

A robust Tfh-dependent B cell response requires efficient delivery of antigen to lymph nodes to encounter B cells. We employed 2D and 3D confocal fluorescent imaging to assess the homing efficiency of ACNVax to the draining lymph nodes. The results showed that FITC-labeled ACNVax penetrated deep inside lymph nodes where B cells reside in both B cell zone and cortex (**Figure 2.4a, S14, S32**). As a comparison, IONPVax without antigen-clustered topography was mainly localized on the surface of the lymph nodes (**Figure S14, S33**). We also tested antigen uptake by B cells in the lymph nodes in mice by IVIS following injection (s.c.) **(Figure S15a and S15b**). Results showed that more ACNVax was internalized by B cells than other control groups, which suggests that antigen-clustered topography of ACNVax increases B cell uptake.

To study how ACNVax stimulates the immune responses *in vivo*, we used CyTOF to investigate immune cell composition in the draining lymph nodes of normal BALB/c mice 10 days after three vaccinations (**Table S7, Figure S16**)[78]. Global analysis using spanning-tree progression analysis of density-normalized events (SPADE) confirmed that ACNVax induced a higher level of GC B, Tfh and plasma cells in the lymph nodes and HER2 Specific antibody titer serum than IONPVax and PepVax groups (**Figure 2.4b, 2.4c**), whereas CD8 T cell frequency was not changed after vaccination (**Figure 2.4b**). This result suggests ACNVax induced a robust Tfh-supported GC response.

To confirm the results by flow cytometry and further evaluate the antigen specific GC B and Tfh cells, we enumerated GC B cells and Tfh CD4 T cells in the lymph nodes of BALB/c mice after three vaccinations with ACNVax (at day 24) and in comparison with mice vaccinated with IONPVax or with PepVax of the same antigens. Flow cytometry analysis showed that ACNVax generated a robust GC B cell response (16.21% of all B cells) and antigen-specific GC B cells (7.6% of all GC B cells), which is 2 to 5-fold higher than PepVax or IONPVax groups (**Figure 2.4d, 2.4e, S17a, S17b**). ACNVax vaccinations also increased Tfh cells by 4.7-fold and 3-fold compared to PepVax and IONPVax (**Figure 2.4f, S17c**).

To determine if ACNVax vaccination activated antigen specific Tfh cells, we used the activation-induced markers (AIM) assay to measure antigen-specific Tfh cells activation. ACNVax vaccination increased the frequency of antigen specific Tfh cells by 4.2-fold (**Figure 2.4g, 2.4h,**

**S18**) and the frequency of antigen-specific CD4 T cells by 4.5-fold (**Figure 2.4g, 2.4i, S19**) compared to IONPVax and PepVax vaccinations.

Since robust GC responses generate robust antigen-specific IgG, we examined the HER2 specific IgG in serum after three vaccinations on day 38. ACNVax vaccination generated a 4-fold higher HER2-specific IgG titer, a 3-fold higher HER2-specific IgG1 titer, and a 5-fold higher HER2-specific IgG2a titer than vaccination with IONPVax (**Figure 2.4c, S20a-S20d**). The HER2 antibody specificity was confirmed by testing antibody binding to D2F2/E2 $HER2^+$ cell line by flow cytometry (**Figure S20e-S20g**). These data suggest that ACNVax with the antigen cluster structure uniquely enhanced the Tfh-dependent B cell response and antigen-specific IgG production comparison with nanoparticles with the same core but uniformly distributed antigen on their surface (IONPVax) or PepVax.

**ACNVax combined with anti-PD-1 antibody achieved long-term remission of $HER2^+$ breast cancer**

To compare the efficacy of ACNVax combined with anti-PD-1 antibody to current clinically approved treatment options for $HER2^+$ cancer, we used three vaccinations (day 4, 11, 18) in BALB/c mice with subcutaneous $HER2^+$ breast cancer using HER2 overexpression mouse cancer cell line (D2F2/E2)[79]. The results showed ACNVax plus anti-PD-1 had much better tumor inhibition effect compared to murine HER2 antibody (**Table S8**) plus anti-PD-1, clinically tested Neu-Vax vaccine (composed of E75 as HER2 CD8 epitope and GM-CSF) plus anti-PD-1, and anti-PD-1 alone (**Figure 2.5a**)[80-83].

To investigate how antigen-clustered topography in ACNVax influenced its anticancer efficacy, we compared its efficacy with IONPVax (the core component of ACN 35 nm with antigen uniformly conjugated on the nanoparticle surface, but without antigen cluster structure), the AuNP- B/CD4 (the surface component of ACN 2-5 nm, but without antigen cluster structure) and lipoVax (liposome with antigen uniformly conjugated on the nanoparticle surface, but without antigen cluster topography). The data showed that ACNVax after 3 vaccinations induced significantly better tumor inhibition with 57% complete response (CR) compared to other nanovaccine groups, which only slightly inhibited tumor growth with no CR (0%) (**Figure 2.5b**). These data suggest that the antigen-clustered structure of ACNVax indeed plays a critical role for its superior anticancer efficacy than IONPVax and AuNPVax.

Since the presence of TLS, along with B/CD4 T cell crosstalk, is associated with better responses to anti-PD-1 immunotherapy[35-39]. We combined a peptide of LIGHT, a member of the tumor necrosis factor (TNF) ligand family that can stimulate immune cell tumor infiltration and TLS formation[67, 68], with ACNVax to test whether it could enhance anticancer activity further. LIGHT has been previously reported to induce robust de novo formation of TLSs in tumors and to greatly enhance anti-tumor immune responses and efficacy[67, 68]. ACNVax (with LIGHT) combined with anti-PD-1 antibody (three vaccination doses) inhibited tumor growth by 96% and achieved long-term cancer remission (>200 days) with a complete response (CR) rate of 44% (**Figure 2.5c**), which is more significant than ACNVax (without LIGHT) plus anti-PD-1 antibody (cancer growth inhibition by 85%, CR rate of 11%). Following a clinical used dose regimen (five vaccination at day 4, 11, 18, 32, 46), ACNVax (with LIGHT), combined with anti-PD-1 antibody, enhanced the complete response (CR) rate to 80% (>200 days, **Figure 2.5d**). In contrast, both IONPVax and PepVax plus anti-PD-1 only slightly inhibited tumor growth. The addition of LIGHT did not significantly improve the anticancer efficacy in either the IONPVax plus anti-PD-1 or PepVax plus anti-PD-1 groups (**Figure 2.5d**). In addition, ACNVax-T, which used the same ACN but conjugated with the HER2 CD8 T cell epitope (E75), did not significantly inhibit tumor growth (vs. control) (**Figure 2.5c**). These results demonstrated that ACNVax with LIGHT achieve long-term anticancer efficacy in HER2 positive breast cancer.

To test if ACNVax would show therapeutic efficacy in HER2-low breast cancer, we tested the efficacy of ACNVax on two mouse breast cancer models with low HER2 levels: transgenic PyMT-MMTV breast cancer and 4T1 subcutaneous breast cancer (**Figure S21**)[84,85]. The data showed that ACNVax had significant better anticancer efficacy than control and PepVax groups on PyMT-MMTV and 4T1 tumor mouse model (**Figure S21)**. Because 70% of breast cancer patients show a low-level expression of HER2 (HER2-low) despite not defined as HER2 positive tumor[86], these data suggest that ACNVax may offer therapeutic advantages in broad range of breast cancer populations.

## ACNVax induces B/T lymphocytes infiltration into the tumor.

To understand how ACNVax influences immune cell infiltration in tumor, we used CyTOF to profile all immune cells in tumor tissues from BALB/c mice with subcutaneous $HER2^+$ breast cancer (D2F2/E2) at 28 days after vaccination. The cell composition in tumor tissues was compared in mice treated with anti-PD-1 antibody, anti-PD-1 and murine HER2 antibody, and a CD8 T cell vaccine NeoVax (E75and GM-CSF). Results showed that ACNVax combined with anti-PD-1 antibody dramatically increased the frequency of tumor-infiltrating B cells by 13.7-fold, CD4 T

cells by 9.5-fold and CD8 T cells by 5.2-fold among total cells in tumor compared to the other treatment groups (**Figure 2.6, S16, S22, Table S9**).

### ACNVax remodels the tumor immune microenvironment.

To comprehensively analyze how ACNVax remodels the tumor immune microenvironment, we performed single-cell RNA-seq of tumor immune cells from BALB/c mice with $HER2^+$ breast cancer after vaccination with ACNVax, ACNVax with LIGHT or IONPVax in combination with anti-PD-1 antibody.

Single-cell RNA-seq analysis results suggest that ACNVax (w/o LIGHT) enhances B and CD4 T cell interaction in tumors than IONPVax and control group. For instance, ACNVax (B cells: 14.99%, CD4 T cells: 14.74%) and ACNVax/LIGHT (B cells: 16.53%, CD4 T cells: 10.41%) showed significantly higher proportions of B cells and CD4 T cells than those of the IONPVax group (B cells: 10.33%, CD4 T cells: 7.15%) (**Figure 2.7a, 2.7b**). ACNVax induced higher levels of CD40 in B cell and CD40L gene expression in T cell (**Figure 2.7c, S23a, S23b**) than vaccination with IONPVax or control treatments. CD40 and CD40L are implicated in effective B and CD 4 T cell interactions. ACNVax vaccination also induced significantly higher expression of *Aicda* in B cells in tumors than IONPVax vaccination or control treatments. *Aicda* encodes the enzyme needed to initiate somatic hypermutation and Ig gene class switch recombination, features of effective germinal center responses[87, 88]. Furthermore, ACNVax increased the expression of genes relate to GC-Tfh responses, including BCL-6 and IL21 compared to IONPVax or control groups (**Figure 2.7c, S23a, S23b**). These data suggest that ACNVax induced a potent CD4 T cell-dependent B cell activation in tumors compared to IONPVax and control groups.

Since anticancer immune response relies on CD4 and CD8 T cell activation, and previous reports suggested Tfh-dependent B cell activation promote anticancer CD4 and CD8 T cell immunity[35, 37, 41, 42], we further investigated if ACNVax altered the subpopulations of CD4 T cells (memory, regulatory, and Tfh) and CD8 T cells (memory, cytotoxic, and exhausted) in tumors, in comparison with IONPVax and control group. Among different sub-population of CD4 T cells, vaccination with ACNVax (combined with anti-PD-1) increased 1.5 to 3-fold memory CD4 T cells, increased 1.5 to 5-fold Tfh, and decreased 1.5 to 2-fold Treg in tumors compared to vaccination with IONPVax (combined with anti-PD-1) or control group (**Figure 2.7d, S24a**). Among different sub-populations of CD8 T cells, ACNVax vaccination (combined with anti-PD-1) increased memory CD8 T cells by 9-fold, cytotoxic CD8 T cells by 3.5-fold, and decreased exhausted CD8 T cells by 20-fold compared to control groups. ACNVax increased memory CD8 T cells by 1.5-fold in comparison with vaccination with IONPVax (**Figure 2.7e, S24b**). In addition, ACNVax also

induced higher expression of genes encoding antitumor cytokines, such as interferon-gamma, tumor necrosis factor, interleukins and granzyme B, in immune cells and T cells than IONPVax or control groups (**Figure 2.7f, S23b, S23c**). This data demonstrated the effect of ACNVax to promote CD4 and CD 8 T cells response and anticancer cytokine production, which may explain the potent anticancer efficacy of ACNVax.

Single-cell RNA-seq analysis results also suggested that ACNVax increased gene expression related to organized aggregates of immune cells formation in tumors compared to the IONPVax and control treatments (**Figure 2.7f, S23c**). ACNVax increased the levels of the chemotaxis factors CCL19, CCL21a, CXCL13 and CCL2 compared with those of the IONPVax and control (**Figure S23a, S23b**). ACNVax also induced increased gene expression of receptors for chemotaxis factors and adhesion receptors, such as CXCR4, CXCR5, CCR7 and L-selectin, CD11a and VLA-4, in tumor infiltrating B and T cells compared with those of the IONPVax and control groups (**Figure S23a, S23b**), similar to literature reports[35, 36,37]

To confirm the formation of organized aggregates of immune cells, we use both fluorescent staining to analysze tumor tissues after vaccination (**Figure 2.7g, S25, S26**). Fluorescent staining showed that ACNVax plus anti-PD-1 antibody (with LIGHT) increased the presence of TLS-like structure, where B cells (CD20, **Figure 2.7g, S25, S26**) were surrounded by T cells (CD3, **Figure 2.7g, S25, S26**). We also observed the presence offollicular dendritic cells (CD23, CD21/CD35 (CR1/CR2), **Figure 2.7g, S25**) with scattered high endothelial venules (PNAd, **Figure 2.7g**) in ACNVax plus anti-PD-1 antibody (with LIGHT) group in comparison with other treatment groups. similar to the literature TLS[35, 36, 89].

**ACNVax induced long-term antigen-specific memory B cells, CD4 T cells, and CD8 T cells**

To test whether ACNVax vaccination induced a persistent immune memory against cancer growth, we rechallenged five mice whose tumors were eliminated after three vaccinations at 200 days by subcutaneous injection of $2.5 \times 10^5$ D2F2/E2 $HER2^+$ cancer cells. The data showed that each of the five mice completely rejected tumors whereas every unvaccinated mouse rapidly grew tumors (**Figure 2.5, 2.8a**). The results demonstrated that ACNVax vaccination generated long-term persistent immune memory against cancer growth.

To further examine whether ACNVax vaccination could generate long-term antigen-specific memory B, CD4, and CD8 T cells, we used flow cytometry and activation-induced markers (AIM) assay to enumerate these cells in the mice that rejected tumors following re-challenge.

ACNVax vaccination increased class switch memory B cells ($B220^+$ $CD38^+$ $GL\text{-}7^-IgD^-$ $IgM^-$) by 3.5-, 2.5-, 2-, 1.5-fold in spleen, lymph nodes, bone marrow, and peripheral blood, respectively **(Figure 2.8b, S27)**; increased antigen-specific class switch memory B cells ($B220^+$ $CD38^+$ $GL\text{-}7^-$ $IgD^-$ $IgM^-$ $Tetramer^+$) by 10-, 13-, 7-, and 5.6-fold in in spleen, lymph nodes, bone marrow, and peripheral blood, respectively (**Figure 2.8c, S27**); and increased antigen-specific plasma cells (markers) by 20-fold in the bone marrow of the mice (**Figure S28**), in comparison with control mice.

ACNVax vaccination induced CD4 T effector memory cells (CD4 TEM: $CD8^-$ $CD4^+$ $CD44^+$ $CD62L^-$) by 2-fold in the lymph nodes and peripheral blood (**Figure 2.8d, S29**); increased antigen-specific CD4 T effector memory cells ($AIM^+$ CD4 TEM: $CD8^-$ $CD4^+$ $CD44^+$ $CD62L^-$ $CD69^+CD40L^{+/-}$) by 14-fold in the spleen (**Figure 2.8e, S30a**); increased CD4 T central memory cells (CD4 TCM: $CD8^-$ $CD4^+$ $CD44^+$ $CD62L^+$) by 10- and 7-fold in the lymph nodes and peripheral blood, respectively, (**Figure 2.8d, S29**); increased antigen-specific CD4 T central memory cells ($AIM^+$ CD4 TCM: $CD8^-$ $CD4^+$ $CD44^+$ $CD62L^+$ $CD69^+$ $CD40L^{+/-}$) by 12.5-fold in the spleen (**Figure 2.8e, S30a**); increased tissue resident memory CD4 T cells (CD4 TRM: $CD8^-CD4^+$ $CD69^+$ $CD103^+$) by 3.5- and 9.8-fold in the fat pad and lungs of the mice, respectively, (**Figure S31a-S31c**), in comparison with control mice.

ACNVax vaccination also increased CD8 T effector memory cells (CD8 TEM: $CD4^-CD8^+$ $CD44^+$ $CD62L^-$) by 3.6-fold, 3.3-fold in the lymph nodes and peripheral blood, respectively (**Figure 2.8f, S29**); increased antigen-specific CD8 T effector memory cells ($AIM^+$ CD8 TEM: $CD4^-$ $CD8^+$ $CD44^+$ $CD62L^-$ $CD25^+$ $OX40^{+/-}$) by 6-fold in the spleen (**Figure 2.8g, S30b**); increased CD8 T central memory cells (CD8 TCM: $CD4^-$ $CD8^+$ $CD44^+$ $CD62L^+$) by 5-fold in the lymph nodes and peripheral blood (**Figure 2.8f, S29**); increased antigen-specific CD8 T central memory ($AIM^+$ CD8 TCM: $CD4^-CD8^+$ $CD44^+$ $CD62L^+$ $CD25^+OX40^{+/-}$) by more than 10-fold in the spleen (**Figure 2.8g, S30b**); increased tissue resident memory CD8 T cells (CD8 TRM: $CD4^-$ $CD8^+$ $CD69^+$ $CD103^+$) by 2.5- and 19.3-fold in the fat pads and lungs of mice, respectively (**Figure S31a, S31b, S31d**), in comparison with control mice.

Our results suggest that ACNVax induced a persistent anti-cancer immune memory through promoting long-term antigen-specific memory B, CD4 T and CD8 T cells. Since ACNVax vaccinations does not contain CD8 T cell epitope, the increased CD8 memory cells are likely as a secondary consequence of anti-tumor CD4 T and B cells activation in response to tumor antigens.

## 2. 4 Discussion and Conclusion

The development of therapeutic cancer vaccines has mainly focused on T cell cancer vaccines, but these have had limited clinical success. Inspired by recent findings that B cell tumor infiltration and and B/CD4 T cell crosstalk are strongly associated with better clinical efficacy of checkpoint blockade immunotherapy, we designed a antigen-clustered nanovaccine (ACNVax) that achieved long-term tumor remission with a complete response rate of 80% (>200 days, **Figure 2.5**) when combined with anti-PD-1 antibody. Unlike other T cell cancer vaccines, ACNVax achieved superior anticancer efficacy by promoting B cell antigen presentation-mediated B/CD4 T cell crosstalk (**Figure 2.3**)[50, 52, 53, 56, 57, 59-61, 66, 90-92], Tfh dependent B cell activation (**Figure 2.3 and 2.4**), and remodeling tumor immune microenvironment (**Figure 2.6 and 2.7**). The long-term efficacy of ACNVax was mediated by a concerted long-term antigen-specific memory B cell, CD4 T, and CD8 T cell immunity (**Figure 2.1 and 2.8**). The ACNVax has an antigen-clustered topography on its surface, featuring a high density of HER2 B and CD4 T cell epitopes on the cluster (150 peptides/cluster) and optimal distance (5-10 nm) between antigen clusters for efficient crosslink with BCR (**Figure 2.2**)[56, 57, 59-61, 65, 90-92]. This unique topography promoted lymph nodes trafficking (**Figure 2.4**), crosslinking with B cell receptor (BCR) (**Figure 2.2**), and B cell antigen presentation-mediated B/CD4 T cell crosstalk (**Figure 2.3**)[50, 52, 53, 56, 57, 59-61, 66, 90-92]. Subsequently, ACNVax promoted very strong Tfh-dependent GC responses in lymphoid organs as measured by both CyTOF and flow cytometry. More importantly, ACNVax remodeled the tumor immune microenvironment by enhancing infiltration of B cells, CD4 and CD8 T cells as measured by both CyTOF and single-cell RNA-seq. In addition, ACNVax, combined with anti-PD-1, not only activated long-term antigen-specific B and CD4 T cell memory, but also generated long-term antigen-specific CD8 T cell memory (**Figure 2.7, 2.8**), which contributed to its efficacy in complete rejection of tumor rechallenges at 222 days in cured mice with $HER2^+$ breast cancer (**Figure 2.8**).

The findings in our study have two important implications. First, our study suggests that incorporating B cell immunity in the cancer vaccine design by promoting B cell antigen presentation- mediated B/CD4 T cell crosstalk achieves long-term durable anticancer efficacy when combined with anti-PD-1 immunotherapy. Second, the cancer vaccine design for this purpose needs an optimal delivery system, which facilitate lymph node penetrate allowing antigen to direct interact with B cells for BCR crosslinking and B cell antigen presentation mediated B/CD4 T cell crosstalk. Most other nanoparticle systems, which encapsulate the antigen inside, would enhance uptake and antigen presentation by DCs or macrophages since the function of these APCs is to uptake nanoparticles; but those nanoparticle delivery systems would not able to

enhance the uptake and antigen presentation by B cells since B cell antigen presentation requires antigen binding to BCR to trigger crosslink[19, 50]. Our ACNVax with antigen-clustered topography, which has high density of antigens on the cluster and optimal distance (5-10 nm) between antigen clusters, is more efficiently to crosslink with BCR, promoting B cell antigen presentation-mediated B/CD4 T cell crosstalk compared to IONPVax without surface antigen cluster structure. Furthermore, ACNVax vrial like structure might also enhance lymph node draining and penetrationto induce B/CD4 T cell crosstalk[50, 93].

In conclusion, our data provide a novel cancer nanovaccine design with B/CD4 epitopes in an antigen-clustered topography to achieve long-term durable anticancer efficacy by promoting B cell antigen presentation-mediated B/CD4 T cell crosstalk and remodeling tumor immune microenvironment.

### 2.5 Methods

#### Materials

All reagents were obtained from commercial sources without further purification, except γ-methacryloxypropyltrimethoxysilane (98%), which was purified by distillation under reduced pressure, and 2,2-azobis(isobutyronitrile) (98%), which was purified by recrystallization in ethanol. Iron oxide (III) (FeO(OH), hydrated, catalyst grade, 30−50 mesh), oleic acid (technical grade, 90%), ammonium iron (II) sulfate hexahydrate (ACS reagent, 99%), 1-octadecene (technical grade, 90%), anhydrous tetrahydrofuran (THF, 99.8%), carbon disulfide (99.9%), magnesium turnings (>99.5%), 2-chloro-2-phenylacetyl chloride (CPAC, 90%), poly(ethylene oxide) monomethyl ether (PEO), anhydrous dioxane (99.8%), dimethylformamide (DMF, 99.9%), dimethyl sulfoxide (DMSO, 99.9%), o-phenanthroline monohydrate (ACS reagent, 99%), hydroquinone (ACS reagent, 99%, sodium sulfide, chloroauric acid, nitric acid (ACS reagent, 70%), and hydrochloric acid (ACS reagent, 37%) were purchased from Sigma-Aldrich. Dulbecco's phosphate-buffered saline (DPBS) and Hank’s buffered salt solution (HBSS) were obtained from Fisher Scientific. Mouse uncoated IgG and IgM Total ELISA Kits, 1-Step Ultra TMB-ELISA substrate solution, HRP-conjugated goat anti-mouse IgG1 secondary antibody, HRP-conjugated goat anti-mouse IgG2a secondary antibody, Nunc Immobilizer Amino 96-well ELISA plates, BupH carbonate bicarbonate buffer packs (coating buffer), Pierce protein-free PBS-tween blocking buffer, 20x PBS-Tween wash buffer, geneticin (G418) selective antibiotic, Invitrogen eBioscience fixable viability dye eFluor 780, and Molecular Probes streptavidin Alexa Fluor 647 conjugate were obtained from Thermo Fisher Scientific. The EasySep™ Mouse B Cell Isolation Kit,

EasySep™ Mouse CD4 T Cell Isolation Kit, and EasySep™ Mouse CD19 Positive Selection Kit II were purchased from StemCell Technologies. Fluo-4 AM was purchased from Thermo Fisher Scientific. AF488-AffiniPure Fab Fragment Goat Anti-Mouse IgM and μ Chain Specific were purchased from Jackson Immuno Research Laboratory Inc. Alexa Fluor™ Plus 405 phalloidin was purchased from Thermo Scientific. Anti-mouse PD-1 antibody (CD279) was purchased from Bio X Cell. Mouse GM-CSF was obtained from SHENANDOAH Biotechnology Inc. LIGHT (TNFSF14) was purchased from Sino Biological. HRP-conjugated goat anti-mouse IgG secondary antibody, Zombie UV fixable viability kit, FITC anti-mouse CD19, PE/Dazzle 594 anti-mouse IgD, Alexa Fluor® 647 anti-mouse/house GL7 antigen, Brilliant Violet 421 and PE/Dazzle 594 anti-mouse/human CD45R/B220, FITC anti-mouse CD95, Brilliant Violet 421 anti-mouse/human CD11b, Alexa Fluor® 647 anti-mouse CD21/CD35 (CR2/CR1), Alexa Fluor® 594 anti-mouse CD169, FITC anti-mouse CD169 and PE goat anti-mouse IgG secondary antibody, FITC anti-mouse CD19, Brilliant Violet 605 anti-mouse CD19, Alexa Fluor® 594 anti-mouse CD19, APC/Cyanine7 anti-mouse CD86, and FITC anti-mouse CD3 were purchased from BioLegend. HER2 peptides (CDDDPESFDGDPASNTAPLQPEQLQ (Human HER2 CD4/B epitope), Biotin-PESFDGDPASNTAPLQPEQLQ, CDDDPESFDGDPASNTAPLQPEQLQGGGK, CDDDPESFDGDPASNTAPLQPEQLQ-GGG-Lys (NP), CDDDPESFDGDPASNTAPLQPEQLQ-(Lys(N3)-DBCO-Cy3) -GGG-(Lys (NP)), CDDDPESFDGDPASNTAPLQPEQLQ-EDFITC), CDDDKIFGSLAFL (Human/Mouse HER2 CD 8 epitope) and E75 (KIFGSLAFL, Human/Mouse HER2 CD 8 epitope), $OVA_{323-339}$ (CISQAVHAAHAEINEAGR, recognize by CD4 T cell from OT-II mice) were custom synthesized by LifeTein. Iron oxide nanoparticles (30 nm) stabilized by oleic acid in chloroform were purchased from Ocean Nanotech. Cyclic [G(2′,5′)pA(3′,5′)p] (2′3′-cGAMP) was acquired from InvivoGen. Fluorescamine was purchased from MP Biomedicals. Sulfo-Cy5.5 NHS ester was acquired from Lumiprobe. Microvette 500 Z-Gel serum collection vials with clotting factors were obtained from Sarstedt. Matrigel basement membrane matrix was purchased from Corning. Gold and iron standards were purchased from Fluka Analytical. Murine HER2 antibody (Murine 2C4)[94]: Mouse IgG2a constant chain chimeric with same variable region as human pertuzumab (Perjeta®) were purchased from GenScript. The amino acid sequences of murine 2C4 are listed in **Table S8**.

**Mice**

All animal experiments were conducted according to protocols approved by the University of Michigan Committee on Use and Care of Animals (UCUCA). BALB/c mice aged 5−7 weeks were purchased from Charles River Labs (Wilmington, MA).

## Cells

All cells were maintained at 37 °C in a 5% $CO_2$/95% air atmosphere and approximately 85% relative humidity. D2F2/E2 cells were generated by cotransfection with pRSV/neo and pCMV/E2 encoding human ErbB-2 (HER2) (provided by Dr. Wei-Zen Wei)[79]. The cells were cultured in complete high-glucose DMEM supplemented with 10% NCTC 109 media, 1% L-glutamine, 1% MEM nonessential amino acids, 0.5% sodium pyruvate, 2.5% sodium bicarbonate, 1% pen/strep, 5% cosmic calf serum, and 5% fetal bovine D2F2/E2 cells generated by cotransfection with pRSV/neo and pCMV/E2 encoding human ErbB-2 (HER2), 500 μg/mL geneticin and 50 μM 2-mercaptoethanol. RAW264.7 macrophages were cultured in complete RPMI-1640 media supplemented with 10% fetal bovine serum, 1% L-glutamine, 1% MEM nonessential amino acid solution, 1% sodium pyruvate and 1% pen/strep. Primary B-cells, CD4 T cells and splenocytes were cultured in RPMI-1640 media supplemented with 10% fetal bovine serum, 2-Mercaptoethanol (50 μM) and 1% pen/strep. 4T1 cells were cultured ATCC-formulated RPMI-1640 Medium with 10% fetal bovine serum and 1% pen/strep.

## Preparation and characterization of ACN

ACN was prepared based on previously reported protocols[70]. IONP-Polymer were made by thermal decomposition and further coated with a polysiloxane-containing copolymer. AuNPs (2 nm) were synthesized by reacting sodium sulfide ($Na_2S$) as the reducing reagent with gold in the form of chloroauric acid (HAuCl4). AuNPs were then attached onto the surface of IONP-Polymer to produce a spiky topography. The final Au:Fe ratio of the formulated ACN was quantified by inductively coupled plasma–mass spectrometry (ICP-MS) using a Perkin-Elmer Nexion 2000 based on previously reported protocols modified from the analysis by inductively coupled plasma–optical emission spectroscopy (ICP-OES)[95]. ACN formulations were imaged by STEM using a JEOL 2100F with a CEOS probe corrector. The true particle sizes of AuNPs, IONP-Polymer and ACN were quantified using ImageJ software. The volume-weighted hydrodynamic particle size, polydispersity index and zeta potential of all formulations in Milli-Q water at 25 °C were evaluated with a Malvern Zetasizer Nano-ZS using DLS and phase analysis light scattering, respectively.

## Preparation and characterization of lipid-coated IONP

Lipid-coated iron-oxide nanoparticles were prepared by the thin-film hydration method based on previously reported methods[96]. DSPE-PEG (2000)-maleimide (10 mg) was added to 1 mg of 30-nm iron-oxide nanoparticles stabilized by oleic acid in chloroform and gently mixed. The resulting

solution was subjected to solvent rotary evaporation to remove all chloroform and form a thin film. Simultaneously, this film and 100 mM PBS pH 7.4 were heated to 75 °C in an oven. When it reached 75 °C, hot PBS was rapidly added to the film and mixed immediately and vigorously to facilitate thin film hydration. The resulting nanoparticle solution was stored at 4 °C to promote lipid self-assembly. Free phospholipids were removed by magnetic separation overnight at 4 °C using an EasySep™ magnetic separator device (StemCell Technologies). The volume-weighted hydrodynamic particle size, polydispersity index and zeta potential of all formulations in Milli-Q water at 25 °C were evaluated with a Malvern Zetasizer Nano-ZS using DLS and phase analysis light scattering, respectively.

**Preparation and characterization of ACNVax and IONPVax**

HER2 peptides were conjugated to ACNVax via a gold-thiol linkage. HER2 peptide was added to ACNVax at a 5× weight ratio excess in Milli-Q water and incubated overnight at 4 °C. HER2 peptides were conjugated to lipid coated IONP via maleimide-thiol chemistry. Both materials were purified either by magnetic separation overnight at 4 °C or by centrifugal separation at 10,000 × g for 30 minutes at 4 °C. Peptide loading was determined by fluorescence quantification using a modified fluorescamine peptide quantification assay in the presence of ACN or IONP-Lipid (Ex/Em: 390/465 nm, Biotek Cytation 5)[97]. Quantification was performed using a standard curve with increasing peptide concentration with a standardized concentration of nanoparticles (IONP-Lipid or ACN) to account for quenching effects.

**Investigation of BCR crosslink**

***Crosslinking activation imaging[76]:*** B cells were isolated from splenocytes of QM mice through negative selection using the EasySep™ Mouse B Cell Isolation Kit (STEMCELL: 19854).

B cells isolated from QM mice (5 * $10^6$ cells/mL) were then incubated with 20 µg/ml Alexa Fluor 488-AffiniPure Fab Fragment Goat Anti-Mouse IgM (µ Chain Specific) on ice for 30 minutes in the dark (Jackson: 115-167-020). Cells (2 × $10^6$ cells/mL) were washed and then incubated with antigen (equal amount of epitope, 20 nM, Cy3 labeled and NP conjugated) in a total volume of 400 µL for 1 minute and 5 minutes at 37 °C. After antigen incubation, cells were fixed with 6% paraformaldehyde (800 µL) for 10 minutes immediately at 37 °C, permeabilized with a 0.1% Triton X HBSS solution (800 µL) for 10 minutes, and then incubated with Alexa Fluor™ Plus 405 phalloidin in staining buffer (200 µL, 5 mg/mL BSA, 0.1% Triton X in HBSS) on ice for 2 hours.

After two washes, the cells were plated onto eight-well glass chambers pretreated with 0.1% poly-l-lysine (LabTech II) on ice for at least 4 hours before confocal imaging.

***Calculation of crosslinking ratio:*** Cells with significant red (B cell receptors, (BCRs)) fluorescence were circled and quantified in ImageJ (NIH) to calculate the fluorescence intensity of different channels (blue, phalloidin; red, BCRs; green, antigen) in all images. The intensity of green (antigen) fluorescence was divided by the intensity of red (BCR) fluorescence to calculate the crosslinking ratio of the cells. Up to 50 cells (10 cells from each corner of images and 10 cells from middle) in each image (or all cells if there were fewer than 50 cells) were used to calculate the crosslinking ratio for each time point of each sample:

$$Crosslinking\ Ratio = \frac{Fluorescent\ Intensity\ of\ antigen\ (Green)}{Fluorescent\ Intensity\ of\ BCR\ (Red)}$$

**Investigation of B/CD4 T cell crosstalk *in vitro***

CD4 T cells were isolated from splenocytes of OT-II mice (The Jackson Laboratory, Strain, #004194) through negative selection using the EasySep™ Mouse CD4 T Cell Isolation Kit (STEMCELL: 19852). B cells were isolated from splenocytes of QM mice through negative selection using the EasySep™ Mouse B Cell Isolation Kit (STEMCELL: 19854). Splenocytes from QM mice deplete B cells through positive selection using the EasySep™ Mouse CD19 Positive Selection Kit II (STEMCELL: 18954). For activation and proliferation, markers, CD4-PE; B220-Alexa Fluor 594, CD69-Brilliant violet 421, CD86-Alexa Fluor 647, CD25-APC/Fire750 and CFSE are used. All antibody markers are from Biolegend.

Cell mixtures within each well of 24 well plate including: CD4 T cells (0.5 million, labeled with CFSE) isolated from splenocytes of OT-II mice, B cells (1 million, labeled with CFSE) isolated from splenocytes of QM mice, full slpeenocytes (1.5 million, no CFSE label) from QM mice. Cell mixtures are then coincubated with soluble peptides, IONPVax and ACNVax for 24h, 72h and 96h (All with the same amount of antigens, OT-II CD4 epitope, $OVA_{323-339}$ (CISQAVHAAHAEINEAGR), 2 μM and hapten conjugated HER2 B/CD4 epitope, CDDDPESFDGDPASNTAPLQPEQLQ-GGG-(Lys (hapten), 2 μM). After each time point, cells are collected for flow cytometry analysis.

**Immunofluorescence staining of lymph nodes**

To determine the ACNVax (conjugated to ED-FITC labeled HER2-B/CD4 peptide, 233.6 nmol HER2 epitope) distribution, lymph nodes were harvested 12 hours after subcutaneous injections.

Harvested tissues were immediately fixed in 1% paraformaldehyde for 1 hour and then immersed in 30% sucrose in 0.1% $NaN_3$ in PBS overnight. Treated tissues were then embedded in optical coherence tomography (OCT) compound and frozen in a $CO_{2(s)}$ + EtOH bath. Tissue sections (15 µm) were prepared and dried for 0.5 hours before staining. After incubation with blocking buffer and staining solution, slides were mounted with VECTASHIELD® Mounting Medium for confocal imaging. Brilliant Violet 421 B220, Alexa Fluor® 594 CD 3 and Alexa Fluor® 647 CD169 were used for lymph node immune fluorescence staining.

**CyTOF analysis of immune patterns from lymph nodes and tumors**

Lymph node and tumor samples were harvested and dissociated into single-cell suspensions 10 days after the second booster vaccination. CyTOF antibody conjugation and data acquisition were done as previously described[98, 99]. Briefly, antibodies were conjugated to lanthanide metals (Fluidigm) using the Maxpar Antibody Labeling Kit (Fluidigm). Unstimulated single-cell suspensions were washed once with heavy-metal-free PBS and stained with 1.25 µM Cel1-ID cisplatin-195Pt (Fluidigm) at room temperature for 5 minutes. Fc receptors were blocked with TruStain FcX (anti-mouse CD16/32, Biolegend), and surface staining was done on ice for 60 minutes. Cells were then fixed with 1.6% paraformaldehyde and permeabilized with Invitrogen permeabilization buffer before intracellular antibody staining. Cells were left in 62.5 nM Cell-ID intercalator iridium-191/193 (Fluidigm) in 1.6% paraformaldehyde in PBS overnight at 4 °C before acquisition on a CyTOF Helios system (Fluidigm). A signal-correction algorithm based on the calibration bead signal was used to correct for any temporal variation in detector sensitivity.

CyTOF data were analyzed as previously described[99]. All events were gated to remove noncellular events (negative for DNA intercalator), dead cells (negative for uptake of cisplatin), and doublets. SPADE clustering and the viSNE algorithm were applied using the Cytobank platform. SPADE nodes were manually bubbled based on phenotypic markers, and viSNE populations were manually gated using the same markers.

**Analysis of germinal center B cells, antigen-specific germinal center B cells and T follicular helper cells by flow cytometry**

Mice were immunized as described in manuscripts. At day 10 after the second booster, mice were sacrificed, and lymph nodes were dissected for *ex vivo* analysis by flow cytometry. $CD3^-B220^+$ $CD95^+$ $GL\text{-}7^+$ populations were identified as germinal center B cells. Germinal center derived antigen-specific B-cell analysis was accomplished using tetramer staining based on previously

established protocols with minor modifications[100]. HER2/neu peptide tetramers were prepared by mixing biotin-labeled HER2 peptide with brilliant violet 421-labeled streptavidin at an 8:1 molar ratio at room temperature for 1 hour without further purification. Markers used are, CD3-Alexa Fluor 647, B220-APC/Fire750, CD95-brilliant violet 605, GL-7-FITC. $B220^{-}CD4^{+}$ $CXCR5^{+}$ $PD\text{-}1^{+}$ populations were identified as Tfh cells. Markers used are, CD4-FITC, B220-Alexa Fluor 594, CXCR5-brilliant violet 421, PD-1- APC/Fire750.

**Analysis of Activation Induced Marker assay for T cells by flow cytometry[101, 102]**

Mice were immunized as described in manuscripts. At day 10 after the second booster, mice were sacrificed, and spleen were harvest for single cell suspension. Spleen cells (2 million) from different vaccination groups were then incubated with HER2-B/CD4 peptide (2 μg/mL) for 20h at 24 well plate. After incubation, cells were then collected and measured by flow cytometry. $B220^{-}$ $CD4^{+}$ $CXCR5^{+}$ $PD\text{-}1^{+}$ populations were identified as Tfh cells. $CD69^{+}$ $CD40L^{+/-}$ populations from Tfh cells were identified as $AIM^{+}$ Tfh cells. Markers, CD4-FITC, B220-Alexa Fluor 594, CXCR5-brilliant violet 421, PD-1- APC/Fire750, CD69-PE and CD40L-APC are used. $B220^{-}$ $CD4^{+}$ $CD62L^{+}$ $CD69^{+}$ $CD40L^{+/-}$ populations were identified as $AIM^{+}$ antigen experienced CD4 T cells. $B220^{-}$ $CD4^{+}$ $CD62L^{-}$ $CD69^{+}$ $CD40L^{+/-}$ populations were identified as $AIM^{+}$ naïve CD4 T cells. Markers, CD4-FITC, B220-Alexa Fluor 594, CD44-brilliant violet 421, CD62L- APC/Fire750, CD69-PE and CD40L-APC are used.

**Enzyme-linked immunosorbent assay (ELISA) for antibody titer measurements**

At day 0, mice were immunized with the equivalent of 14.6 nmol or 1.46 nmol of HER2 peptide plus 13.9 nmol 2′3′-cGAMP regardless of formulation type. Starting at day 14, mice were boosted twice at two-week intervals with 50% of the original dosage of both antigen and adjuvant (days 14 and 28). To evaluate serum antibody titers, blood was collected by submandibular puncture 10 days after each immunization (days 10, 24 and 38). Serum was separated from whole blood by centrifugal separation at 10,000 × g for 5 minutes at 25 °C using Microvette 500 Ser-Gel collection vessels with a clotting activator.

Absolution quantification of total IgG and total IgM antibody analysis was performed using the mouse uncoated total IgG and total IgM ELISA kits based on manufacturer-recommended protocols (Thermo Fisher). Antigen-specific IgG, IgG1 and IgG2a antibody titers were quantified based on previously established protocols for indirect ELISA, with minor modifications[103]. Specifically, HER2 peptides (200 μL, 100 μg/mL in 100 mM carbonate buffer, pH 9.4) were

chemically conjugated to ELISA plates through the terminal amine group utilizing Nunc Immobilizer Amino immunoassay plates by overnight incubation with exposure to light at room temperature. Following overnight incubation, ELISA plates were washed three times with 100 mM PBS pH 7.4 with 2% Tween-20. The ELISA plates were then blocked overnight at 4 °C with 300 µL of ELISA blocker (Pierce Protein-Free PBS Blocking Buffer) and washed three times. Serum samples containing primary antibodies were serially diluted ($10^1$-$10^8$-fold) using 100 mM PBS pH 7.4 containing 10% ELISA blocker reagent and were added to each well (to200 µL total volume) for 2 hours incubation at room temperature. After three washes,100 µL of 500-fold diluted anti-IgG-HRP, anti-IgG1-HRP, or anti-IgG2a-HRP was added to each well and incubated for 1 hour at room temperature. The ELISA plates were washed five times, and then 100 µL of 1-Step Ultra TMB Substrate Solution was added to each well. The solution was allowed to incubate and develop color for 15-20 minutes at room temperature with gentle agitation. Color development was stopped by the addition of 100 µL of 100 mM sulfuric acid. Colorimetric development was quantified by absorbance spectroscopy at 450 nm using a BioTek Cytation 5 plate reader. Antibody titers were determined by any absorbance signal at a given dilution factor that was greater than the PBS control absorbance signal plus three standard deviations.

**Anticancer efficacy in BALB/c mice with $HER2^+$ breast cancer**

BALB/c mice were inoculated with $2.5 \times 10^5$ D2F2/E2 cells subcutaneously in the right flank. D2F2/E2 cells were prepared at a concentration of $2.5 \times 10^6$ cells/mL in 100 µL and were mixed with an equal volume with Matrigel matrix. Mice were subcutaneously immunized with different vaccine formulations, some in combination with anti-PD-1 antibody, via intraperitoneal injection. Tumor size was measured every 2 days. Tumor volumes were calculated as volume = $(\text{width})^2 \times \text{length}/2$. End points were determined by using the End-Stage Illness Scoring System; mice receiving an End-Stage Illness Score greater than 6 were euthanized by $CO_2$ asphyxiation. Survival rates were calculated by the Kaplan–Meier method and were compared by the log-rank test.

**Single-cell sequencing for immune fingerprints of tumors and data processing**

Tumor samples were harvested at 42 days after inoculation and dissociated into single-cell suspensions using a MA900 Cell Sorter (Sony). Single-cell suspensions were subjected to final cell counting on a Countess II Automated Cell Counter (Thermo Fisher) and diluted to a concentration of 700–1000 nuclei/µl. We built 3′ single-nucleus libraries using the 10x Genomics Chromium Controller and following the manufacturer's protocol for 3′ V3.1 chemistry with

NextGEM Chip G reagents (10x Genomics). Final library quality was assessed using TapeStation 4200 (Agilent), and libraries were quantified by Kapa qPCR (Roche). Pooled libraries were subjected to 150 bp paired-end sequencing according to the manufacturer's protocol (Illumina NovaSeq 6000). Bcl2fastq2 Conversion Software (Illumina) was used to generate de-multiplexed Fastq files, and aCellRanger Pipeline (10x Genomics) was used to align reads and generate count matrices.

CellRanger output and single-cell RNA-seq data were analyzed using the R package Seurat version 4.0. Quality control parameters were utilized to filter out dead cells, doublets, and cells without the minimal number of expressed genes. Raw unique molecular identifier (UMI) counts were log-normalized. Various genes were identified using the standard deviation from the mean (using only nonzero values). Data were scaled and centered by regressing library size and mitochondrial mRNA counts. Principal component analysis (PCA) was performed using various genes. The first 15 principal components were used as the input for uniform manifold approximation and projection (UMAP) to reduce the dimensionality of the single-cell data and project them onto two-dimensional graphs. Clusters were identified using a shared nearest neighbor (SNN) modularity optimization–based clustering algorithm. Marker genes defining each cluster were identified using Seurat's FindAllMarkers function, which employs a Wilcoxon rank sum test to determine significant genes. The SingleR package[104] and the ImmGen reference (website: http://rstats.immgen.org/DataPage/)[105] were used to assign cluster identity to individual cell types. The top 50 genes were analyzed in established gene expression data of immune cells, which can be obtained from ImmGen Datasets. In addition, cell clusters and markers were analyzed using the CellMarker database (website: http://bio-bigdata.hrbmu.edu.cn/CellMarker/index.jsp)[106] and published signatures[42].

Gene expression: For each cell, the gene expression measurement was normalized by its total expression, multiplied by a scale-factor of 10,000, and log-transformed. The collapsed gene signature score for each sample was computed as follows: The sum of the normalized count values of each gene in the signature was used to identify B/T cell clusters or all cells in a given sample. The median gene expression signature was scored for each sample to draw heatmaps and boxplots.

**Immunofluorescence staining of tumor lymphoid follicle**

For immunofluorescence staining, tumor tissues were harvested at the endpoint. Harvested tissues were immediately fixed in 1% paraformaldehyde for 1 hour and then immersed in 30%

sucrose in 0.1% $NaN_3$ in PBS overnight. Treated tissues were then embedded in optical coherence tomography (OCT) compound and frozen in a $CO_{2(s)}$+EtOH bath. Tissue sections (15 µm) were prepared and dried for 0.5 hours before staining. Sections were then incubated with blocking solution for 1h. For **Figure 6g**, Secondary antibody staining methods were used. Primary antibodies used are, rabbit anti-mouse CD20 antibody (Invivogen), goat anti-mouse CD3 antibody (R&D Systems), mouse anti-mouse CD23 antibody (Invivogen) and rat anti-mouse PNAd antibody (Biolegend). Secondary antibodies (Abcam) used are, donkey anti-rabbit antibody-AF488, donkey anti-goat antibody-AF594, donkey anti-mouse antibody-AF647, donkey anti-rat antibody-AF405. For **Figure S25**, primary staining with antibody conjugated to fluorophores were used. Markers used are Alexa Fluor® 594 CD19 (B cells), FITC CD3 (T cells) and Alexa Fluor® 647 anti-mouse CD21/CD35 (CR2/CR1). After staining, slides were mounted with VECTASHIELD® Mounting Medium or DAPI Fluoromount-G® for confocal imaging.

**Immunohistochemistry (IHC) on tumor tissues**

Tumor tissues were harvested at the endpoint and immediately fixed in paraformaldehyde. The fixed tissues were then embedded in paraffin for preparation of 5 µm tissue sections. After deparaffinization, rehydration and antigen unmasking, slides were incubated with primary and secondary antibodies for immunostaining. Antibodies were used to identify different populations of immune cells: CD20 (B cells) and CD3 (T cells).

**Tumor rechallenge and analysis of immune memory cells and activation induced marker assay by flow cytometry**

At day 200, the mice with complete tumor remission after treatment were rechallenged by subcutaneous inoculation of $2.5 \times 10^5$ D2F2/E2 cancer cells. The control group was normal BALB/c mice. The mice were observed for 40 more days without any additional treatment. At 40 days after the rechallenge, mice were sacrificed. The lymph nodes, spleen, bone marrow and peripheral blood were harvested for flow cytometry. Tetramer staining optimization are same as antigen specific germinal center B cells. $B220^+$ $CD38^+$ $GL\text{-}7^-$ $IgD^-$ $IgM^-$ populations were identified as class switched memory B cells. HER2 tetramer positive class switched memory B cells were identified as antigen specific class switched memory B cells. Markers used are, B220-Alexa Fluor 594, CD38-APC/Fire650, GL-7-FITC, IgD-Alexa Fluor700, IgM-PE. $CD3^-B220^{low}Ig(H^+L)^+tetramer^+$ were identified as antigen specific plasma cells. Markers used are, CD3-Alexa Fluor647, B220-APC/Fire750, $Ig(H^+L)$-PE. $CD8^-$ $CD4^+$ $CD44^+$ $CD62L^-$ populations were identified as CD4 T effector memory cells, $CD8^-$ $CD4^+$ $CD44^+$ $CD62L^+$ populations were identified as CD4 T central

memory cells. $CD4^-$ $CD8^+$ $CD44^+$ $CD62L^-$ populations were identified as CD8 T effector memory cells, $CD4^-$ $CD8^+$ $CD44^+$ $CD62L^+$ populations were identified as CD8 T central memory cells. Markers used are CD4-PE, CD8-brilliant violet421, CD44-Alexa Fluor 647, CD62L-FITC. $CD8^-$ $CD4^+$ $CD69^+$ $CD103^{-/+}$ populations were identified as CD4 Tissue resident memory T cells. $CD4^-$ $CD8^+$ $CD69^+$ $CD103^+$ populations were identified as CD8 Tissue resident memory T cells. Markers used are CD4-PE, CD8-brilliant violet 421, CD69-APC/Fire750, CD103-Alexa Fluor 488.

Spleen cells (2 million) from different vaccination groups were then incubated with HER2-B/CD4/CD8 peptides (2 μg/mL) for 20h at 24 well plate. After incubation, cells were then collected and measured by flow cytometry. $CD8^-$ $CD4^+$ $CD44^+$ $CD62L^+$ populations were identified as CD4 TCM cells. $CD69^+$ $CD40L^{+/-}$ populations from CD4 TEM/TCM cells were identified as $AIM^+$ CD4 TEM/TCM cells. Markers used are, CD8-Alexa Fluor 594, CD4-FITC, CD44-brilliant violet 421, CD62L-APC/Fire750, CD69-PE, CD40L-APC. $CD4^-$ $CD8^+$ $CD44^+$ $CD62L^+$ populations were identified as CD8 TCM cells. $CD25^+$ $OX40^{+/-}$ populations from CD8 TEM/TCM cells were identified as $AIM^+$ CD8 TEM/TCM cells. Markers used are, CD8-Alexa Fluor 594, CD4-FITC, CD44-brilliant violet 421, CD62L-APC/Fire750, CD25-PE, OX40-APC.

**Statistics**

Data are expressed as the mean ± standard deviation (SD), unless otherwise specified. Two groups were compared using the unpaired Student's *t*-test. Means of multiple groups were compared with one-way analysis of variance (ANOVA) followed by Tukey's post hoc pairwise comparison. All probability values are two-sided, and $p < 0.05$ was considered statistically significant. Statistical analyses were carried out using the GraphPad Prism 9 software package.

**Data availability:**

The data that support the plots in this paper and other findings of this study are available from the corresponding author upon reasonable request. The code for single cell RNA-Seq analysis is available at: https://github.com/hebinghb/Tumor_B_Cell_Vaccine.

## Supporting Information

Supporting Information Available: Addtional nanoparticle characterization; in vitro crosslink test; B cell uptake; Gating strategies for flow cytometry; Addtional results for B/CD4 crosstalk; confocol image of lymph node distribution and delivery efficiency; In vivo measurement of GC and Tfh in lymph node and spleen; In vivo measurement of antigen

specific CD4 T cells; HER2-specific antibody production; Efficacy on PyMT and 4T-1 tumor; Addtional results for single cell analysis; Evaluate TLS formation

### 2.6 Figures

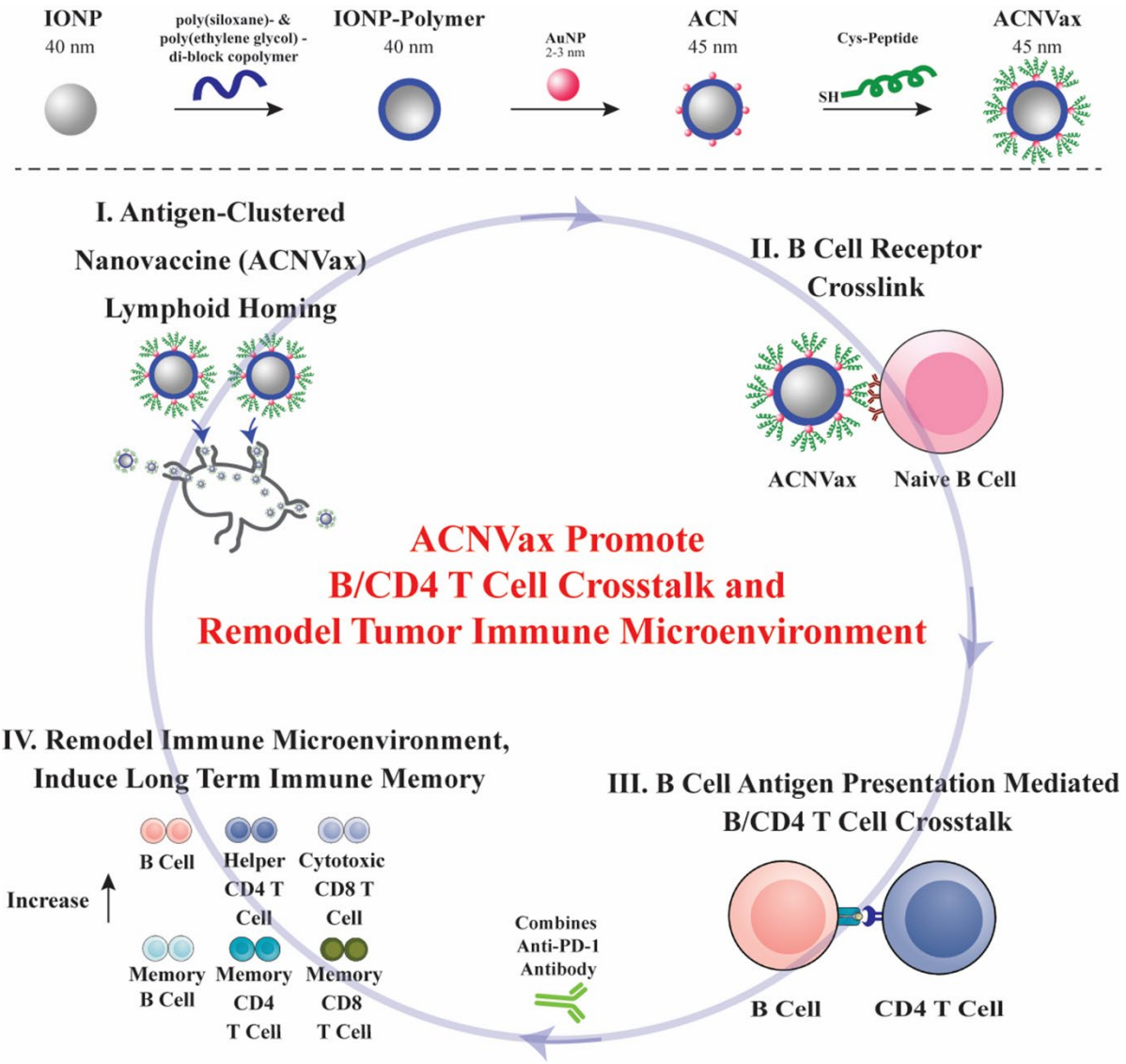


**Figure 2.1. Antigen-clustered nanovaccine (ACNVax), combined with anti-PD-1, achieves long term tumor remission by promoting B cell antigen presentation-mediated B/CD4 T cell crosstalk.** ACNVax efficiently penetrates the lymph node, crosslinks with B cell receptor (BCR) and promotes B cell antigen presentation- mediated B/CD4 T cells crosstalk. ACNVax vaccination, in combination with anti-PD-1, achieved long-term tumor remission through remodeling immune microenvironment with increased memory B/CD4/CD8 immunity.

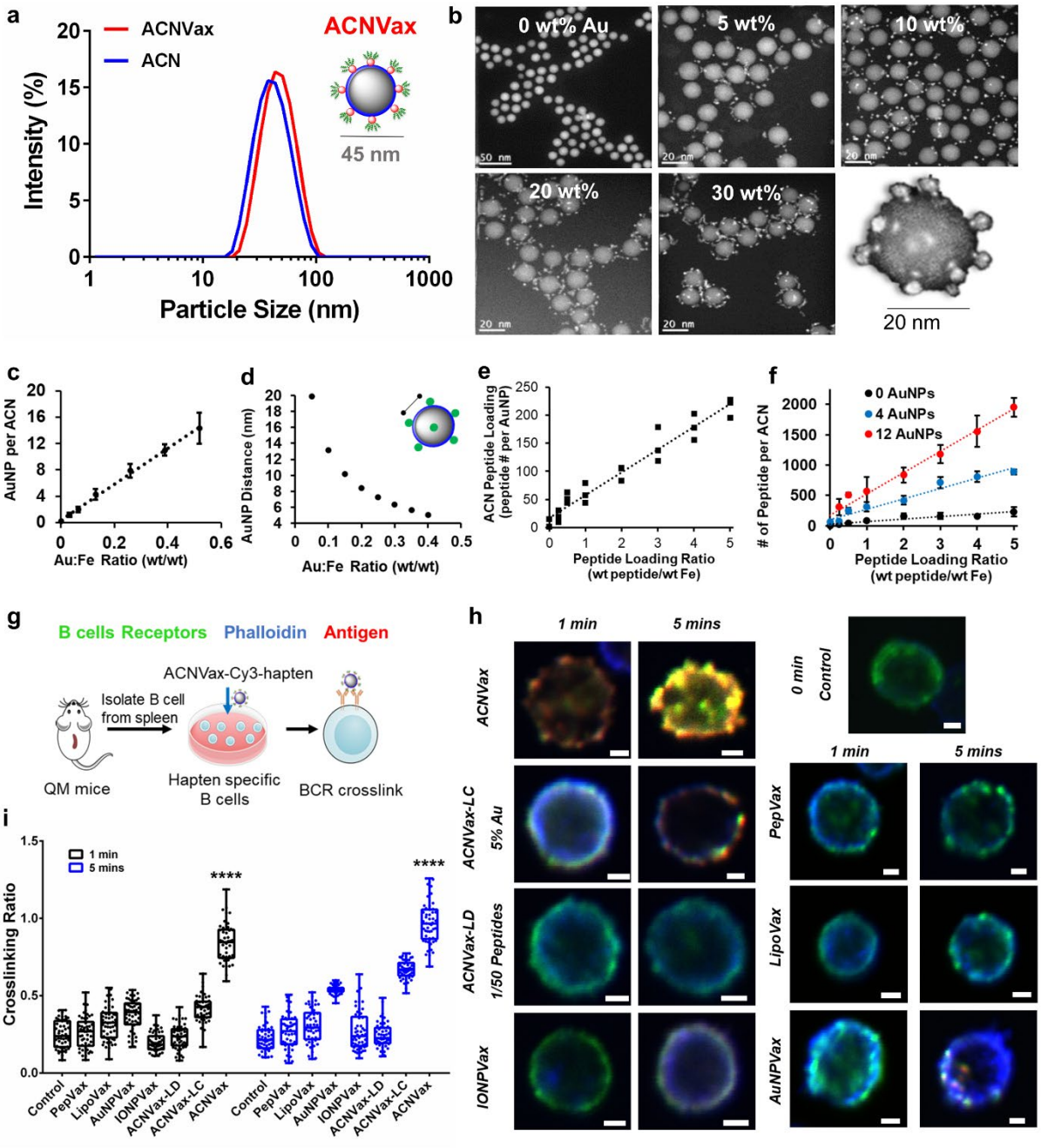


**Figure 2.2. Engineer ACNVax with antigen-clustered topography to effectively crosslink with B cell receptor (BCR).** (**a**) Size of the ACN and ACN with antigen (ACNVax) by Dynamic Light Scattering (DLS) analysis. (**b**) Scanning transmission electron microscopy (STEM) high-angle annular dark-field (HAADF) images of ACN with different ratios of AuNP/IONP from 0–30%; scale bar is 50 nm at 0% condition; scalebar is 20 nm at 5–30% conditions. STEM image of a single ACNVax (bottom right of A). (**c**) Number of surface AuNP per ACN. (**d**) distances between AuNPs on ACN surfaces when different Au:Fe ratios was used to generate the ACN as calculated by mathematical modeling (**Supporting method, Figure S1, Table S1-S4**). (**e**) Peptide loading of ACN standardized on a per gold nanoparticle basis (R = 0.95). (**f**) the number of peptides on

ACNVax with variable AuNP number (0 AuNP - black; 4 AuNPs - blue; 12 AuNPs - red) as determined by a modified fluorescamine fluorescence detection assay. Data for quantification are shown as mean ± SD, n = 3. (**g**) Schematic illustration of B cell receptor crosslink experiments and results as shown in (**h**) and (**i**). (**h**) Confocal image of Cy3 and hapten labeled ACNVax (red, 20 nM antigens) binding/crosslinking (yellow) with B cell receptor (antibody staining, green) in hapten-specific B cells from QM mice splenocytes, compared with other control groups (20 nM antigens): Cy3 and hapten labeled CD4/B antigen (PepVax), Cy3 and hapten labeled IONPVax, Cy3 and hapten labeled AuNPVax, Cy3 and hapten labeled ACNVax with longer distance (~15 nm) between clusters (ACNVax-LC) and Cy3 and hapten labeled ACNVax with low density of antigen (2% of peptide loading, ACNVax-LD). Blue, phalloidin stain of actin filaments; green, B cell receptor staining using Alexa Fluor 488-AffiniPure Fab Fragment Goat Anti-Mouse IgM (μ Chain Specific) antibody; red: Cy3-labeled CD4/B-hapten epitope. The scale bar is 2.5 μm. (**i**) Quantification of crosslinking signals from (**h**). Statistical comparisons were conducted between ACNVax versus all other groups. Statistical comparisons are based on one-way ANOVA, followed by post hoc Tukey's pairwise comparisons or by Student's unpaired T-test. The asterisks denote statistical significance at the level of **** $p < 0.0001$. ANOVA, analysis of variance; SD, standard deviation; n.s., no statistical significance.

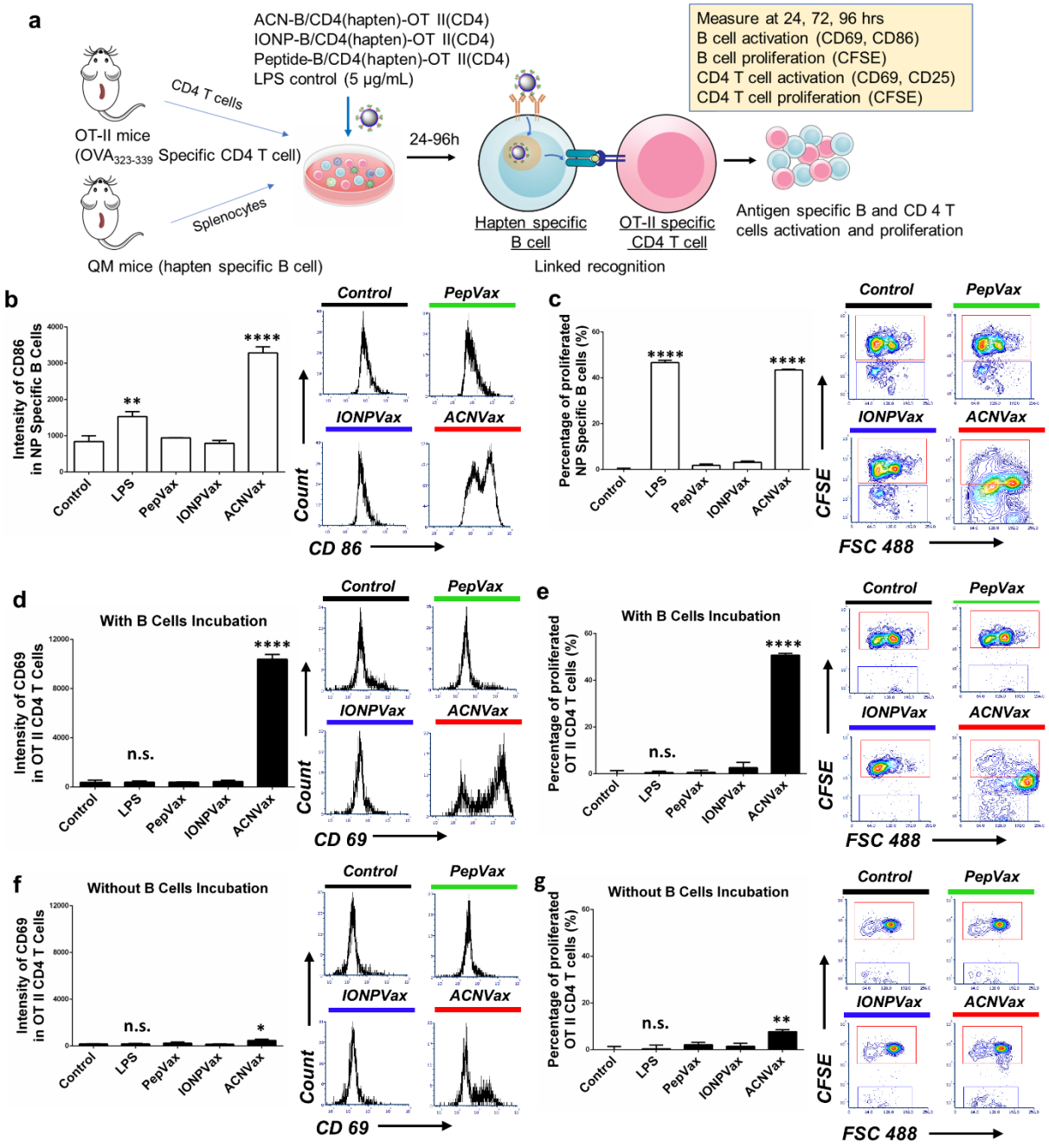


**Figure 2.3. ACNVax promoted B cell antigen presentation to CD4 T cells resulting in antigen-specific T cell activation and proliferation. (a)** Diagram of experimental design. ACN with HER2-B/CD4 antigen-hapten and OT-II CD4 epitope was incubated with splenocytes from QM mice (with a portion of B cells labeled with CFSE), and OT-II specific CD4 T cells (labeled with CFSE) from the splenocytes of OT-II transgenic mice. IONPVax and PepVax with the same amount of antigen as ACNVax particles were used as controls. (**b**) Representative flow cytometry analysis and quantification (96 h) of hapten-specific B cell activation by measuring geometric mean intensity of CD86 marker. (**c**) Representative flow cytometry analysis and quantification (96 h) of hapten-specific B cell proliferation, measured by the percentage of decrease in $CFSE^{+}$

hapten-specific B cells compared to controls. (**d**) Representative flow cytometry analysis and quantification (96 h) of OT-II specific CD4 T cell activation with B cell incubation by measuring geometric mean intensity of CD69 marker. (**e**) Representative flow cytometry analysis and quantification (96 h) of OT-II specific CD4 T cell proliferation with B cell incubation by measuring the percentage of decreased $CFSE^+$ OT-II specific CD4 T cells compared to control. (**f**) Representative flow cytometry analysis and quantification (96 h) of OT-II specific CD4 T cell activation without B cell incubation, measured by the geometric mean intensity of CD69 marker. (**g**) Representative flow cytometry analysis and quantification (96 h) of OT-II specific CD4 T cell proliferation without B cell incubation was measured by measuring the percentage of decreased $CFSE^+$ OT-II specific CD4 T cells compared to control. Data for quantification are shown as mean ± SD, n = 3. For figure **2b-g**, statistical comparisons were conducted among ACNVax and LPS with other groups. Statistical comparisons are based on one-way ANOVA, followed by post hoc Tukey's pairwise comparisons or by Student's unpaired T-test. The asterisks denote statistical significance at the level of * $p < 0.05$, ** $p < 0.01$, *** $p < 0.001$, **** $p < 0.0001$. ANOVA, analysis of variance; SD, standard deviation; n.s., no statistical significance.

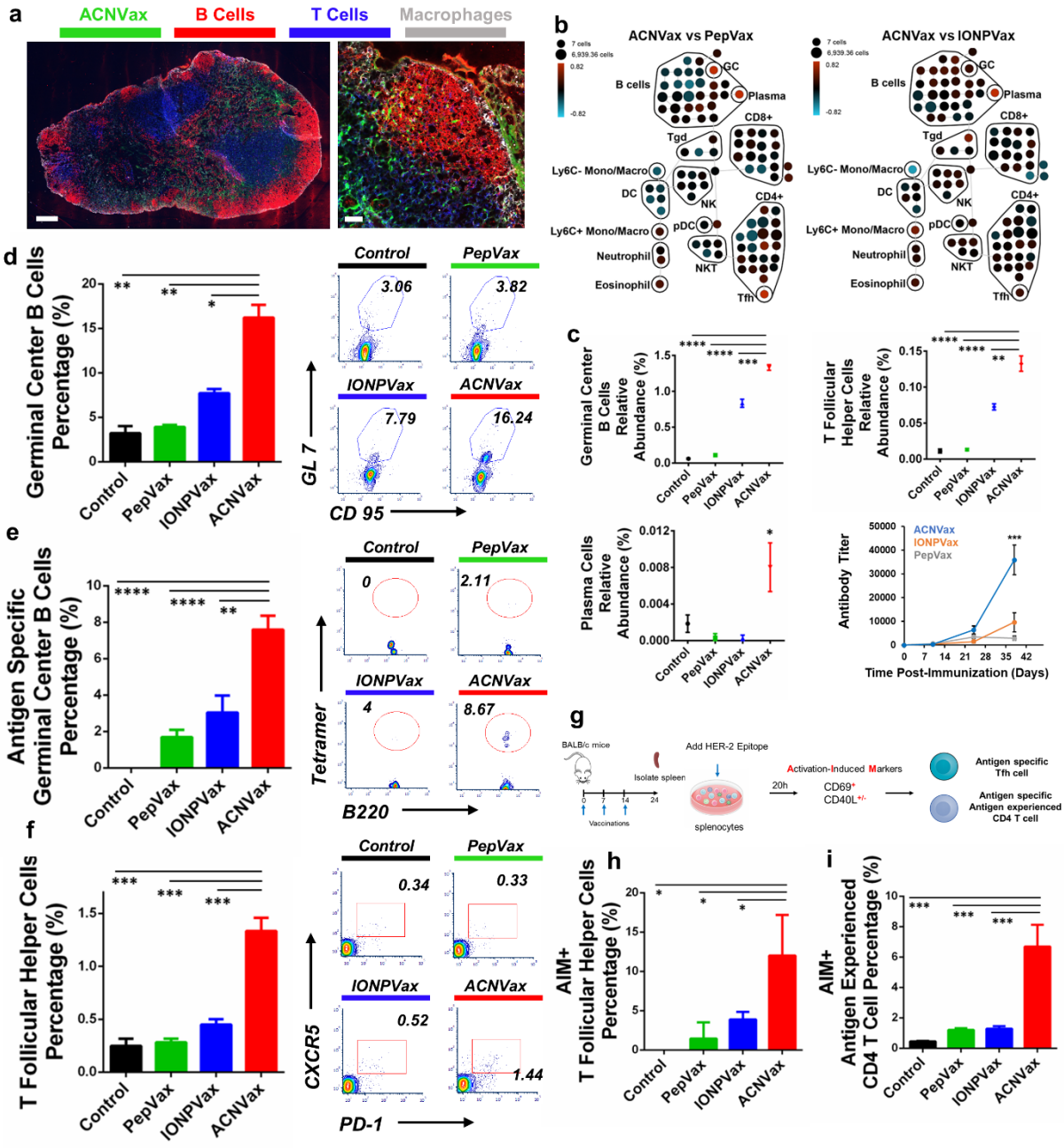


**Figure 2.4. ACNVax penetrated efficiently into the lymph node and induced a robust Tfh cell–supported germinal center (GC) response *in vivo*. (a)** Confocal imaging of ACNVax penetration into lymph nodes. Scale bar is 200 μm in whole-lymph-node images and 50 μm in magnified images. (**b**) CyTOF analysis of immune cells from lymph nodes (n = 3). SPADE analysis. Node sizes indicate absolute number of cells. Nodes are colored based on the log ratio of the relative number of immune cells in the ACNVax group to that in the PepVax or IONPVax group in the same lymph node. Red indicates a higher relative number of immune cells in the ACNVax group, and blue indicates a lower relative number. (**c**) Quantification of GC B cells and Tfh cells by CyTOF. CyTOF markers for each immune cell population are shown in **Figure S16**. **(d-f)** GC B cells, antigen-specific GC B cells, and Tfh cells in the lymph nodes after three

vaccinations in BALB/c mice using control (PBS), HER2-B/CD4 peptide, IONPVax or ACNVax (14.6 nmol antigen and 13.9 nmol 2′3′-cGAMP as adjuvant) at days 0, 7, and 14, and analyzed at day 24. (**d, e**) Representative flow cytometry analysis and quantification of germinal center B cells (**d**) and HER2-specific germinal center B-cells (**e**) in lymph nodes using B-cell receptor tetramer staining. $CD3^{-}B220^{+}$ $CD95^{+}$ $GL\text{-}7^{+}$ populations were identified as GC B cells. Data for quantification are shown as mean ± SD, n = 3. (**f**) Flow cytometry quantification of Tfh cells in lymph nodes. $B220^{-}CD4^{+}CXCR5^{+}PD\text{-}1^{+}$ populations were identified as Tfh cells. (**g**) Diagram of experimental design for activation-induced markers assay (AIM) for measuring antigen specific Tfh and antigen experienced CD4 T cells. (**h, i**) Representative flow cytometry analysis and quantification of $AIM^{+}$ Tfh cells (**h**), $AIM^{+}$ antigen experienced CD4 T cells (**i**). $B220^{-}CD4^{+}CXCR5^{+}PD\text{-}1^{+}$ populations were identified as Tfh cells. $CD69^{+}CD40L^{+/-}$ populations from Tfh cells were identified as $AIM^{+}$ Tfh cells. $B220^{-}CD4^{+}CD62L^{+}CD69^{+}CD40L^{+/-}$ populations were identified as $AIM^{+}$ antigen experienced CD4 T cells. Data for quantification are shown as mean ± SD, n = 3. Statistical comparisons were conducted between ACNVax and IONPVax, PepVax, and control groups. Statistical comparisons are based on one-way ANOVA, followed by post hoc Tukey's pairwise comparisons or by Student's unpaired T-test. The asterisks denote statistical significance at the level of * $p < 0.05$, ** $p < 0.01$, *** $p < 0.001$, **** $p < 0.0001$. ANOVA, analysis of variance; SD, standard deviation.

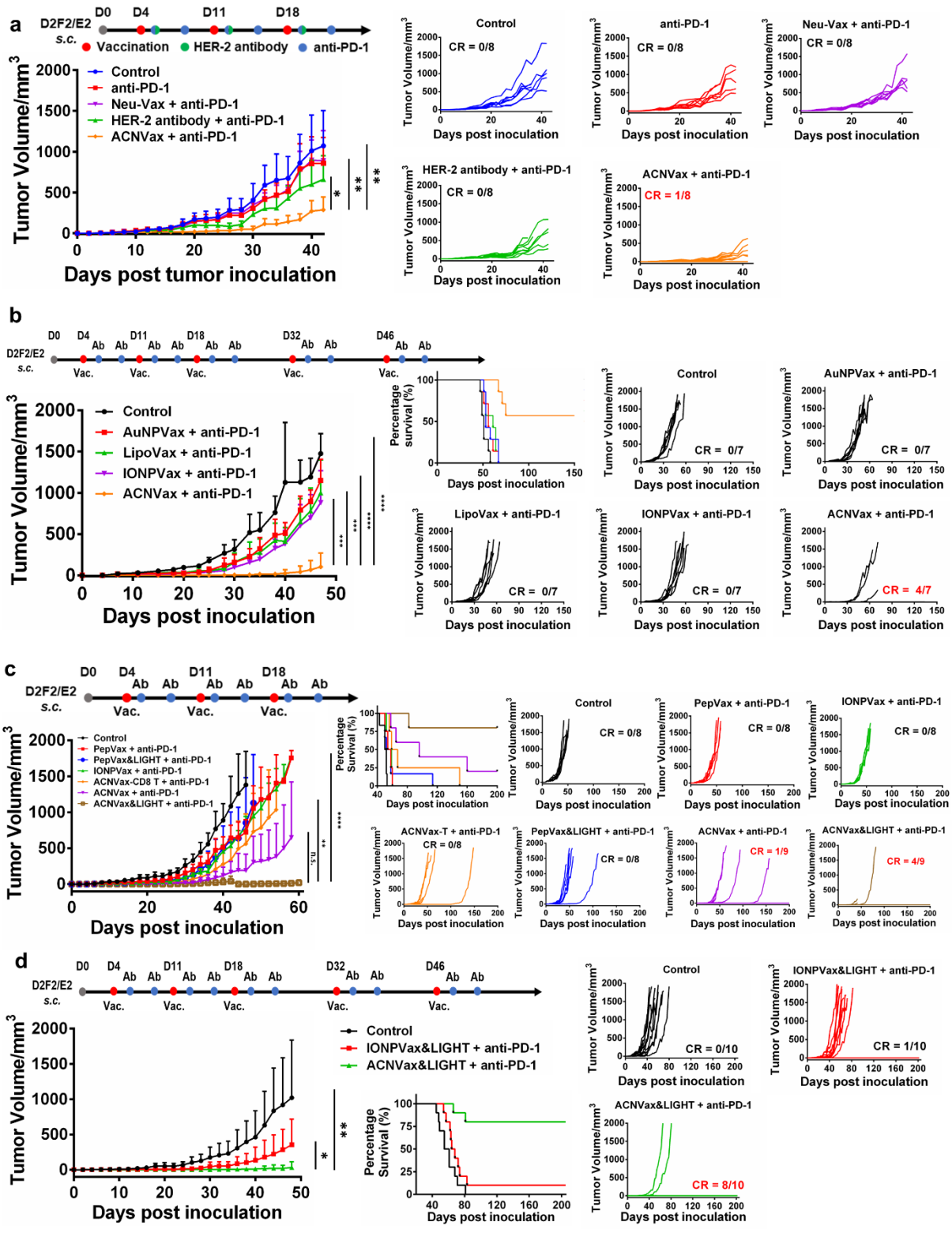


**Figure 2.5. ACNVax combined with anti-PD-1 antibody achieved long-term remission of HER2$^+$ breast cancer.** A HER2 breast cancer model was established by inoculating BALB/c mice s.c. with 2.5 × $10^5$ D2F2/E2 mouse mammary tumor cells encoding human ErbB-2 (HER2). Four

days after tumor inoculation, mice were treated with different vaccine formulations in combination with anti-PD-1 antibody. For each vaccine, we used 14.6 nmol HER2 CD4 and B cell epitope ((CDDD-PESFDGDPASNTAPLQPEQLQ-(GGK)) with 13.9 nmol 2′3′-cGAMP as the adjuvant. ACNVax-T had the same ACN but conjugated with the HER2 CD8 T cell epitope (E75). **(a**) Antitumor efficacy of ACNVax vs. clinical treatment for HER2 breast cancer. Average tumor volume changes of HER2 breast cancer mice after treatment with PBS (control), anti-PD-1 antibody (100 μg), murine HER2 antibody (100 μg**, Table S8**) plus anti-PD-1 antibody (100 μg), NeuVax (E75, 14.6 nmol combined with GM-CSF, 5 μg) plus anti-PD-1 antibody (100 μg) or ACNVax (14.6 nmol HER2 epitope, 13.9 nmol 2′3′-cGAMP) plus anti-PD-1 antibody (100 μg). The data represent the mean ± SD; n = 7 for the control, anti-PD-1, HER2 antibody plus anti-PD-1 and NeuVax plus anti-PD-1 groups; n = 8 for the ACNVaxplus anti-PD-1. (**b**) Antitumor efficacy of ACNVax compared with different nanovaccine after three vaccinations. IONPVax: the core component of ACN (35 nm) with antigen uniformly conjugated on the nanoparticle surface; AuNPVax: the surface single antigen cluster component of ACN (2-5 nm) and LipoVax: liposome with antigen uniformly conjugated on the nanoparticle surface. For each vaccine, we used 14.6 nmol epitopes with 13.9 nmol 2′3′-cGAMP as the adjuvant. n = 7 for each group. (**c**) Antitumor efficacy of ACNVax with LIGHT (50 ng) plus anti-PD-1 antibody compared with other vaccine groups. Data represent the mean ± SD, n = 8 for the control, PepVax + anti-PD-1, IONPVax + anti-PD-1, ACNVax-T + anti-PD-1 and PepVax/LIGHT + anti-PD-1 groups; n = 9 for the ACNVax + anti-PD-1 and ACNVax&LIGHT + anti-PD-1 groups. (**d**) Antitumor efficacy of ACNVax with LIGHT (50 ng) plus anti-PD-1 compared with IONPVax with LIGHT plus anti-PD-1 after five vaccination. Data represent the mean ± SD, n = 10 for all groups. Statistical comparisons were conducted between ACNVax + anti-PD-1 and other groups in figure **4a** and **4b** and between ACNVax&LIGHT + anti-PD-1 and other groups in figure **4c** and **4d**. Statistical comparisons are based on one-way ANOVA, followed by post hoc Tukey's pairwise comparisons or by Student's unpaired T-test. The asterisks denote statistical significance at the level of * $p < 0.05$, ** $p < 0.01$, *** $p < 0.001$, **** $p < 0.0001$. ANOVA, analysis of variance; SD, standard deviation; n.s., no statistical significance.

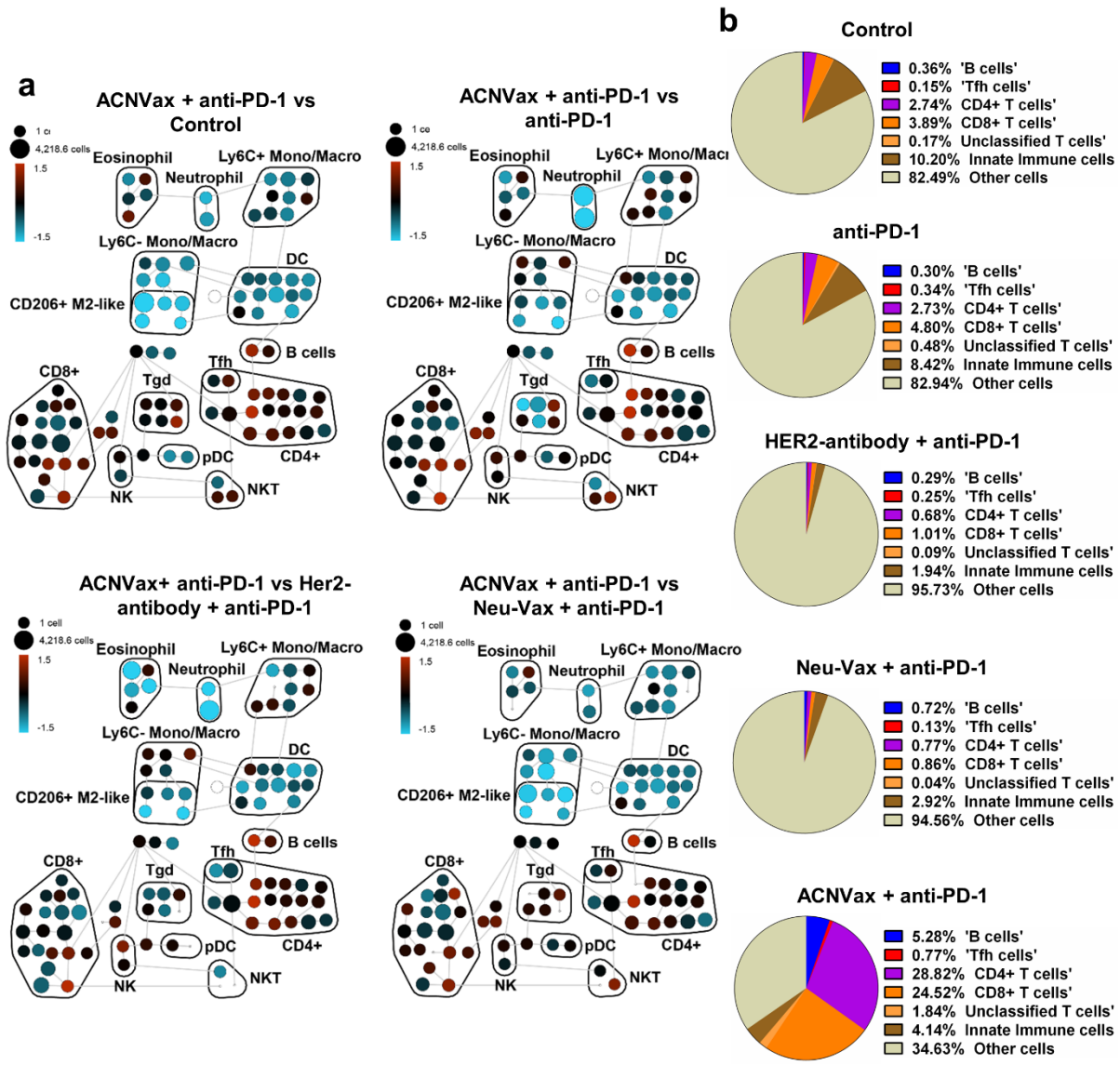


**Figure 2.6. ACNVax induced robust B/CD4/CD8 immune cell infiltration in tumor.** (**a**) Cytometry by Time-of-Flight (CyTOF) analysis of the immune cell population from tumor samples of mice 10 days after different treatments (3 vaccinations). Global analysis using SPADE unsupervised clustering analysis of tumor-infiltrating immune cells. Nodes are colored based on the log ratio of the relative number of immune cells in the ACNVax group to that in the anti-PD-1 antibody group in the same node: red indicates higher and blue indicates lower numbers in the ACNVax than the comparison groups. (Markers information can be found in **Figure S16**, **Table S9**). (**b**) Quantification of immune cells among total cells in tumor after different treatments, expressed as a fraction of total cells from the samples.

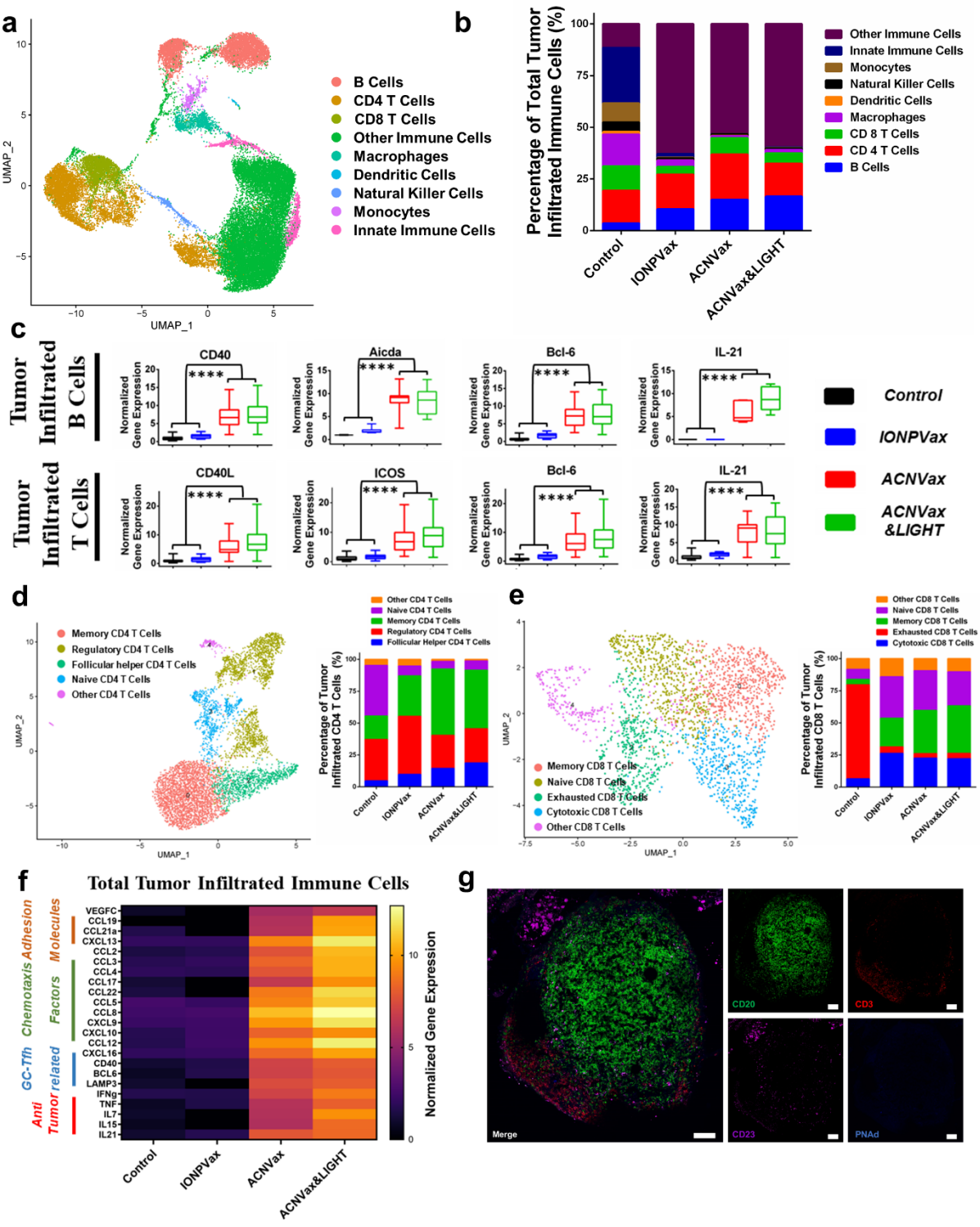


**Figure 2.7. ACNVax remodeled the tumor immune microenvironment.** Control (PBS), IONPVax (14.6 nmol HER2 epitope with 13.9 nmol 2'3'-cGAMP), ACNVax (14.6 nmol HER2 epitope with 13.9 nmol 2′3′-cGAMP) and ACNVax/LIGHT (14.6 nmol antigen, 13.9 nmol 2′3′-cGAMP, 50 ng LIGHT). Vaccines were given on days 4, 11, and 18 in combination with 100 μg anti-PD-1 antibody biweekly for 3 weeks in D2F2/E2 tumor-bearing mice. (**a**) Uniform manifold

approximation and projection (UMAP) plot of tumor-infiltrating immune cells. (**b**) Stacked bar charts show the quantified ratio of different phenotypes of immune cells in different treatment groups. (**c**) Boxplot of selected gene expression levels in tumor infiltrated B and T cells from single-cell RNA sequencing. Statistical comparisons were conducted between ACNVax&LIGHT and ACNVax with IONPVax and control. (**d, e**) Uniform manifold approximation and projection (UMAP) plot of CD4 T cell subclusters (**d**) and CD8 T cell subclusters (**e**) from tumor-infiltrating immune cells. (**f**) Heatmap of selected gene expression levels related to organized aggregates of immune cells in total tumor infiltrated immune cells from single-cell RNA sequencing. (**g**) Immunofluorescent staining of tumor lymphoid follicle from mouse tumor samples in the ACNVax&LIGHT + anti-PD-1 antibody group (14.6 nmol HER2 B/CD4 epitope, 13.9 nmol 2′3′-cGAMP, 50 ng LIGHT, 3 times every 7 days, 100 μg anti-PD-1 antibody biweekly for 3 weeks). Primary antibodies used are, rabbit anti-mouse CD20 antibody (Invivogen), goat anti-mouse CD3 antibody (R&D Systems), mouse anti-mouse CD23 antibody (Invivogen) and rat anti-mouse PNAd antibody (Biolegend). Secondary antibodies (Abcam) used are, donkey anti-rabbit antibody-AF488, donkey anti-goat antibody-AF594, donkey anti-mouse antibody-AF647, donkey anti-rat antibody-AF405. Scale bar is 100 μm. Statistical comparisons are based on one-way ANOVA, followed by post hoc Tukey's pairwise comparisons or by Student's unpaired T-test. The asterisks denote statistical significance at the level of **** $p < 0.0001$. ANOVA, analysis of variance; SD, standard deviation.

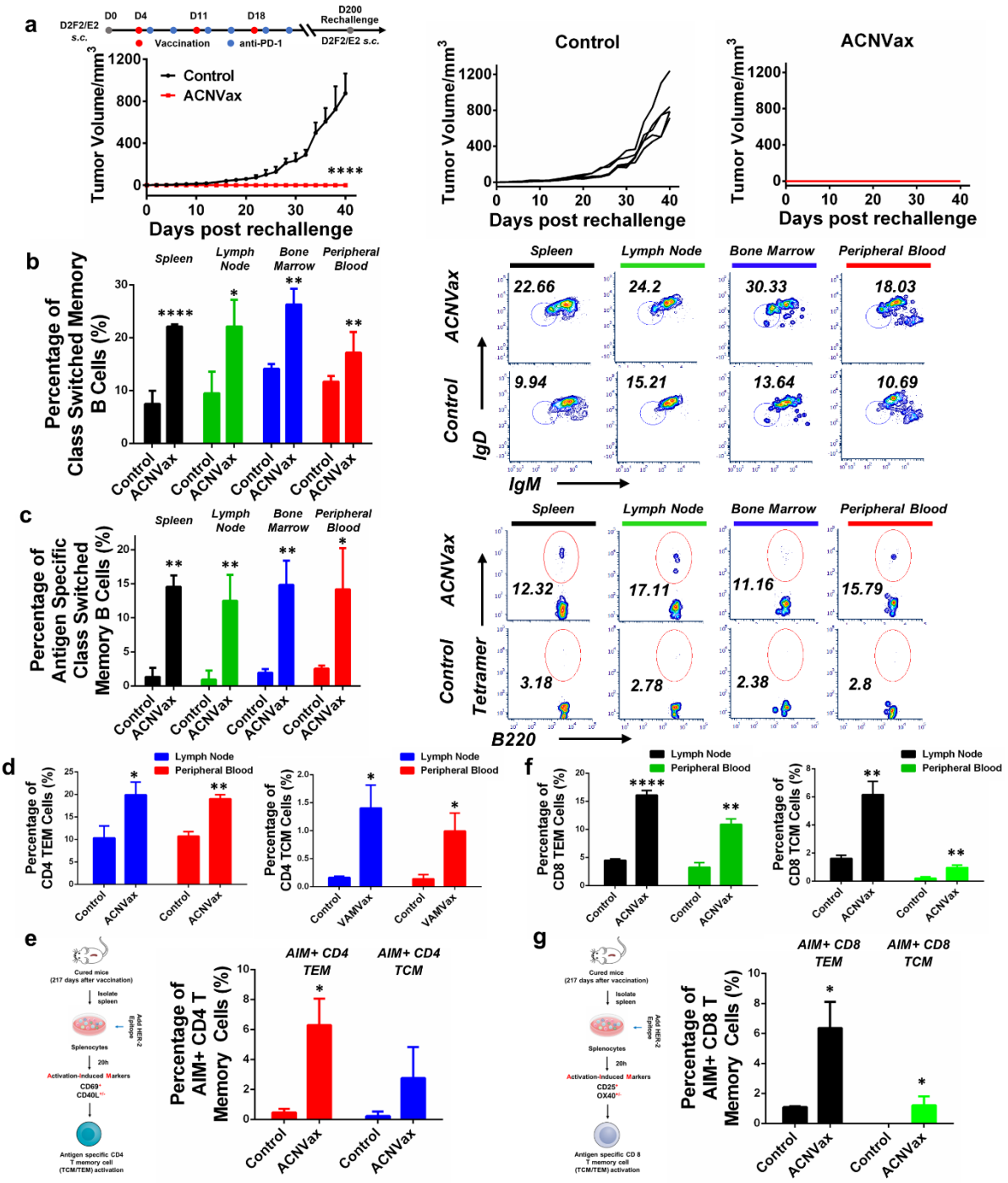


**Fig 2.8. ACNVax induced long-term immune memory against tumor rechallenge and increased long-term antigen-specific memory B, CD4 and CD8 T cells.** (**a**) Tumors rechallenge at 200 days for mice with long-term remission after three times of vaccination (ACNVax). D2F2/E2 HER2 cancer cells ($2.5 \times 10^5$) were s.c. injected into the mice with long-term remission and control mice (normal BALB/c mice). Average and individual tumor growth curves were measured. Data represent the mean ± SD, n = 5. (**b, c**) Representative flow cytometry analysis and quantification of class switched memory B cells (**b**) and antigen specific class

switched memory B cells (**c**) from spleen, lymph node, bone marrow and peripheral blood of the mice in **Figure 7a**. $B220^{+}$ $CD38^{+}$ $GL\text{-}7^{-}IgD^{-}$ $IgM^{-}$ populations were identified as class switched memory B cells. HER2 tetramer positive class switched memory B cells were identified as antigen specific class switched memory B cells. Data for quantification are shown as mean ± SD, n = 3. (**d**) Quantification of flow cytometry results of CD4 T effector memory (TEM) and CD4 T central memory (TCM) cells from lymph node and peripheral blood of the mice in **Figure 7a**. $CD8^{-}$ $CD4^{+}$ $CD44^{+}$ $CD62L^{-}$ populations were identified as CD4 TEM cells, $CD8^{-}$ $CD4^{+}$ $CD44^{+}$ $CD62L^{+}$ populations were identified as CD4 TCM cells. (**e**) Diagram of experimental design for activation-induced markers assay (AIM) for measuring antigen specific CD4 TEM/TCM cells from spleen. Representative flow cytometry analysis and quantification of $AIM^{+}$ CD4 TEM/TCM cells. $CD69^{+}$ $CD40L^{+/-}$ populations from CD4 TEM/TCM cells were identified as $AIM^{+}$ CD4 TEM/TCM cells. (**f**) Quantification of flow cytometry results of CD8 TEM and CD8 TCM cells from lymph node and peripheral blood of the mice in **Figure 7a**. $CD4^{-}$ $CD8^{+}$ $CD44^{+}$ $CD62L^{-}$ populations were identified as CD8 TEM cells, $CD4^{-}$ $CD8^{+}$ $CD44^{+}$ $CD62L^{+}$ populations were identified as CD8 TCM cells. (**g**) Diagram of experimental design for activation-induced markers assay (AIM) for measuring antigen specific CD8 TEM/TCM cells from spleen. Representative flow cytometry analysis and quantification of $AIM^{+}$ CD8 TEM/TCM cells. $CD25^{+}$ $OX40^{+/-}$ populations from CD8 TEM/TCM cells were identified as $AIM^{+}$ CD8 TEM/TCM cells. Data for quantification are shown as mean ± SD, n = 3. Statistical comparisons were conducted between ACNVax and control. Statistical comparisons are based on one-way ANOVA, followed by post hoc Tukey's pairwise comparisons or by Student's unpaired T-test. The asterisks denote statistical significance at the level of * $p < 0.05$, ** $p < 0.01$, *** $p < 0.001$, **** $p < 0.0001$. ANOVA, analysis of variance; SD, standard deviation.

## 2.7 Bibliography


1. Saxena, M.; van der Burg, S. H.; Melief, C. J. M.; Bhardwaj, N., Therapeutic cancer vaccines. *Nature Reviews Cancer* **2021,** *21* (6), 360-378.
2. Hollingsworth, R. E.; Jansen, K., Turning the corner on therapeutic cancer vaccines. *NPJ vaccines* **2019,** *4*, 7.
3. Jiang, T.; Shi, T.; Zhang, H.; Hu, J.; Song, Y.; Wei, J.; Ren, S.; Zhou, C., Tumor neoantigens: from basic research to clinical applications. *Journal of hematology & oncology* **2019,** *12* (1), 93.
4. Hu, Z.; Leet, D. E.; Allesøe, R. L.; Oliveira, G.; Li, S.; Luoma, A. M.; Liu, J.; Forman, J.; Huang, T.; Iorgulescu, J. B.; Holden, R.; Sarkizova, S.; Gohil, S. H.; Redd, R. A.; Sun, J.; Elagina, L.; Giobbie-Hurder, A.; Zhang, W.; Peter, L.; Ciantra, Z.; Rodig, S.; Olive, O.; Shetty, K.; Pyrdol, J.; Uduman, M.; Lee, P. C.; Bachireddy, P.; Buchbinder, E. I.; Yoon, C. H.; Neuberg, D.; Pentelute, B. L.; Hacohen, N.; Livak, K. J.; Shukla, S. A.; Olsen, L. R.; Barouch, D. H.; Wucherpfennig, K. W.; Fritsch, E. F.; Keskin, D. B.; Wu, C. J.; Ott, P. A., Personal neoantigen vaccines induce persistent memory T cell responses and epitope spreading in patients with melanoma. *Nat Med* **2021,** *27* (3), 515-525.
5. Ott, P. A.; Hu, Z.; Keskin, D. B.; Shukla, S. A.; Sun, J.; Bozym, D. J.; Zhang, W.; Luoma, A.; Giobbie-Hurder, A.; Peter, L.; Chen, C.; Olive, O.; Carter, T. A.; Li, S.; Lieb, D. J.; Eisenhaure, T.; Gjini, E.; Stevens, J.; Lane, W. J.; Javeri, I.; Nellaiappan, K.; Salazar, A. M.; Daley, H.; Seaman, M.; Buchbinder, E. I.; Yoon, C. H.; Harden, M.; Lennon, N.; Gabriel, S.; Rodig, S. J.; Barouch, D. H.; Aster, J. C.; Getz, G.; Wucherpfennig, K.; Neuberg, D.; Ritz, J.; Lander, E. S.; Fritsch, E. F.; Hacohen, N.; Wu, C. J., An immunogenic personal neoantigen vaccine for patients with melanoma. *Nature* **2017,** *547* (7662), 217-221.
6. Ott, P. A.; Hu-Lieskovan, S.; Chmielowski, B.; Govindan, R.; Naing, A.; Bhardwaj, N.; Margolin, K.; Awad, M. M.; Hellmann, M. D.; Lin, J. J.; Friedlander, T.; Bushway, M. E.; Balogh, K. N.; Sciuto, T. E.; Kohler, V.; Turnbull, S. J.; Besada, R.; Curran, R. R.; Trapp, B.; Scherer, J.; Poran, A.; Harjanto, D.; Barthelme, D.; Ting, Y. S.; Dong, J. Z.; Ware, Y.; Huang, Y.; Huang, Z.; Wanamaker, A.; Cleary, L. D.; Moles, M. A.; Manson, K.; Greshock, J.; Khondker, Z. S.; Fritsch, E.; Rooney, M. S.; DeMario, M.; Gaynor, R. B.; Srinivasan, L., A Phase Ib Trial of Personalized Neoantigen Therapy Plus Anti-PD-1 in Patients with Advanced Melanoma, Non-small Cell Lung Cancer, or Bladder Cancer. *Cell* **2020,** *183* (2), 347-362.e24.
7. Sahin, U.; Oehm, P.; Derhovanessian, E.; Jabulowsky, R. A.; Vormehr, M.; Gold, M.; Maurus, D.; Schwarck-Kokarakis, D.; Kuhn, A. N.; Omokoko, T.; Kranz, L. M.; Diken, M.; Kreiter, S.; Haas, H.; Attig, S.; Rae, R.; Cuk, K.; Kemmer-Brück, A.; Breitkreuz, A.; Tolliver, C.; Caspar, J.; Quinkhardt, J.; Hebich, L.; Stein, M.; Hohberger, A.; Vogler, I.; Liebig, I.; Renken, S.; Sikorski, J.; Leierer, M.; Müller, V.; Mitzel-Rink, H.; Miederer, M.; Huber, C.; Grabbe, S.; Utikal, J.; Pinter, A.; Kaufmann, R.; Hassel, J. C.; Loquai, C.; Türeci, Ö., An RNA vaccine drives immunity in checkpoint-inhibitor-treated melanoma. *Nature* **2020,** *585* (7823), 107-112.
8. Press-Release, Moderna and Merck announce mTNA-4157/V940, an investigational personalized mTNA cancer vaccine, in combination with Keytruda, was granted breakthrough therapy designation by the FDA for adjuvant treatment of patients with high-risk melanoma following complete resection. *https://investors.modernatx.com/news/news-details/2023/Moderna-and-Merck-Announce-mRNA-4157V940-an-Investigational-Personalized-mRNA-Cancer-Vaccine-in-Combination-With-KEYTRUDAR-pembrolizumab-was-Granted-Breakthrough-Therapy-Designation-by-the-FDA-for-Adjuvant-Treatment-of-Patients-With-High-Risk-Melanom/default.aspx* **February 22 2023**.
9. Press-Release, MSK mRNA Pancreatic Cancer Vaccine Trial Shows Promising Results. *https://www.mskcc.org/news/can-mrna-vaccines-fight-pancreatic-cancer-msk-clinical-researchers-are-trying-find-out* **May 31 2022**.

10. Cafri, G.; Gartner, J. J.; Zaks, T.; Hopson, K.; Levin, N.; Paria, B. C.; Parkhurst, M. R.; Yossef, R.; Lowery, F. J.; Jafferji, M. S.; Prickett, T. D.; Goff, S. L.; McGowan, C. T.; Seitter, S.; Shindorf, M. L.; Parikh, A.; Chatani, P. D.; Robbins, P. F.; Rosenberg, S. A., mRNA vaccine-induced neoantigen-specific T cell immunity in patients with gastrointestinal cancer. *J Clin Invest* **2020,** *130* (11), 5976-5988.
11. Palmer, C. D.; Rappaport, A. R.; Davis, M. J.; Hart, M. G.; Scallan, C. D.; Hong, S. J.; Gitlin, L.; Kraemer, L. D.; Kounlavouth, S.; Yang, A.; Smith, L.; Schenk, D.; Skoberne, M.; Taquechel, K.; Marrali, M.; Jaroslavsky, J. R.; Nganje, C. N.; Maloney, E.; Zhou, R.; Navarro-Gomez, D.; Greene, A. C.; Grotenbreg, G.; Greer, R.; Blair, W.; Cao, M. D.; Chan, S.; Bae, K.; Spira, A. I.; Roychowdhury, S.; Carbone, D. P.; Henick, B. S.; Drake, C. G.; Solomon, B. J.; Ahn, D. H.; Mahipal, A.; Maron, S. B.; Johnson, B.; Rousseau, R.; Yelensky, R.; Liao, C. Y.; Catenacci, D. V. T.; Allen, A.; Ferguson, A. R.; Jooss, K., Individualized, heterologous chimpanzee adenovirus and self-amplifying mRNA neoantigen vaccine for advanced metastatic solid tumors: phase 1 trial interim results. *Nat Med* **2022,** *28* (8), 1619-1629.
12. Platten, M.; Bunse, L.; Wick, A.; Bunse, T.; Le Cornet, L.; Harting, I.; Sahm, F.; Sanghvi, K.; Tan, C. L.; Poschke, I.; Green, E.; Justesen, S.; Behrens, G. A.; Breckwoldt, M. O.; Freitag, A.; Rother, L. M.; Schmitt, A.; Schnell, O.; Hense, J.; Misch, M.; Krex, D.; Stevanovic, S.; Tabatabai, G.; Steinbach, J. P.; Bendszus, M.; von Deimling, A.; Schmitt, M.; Wick, W., A vaccine targeting mutant IDH1 in newly diagnosed glioma. *Nature* **2021,** *592* (7854), 463-468.
13. Awad, M. M.; Govindan, R.; Balogh, K. N.; Spigel, D. R.; Garon, E. B.; Bushway, M. E.; Poran, A.; Sheen, J. H.; Kohler, V.; Esaulova, E.; Srouji, J.; Ramesh, S.; Vyasamneni, R.; Karki, B.; Sciuto, T. E.; Sethi, H.; Dong, J. Z.; Moles, M. A.; Manson, K.; Rooney, M. S.; Khondker, Z. S.; DeMario, M.; Gaynor, R. B.; Srinivasan, L., Personalized neoantigen vaccine NEO-PV-01 with chemotherapy and anti-PD-1 as first-line treatment for non-squamous non-small cell lung cancer. *Cancer Cell* **2022,** *40* (9), 1010-1026.e11.
14. Keskin, D. B.; Anandappa, A. J.; Sun, J.; Tirosh, I.; Mathewson, N. D.; Li, S.; Oliveira, G.; Giobbie-Hurder, A.; Felt, K.; Gjini, E.; Shukla, S. A.; Hu, Z.; Li, L.; Le, P. M.; Allesøe, R. L.; Richman, A. R.; Kowalczyk, M. S.; Abdelrahman, S.; Geduldig, J. E.; Charbonneau, S.; Pelton, K.; Iorgulescu, J. B.; Elagina, L.; Zhang, W.; Olive, O.; McCluskey, C.; Olsen, L. R.; Stevens, J.; Lane, W. J.; Salazar, A. M.; Daley, H.; Wen, P. Y.; Chiocca, E. A.; Harden, M.; Lennon, N. J.; Gabriel, S.; Getz, G.; Lander, E. S.; Regev, A.; Ritz, J.; Neuberg, D.; Rodig, S. J.; Ligon, K. L.; Suvà, M. L.; Wucherpfennig, K. W.; Hacohen, N.; Fritsch, E. F.; Livak, K. J.; Ott, P. A.; Wu, C. J.; Reardon, D. A., Neoantigen vaccine generates intratumoral T cell responses in phase Ib glioblastoma trial. *Nature* **2019,** *565* (7738), 234-239.
15. Kissick, H. T., Is It Possible to Develop Cancer Vaccines to Neoantigens, What Are the Major Challenges, and How Can These Be Overcome? Neoantigens as Vaccine Targets for Cancer. *Cold Spring Harb Perspect Biol* **2018,** *10* (11).
16. Kissick, H. T.; Sanda, M. G., The role of active vaccination in cancer immunotherapy: lessons from clinical trials. *Curr Opin Immunol* **2015,** *35*, 15-22.
17. Hailemichael, Y.; Dai, Z. M.; Jaffarzad, N.; Ye, Y.; Medina, M. A.; Huang, X. F.; Dorta-Estremera, S. M.; Greeley, N. R.; Nitti, G.; Peng, W. Y.; Liu, C. W.; Lou, Y. Y.; Wang, Z. Q.; Ma, W. C.; Rabinovich, B.; Schluns, K. S.; Davis, R. E.; Hwu, P.; Overwijk, W. W., Persistent antigen at vaccination sites induces tumor-specific CD8(+) T cell sequestration, dysfunction and deletion. *Nat Med* **2013,** *19* (4), 465-+.
18. Finn, O. J.; Rammensee, H. G., Is It Possible to Develop Cancer Vaccines to Neoantigens, What Are the Major Challenges, and How Can These Be Overcome? Neoantigens: Nothing New in Spite of the Name. *Cold Spring Harb Perspect Biol* **2018,** *10* (11).
19. Sellars, M. C.; Wu, C. J.; Fritsch, E. F., Cancer vaccines: Building a bridge over troubled waters. *Cell* **2022,** *185* (15), 2770-2788.

20. Sette, A.; Crotty, S., Adaptive immunity to SARS-CoV-2 and COVID-19. *Cell* **2021,** *184* (4), 861-880.
21. Heitmann, J. S.; Bilich, T.; Tandler, C.; Nelde, A.; Maringer, Y.; Marconato, M.; Reusch, J.; Jäger, S.; Denk, M.; Richter, M.; Anton, L.; Weber, L. M.; Roerden, M.; Bauer, J.; Rieth, J.; Wacker, M.; Hörber, S.; Peter, A.; Meisner, C.; Fischer, I.; Löffler, M. W.; Karbach, J.; Jäger, E.; Klein, R.; Rammensee, H. G.; Salih, H. R.; Walz, J. S., A COVID-19 peptide vaccine for the induction of SARS-CoV-2 T cell immunity. *Nature* **2022,** *601* (7894), 617-622.
22. Keeton, R.; Tincho, M. B.; Ngomti, A.; Baguma, R.; Benede, N.; Suzuki, A.; Khan, K.; Cele, S.; Bernstein, M.; Karim, F.; Madzorera, S. V.; Moyo-Gwete, T.; Mennen, M.; Skelem, S.; Adriaanse, M.; Mutithu, D.; Aremu, O.; Stek, C.; du Bruyn, E.; Van Der Mescht, M. A.; de Beer, Z.; de Villiers, T. R.; Bodenstein, A.; van den Berg, G.; Mendes, A.; Strydom, A.; Venter, M.; Giandhari, J.; Naidoo, Y.; Pillay, S.; Tegally, H.; Grifoni, A.; Weiskopf, D.; Sette, A.; Wilkinson, R. J.; de Oliveira, T.; Bekker, L. G.; Gray, G.; Ueckermann, V.; Rossouw, T.; Boswell, M. T.; Bhiman, J. N.; Moore, P. L.; Sigal, A.; Ntusi, N. A. B.; Burgers, W. A.; Riou, C., T cell responses to SARS-CoV-2 spike cross-recognize Omicron. *Nature* **2022,** *603* (7901), 488-492.
23. Tarke, A.; Coelho, C. H.; Zhang, Z.; Dan, J. M.; Yu, E. D.; Methot, N.; Bloom, N. I.; Goodwin, B.; Phillips, E.; Mallal, S.; Sidney, J.; Filaci, G.; Weiskopf, D.; da Silva Antunes, R.; Crotty, S.; Grifoni, A.; Sette, A., SARS-CoV-2 vaccination induces immunological T cell memory able to cross-recognize variants from Alpha to Omicron. *Cell* **2022,** *185* (5), 847-859.e11.
24. Zhang, Z.; Mateus, J.; Coelho, C. H.; Dan, J. M.; Moderbacher, C. R.; Gálvez, R. I.; Cortes, F. H.; Grifoni, A.; Tarke, A.; Chang, J.; Escarrega, E. A.; Kim, C.; Goodwin, B.; Bloom, N. I.; Frazier, A.; Weiskopf, D.; Sette, A.; Crotty, S., Humoral and cellular immune memory to four COVID-19 vaccines. *Cell* **2022,** *185* (14), 2434-2451.e17.
25. Yuen, G. J.; Demissie, E.; Pillai, S., B lymphocytes and cancer: a love-hate relationship. *Trends Cancer* **2016,** *2* (12), 747-757.
26. Qin, Z.; Richter, G.; Schuler, T.; Ibe, S.; Cao, X.; Blankenstein, T., B cells inhibit induction of T cell-dependent tumor immunity. *Nat Med* **1998,** *4* (5), 627-30.
27. Shah, S.; Divekar, A. A.; Hilchey, S. P.; Cho, H. M.; Newman, C. L.; Shin, S. U.; Nechustan, H.; Challita-Eid, P. M.; Segal, B. M.; Yi, K. H.; Rosenblatt, J. D., Increased rejection of primary tumors in mice lacking B cells: inhibition of anti-tumor CTL and TH1 cytokine responses by B cells. *Int J Cancer* **2005,** *117* (4), 574-86.
28. Brodt, P.; Gordon, J., Anti-tumor immunity in B lymphocyte-deprived mice. I. Immunity to a chemically induced tumor. *J Immunol* **1978,** *121* (1), 359-62.
29. Barbera-Guillem, E.; Nelson, M. B.; Barr, B.; Nyhus, J. K.; May, K. F., Jr.; Feng, L.; Sampsel, J. W., B lymphocyte pathology in human colorectal cancer. Experimental and clinical therapeutic effects of partial B cell depletion. *Cancer Immunol Immunother* **2000,** *48* (10), 541-9.
30. Shen, P.; Fillatreau, S., Antibody-independent functions of B cells: a focus on cytokines. *Nat Rev Immunol* **2015,** *15* (7), 441-51.
31. DiLillo, D. J.; Yanaba, K.; Tedder, T. F., B cells are required for optimal CD4+ and CD8+ T cell tumor immunity: therapeutic B cell depletion enhances B16 melanoma growth in mice. *J Immunol* **2010,** *184* (7), 4006-16.
32. de Jonge, K.; Tille, L.; Lourenco, J.; Maby-El Hajjami, H.; Nassiri, S.; Racle, J.; Gfeller, D.; Delorenzi, M.; Verdeil, G.; Baumgaertner, P.; Speiser, D. E., Inflammatory B cells correlate with failure to checkpoint blockade in melanoma patients. *Oncoimmunology* **2021,** *10* (1), 1873585.
33. de Visser, K. E.; Korets, L. V.; Coussens, L. M., De novo carcinogenesis promoted by chronic inflammation is B lymphocyte dependent. *Cancer Cell* **2005,** *7* (5), 411-23.

34. Kaumaya, P. T., B-cell epitope peptide cancer vaccines: a new paradigm for combination immunotherapies with novel checkpoint peptide vaccine. *Future Oncology* **2020,** *16* (23), 1767-1791.
35. Helmink, B. A.; Reddy, S. M.; Gao, J.; Zhang, S.; Basar, R.; Thakur, R.; Yizhak, K.; Sade-Feldman, M.; Blando, J.; Han, G.; Gopalakrishnan, V.; Xi, Y.; Zhao, H.; Amaria, R. N.; Tawbi, H. A.; Cogdill, A. P.; Liu, W.; LeBleu, V. S.; Kugeratski, F. G.; Patel, S.; Davies, M. A.; Hwu, P.; Lee, J. E.; Gershenwald, J. E.; Lucci, A.; Arora, R.; Woodman, S.; Keung, E. Z.; Gaudreau, P. O.; Reuben, A.; Spencer, C. N.; Burton, E. M.; Haydu, L. E.; Lazar, A. J.; Zapassodi, R.; Hudgens, C. W.; Ledesma, D. A.; Ong, S.; Bailey, M.; Warren, S.; Rao, D.; Krijgsman, O.; Rozeman, E. A.; Peeper, D.; Blank, C. U.; Schumacher, T. N.; Butterfield, L. H.; Zelazowska, M. A.; McBride, K. M.; Kalluri, R.; Allison, J.; Petitprez, F.; Fridman, W. H.; Sautès-Fridman, C.; Hacohen, N.; Rezvani, K.; Sharma, P.; Tetzlaff, M. T.; Wang, L.; Wargo, J. A., B cells and tertiary lymphoid structures promote immunotherapy response. *Nature* **2020,** *577* (7791), 549-555.
36. Cabrita, R.; Lauss, M.; Sanna, A.; Donia, M.; Skaarup Larsen, M.; Mitra, S.; Johansson, I.; Phung, B.; Harbst, K.; Vallon-Christersson, J.; van Schoiack, A.; Lövgren, K.; Warren, S.; Jirström, K.; Olsson, H.; Pietras, K.; Ingvar, C.; Isaksson, K.; Schadendorf, D.; Schmidt, H.; Bastholt, L.; Carneiro, A.; Wargo, J. A.; Svane, I. M.; Jönsson, G., Tertiary lymphoid structures improve immunotherapy and survival in melanoma. *Nature* **2020,** *577* (7791), 561-565.
37. Petitprez, F.; de Reyniès, A.; Keung, E. Z.; Chen, T. W.; Sun, C. M.; Calderaro, J.; Jeng, Y. M.; Hsiao, L. P.; Lacroix, L.; Bougoüin, A.; Moreira, M.; Lacroix, G.; Natario, I.; Adam, J.; Lucchesi, C.; Laizet, Y. H.; Toulmonde, M.; Burgess, M. A.; Bolejack, V.; Reinke, D.; Wani, K. M.; Wang, W. L.; Lazar, A. J.; Roland, C. L.; Wargo, J. A.; Italiano, A.; Sautès-Fridman, C.; Tawbi, H. A.; Fridman, W. H., B cells are associated with survival and immunotherapy response in sarcoma. *Nature* **2020,** *577* (7791), 556-560.
38. Kroeger, D. R.; Milne, K.; Nelson, B. H., Tumor-Infiltrating Plasma Cells Are Associated with Tertiary Lymphoid Structures, Cytolytic T-Cell Responses, and Superior Prognosis in Ovarian Cancer. *Clinical cancer research : an official journal of the American Association for Cancer Research* **2016,** *22* (12), 3005-15.
39. Garaud, S.; Buisseret, L.; Solinas, C.; Gu-Trantien, C.; de Wind, A.; Van den Eynden, G.; Naveaux, C.; Lodewyckx, J. N.; Boisson, A.; Duvillier, H.; Craciun, L.; Ameye, L.; Veys, I.; Paesmans, M.; Larsimont, D.; Piccart-Gebhart, M.; Willard-Gallo, K., Tumor infiltrating B-cells signal functional humoral immune responses in breast cancer. *JCI Insight* **2019,** *5*.
40. Sagiv-Barfi, I.; Czerwinski, D. K.; Shree, T.; Lohmeyer, J. J. K.; Levy, R., Intratumoral immunotherapy relies on B and T cell collaboration. *Sci Immunol* **2022,** *7* (71), eabn5859.
41. Cui, C.; Wang, J.; Fagerberg, E.; Chen, P. M.; Connolly, K. A.; Damo, M.; Cheung, J. F.; Mao, T.; Askari, A. S.; Chen, S.; Fitzgerald, B.; Foster, G. G.; Eisenbarth, S. C.; Zhao, H.; Craft, J.; Joshi, N. S., Neoantigen-driven B cell and CD4 T follicular helper cell collaboration promotes anti-tumor CD8 T cell responses. *Cell* **2021,** *184* (25), 6101-6118 e13.
42. Hollern, D. P.; Xu, N.; Thennavan, A.; Glodowski, C.; Garcia-Recio, S.; Mott, K. R.; He, X.; Garay, J. P.; Carey-Ewend, K.; Marron, D.; Ford, J.; Liu, S.; Vick, S. C.; Martin, M.; Parker, J. S.; Vincent, B. G.; Serody, J. S.; Perou, C. M., B Cells and T Follicular Helper Cells Mediate Response to Checkpoint Inhibitors in High Mutation Burden Mouse Models of Breast Cancer. *Cell* **2019,** *179* (5), 1191-1206.e21.
43. Wieland, A.; Patel, M. R.; Cardenas, M. A.; Eberhardt, C. S.; Hudson, W. H.; Obeng, R. C.; Griffith, C. C.; Wang, X.; Chen, Z. G.; Kissick, H. T.; Saba, N. F.; Ahmed, R., Defining HPV-specific B cell responses in patients with head and neck cancer. *Nature* **2020**.
44. Chaurio, R. A.; Anadon, C. M.; Lee Costich, T.; Payne, K. K.; Biswas, S.; Harro, C. M.; Moran, C.; Ortiz, A. C.; Cortina, C.; Rigolizzo, K. E.; Sprenger, K. B.; Mine, J. A.; Innamarato, P.; Mandal, G.; Powers, J. J.; Martin, A.; Wang, Z.; Mehta, S.; Perez, B. A.; Li,

R.; Robinson, J.; Kroeger, J. L.; Curiel, T. J.; Yu, X.; Rodriguez, P. C.; Conejo-Garcia, J. R., TGF-β-mediated silencing of genomic organizer SATB1 promotes Tfh cell differentiation and formation of intra-tumoral tertiary lymphoid structures. *Immunity* **2022,** *55* (1), 115-128.e9.
45. Overacre-Delgoffe, A. E.; Bumgarner, H. J.; Cillo, A. R.; Burr, A. H. P.; Tometich, J. T.; Bhattacharjee, A.; Bruno, T. C.; Vignali, D. A. A.; Hand, T. W., Microbiota-specific T follicular helper cells drive tertiary lymphoid structures and anti-tumor immunity against colorectal cancer. *Immunity* **2021,** *54* (12), 2812-2824.e4.
46. Graalmann, T.; Borst, K.; Manchanda, H.; Vaas, L.; Bruhn, M.; Graalmann, L.; Koster, M.; Verboom, M.; Hallensleben, M.; Guzman, C. A.; Sutter, G.; Schmidt, R. E.; Witte, T.; Kalinke, U., B cell depletion impairs vaccination-induced CD8(+) T cell responses in a type I interferon-dependent manner. *Ann Rheum Dis* **2021,** *80* (12), 1537-1544.
47. Guo, L.; Kapur, R.; Aslam, R.; Speck, E. R.; Zufferey, A.; Zhao, Y.; Kim, M.; Lazarus, A. H.; Ni, H.; Semple, J. W., CD20+ B-cell depletion therapy suppresses murine CD8+ T-cell-mediated immune thrombocytopenia. *Blood* **2016,** *127* (6), 735-8.
48. Klarquist, J.; Cross, E. W.; Thompson, S. B.; Willett, B.; Aldridge, D. L.; Caffrey-Carr, A. K.; Xu, Z.; Hunter, C. A.; Getahun, A.; Kedl, R. M., B cells promote CD8 T cell primary and memory responses to subunit vaccines. *Cell Rep* **2021,** *36* (8), 109591.
49. Tanchot, C.; Rocha, B., CD8 and B cell memory: same strategy, same signals. *Nat Immunol* **2003,** *4* (5), 431-2.
50. Schudel, A.; Francis, D. M.; Thomas, S. N., Material design for lymph node drug delivery. *Nature reviews. Materials* **2019,** *4* (6), 415-428.
51. Wang, J.; Hu, X.; Xiang, D., Nanoparticle drug delivery systems: an excellent carrier for tumor peptide vaccines. *Drug delivery* **2018,** *25* (1), 1319-1327.
52. Fries, C. N.; Curvino, E. J.; Chen, J. L.; Permar, S. R.; Fouda, G. G.; Collier, J. H., Advances in nanomaterial vaccine strategies to address infectious diseases impacting global health. *Nat Nanotechnol* **2020**.
53. Bachmann, M. F.; Jennings, G. T., Vaccine delivery: a matter of size, geometry, kinetics and molecular patterns. *Nat Rev Immunol* **2010,** *10* (11), 787-96.
54. Singh, A., Eliciting B cell immunity against infectious diseases using nanovaccines. *Nat Nanotechnol* **2021,** *16* (1), 16-24.
55. Cheng, W., The Density Code for the Development of a Vaccine? *J Pharm Sci* **2016,** *105* (11), 3223-3232.
56. Hinton, H. J.; Jegerlehner, A.; Bachmann, M. F., Pattern recognition by B cells: the role of antigen repetitiveness versus Toll-like receptors. *Curr Top Microbiol Immunol* **2008,** *319*, 1-15.
57. Pierce, S. K.; Liu, W. L., The tipping points in the initiation of B cell signalling: how small changes make big differences. *Nature Reviews Immunology* **2010,** *10* (11), 767-777.
58. Zabel, F.; Kundig, T. M.; Bachmann, M. F., Virus-induced humoral immunity: on how B cell responses are initiated. *Curr Opin Virol* **2013,** *3* (3), 357-62.
59. Kim, Y. M.; Pan, J. Y.; Korbel, G. A.; Peperzak, V.; Boes, M.; Ploegh, H. L., Monovalent ligation of the B cell receptor induces receptor activation but fails to promote antigen presentation. *Proceedings of the National Academy of Sciences of the United States of America* **2006,** *103* (9), 3327-32.
60. Turner, J. S.; Ke, F.; Grigorova, I. L., B Cell Receptor Crosslinking Augments Germinal Center B Cell Selection when T Cell Help Is Limiting. *Cell Rep* **2018,** *25* (6), 1395-1403.e4.
61. Maeda, F. Y.; van Haaren, J. J.; Langley, D. B.; Christ, D.; Andrews, N. W.; Song, W., Surface-associated antigen induces permeabilization of primary mouse B-cells and lysosome exocytosis facilitating antigen uptake and presentation to T-cells. *eLife* **2021,** *10*.
62. Mohsen, M. O.; Augusto, G.; Bachmann, M. F., The 3Ds in virus-like particle based-vaccines: "Design, Delivery and Dynamics". *Immunol Rev* **2020,** *296* (1), 155-168.

63. Chen, Z.; Wholey, W. Y.; Hassani Najafabadi, A.; Moon, J. J.; Grigorova, I.; Chackerian, B.; Cheng, W., Self-Antigens Displayed on Liposomal Nanoparticles above a Threshold of Epitope Density Elicit Class-Switched Autoreactive Antibodies Independent of T Cell Help. *J Immunol* **2020,** *204* (2), 335-347.
64. Ingale, J.; Stano, A.; Guenaga, J.; Sharma, S. K.; Nemazee, D.; Zwick, M. B.; Wyatt, R. T., High-Density Array of Well-Ordered HIV-1 Spikes on Synthetic Liposomal Nanoparticles Efficiently Activate B Cells. *Cell Rep* **2016,** *15* (9), 1986-99.
65. Cheng, W., The Density Code for the Development of a Vaccine? *J. Pharm. Sci.* **2016,** *105* (11), 3223-3232.
66. Junt, T.; Moseman, E. A.; Iannacone, M.; Massberg, S.; Lang, P. A.; Boes, M.; Fink, K.; Henrickson, S. E.; Shayakhmetov, D. M.; Di Paolo, N. C.; van Rooijen, N.; Mempel, T. R.; Whelan, S. P.; von Andrian, U. H., Subcapsular sinus macrophages in lymph nodes clear lymph-borne viruses and present them to antiviral B cells. *Nature* **2007,** *450* (7166), 110-4.
67. Lu, T. T.; Browning, J. L., Role of the Lymphotoxin/LIGHT System in the Development and Maintenance of Reticular Networks and Vasculature in Lymphoid Tissues. *Frontiers in immunology* **2014,** *5*, 47.
68. Johansson-Percival, A.; He, B.; Li, Z. J.; Kjellén, A.; Russell, K.; Li, J.; Larma, I.; Ganss, R., De novo induction of intratumoral lymphoid structures and vessel normalization enhances immunotherapy in resistant tumors. *Nat Immunol* **2017,** *18* (11), 1207-1217.
69. Tan, Y. S.; Sansanaphongpricha, K.; Xie, Y.; Donnelly, C. R.; Luo, X.; Heath, B. R.; Zhao, X.; Bellile, E.; Hu, H.; Chen, H.; Polverini, P. J.; Chen, Q.; Young, S.; Carey, T. E.; Nor, J. E.; Ferris, R. L.; Wolf, G. T.; Sun, D.; Lei, Y. L., Mitigating SOX2-potentiated Immune Escape of Head and Neck Squamous Cell Carcinoma with a STING-inducing Nanosatellite Vaccine. *Clin Cancer Res* **2018,** *24* (17), 4242-4255.
70. Chen, H. W.; Ren, X. Q.; Paholak, H. L. J.; Burnett, J.; Ni, F.; Fang, X. L.; Sun, D. X., Facile Fabrication of Near-Infrared-Resonant and Magnetic Resonance Imaging-Capable Nanomediators for Photothermal Therapy. *Acs Appl Mater Inter* **2015,** *7* (23), 12814-12823.
71. Chen, H. W.; Burnett, J.; Zhang, F. X.; Zhang, J. M.; Paholak, H.; Sun, D. X., Highly crystallized iron oxide nanoparticles as effective and biodegradable mediators for photothermal cancer therapy. *J Mater Chem B* **2014,** *2* (7), 757-765.
72. Rockberg, J.; Schwenk, J. M.; Uhlén, M., Discovery of epitopes for targeting the human epidermal growth factor receptor 2 (HER2) with antibodies. *Molecular oncology* **2009,** *3* (3), 238-47.
73. Shukla, S.; Wen, A. M.; Commandeur, U.; Steinmetz, N. F., Presentation of HER2 epitopes using a filamentous plant virus-based vaccination platform. *J Mater Chem B* **2014,** *2* (37), 6249-6258.
74. Jasinska, J.; Wagner, S.; Radauer, C.; Sedivy, R.; Brodowicz, T.; Wiltschke, C.; Breiteneder, H.; Pehamberger, H.; Scheiner, O.; Wiedermann, U.; Zielinski, C. C., Inhibition of tumor cell growth by antibodies induced after vaccination with peptides derived from the extracellular domain of Her-2/neu. *Int J Cancer* **2003,** *107* (6), 976-83.
75. Cascalho, M.; Ma, A.; Lee, S.; Masat, L.; Wabl, M., A quasi-monoclonal mouse. *Science (New York, N.Y.)* **1996,** *272* (5268), 1649-52.
76. Veneziano, R.; Moyer, T. J.; Stone, M. B.; Wamhoff, E. C.; Read, B. J.; Mukherjee, S.; Shepherd, T. R.; Das, J.; Schief, W. R.; Irvine, D. J.; Bathe, M., Role of nanoscale antigen organization on B-cell activation probed using DNA origami. *Nat Nanotechnol* **2020,** *15* (8), 716-723.
77. Barnden, M. J.; Allison, J.; Heath, W. R.; Carbone, F. R., Defective TCR expression in transgenic mice constructed using cDNA-based alpha- and beta-chain genes under the control of heterologous regulatory elements. *Immunology and cell biology* **1998,** *76* (1), 34-40.
78. Galluzzi, L.; Yamazaki, T.; Demaria, S., Heavy Metal to Rock the Immune Infiltrate. *Trends Immunol* **2017,** *38* (8), 539-541.

79. Whittington, P. J.; Radkevich-Brown, O.; Jacob, J. B.; Jones, R. F.; Weise, A. M.; Wei, W. Z., Her-2 DNA versus cell vaccine: immunogenicity and anti-tumor activity. *Cancer Immunol Immunother* **2009,** *58* (5), 759-67.
80. Clifton, G. T.; Gall, V.; Peoples, G. E.; Mittendorf, E. A., Clinical Development of the E75 Vaccine in Breast Cancer. *Breast care (Basel, Switzerland)* **2016,** *11* (2), 116-21.
81. Peoples, G. E.; Holmes, J. P.; Hueman, M. T.; Mittendorf, E. A.; Amin, A.; Khoo, S.; Dehqanzada, Z. A.; Gurney, J. M.; Woll, M. M.; Ryan, G. B.; Storrer, C. E.; Craig, D.; Ioannides, C. G.; Ponniah, S., Combined clinical trial results of a HER2/neu (E75) vaccine for the prevention of recurrence in high-risk breast cancer patients: U.S. Military Cancer Institute Clinical Trials Group Study I-01 and I-02. *Clin Cancer Res* **2008,** *14* (3), 797-803.
82. Mittendorf, E. A.; Clifton, G. T.; Holmes, J. P.; Schneble, E.; van Echo, D.; Ponniah, S.; Peoples, G. E., Final report of the phase I/II clinical trial of the E75 (nelipepimut-S) vaccine with booster inoculations to prevent disease recurrence in high-risk breast cancer patients. *Ann Oncol* **2014,** *25* (9), 1735-42.
83. Costa, R. L. B.; Soliman, H.; Czerniecki, B. J., The clinical development of vaccines for HER2(+) breast cancer: Current landscape and future perspectives. *Cancer Treat Rev* **2017,** *61*, 107-115.
84. Schrörs, B.; Boegel, S.; Albrecht, C.; Bukur, T.; Bukur, V.; Holtsträter, C.; Ritzel, C.; Manninen, K.; Tadmor, A. D.; Vormehr, M.; Sahin, U.; Löwer, M., Multi-Omics Characterization of the 4T1 Murine Mammary Gland Tumor Model. *Frontiers in oncology* **2020,** *10*, 1195.
85. Lin, E. Y.; Jones, J. G.; Li, P.; Zhu, L.; Whitney, K. D.; Muller, W. J.; Pollard, J. W., Progression to malignancy in the polyoma middle T oncoprotein mouse breast cancer model provides a reliable model for human diseases. *The American journal of pathology* **2003,** *163* (5), 2113-26.
86. Tarantino, P.; Curigliano, G.; Tolaney, S. M., Navigating the HER2-Low Paradigm in Breast Oncology: New Standards, Future Horizons. *Cancer discovery* **2022,** *12* (9), 2026-2030.
87. Muramatsu, M.; Sankaranand, V. S.; Anant, S.; Sugai, M.; Kinoshita, K.; Davidson, N. O.; Honjo, T., Specific expression of activation-induced cytidine deaminase (AID), a novel member of the RNA-editing deaminase family in germinal center B cells. *The Journal of biological chemistry* **1999,** *274* (26), 18470-6.
88. Klein, U.; Dalla-Favera, R., Germinal centres: role in B-cell physiology and malignancy. *Nat Rev Immunol* **2008,** *8* (1), 22-33.
89. Schumacher, T. N.; Thommen, D. S., Tertiary lymphoid structures in cancer. *Science (New York, N.Y.)* **2022,** *375* (6576), eabf9419.
90. Senapati, S.; Darling, R. J.; Ross, K. A.; Wannemeuhler, M. J.; Narasimhan, B.; Mallapragada, S. K., Self-assembling synthetic nanoadjuvant scaffolds cross-link B cell receptors and represent new platform technology for therapeutic antibody production. *Science advances* **2021,** *7* (32).
91. Srinivas Reddy, A.; Tsourkas, P. K.; Raychaudhuri, S., Monte Carlo study of B-cell receptor clustering mediated by antigen crosslinking and directed transport. *Cellular & molecular immunology* **2011,** *8* (3), 255-64.
92. Bonasia, C. G.; Abdulahad, W. H.; Rutgers, A.; Heeringa, P.; Bos, N. A., B Cell Activation and Escape of Tolerance Checkpoints: Recent Insights from Studying Autoreactive B Cells. *Cells* **2021,** *10* (5).
93. Thierry, G. R.; Kuka, M.; De Giovanni, M.; Mondor, I.; Brouilly, N.; Iannacone, M.; Bajénoff, M., The conduit system exports locally secreted IgM from lymph nodes. *J Exp Med* **2018,** *215* (12), 2972-2983.
94. Franklin, M. C.; Carey, K. D.; Vajdos, F. F.; Leahy, D. J.; de Vos, A. M.; Sliwkowski, M. X., Insights into ErbB signaling from the structure of the ErbB2-pertuzumab complex. *Cancer Cell* **2004,** *5* (4), 317-28.

95. Clauson, R. M.; Chen, M.; Scheetz, L. M.; Berg, B.; Chertok, B., Size-Controlled Iron Oxide Nanoplatforms with Lipidoid-Stabilized Shells for Efficient Magnetic Resonance Imaging-Trackable Lymph Node Targeting and High-Capacity Biomolecule Display. *ACS Appl Mater Interfaces* **2018,** *10* (24), 20281-20295.
96. Tong, S.; Hou, S.; Ren, B.; Zheng, Z.; Bao, G., Self-assembly of phospholipid-PEG coating on nanoparticles through dual solvent exchange. *Nano letters* **2011,** *11* (9), 3720-6.
97. Udenfriend, S.; Stein, S.; Böhlen, P.; Dairman, W.; Leimgruber, W.; Weigele, M., Fluorescamine: a reagent for assay of amino acids, peptides, proteins, and primary amines in the picomole range. *Science (New York, N.Y.)* **1972,** *178* (4063), 871-2.
98. Mingueneau, M.; Krishnaswamy, S.; Spitzer, M. H.; Bendall, S. C.; Stone, E. L.; Hedrick, S. M.; Pe'er, D.; Mathis, D.; Nolan, G. P.; Benoist, C., Single-cell mass cytometry of TCR signaling: amplification of small initial differences results in low ERK activation in NOD mice. *Proceedings of the National Academy of Sciences of the United States of America* **2014,** *111* (46), 16466-71.
99. Billi, A. C.; Gharaee-Kermani, M.; Fullmer, J.; Tsoi, L. C.; Hill, B. D.; Gruszka, D.; Ludwig, J.; Xing, X.; Estadt, S.; Wolf, S. J.; Rizvi, S. M.; Berthier, C. C.; Hodgin, J. B.; Beamer, M. A.; Sarkar, M. K.; Liang, Y.; Uppala, R.; Shao, S.; Zeng, C.; Harms, P. W.; Verhaegen, M. E.; Voorhees, J. J.; Wen, F.; Ward, N. L.; Dlugosz, A. A.; Kahlenberg, J. M.; Gudjonsson, J. E., The female-biased factor VGLL3 drives cutaneous and systemic autoimmunity. *JCI Insight* **2019,** *4* (8).
100. Franz, B.; May, K. F., Jr.; Dranoff, G.; Wucherpfennig, K., Ex vivo characterization and isolation of rare memory B cells with antigen tetramers. *Blood* **2011,** *118* (2), 348-57.
101. DiPiazza, A. T.; Leist, S. R.; Abiona, O. M.; Moliva, J. I.; Werner, A.; Minai, M.; Nagata, B. M.; Bock, K. W.; Phung, E.; Schäfer, A.; Dinnon, K. H., 3rd; Chang, L. A.; Loomis, R. J.; Boyoglu-Barnum, S.; Alvarado, G. S.; Sullivan, N. J.; Edwards, D. K.; Morabito, K. M.; Mascola, J. R.; Carfi, A.; Corbett, K. S.; Moore, I. N.; Baric, R. S.; Graham, B. S.; Ruckwardt, T. J., COVID-19 vaccine mRNA-1273 elicits a protective immune profile in mice that is not associated with vaccine-enhanced disease upon SARS-CoV-2 challenge. *Immunity* **2021,** *54* (8), 1869-1882.e6.
102. Reiss, S.; Baxter, A. E.; Cirelli, K. M.; Dan, J. M.; Morou, A.; Daigneault, A.; Brassard, N.; Silvestri, G.; Routy, J. P.; Havenar-Daughton, C.; Crotty, S.; Kaufmann, D. E., Comparative analysis of activation induced marker (AIM) assays for sensitive identification of antigen-specific CD4 T cells. *PloS one* **2017,** *12* (10), e0186998.
103. Sanchez, A. B.; Nguyen, T.; Dema-Ala, R.; Kummel, A. C.; Kipps, T. J.; Messmer, B. T., A general process for the development of peptide-based immunoassays for monoclonal antibodies. *Cancer chemotherapy and pharmacology* **2010,** *66* (5), 919-25.
104. Aran, D.; Looney, A. P.; Liu, L.; Wu, E.; Fong, V.; Hsu, A.; Chak, S.; Naikawadi, R. P.; Wolters, P. J.; Abate, A. R.; Butte, A. J.; Bhattacharya, M., Reference-based analysis of lung single-cell sequencing reveals a transitional profibrotic macrophage. *Nat Immunol* **2019,** *20* (2), 163-172.
105. Heng, T. S.; Painter, M. W., The Immunological Genome Project: networks of gene expression in immune cells. *Nat Immunol* **2008,** *9* (10), 1091-4.
106. Zhang, X.; Lan, Y.; Xu, J.; Quan, F.; Zhao, E.; Deng, C.; Luo, T.; Xu, L.; Liao, G.; Yan, M.; Ping, Y.; Li, F.; Shi, A.; Bai, J.; Zhao, T.; Li, X.; Xiao, Y., CellMarker: a manually curated resource of cell markers in human and mouse. *Nucleic acids research* **2019,** *47* (D1), D721-d728.

# Chapter 3

# SARS-CoV-2 Epitope-Guided Neoantigen Cancer Vaccine Promotes B/CD4 T Cell Crosstalk to Enhance Antitumor Efficacy


## 3.1 Abstract

B cell immunity plays critical roles in antitumor immune response and is associated with immune checkpoint blockade (ICB) and overall survival in various types of cancer through B cell antigen presentation mediated B/CD4 T cell collaboration. Nevertheless, all current neoantigen cancer vaccine designed to potentiate antitumor CD4 T and CD8 T cell immunity and to amplify ICB immune responses are unable to stimulate B cell immunity and promotes B/CD4 T cell collaboration. Hence, we demonstrate a cancer epitope designing strategy using foreign viral SARS-CoV-2 B epitope combined with tumor CD4 T and CD8 T antigens. SARS-CoV-2 B epitope displayed on the surface of antigen cluster nanoparticles (ACN), combined with tumor T antigens (ACN-SpB&T), efficiently crosslinks with B cell receptor of SARS-CoV-2 B epitope specific B cells, facilitates subsequent antigen internalization and presentation through MHC-II complex to tumor CD4 T antigen specific T cell. ACN-SpB&T promotes B/CD4 T cell collaboration with up to 4.7-fold higher germinal center (GC) B and T follicular helper (Tfh) cells responses and up to 14.7-fold greater frequencies of neoantigen specific CD4 T and CD8 T cells compared to vaccine contains only T antigens. Moreover, SARS-CoV-2 B epitope strategy were further validated both at peptide and mRNA platforms with potent tumor growth inhibition across multiple tumor models, represent a novel and highly clinical translatable approach for neoantigen cancer vaccine.


## 3.2 Introduction

Neoantigen cancer vaccine has been extensively explored to synergize with ICB for amplified antitumor CD8 T cell immune responses[1-9]. These vaccines are designed to promote dendritic cell/macrophage-mediated antigen presentation to activate CD4 and CD8 T cells. However, despite some promising results in certain cancer type (e.g. melanoma) in preclinical and clinical

studies, most of these vaccines have yet to achieve long-term efficacy across different types of cancers[1, 3-12].

The role of B cell immunity in cancer vaccines has been a subject of debate for several decades,[13-21] and thus therapeutic cancer vaccines have not typically been designed to activate B cell immunity. However, recent clinical studies suggest that B cell immunity is essential for achieving long-term anticancer efficacy in immunotherapy[22-26]. High densities of B cells in tumors have been shown to be strongly associated with better clinical responses to immune checkpoint blockade in various types of cancer[22-27].

These studies also suggest that the role of B cells in inducing B/CD4 T cell crosstalk plays a critical part in driving anticancer immunity, beyond merely producing antibodies.[22-32] In this process, B cells act like antigen presenting cells, they first recognize B cell epitopes on an antigen through the B cell receptor (BCR), then process and present CD4 epitopes to antigen-specific CD4 T cells for B/CD4 T cell crosstalk. Then, activated B cells and CD 4 T cells goes to follicular, where the B/CD4 T cell crosstalk further drives a T follicular helper (Tfh) cell-dependent germinal center (GC) response, which promotes differentiation and expansion of antigen-specific GC B and Tfh cells. Studies have shown that blocking B cell-mediated antigen presentation or B/CD4 T cell interaction (such as ICOS-ICOSL and CD40-CD40L interaction) impairs the anticancer immune responses and efficacy of immunotherapy.[28, 29] Recent findings demonstrated that GC B cell and Tfh cell activation is critical to facilitate the antitumor response of ICB in breast and head and neck cancers.[27] The B/CD4 crosstalk induced Tfh cells can also promote antitumor immune responses and efficacy by enhancing CD8 effector T cell functions. In addition, B cell activation is essential to provide crucial help for the survival/expansion of primary and memory CD4 and CD8 T cells in antitumor immune responses.[33-36] The latest studies show that the expansion/survival of long-term memory CD8 T cells require not only CD4 T cell help[37-42] but also B cell activation[33-36].

Most current neoantigen cancer vaccines only contain CD4/CD8 T cell epitopes, without B cell epitopes, could not promote B cell-mediated antigen presentation for B/CD4 T cell crosstalk.[29, 42] These vaccines are taken up only by DC/macrophages since DCs or macrophages are able to endocytose antigens in a non-specific manner, [43] which can present the T cell epitopes to CD4 or CD8 T cells to generate antigen specific CD4/CD8 T cells. These vaccines cannot be taken up by B cells in an antigen specific manner for potent antigen presentation (without B cell epitope binding to B cell receptor on B cells).

Identifying tumor B cell epitopes for vaccine design presents significant challenges. The most neoantigens are either CD4 (~70%) or CD8 (~30%) T cell epitopes, and no B cell epitope neoantigen has been discovered yet.[42] B cell epitope of tumor-associated antigens (TAA), such as HER-2, VEGF, and EGFR, can be used to enhance B/CD4 crosstalk in vaccine desgine.[44] However, these TAAs are expressed in both cancer cells and normal cells, which may lead to either immune tolerance or toxicity to normal tissues.[45]

Since B cell antigen presentation mediated B/CD4 crosstalk is critical for its durable anticancer efficacy, while tumor specific antibody by induced by tumor specific B cell epitope is less important. We hypothesize that a “promiscuous” viral B cell epitope with robust immunogenicity could be used to promote its binding/crosslink with BCR, which enhance B cell mediated antigen presentation of tumor neoantigen to activate the required B/CD4 T cell crosstalk for durable anticancer efficacy. This will offer significant advantage in the novel cancer vaccine design since most tumor neoantigens are CD4 T cell epitopes (less are CD8 T cell epitopes) and no B cell neoantigens have been found in tumors.

In addition, to promote B and CD4 T cell crosstalk, a vaccine system should also have an optimized delivery system that enables B cell-mediated antigen presentation to activate CD4 T cells. [46-49] Most current neoantigen cancer vaccine delivery carriers, either using soluble peptide antigen or nanoformulation encapsulated antigens inside, mainly promote DC/macrophage-mediated antigen presentation since DC/macrophage can uptake these antigens in a non-specific manner.[43, 50-53] In contrast, although there are larger number of B cells residing inside the lymph nodes, the B cells have limited ability to internalize antigens for presentation without B cell epitope binding and crosslinking with the B cell receptor.[43] Therefore, to facilitate B cell-mediated antigen presentation, the delivery system must have B cell epitope on the surface, penetrate inside the lymph nodes, reach B cell zone or cortex to bind B cell receptor (BCR), crosslink with BCR. These processes will result in the efficient uptake of antigen to inside B cells for antigen presentation of the CD4 epitope through the MHCII complex to CD4 T cells.

In this study, we developed a cancer vaccine design strategy utilizing viral SARS-CoV-2 B epitopes, combined with tumor-specific CD4/CD8 T neoantigens, to promote B/CD4 T cell crosstalk and enhance the efficacy of CD4/CD8 T cell neoantigen vaccines. To prove the concept, we used two specifically designed nanocarriers to deliver peptide and mRNA antigens, respectively. First, the viral-antigen-mimicry nanoparticle (VAM), previously designed by our group and shown to effectively promote B and CD4 T cell crosstalk, was used to deliver peptide

antigens. The mRNA vaccine was prepared using lipid nanoparticles that encapsulate mRNA encoding tumor T cell neoantigens, with the surface conjugated to the SARS-CoV-2 B epitope. Our results demonstrated that strategically adding foreign SARS-CoV-2 B epitopes with T cell antigens facilitates vaccine binding and crosslinking with BCR, and antigen presentation by SARS-CoV-2 B epitope-specific B cells to tumor-specific CD4 T cells. The SARS-CoV-2 B epitope strategy significantly amplified antitumor immune responses and efficacy, with robust B/CD4 T crosstalk and enhanced GC B and Tfh cell responses compared to vaccines containing only tumor T neoantigens in multiple cancer models. The mRNA cancer vaccine with the SARS-CoV-2 B epitope strategy showed superior anticancer efficacy, with robust B/CD4 T crosstalk and neoantigen-specific cytotoxic CD8 T cell activation. Overall, the SARS-CoV-2 B epitope guided neoantigen vaccine provides a generalized strategy to optimize B/CD4 T crosstalk and amplify antitumor immune responses and efficacy for neoantigen cancer vaccine design.

### 3.3 Results

**SARS-CoV-2 B epitope guided peptide vaccine promotes B cell antigen presentation mediated B/CD4 T cell crosstalk.**

To further investigate whether SARS-CoV-2 B epitope could promote B/CD4 T cell crosstalk, we chose a previously identified SARS-CoV-2 B peptide epitope (CDDDTESNKKFLPFQQFGRDIA and CDDDPSKPSKRSFIEDLLFNKV)[54, 55] and linked on the surface of an antigen cluster nanoparticle (ACN). ACN was previously engineered by our group, which has an iron nanoparticle (IONP) core and surface attached with small gold nanoparticle. By conjugating antigen peptides with gold nanoparticle on ACN through thiol-Au reaction, it forms a viral antigen-cluster-mimicry topography with high density of peptide epitopes on the cluster (150 peptides/cluster) and optimal distance (5 - 10 nm) between two antigen clusters (30 nm, Figure S1a). The unique structure of ACN promotes lymph node trafficking, crosslink B cell receptor (BCR), and B cell-mediated antigen presentation to induce a robust B/CD4 T cell crosstalk. We have shown that ACN with SARS-CoV-2 B peptide epitope linked on the surface deeply penetrates inside the cortex and B cell zone of lymph node (Figure 3.1a), increasing the probability of antigens encountering B cells. To investigate whether antigen cluster structure of ACN can further facilitate the binding of antigens with BCR through crosslinking after encountering B cells. We incubate hapten-specific B cells from QM transgenic mice with Cy3 labeled and hapten conjugated peptide (Pep-NP) presents by ACN (ACN-Pep-NP). ACN-Pep-NP showed significantly increased BCR crosslinking efficiency compared to Pep-NP (Figure 3.1b and S1b).

To further investigate whether SARS-CoV-2 B epitope could promote B/CD4 T cell crosstalk, we conjugated SARS-CoV-2 B epitope and OT-II CD4 T epitope (chicken ovalbumin$_{323-339}$) with ACN (ACN-SpB/OT-II), incubated with B cells from lymph node and spleen of SARS-CoV-2 spike protein immunized mice and OT-II specific CD4 T cells from the spleen of OT-II transgenic mice for 24 h or 96 h (Figure 3.1c, 1d, S2-S6). LPS mixed with OT-II CD4 T epitope (LPS&OT-II Peptide) and OT-II CD4 T epitope conjugated with ACN (ACN-OT-II) were used as comparison. We firstly monitored the activation and proliferation of B cells from spike protein immunized mice (B cells labeled with CFSE tracker). ACN-SpB/OT-II indicated 3.2-fold (as monitored by CD86 intensity) and 15.6-fold (as monitored by CD69 intensity) higher activation and 33.2-fold higher proliferation (as monitored by CFSE intensity) than ACN-OT-II (Figure 1c and S2). To investigate whether ACN-SpB/OT-II activated B cells could process and present OT-II CD4 T epitope to activate OT-II CD4 T cells, we measured the activation and proliferation of OT-II CD4 T cells (labeled with CFSE tracker) by flow cytometry. ACN-SpB/OT-II stimulated 9.4-fold (as monitored by CD69 intensity) and 2.2-fold (as monitored by CD25 intensity) higher activation and 204.9-fold higher proliferation (as monitored by CFSE intensity) than ACN-OT-II (Figure 3.1d and S3). No statistical differences of activation and proliferation were observed in CD4 T cells (not OT-II CD4 T epitope specific) between ACN-SpB/OT-II and ACN-OT-II (Figure S4), which indicate the antigen specific activation manner of CD4 T cells by ACN-SpB/OT-II activated B cells.

Moreover, to confirm the B cell is critical in promoting B/CD4 T cell crosstalk by ACN-SpB/OT-II, we specifically removed B cells from splenocytes and lymph node cells and mixed with OT-II specific CD4 T cells. Results showed that depletion of B cells severely impaired the activation and proliferation of OT-II specific CD4 T cells (Figure S5 and S6). To further confirm ACN-SpB/OT-II induced B/CD4 T cell crosstalk is dependent on B cell mediated antigen presentation, we pre-incubated B cells from lymph node and spleen of spike protein immunized mice with αMHC-II, αCD40L or αICOS antibodies, respectively, and then mixed with OT-II specific CD4 T cells. The blocking of antigen presentation between B cells and CD4 T cells significantly eliminated the activation and proliferation of OT-II specific CD4 T cells by ACN-SpB/OT-II (Figure S2 and S6). These results indicate that SARS-CoV-2 B epitope promotes robust in vitro B cell antigen presentation mediated B/CD4 T cell crosstalk.

To investigate how SARS-CoV-2 B epitope guided ACN tumor vaccine stimulates the in vivo B/CD4 T cell crosstalk, we immunized the mice with SARS-CoV-2 B epitope and human HER2 CD4 T epitope conjugated ACN (ACN-SpB&HER2) or human HER2 CD4 T epitope conjugated ACN (ACN-HER2) and monitored the germinal center (GC) responses and antigen specific CD4

T cell activation. Results indicated that ACN-SpB&HER2 stimulated robust GC B cells (7.0% of all B cells) and antigen specific GC B cells (5.0% of all GC B cells) compared to ACN-HER2 (4.4% GC B cells and 0.9% antigen specific GC B cells) (Figure 3.1e). ACN-SpB&HER2 also induced a 3.5-fold (3.0% vs 0.8%) higher T follicular helper (Tfh) cells and 5.2-fold (18.3% vs 3.5%) antigen specific Tfh cells compared to ACN-HER2 (Figure 3.1e and 3.1f). We also monitored the activation of antigen specific CD4 T cells after antigen encounter after ACN-SpB&HER2 vaccination. ACN-SpB&HER2 stimulated 3.7-fold and 3.8-fold higher activation of antigen experienced CD4 T cells than ACN-HER2 in lymph node and spleen, respectively (Figure 3.1g and 3.1i). In comparison, naive CD4 T cells showed no differences after ACN-SpB&HER2 and ACN-HER2 immunizations (Figure 3.1h and 3.1j). Furthermore, to confirm the ACN-SpB&HER2 induced in vivo B/CD4 T cell crosstalk is mediated through B cell antigen presentation, we blocked the MHC-II antigen presentation pathways by administration mice with αMHC-II, αCD40L or αICOS antibodies before vaccinations. Results indicated blocking of MHC-II antigen presentation pathway severely compromised the activation of antigen specific GC B, antigen specific Tfh and antigen specific CD4 T cells by ACN-SpB&HER2 (Figure S7 and S8). These results indicated that SARS-CoV-2 B epitope promotes robust in vivo B cell antigen presentation mediated B/CD4 T cell crosstalk.

**SARS-CoV-2 B epitope guided tumor peptide vaccine enhance anticancer efficacy through promoting B/CD4 T cell crosstalk and suppressing follicular regulatory T cells.**

To investigate whether a SARS-CoV-2 B epitope-guided tumor peptide vaccine could enhance anticancer efficacy, we prepared a peptide vaccine using human HER2 T cell antigens with or without the SARS-CoV-2 B epitope, conjugated to ACN (ACN-SpB&D2 or ACN-D2), and compared their anticancer efficacy in a breast cancer model using D2E7/F2 cells (a mouse breast cancer cell line expressing human HER2). ACN-SpB&D2 showed significant delay of tumor growth with 43% complete response rate compared to ACN-D2 (Figure 3.2a and S9). Moreover, single antigen including SARS-CoV-2 B epitope, human HER2 CD4T, human HER2 CD8 T, that conjugated to ACN, all indicated significantly rapid tumor growth than combining B and T epitopes (Figure S9).

To study whether ACN-SpB&D2 induces B and CD4 crosstalk contributing to the in vivo efficacy, we used Cytometry by Time-of-Flight (CyTOF) to profile the immune cell composition in both lymph nodes and tumors. Global analysis using spanning-tree progression analysis of density-normalized events (SPADE) confirmed that ACN-SpB&D2 showed significantly increased GC B

and Tfh cells than ACN-D2 in lymph node (Figure 3.2b). ACN-SpB&D2 also stimulates higher tumor immune infiltration, total GC B cells and Tfh cells (Figure 3.2c) than ACN-D2. Surprisingly, we also observed a significant decrease of follicular regulatory (Tfr, Foxp3+ Tfh) cells after ACN-SpB&D2 immunization compared to ACN-D2 both at lymph node and tumor by SPADE analysis (Figure 3.2b, 3.2c and S10). Recent studies have shown that Tfr curtails anti-PD-1 efficacy. Suppresses Tfr might contribute to the enhanced antitumor immune responses and efficacy. Flow cytometry analysis further confirmed ACN-SpB&D2 increased the GC B cells and Tfh cells while suppressing Tfr cells compared to ACN-D2 at lymph node and tumor (Figure 3.2d and 3.2e). Interestingly, we also studied the immune responses and efficacy of ACN-SpB&D2 immunization with blocking of B/CD4 T cell crosstalk by using αCD40L or αICOS antibodies. Blocking B/CD4 T cell crosstalk by αCD40L or αICOS antibodies severely compromises the antitumor efficacy of ACN-SpB&D2 (Figure S11). CyTOF and flow cytometry confirmed that αCD40L antibody significantly decreased B/CD4 T cell crosstalk with low level of GC B and Tfh cells by ACN-SpB&D2, while reverse the induction of Tfr cells both at lymph node (Figure S12 and S13) and tumor (Figure S14, S15). These results indicate that SARS-CoV-2 B epitope can promote B/CD4 T cell crosstalk in tumor model, which is critical for enhanced antitumor immune responses and efficacy.

**SARS-CoV-2 B epitope guided peptide and mRNA neoantigen cancer vaccines achieved better anti-cancer efficacy through promoting B/CD4 T cell crosstalk.**

We next evaluate whether the SARS-CoV-2 B epitope strategy could improve neoantigen cancer vaccine antitumor efficacy in melanoma model with B16F10 cells. SARS-CoV-2 B epitope combined with B16F10 neoantigens (MHC-I-restricted M27 and MHC-II-restricted M30) conjugated to ACN (ACN-SpB&B16) was compared with B16F10 neoantigens conjugated to ACN (ACN-B16) for antitumor efficacy. Results showed that ACN-SpB&B16 significantly inhibits tumor growth compared to ACN-B16 (Figure 3.3a). B16F10 tumor bearing mice immunized with ACN-SpB&B16 elicits 2.6-fold of GC B cells, 4.3-fold of Tfh cells and 14.7-fold of antigen specific CD4 T cells than ACN-B16 (Figure 3.3b). Interestingly, ACN-SpB&B16 even induced stronger antigen specific cytotoxic CD8 T cell responses by flow cytometry (6.8-fold) and ELISPOT (5.7-fold) than ACN-B16 (Figure 3.3b, 3.3c, S16 and S17).

We further confirmed the SARS-CoV-2 B epitope strategy in pancreatic cancer model with KPC6422 cells. SARS-CoV-2 B epitope combined with KPC neoantigens (Kras G12D and Tp53 R172H) conjugated to ACN (ACN-SpB&KPC) was compared with KPC neoantigens conjugated

to ACN (ACN-KPC) for antitumor efficacy. ACN-SpB&T substantially slowed tumor growth (Figure 3.3d and S18a) and remodeled tumor immune microenvironment (Figure 3.3e) compared ACN-T. ACN-SpB&T activated 2.7-fold of GC B cells and 4.2-fold of Tfh cells than ACN-KPC (Figure 3.3e and S19). ACN-SpB&KPC immunization also elicits 13-fold of antigen specific CD4 T cells and 7.5-fold of antigen specific CD8 T cells induction (Figure 3.3e - 3.3g, S18b and S19).

To further examine the clinical translation potential of SARS-CoV-2 B epitope strategy in neoantigen cancer vaccine settings, we adapted the strategy to mRNA platform for pancreatic cancer model with KPC6422 cells. To present SARS-CoV-2 B epitope at the surface of mRNA nanocarrier, we modified the lipid nanoparticle (LNP) formulation with lipids possess maleimide group to react with cysteine at the N-terminal of SARS-CoV-2 B epitope. Optimized LNP formulation (120 nm, Figure S20) showed comparable cellular transfection efficiency compared to clinical used LNP formulation (Figure S21 and S22). mRNA encoding KPC neoantigens (Kras G12D and Tp53 R172H) were then encapsulated in the LNP with or without SARS-CoV-2 B epitope (LNP(mRNA-T)-SpB or LNP(mRNA-T)) conjugation at the surface to mimic antigen cluster structure. LNP(mRNA-T)-SpB significantly delayed the tumor growth (Figure 3.3h) and promotes robust B/CD4 T cell crosstalk, which stimulates 2.8-fold of GC B cells, 2.8-fold of Tfh cells, 2.5-fold of antigen specific CD4 T cells and 6.2-fold of granzyme $B^+$ CD4 T cells than LNP(mRNA-T) vaccination (Figure 3.3i, 3.3j, S23 and S24). LNP(mRNA-T)-SpB also induced 3.7-fold of antigen specific CD8 T cell and 6.7-fold of granzyme $B^+$ CD8 T cell activation than LNP(mRNA-T) (Figure 3.3k and S24), which further experiments are needed to explain the association between B/CD4 T cell crosstalk and CD8 T cell activation.

**SARS-CoV-2 B epitope improves anti-cancer efficacy of cancer vaccine is dependent on B/CD4 T cell crosstalk.**

To confirm that the improved antitumor efficacy by SARS-CoV-2 B epitope strategy compared to T neoantigen cancer vaccine is dependent on B/CD4 T cell crosstalk, we conducted antitumor efficacy study at normal mice and μMT mice (Figure S25, without mature B cells) in melanoma model with B16-OVA cells. SARS-CoV-2 B epitope combined with B16-OVA T antigens (MHC-I-restricted $OVA_{257-264}$ peptide and MHC-II-restricted $OVA_{323-339}$) conjugated to ACN (ACN-SpB&OVA) was compared with B16-OVA T antigens conjugated to ACN (ACN-OVA) for antitumor efficacy. ACN-SpB&OVA induced robust tumor growth inhibition (Figure 3.4a) and stimulates robust B/CD4 T crosstalk and CD8 T cell activation with 2-fold of GC B, 6.8-fold of Tfh, 4-fold of

antigen specific CD4 T and 2.5-fold of antigen specific CD8 T cells at normal tumor bearing mice than ACN-OVA (Figure 3.4b).

In comparison, no differences of B/CD4 T cell crosstalk and efficacy responses were observed between ACN-SpB&OVA immunization group and control group at μMT mice (Figure 3.4a and 3.4c). B cells tail vein infusing before immunization significantly reversed the immune responses and efficacy of ACN-SpB&OVA immunization at μMT mice (Figure 3.4a and 3.4c). These results showed that B/CD4 T cell crosstalk is essential for SARS-CoV-2 B epitope to improve antitumor efficacy of T neoantigen cancer vaccine.

To further confirm that the improved antitumor efficacy by SARS-CoV-2 B epitope strategy compared to T neoantigen cancer vaccine is dependent on B cell antigen presentation mediated B/CD4 T cell crosstalk, we compared antitumor efficacy of ACN-SpB&OVA with or without blocking the B and CD4 T cell interaction processes by dosing mice with αMHC-II (Figure 3.5a), αCD40L (Figure 3.5c) or αICOS (Figure S26) antibodies. After blocking the in vivo MHC-II presentation process using αMHC-II antibody, B/CD4 T cell crosstalk was severely hindered with 1.6-fold lower of GC B and 5.8-fold lower of Tfh cells after ACN-SpB&OVA immunization (Figure 3.5b). ACN-SpB&OVA also showed significantly compromised anti-tumor CD8 T cell responses and antitumor efficacy (Figure 3.5a and 3.5b) in αMHC-II antibody administration group, which proved the essential role of B cell antigen presentation mediated B/CD4 T cell crosstalk for antitumor CD8 responses and efficacy. By blocking the costimulatory signals (CD40L and ICOS) between B and CD4 T cells interaction, B/CD4 T cells crosstalk can not be established, and results showed low levels of GC B and Tfh cells (Figure 3.5d and S27) with ACN-SpB&OVA vaccination. After blocking of CD40L and ICOS pathways, mice immunized with ACN-SpB&OVA showed rapid tumor growth and compromised antigen specific cytotoxic CD8 T cell responses compared to ACN-SpB&OVA vaccinated mice without blocking of costimulatory signals (Figure 3.5d and S26).

**3.4 Discussion and Conclusion**

Despite the tremendous potential of cancer vaccine to synergize with anti-PD-1 therapy and to amplify the antitumor cytotoxic CD8 T cell immune responses, their efficacy is still limited in clinical trials. The activation of CD8 T cells alone by cancer vaccines only induces short-term efficacy due to dysfunctional immune system and exhausted cytotoxic CD8 T cell immunity of cancer patients[3, 4]. Later studies found that help from CD4 T cells is critical to maintain the expansion and survival for long-term memory CD8 T cells in antitumor immune responses[56]. The most current neoantigen cancer vaccines designed to activates both CD4 and CD8 T cell although revealed

promising clinical results in only a few types of cancer (e.g., melanoma), their anti-tumor efficacy remains disappointing across multiple types of cancer[1, 3-12]. Recent clinical studies suggest that high tumor B cell infiltration is associated with better ICB responses and overall survival in various types of cancer [22-27]. B cell immunity is essential to activate long-term memory CD4/CD8 T immunity[22-26] and to achieve long-term antitumor efficacy[33-36]. Moreover, B/CD4 T cell crosstalk mediated through B cell antigen presentation, has been approved to correlated with clinical responses and antitumor efficacy of ICB[22-32]. Immunotherapy that activates B immunity and promotes B/CD4 T cell crosstalk would be promising to overcome the T cell exhaustion and short-term efficacy problems. Nevertheless, all current peptide and mRNA cancer vaccines without the modality to interplay with B cell immunity are unable to promote B cell antigen presentation mediated B/CD4 T cell crosstalk for mounting robust primary and memory T cell immunity to achieve long-term efficacy[1-9].

In this study, we provided a novel cancer vaccine design strategy to effectively activate B cell immunity and promote B/CD4 T cell crosstalk. We discovered that utilizing viral SARS-CoV-2 B epitopes, combined with tumor-specific CD4/CD8 T neoantigens, can promote B/CD4 T cell crosstalk and enhance the efficacy of CD4/CD8 T cell neoantigen vaccines. We prepared two specifically designed nanocarriers to deliver peptide and mRNA antigens: the viral-antigen-mimicry nanoparticle (ACN) to delivery peptide neoantigen, lipid nanoparticles to delivery mRNA neoantigen. Viral SARS-CoV-2 B epitopes were surface conjugating on both of the nanoparticle, in order to SARS-CoV-2 B epitope specific B cell uptake and present antigen to activate tumor CD4 T cell. We proved that the foreign viral SARS-CoV-2 B epitope carried at the surface of nanoparticle and combined with tumor T cell antigens (ACN-T/SpB) promoted robust SARS-CoV-2 specific B cell and tumor CD4 T cell antigen specific CD4 T cell crosstalk (**Figure 3.2**), increase tumor T cell antigens specific CD4 T and CD8 T cells activation (**Figure 3.3**), profoundly remodel tumor immune microenvironment (**Figure 3.2 and 3.3**) and dramatically enhance antitumor efficacy (**Figure 3.2-3.5**). The mRNA cancer vaccine with the SARS-CoV-2 B epitope strategy showed superior anticancer efficacy, with robust B/CD4 T crosstalk and neoantigen-specific cytotoxic CD8 T cell activation. (**Figure 3.3**) The interplay between SARS-CoV-2 B epitope specific B cells and tumor antigen specific CD4 T cells are mediated through SARS-CoV-2 B epitope specific B cell antigen presentation (**Figure 3.1**). ACN-T/SpB efficiently drains to lymph node, reaches B cell zones and crosslinks with B cell receptors of SARS-CoV-2 B epitope specific B cell, which facilitates the internalization of ACN-T/SpB by the B cell. SARS-CoV-2 B epitope specific B cell then process and upload the tumor T antigen onto MHC-II and present to the

cognate CD4 T cells. The duet between SARS-CoV-2 B epitope specific B cells and tumor T antigen specific CD4 T cells will trigger the activation of tumor T antigen specific CD4 T cells (**Figure 3.1, S2-S6 and S8**) and expansion of the germinal center B cells and T follicular help cells (**Figure 3.1-3.5 and S7**). Recent studies revealed GC B and Tfh cells activation is critical to amplify antitumor response of ICB in melanoma[22, 23, 57], sarcoma[24], breast cancer[27, 58, 59], lung cancer[29, 60, 61], ovarian cancer[25], and head and neck cancer[62, 63]. Tfh cells induced by B/CD4 T cell crosstalk played a critical role in enhancing the antitumor responses and functions of cytotoxic tumor specific CD8 T cells through secretion of interleukin (IL)-21[29, 31, 32].

In conclusion, our SARS-CoV-2 B epitope strategy promotes B cell antigen presentation mediated B/CD4 T cell crosstalk, induces robust GC B and Tfh responses, stimulates amplified tumor specific CD4 and CD8 T cell activation with dramatically improved antitumor efficacy across multiple cancer models compared to current T neoantigen cancer vaccine. As the identification of patients' neoantigens required strict selection processes and is highly personalized, the applying of mRNA technology in neoantigen cancer vaccine significantly curtails the developing time window and provides cancer patients with more flexibility. Our study further indicated that SARS-CoV-2 B epitope strategy can be adapted to mRNA cancer vaccine platform by developing an optimal modified surface epitope presenting lipid nanoparticle to facilitates uptake by B cells through B cell receptor. The superior efficacy by adding SARS-CoV-2 B epitope into current neoantigen vaccine designing framework at both peptide and mRNA platforms, confirmed the promising clinical translation potential.

### 3.5 Methods

#### Animal experiments

All animal experiments were conducted according to protocols approved by the University of Michigan Committee on Use and Care of Animals (UCUCA). Animals were maintained under pathogen-free conditions, in temperature- and humidity-controlled housing, with free access to food and water, under a 12-hour light-dark rhythm at the unit for laboratory animal medicine (ULAM), part of the University of Michigan medical school office of research. Endpoints for anti-tumor efficacy studies were determined using the End-Stage Illness Scoring System, mice receiving an End-Stage Illness Score greater than 6 were euthanized by CO2 asphyxiation.

#### Cells

All cells were maintained at 37 °C in a 5% CO2/95% air atmosphere and approximately 85% relative humidity. Primary B-cells, CD4 T cells and splenocytes were cultured in RPMI-1640 media supplemented with 10% fetal bovine serum, 2-Mercaptoethanol (50 μM) and 1% pen/strep. D2F2/E2 cells generated by cotransfection with pRSV/neo and pCMV/E2 encoding human ErbB-2 (HER2)[64], were cultured in complete high-glucose DMEM supplemented with 10% NCTC 109 media, 1% L-glutamine, 1% MEM nonessential amino acids, 0.5% sodium pyruvate, 2.5% sodium bicarbonate, 1% pen/strep, 5% cosmic calf serum, and 5% fetal bovine. B16-OVA cells were cultured in RPMI-1640 media supplemented with 10% fetal bovine serum, 2-Mercaptoethanol (54 μM), 1X non-essential amino acids, 10 mM HEPES, 1 mg/ml Geneticin and 1% pen/strep. B16F10 cells were cultured in complete high-glucose DMEM supplemented with 10% fetal bovine serum and 1% pen/strep. KPC 6422 cells obtained from kerafast were cultured in DMEM supplemented with 10% fetal bovine serum, glutamax and 1% pen/strep[65]. Bone marrow-derived dendritic cells (BMDCs) were isolated from mouse bone marrow cells and cultured following previously reported protocols[66, 67].

**Preparation, crosslink and lymph node distribution of Antigen cluster nanovaccine**

ACN was prepared based on previously reported protocols[68]. The core of ACN was made by thermal decomposition and further coated with a polysiloxane-containing copolymer. Au nanodots were then attached onto the surface of ACN core to form an antigen cluster topography. The final Au:Fe ratio of the formulated ACN was quantified by inductively coupled plasma–mass spectrometry (ICP-MS) based on previously reported protocols[69]. Peptides were added to ACN at a 5× weight ratio excess in Milli-Q water and incubated overnight at 4 °C. Peptide loading was determined by fluorescence quantification using a modified fluorescamine peptide quantification assay in the presence of ACN (Ex/Em: 390/465 nm, Biotek Cytation 5)[70].

To determine the ACN (conjugated to ED-FITC labeled peptide, CDDDPESFDGDPASNTAPLQPEQLQ, 233.6 nmol) distribution, lymph nodes were harvested 12 hours after subcutaneous injections. Lymph nodes were fixed and embedded in optical coherence tomography (OCT) compound and frozen in a $CO_{2(s)}$ + EtOH bath. Tissue sections (15 μm) were prepared, stained and mounted with VECTASHIELD® Mounting Medium for confocal imaging. Brilliant Violet 421 B220, Alexa Fluor® 594 CD 3 and Alexa Fluor® 647 CD169 were used for lymph node immune fluorescence staining.

*Investigation of BCR crosslink[71]:* B cells were isolated from splenocytes of QM mice by EasySep™ mouse B cell isolation kit (STEMCELL). QM B cells (5 * $10^6$ cells/mL) were then incubated with

Alexa Fluor 488-affinipure fab fragment goat anti-mouse IgM (20 μg/mL) on ice for 30 minutes in the dark (Jackson: 115-167-020). QM B cells ($2 \times 10^6$ cells/mL) were then incubated with cy3 labeled and hapten conjugated antigen (20 nM,) in a total volume of 400 μL for 5 minutes at 37 °C. After incubation, cells were immediately fixed with 6% paraformaldehyde (800 μL) for 10 minutes at 37 °C, permeabilized with a 0.1% Triton X HBSS solution (800 μL) for 10 minutes, and then incubated with Alexa Fluor™ Plus 405 phalloidin in staining buffer (200 μL, 5 mg/mL BSA, 0.1% Triton X in HBSS) on ice for 2 hours in the dark. Finally, the cells were washed and plated onto eight-well glass chambers pretreated with 0.1% poly-l-lysine (LabTech II) on ice for at least 4 hours in the dark before confocal imaging.

**Investigation of B/CD4 T cell crosstalk *in vitro***

CD4 T cells were isolated from splenocytes of OT-II mice (The Jackson Laboratory, Strain, #004194) by EasySep™ mouse CD4 T cell isolation kit (STEMCELL). Mice were immunized with SARS-CoV-2 Spike protein (5 μg, Val16-Pro1213, wild type, Genscript) with Alhydrogel® adjuvant 2% (InvivoGen) by intramuscular injection for three times. B cells were isolated from splenocytes and lymph nodes of spike protein immunized mice by EasySep™ mouse B cell isolation kit (STEMCELL). Cells from spleen and lymph node of spike protein immunized mice were depleted B cells by EasySep™ Mouse CD19 positive selection kit II (STEMCELL). CD4, B220, CD69, CD86, CD25 and CFSE are used as markers to measure activation and proliferation. Cell mixtures within each well of 24 well plate including: CD4 T cells (0.5 million, labeled with CFSE, from OT-II mice), B cells (1 million, labeled with CFSE, from spike protein immunized mice), full splenocytes (1.5 million, no CFSE label, from spike protein immunized mice). Cell mixtures are then incubated with different groups for 24h and 96h (All with the same amount of antigens, OT-II CD4 T epitope ($OVA_{323-339}$, CISQAVHAAHAEINEAGR, 2 μM) and SARS-CoV-2 B epitopes, (CDDDTESNKKFLPFQQFGRDIA, S14P5, 1 μM and CDDDPSKPSKRSFIEDLLFNKV S21P2, 1 μM). After each time point, cells are collected for flow cytometry analysis. For αMHC-II, αICOS and αCD40L antibodies (20 μg/mL) preincubation, all antibodies were preincubated overnight with cells before antigen incubation.

**Analysis of germinal center B cells, antigen-specific germinal center B cells and T follicular helper cells by flow cytometry**

Mice were immunized as described in manuscripts. Lymph nodes were harvested for single cell suspension for flow cytometry analysis 10 days after final immunization. $CD3^-B220^+$ $CD95^+$ $GL\text{-}7^+$ populations were identified as germinal center B cells. Germinal center derived antigen-specific

B-cell analysis was measured by tetramer staining based on previously established protocols with minor modifications[72]. Biotin-labeled SARS-CoV-2 peptides were mixed with brilliant violet 421-labeled streptavidin at an 8:1 molar ratio at room temperature for 1 hour to make peptide tetramers. $B220^{-}CD4^{+}$ $CXCR5^{+}$ $PD\text{-}1^{+}$ populations were identified as Tfh cells. For the αMHC-II (500 μg/mouse), αICOS (200 μg/mouse) or αCD40L (200 μg/mouse) antibodies blocking, antibody was intraperitoneal injected 10 days before vaccination, and then dosed 200 μg every three days.

**Analysis of Activation Induced Marker assay for T cells by flow cytometry[73, 74]**

Mice were immunized as described in manuscripts. Spleen and lymph nodes were harvested for single cell suspension 10 days after final immunization. Cells (2 million) from different groups were then incubated with $B_{SARS}$-$T_{HER2}$ peptides (2 μg/mL) for 20h at 24 well plate before flow cytometry. $B220^{-}$ $CD4^{+}$ $CXCR5^{+}$ $PD\text{-}1^{+}$ populations were identified as Tfh cells. $CD69^{+}$ $CD40L^{+/-}$ populations from Tfh cells were identified as $AIM^{+}$ Tfh cells. $B220^{-}$ $CD4^{+}$ $CD62L^{+}$ $CD69^{+}$ $CD40L^{+/-}$ populations were identified as $AIM^{+}$ antigen experienced CD4 T cells. $B220^{-}$ $CD4^{+}$ $CD62L^{-}$ $CD69^{+}$ $CD40L^{+/-}$ populations were identified as $AIM^{+}$ naïve CD4 T cells.

**In vivo anti-tumor efficacy**

$HER2^{+}$ breast cancer model: $2.5 \times 10^5$ D2F2/E2 cells were subcutaneously inoculated in the right flank of female BALB/c mice at 6 weeks of age. D2F2/E2 cells were prepared at a concentration of $2.5 \times 10^6$ cells/mL in 100 μL and were mixed with an equal volume with Matrigel matrix. Pancreatic cancer model: $5 \times 10^5$ KPC 6422 cells were subcutaneously inoculated at the right flank of male C57BL/6 mice at 6 weeks of age. Melanoma model: $5 \times 10^5$ B16F10 cells were subcutaneously inoculated at the right flank of male C57BL/6 mice at 6 weeks of age. B16-OVA model: $2 \times 10^5$ B16-OVA cells were subcutaneously inoculated at the right flank of male C57BL/6 mice or μMt mice at 6 weeks of age. For B cells infusion, $2 \times 10^6$ B cells isolated from male C57BL/6 mice at 6 weeks of age by EasySep™ mouse B cell isolation kit (STEMCELL) were infused to male μMt mice 1 day and 3 days before immunization through tail vein injection. For the αMHC-II (500 μg/mouse), αICOS (200 μg/mouse) or αCD40L (200 μg/mouse) antibodies blocking, antibody was intraperitoneal injected 10 days before vaccination, and then dosed 200 μg every three days. Tumor volumes were calculated as volume = $(\text{width})^2 \times \text{length}/2$. End points were determined by using the End-Stage Illness Scoring System.

**CyTOF analysis of immune patterns from lymph nodes and tumors**

Lymph node and tumor samples were harvested and dissociated into single-cell suspensions 10 days after the final vaccination. CyTOF antibody conjugation, data acquisition and data analyze were done as previously described[75, 76]. All events were gated to remove noncellular events (negative for DNA intercalator), dead cells (negative for uptake of cisplatin), and doublets. SPADE clustering and the viSNE algorithm were applied using the Cytobank platform. SPADE nodes were manually bubbled based on phenotypic markers, and viSNE populations were manually gated using the same markers.

**Analysis of antigen specific CD4 T and CD8 T cells**

$2 \times 10^6$ cells from lymph nodes or spleen were isolated from each group and incubated with $2 \times 10^5$ antigen stimulated BMDC and 2 μg/mL antigen for 20 h in the presence of Brefeldin A. Cells were then stained with CD45, CD4 and CD8 markers and permeabilized and fixed by Cyto-Fast™ Fix/Perm Buffer Set (Biolegend). Cells were then stained with IFN-γ antibody and measured by flow cytometry. $5 \times 10^5$ splenocytes were isolated from each group and incubated with $2 \times 10^5$ antigen stimulated BMDC and 2 μg/mL antigen for 20 h in the ELISPOT plate (R&D systems). ELISPOT measurement and analysis were conducted according to protocol provided by the manufacturer. Ionomycin and phorbol myristate acetate treated cells were measured as positive control. I-A(b) chicken ova 325-335 QAVHAAHAEIN brilliant violet 421-labeled tetramer, I-A(b) chicken ova 325-335 QAVHAAHAEIN brilliant violet 421-labeled tetramer, I-A(b) chicken ova 325-335 QAVHAAHAEIN brilliant violet 421-labeled tetramer and H-2K(b) chicken ova 257-264 SIINFEKL PE-labeled tetramer provided by NIH tetramer core facility are used for staining antigen specific CD4 T and CD8 T cells in mice B16-OVA model.

**Single-cell RNA sequencing of tumor samples from pancreatic cancer model**

Tumor samples were harvested and dissociated into single-cell suspensions 9 days after the final vaccination. Dead cells were removed using a dead cell removal kit (Miltenyi Biotec). The single-cell suspensions were then stained with TotalSeq™-C Mouse antibody. These suspensions were subjected to final cell counting on a Countess II Automated Cell Counter (Thermo Fisher) and diluted to a concentration of 700-1000 nuclei/μL. We constructed 3′ single-nucleus libraries using the 10x Genomics Chromium Controller and followed the manufacturer's protocol for 3′ V3.1 chemistry with NextGEM Chip G reagents (10x Genomics). The final library quality was assessed using a TapeStation 4200 (Agilent), and the libraries were quantified by Kapa qPCR (Roche). Pooled libraries were subjected to 150 bp paired-end sequencing according to the manufacturer's protocol (Illumina NovaSeq 6000). Bcl2fastq2 Conversion Software (Illumina) was used to

generate demultiplexed Fastq files, and a CellRanger Pipeline (10x Genomics) was used to align reads and generate count matrices.

**Lipid nanoparticle formulation and characterization**

Lipid nanoparticle (LNP) formulation was formulated by mixing an aqueous phase containing the mRNA with an ethanol phase containing the lipids at 3:1 ratio in a microfluidic chip device. The ethanol phase contains a mixture of ionizable lipid (MMT6-54 or MMT6-55), helper phospholipid (1,2-Distearoyl-sn-glycero-3-PC), cholesterol and PEG-lipid (DMG-PEG2000 or DMG-PEG2000-Maleimide) at predetermined molar ratios. The aqueous phase contains corresponding mRNA (firefly luciferase, enhanced green fluorescent protein, KPC neoantigens) in a 50 mM citrate buffer. The resultant LNP formulations were dialyzed against PBS overnight at 4 °C by Pur-A-Lyzer™ Maxi Dialysis Kit (Millipore Sigma). After dialysis, LNP formulations were concentrated using Amicon ultra-centrifugal filters (MWCO 10KDa, Millipore Sigma) at 5000 rcf to reach the desired volume for experiments. After concentration, SARS-CoV-2 epitopes were incubated with LNP formulations at 2:1 molar ratio between DMG-PEG2000-Maleimide with gentle stir for 2h at 4°C. The volume-weighted hydrodynamic particle size, and polydispersity index of LNP formulations in Milli-Q water were evaluated with a Malvern Zetasizer Nano-ZS using DLS at 25°C. The encapsulation efficiency of LNP formulations were measured by Quant-iT™ RiboGreen™ RNA Reagent and Kit (invitrogen) followed the protocol provided by the manufacturer.

**mRNA lipid nanoparticle formulations transfection efficiency**

Firefly luciferase expression was monitored by incubation firefly luciferase mRNA encapsulated LNP formulation with DC2.4 cells. DC cells were plated in 24 well plates at $2 \times 10^5$ cells/mL overnight and transfected with firefly luciferase mRNA encapsulated LNP formulations (2 ug total mRNA/well) for 24h. Cells were then lysed by Glo lysis buffer and measured by Bright-Glo Luciferase Assay System according to the manufacturer's protocol (Promega). Enhanced green fluorescent protein (EGFP) expression was monitored by incubation EGFP mRNA encapsulated LNP formulation with DC2.4 cells. DC cells were plated in confocal plate at $2.5 \times 10^5$ cells/mL overnight and transfected with EGFP mRNA encapsulated LNP formulations (2 ug total mRNA/well) for 6h. Cells were then washed, fixed and imaged by Nikon A1SI confocal.

## 3.6 Figures

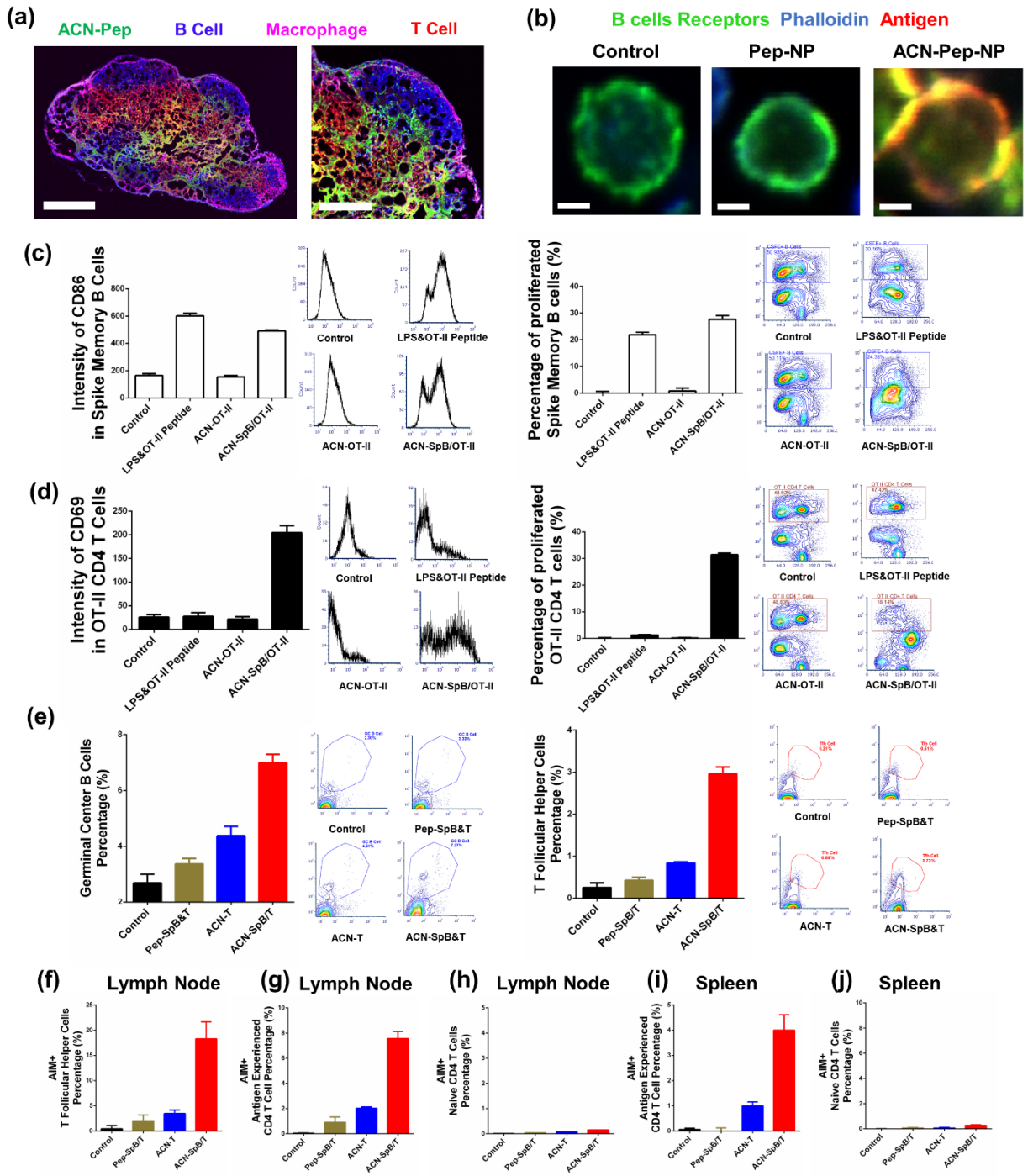


**Figure 3.1. SARS-CoV-2 B epitope promotes B/CD4 T cell crosstalk in vitro and in vivo.** (**a**) Confocal imaging of ACN penetration into lymph nodes. Scale bar is 200 μm in whole-lymph-node images and 100 μm in magnified images. (**b**) Confocal image of Cy3 and hapten labeled ACN-Pep-NP (red) binding/crosslinking (yellow) with B cell receptor (antibody staining, green) in hapten-specific B cells from QM mice splenocytes, compared with Cy3 and hapten labeled CD4/B antigen (Pep-NP). Blue, phalloidin stain of actin filaments; green, B cell receptor staining using Alexa Fluor 488-AffiniPure Fab Fragment

Goat Anti-Mouse IgM (μ Chain Specific) antibody; red: Cy3-labeled CD4/B-hapten epitope. The scale bar is 2.5 μm. (**c**) Left: flow cytometry quantification and representative analysis (96 h) of B cell from spike protein immunized mice activation by measuring geometric mean intensity of CD86 marker. Right: flow cytometry quantification and representative analysis (96 h) of B cell proliferation from spike protein immunized mice, measured by the percentage of decrease in $CFSE^+$ hapten-specific B cells compared to controls. (**d**) Left: flow cytometry quantification and representative analysis (96 h) of OT-II specific CD4 T cell activation with B cell incubation by measuring geometric mean intensity of CD69 marker. Right: flow cytometry quantification and representative analysis (96 h) of OT-II specific CD4 T cell proliferation with B cell incubation by measuring the percentage of decreased $CFSE^+$ OT-II specific CD4 T cells compared to control. (**e**) flow cytometry quantification and representative analysis of germinal center (GC) B cells (**left**) and T follicular helper (Tfh) cells (**right**) in lymph nodes. $CD3^-B220^+CD95^+$ $GL\text{-}7^+$ populations were identified as GC B cells and $B220^-CD4^+$ $CXCR5^+$ $PD\text{-}1^+$ populations were identified as Tfh cells. (**f-j**) flow cytometry quantification of activation-induced markers (AIM) positive Tfh cells with (**f**), $AIM^+$ antigen experienced cells at lymph node (**g**) and spleen (**i**), $AIM^+$ naive cells at lymph node (**h**) and spleen (**j**). $CD69^+$ $CD40L^{+/-}$ populations from Tfh cells were identified as $AIM^+$ Tfh cells. $B220^-$ $CD4^+$ $CD62L^+$ $CD69^+$ $CD40L^{+/-}$ populations were identified as $AIM^+$ antigen experienced CD4 T cells. $B220^-$ $CD4^+$ $CD62L^-$ $CD69^+$ $CD40L^{+/-}$ populations were identified as $AIM^+$ naïve CD4 T cells. Data for quantification are shown as mean ± SD, n = 3.

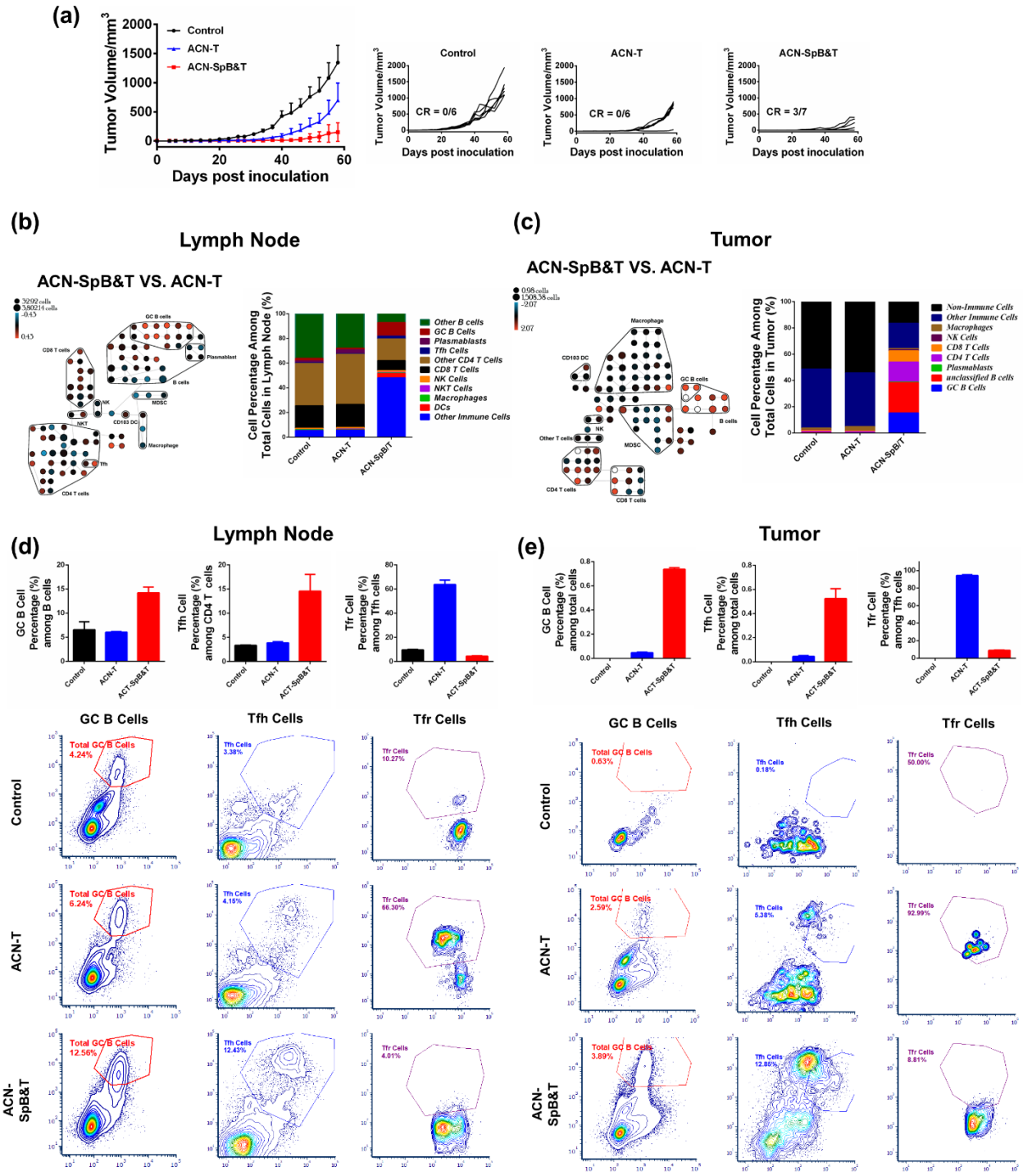


**Figure 3.2. SARS-CoV-2 B epitope enhances antitumor efficacy through promoting B/CD4 T cell crosstalk and suppressing follicular regulatory T cells.** (**a**) Antitumor efficacy of ACN with SARS-CoV-2 B epitope and tumor T cell neoantigens compared with ACN with tumor T cell neoantigens in breast cancer model with D2E2F2 cells. (**b, c**) Cytometry by Time-of-Flight (CyTOF) analysis of the cell population from lymph node (**b**)

and tumor (**c**) samples of mice 10 days after different treatments. (**d**) Flow cytometry quantification and representative analysis of GC B cells, Tfh cells and follicular regulatory cells from lymph node (**d**) and tumor (**e**) 10 days after different treatments.

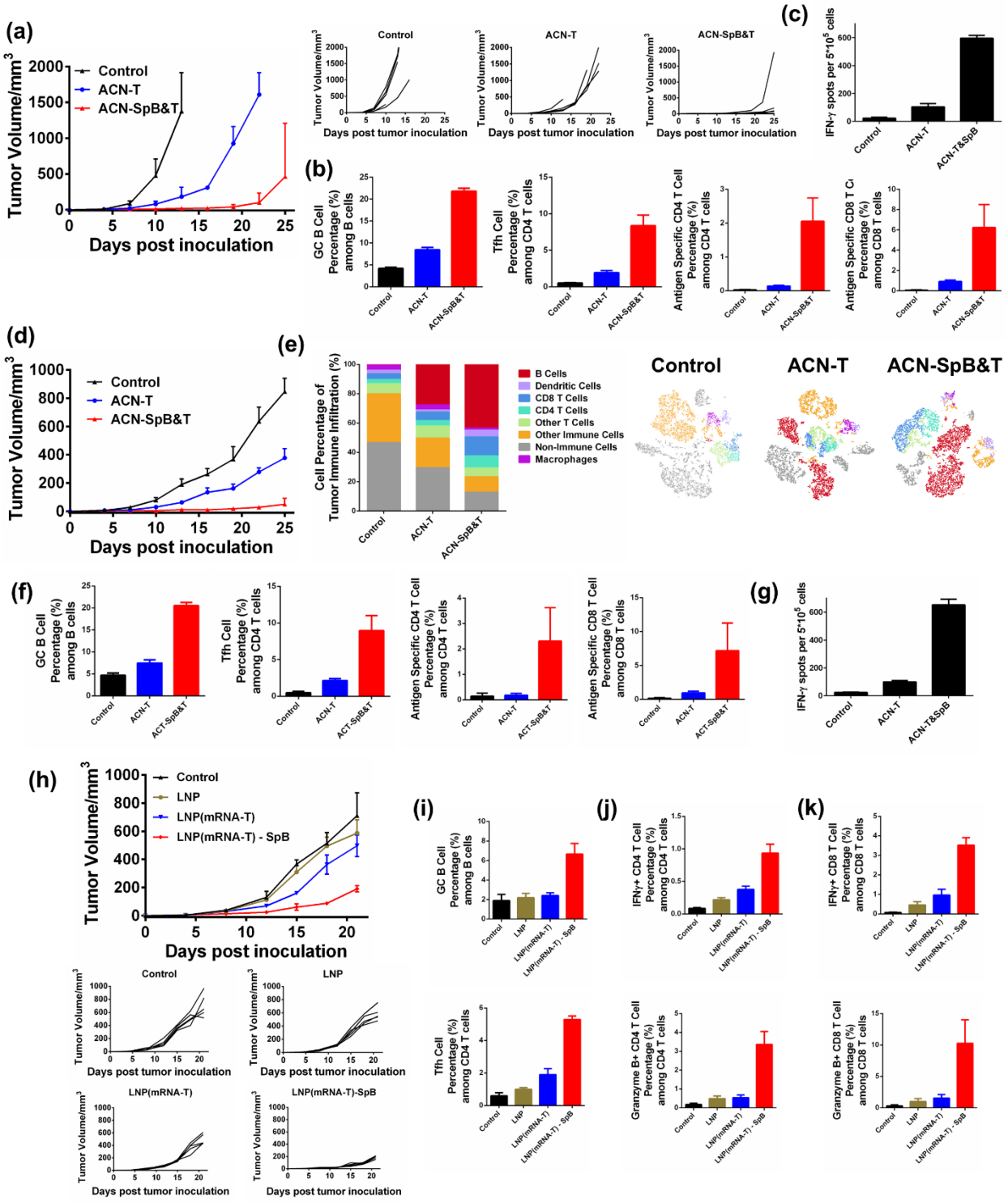

**Figure 3.3. SARS-CoV-2 B epitope enhances antitumor efficacy of peptide and mRNA neoantigen cancer vaccines.** (**a**) Antitumor efficacy of ACN with SARS-CoV-2 B epitope and tumor T cell neoantigens compared with ACN with tumor T cell neoantigens in melanoma model with B16F10 cells. (**b**) Flow cytometry quantification of GC B cells and Tfh cells from lymph node and antigen specific (IFN-γ+) CD4 T cells and antigen specific (IFN-γ+) CD8 T cells from tumor 5 days after the second booster vaccination from (**a**). (**c**) Quantification of IFN-γ+ ELISPOT of splenocytes from (**a**). (**d**) Antitumor efficacy of ACN with SARS-CoV-2 B epitope and tumor T cell neoantigens compared with ACN with tumor T cell neoantigens in pancreatic cancer model with KPC 6422 cells. (**e**) Stacked bar charts show the quantified ratio of cells from (**d**). t-distributed Stochastic Neighbor Embedding (t-SNE) plot of cells from tumor in (**d**). (**f**) Flow cytometry quantification of GC B cells and Tfh cells from lymph node and antigen specific (IFN-γ+) CD4 T cells and antigen specific (IFN-γ+) CD8 T cells from tumor 8 days after the second booster vaccination from (**d**). (**g**) Quantification of IFN-γ+ ELISPOT of splenocytes from (**d**). (**h**) Antitumor efficacy of mRNA cancer vaccine encoding tumor T cell neoantigens with SARS-CoV-2 B epitope displayed at the surface of lipid nanoparticle compared with mRNA cancer vaccine encoding only tumor T cell neoantigens in pancreatic cancer model with KPC 6422 cells. (**i**) Flow cytometry quantification of GC B cells and Tfh cells from lymph node 6 days after the final vaccination from (**h**). (**j**) Flow cytometry quantification of antigen specific (IFN-γ+) CD4 T cells and antigen specific (IFN-γ+) CD8 T cells from lymph node 6 days after the final vaccination from (**h**). (**k**) Flow cytometry quantification of Granzyme B+ CD4 T cells and Granzyme B+ CD8 T cells from lymph node 6 days after the final vaccination from (**h**).

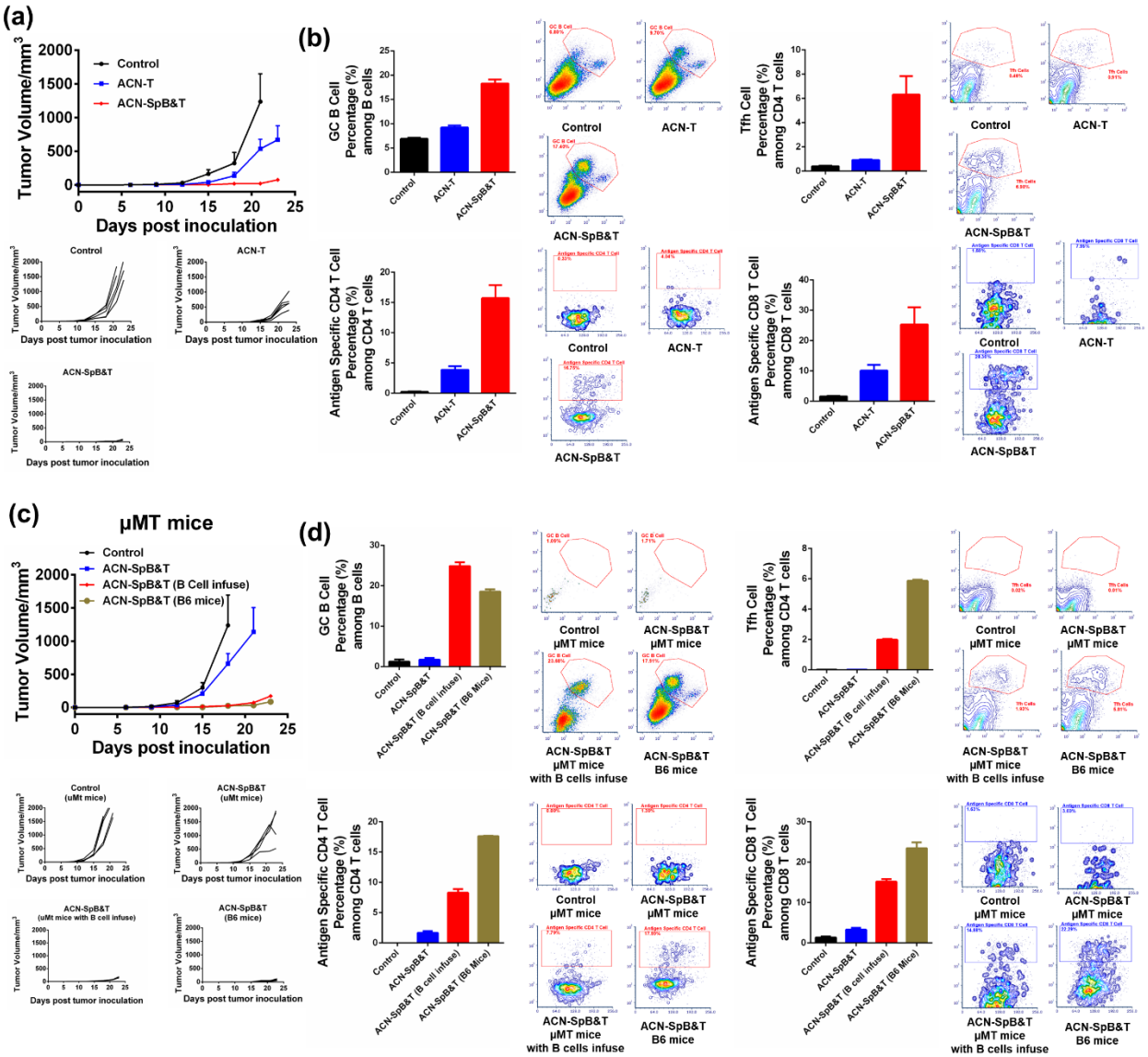


**Figure 3.4. SARS-CoV-2 B epitope enhances antitumor efficacy is dependent on B/CD4 T cell crosstalk.** (**a**) Antitumor efficacy of ACN with SARS-CoV-2 B epitope and tumor T cell neoantigens compared with ACN with tumor T cell neoantigens in melanoma model with B16-OVA cells. (**b**) Flow cytometry quantification of GC B cells and Tfh cells from lymph node and antigen specific (IFN-γ+) CD4 T cells and antigen specific (IFN-γ+) CD8 T cells from tumor 6 days after the second booster vaccination from (**a**). (**c**) Antitumor efficacy of ACN with SARS-CoV-2 B epitope and tumor T cell neoantigens compared with ACN with tumor T cell neoantigens in melanoma model with B16-OVA cells at μMt mice. 2 × $10^6$ B cells isolated from male C57BL/6 mice were infused to male μMt mice 1 day and 3 days before immunization. (**d**) Flow cytometry quantification of GC B cells and Tfh cells from lymph node and antigen specific (IFN-γ+) CD4 T cells and antigen specific (IFN-γ+) CD8 T cells from tumor 6 days after the second booster vaccination from (**c**).

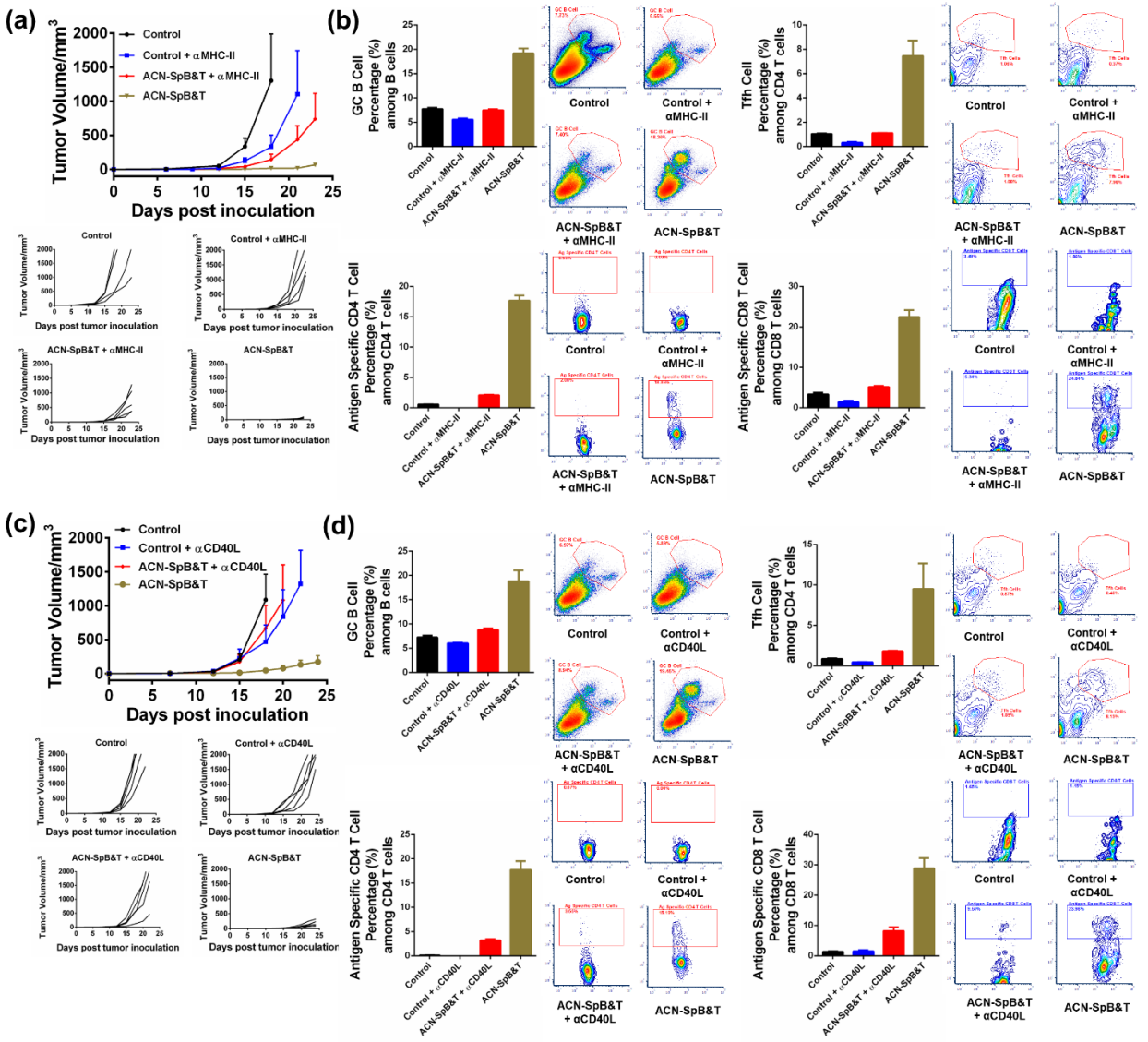


**Figure 3.5. SARS-CoV-2 B epitope enhances antitumor efficacy is dependent on B cell antigen presentation mediated B/CD4 T cell crosstalk.** (**a**) Antitumor efficacy of ACN with SARS-CoV-2 B epitope and tumor T cell neoantigens compared with ACN with tumor T cell neoantigens in melanoma model with B16-OVA cells. For the αMHC-II antibody (500 μg/mouse) blocking, antibody was intraperitoneal injected 10 days before vaccination, and then dosed 200 μg every three days. (**b**) Flow cytometry quantification of GC B cells and Tfh cells from lymph node and antigen specific (IFN-γ+) CD4 T cells and antigen specific (IFN-γ+) CD8 T cells from tumor 6 days after the second booster vaccination from (**a**). (**c**) Antitumor efficacy of ACN with SARS-CoV-2 B epitope and tumor T cell neoantigens compared with ACN with tumor T cell neoantigens in melanoma model with B16-OVA cells. For the αCD40L antibody (200 μg/mouse) blocking, antibody was intraperitoneal injected 10 days before vaccination, and then dosed 200 μg every three days. (**d**) Flow cytometry quantification of GC B cells and Tfh cells from lymph node and

antigen specific (IFN-γ+) CD4 T cells and antigen specific (IFN-γ+) CD8 T cells from tumor 6 days after the second booster vaccination from (**c**).

### 3.7 Bibliography


1. Hailemichael, Y.; Dai, Z. M.; Jaffarzad, N.; Ye, Y.; Medina, M. A.; Huang, X. F.; Dorta-Estremera, S. M.; Greeley, N. R.; Nitti, G.; Peng, W. Y.; Liu, C. W.; Lou, Y. Y.; Wang, Z. Q.; Ma, W. C.; Rabinovich, B.; Schluns, K. S.; Davis, R. E.; Hwu, P.; Overwijk, W. W., Persistent antigen at vaccination sites induces tumor-specific CD8(+) T cell sequestration, dysfunction and deletion. *Nat Med* **2013,** *19* (4), 465-+.
2. Liu, S.; Jiang, Q.; Zhao, X.; Zhao, R.; Wang, Y.; Wang, Y.; Liu, J.; Shang, Y.; Zhao, S.; Wu, T.; Zhang, Y.; Nie, G.; Ding, B., A DNA nanodevice-based vaccine for cancer immunotherapy. *Nature materials* **2021,** *20* (3), 421-430.
3. Kissick, H. T.; Sanda, M. G., The role of active vaccination in cancer immunotherapy: lessons from clinical trials. *Curr Opin Immunol* **2015,** *35*, 15-22.
4. Kissick, H. T., Is It Possible to Develop Cancer Vaccines to Neoantigens, What Are the Major Challenges, and How Can These Be Overcome? Neoantigens as Vaccine Targets for Cancer. *Cold Spring Harb Perspect Biol* **2018,** *10* (11).
5. Finn, O. J.; Rammensee, H. G., Is It Possible to Develop Cancer Vaccines to Neoantigens, What Are the Major Challenges, and How Can These Be Overcome? Neoantigens: Nothing New in Spite of the Name. *Cold Spring Harb Perspect Biol* **2018,** *10* (11).
6. Saxena, M.; van der Burg, S. H.; Melief, C. J. M.; Bhardwaj, N., Therapeutic cancer vaccines. *Nature Reviews Cancer* **2021,** *21* (6), 360-378.
7. Hollingsworth, R. E.; Jansen, K., Turning the corner on therapeutic cancer vaccines. *NPJ vaccines* **2019,** *4*, 7.
8. Jiang, T.; Shi, T.; Zhang, H.; Hu, J.; Song, Y.; Wei, J.; Ren, S.; Zhou, C., Tumor neoantigens: from basic research to clinical applications. *Journal of hematology & oncology* **2019,** *12* (1), 93.
9. Sellars, M. C.; Wu, C. J.; Fritsch, E. F., Cancer vaccines: Building a bridge over troubled waters. *Cell* **2022,** *185* (15), 2770-2788.
10. Curran, M. A.; Glisson, B. S., New Hope for Therapeutic Cancer Vaccines in the Era of Immune Checkpoint Modulation. *Annual review of medicine* **2019,** *70*, 409-424.
11. Blass, E.; Ott, P. A., Advances in the development of personalized neoantigen-based therapeutic cancer vaccines. *Nature reviews. Clinical oncology* **2021,** *18* (4), 215-229.
12. Beura, L. K.; Jameson, S. C.; Masopust, D., Is a Human CD8 T-Cell Vaccine Possible, and if So, What Would It Take? CD8 T-Cell Vaccines: To B or Not to B? *Cold Spring Harb Perspect Biol* **2018,** *10* (9).
13. Yuen, G. J.; Demissie, E.; Pillai, S., B lymphocytes and cancer: a love-hate relationship. *Trends Cancer* **2016,** *2* (12), 747-757.
14. Qin, Z.; Richter, G.; Schuler, T.; Ibe, S.; Cao, X.; Blankenstein, T., B cells inhibit induction of T cell-dependent tumor immunity. *Nat Med* **1998,** *4* (5), 627-30.
15. Shah, S.; Divekar, A. A.; Hilchey, S. P.; Cho, H. M.; Newman, C. L.; Shin, S. U.; Nechustan, H.; Challita-Eid, P. M.; Segal, B. M.; Yi, K. H.; Rosenblatt, J. D., Increased rejection of primary tumors in mice lacking B cells: inhibition of anti-tumor CTL and TH1 cytokine responses by B cells. *Int J Cancer* **2005,** *117* (4), 574-86.
16. Brodt, P.; Gordon, J., Anti-tumor immunity in B lymphocyte-deprived mice. I. Immunity to a chemically induced tumor. *J Immunol* **1978,** *121* (1), 359-62.

17. Barbera-Guillem, E.; Nelson, M. B.; Barr, B.; Nyhus, J. K.; May, K. F., Jr.; Feng, L.; Sampsel, J. W., B lymphocyte pathology in human colorectal cancer. Experimental and clinical therapeutic effects of partial B cell depletion. *Cancer Immunol Immunother* **2000,** *48* (10), 541-9.
18. Shen, P.; Fillatreau, S., Antibody-independent functions of B cells: a focus on cytokines. *Nat Rev Immunol* **2015,** *15* (7), 441-51.
19. DiLillo, D. J.; Yanaba, K.; Tedder, T. F., B cells are required for optimal CD4+ and CD8+ T cell tumor immunity: therapeutic B cell depletion enhances B16 melanoma growth in mice. *J Immunol* **2010,** *184* (7), 4006-16.
20. de Jonge, K.; Tille, L.; Lourenco, J.; Maby-El Hajjami, H.; Nassiri, S.; Racle, J.; Gfeller, D.; Delorenzi, M.; Verdeil, G.; Baumgaertner, P.; Speiser, D. E., Inflammatory B cells correlate with failure to checkpoint blockade in melanoma patients. *Oncoimmunology* **2021,** *10* (1), 1873585.
21. de Visser, K. E.; Korets, L. V.; Coussens, L. M., De novo carcinogenesis promoted by chronic inflammation is B lymphocyte dependent. *Cancer Cell* **2005,** *7* (5), 411-23.
22. Helmink, B. A.; Reddy, S. M.; Gao, J.; Zhang, S.; Basar, R.; Thakur, R.; Yizhak, K.; Sade-Feldman, M.; Blando, J.; Han, G.; Gopalakrishnan, V.; Xi, Y.; Zhao, H.; Amaria, R. N.; Tawbi, H. A.; Cogdill, A. P.; Liu, W.; LeBleu, V. S.; Kugeratski, F. G.; Patel, S.; Davies, M. A.; Hwu, P.; Lee, J. E.; Gershenwald, J. E.; Lucci, A.; Arora, R.; Woodman, S.; Keung, E. Z.; Gaudreau, P. O.; Reuben, A.; Spencer, C. N.; Burton, E. M.; Haydu, L. E.; Lazar, A. J.; Zapassodi, R.; Hudgens, C. W.; Ledesma, D. A.; Ong, S.; Bailey, M.; Warren, S.; Rao, D.; Krijgsman, O.; Rozeman, E. A.; Peeper, D.; Blank, C. U.; Schumacher, T. N.; Butterfield, L. H.; Zelazowska, M. A.; McBride, K. M.; Kalluri, R.; Allison, J.; Petitprez, F.; Fridman, W. H.; Sautès-Fridman, C.; Hacohen, N.; Rezvani, K.; Sharma, P.; Tetzlaff, M. T.; Wang, L.; Wargo, J. A., B cells and tertiary lymphoid structures promote immunotherapy response. *Nature* **2020,** *577* (7791), 549-555.
23. Cabrita, R.; Lauss, M.; Sanna, A.; Donia, M.; Skaarup Larsen, M.; Mitra, S.; Johansson, I.; Phung, B.; Harbst, K.; Vallon-Christersson, J.; van Schoiack, A.; Lövgren, K.; Warren, S.; Jirström, K.; Olsson, H.; Pietras, K.; Ingvar, C.; Isaksson, K.; Schadendorf, D.; Schmidt, H.; Bastholt, L.; Carneiro, A.; Wargo, J. A.; Svane, I. M.; Jönsson, G., Tertiary lymphoid structures improve immunotherapy and survival in melanoma. *Nature* **2020,** *577* (7791), 561-565.
24. Petitprez, F.; de Reyniès, A.; Keung, E. Z.; Chen, T. W.; Sun, C. M.; Calderaro, J.; Jeng, Y. M.; Hsiao, L. P.; Lacroix, L.; Bougoüin, A.; Moreira, M.; Lacroix, G.; Natario, I.; Adam, J.; Lucchesi, C.; Laizet, Y. H.; Toulmonde, M.; Burgess, M. A.; Bolejack, V.; Reinke, D.; Wani, K. M.; Wang, W. L.; Lazar, A. J.; Roland, C. L.; Wargo, J. A.; Italiano, A.; Sautès-Fridman, C.; Tawbi, H. A.; Fridman, W. H., B cells are associated with survival and immunotherapy response in sarcoma. *Nature* **2020,** *577* (7791), 556-560.
25. Kroeger, D. R.; Milne, K.; Nelson, B. H., Tumor-Infiltrating Plasma Cells Are Associated with Tertiary Lymphoid Structures, Cytolytic T-Cell Responses, and Superior Prognosis in Ovarian Cancer. *Clinical cancer research : an official journal of the American Association for Cancer Research* **2016,** *22* (12), 3005-15.
26. Garaud, S.; Buisseret, L.; Solinas, C.; Gu-Trantien, C.; de Wind, A.; Van den Eynden, G.; Naveaux, C.; Lodewyckx, J. N.; Boisson, A.; Duvillier, H.; Craciun, L.; Ameye, L.; Veys, I.; Paesmans, M.; Larsimont, D.; Piccart-Gebhart, M.; Willard-Gallo, K., Tumor infiltrating B-cells signal functional humoral immune responses in breast cancer. *JCI Insight* **2019,** *5*.
27. Hollern, D. P.; Xu, N.; Thennavan, A.; Glodowski, C.; Garcia-Recio, S.; Mott, K. R.; He, X.; Garay, J. P.; Carey-Ewend, K.; Marron, D.; Ford, J.; Liu, S.; Vick, S. C.; Martin, M.; Parker, J. S.; Vincent, B. G.; Serody, J. S.; Perou, C. M., B Cells and T Follicular Helper Cells Mediate Response to Checkpoint Inhibitors in High Mutation Burden Mouse Models of Breast Cancer. *Cell* **2019,** *179* (5), 1191-1206.e21.

28. Sagiv-Barfi, I.; Czerwinski, D. K.; Shree, T.; Lohmeyer, J. J. K.; Levy, R., Intratumoral immunotherapy relies on B and T cell collaboration. *Sci Immunol* **2022,** *7* (71), eabn5859.
29. Cui, C.; Wang, J.; Fagerberg, E.; Chen, P. M.; Connolly, K. A.; Damo, M.; Cheung, J. F.; Mao, T.; Askari, A. S.; Chen, S.; Fitzgerald, B.; Foster, G. G.; Eisenbarth, S. C.; Zhao, H.; Craft, J.; Joshi, N. S., Neoantigen-driven B cell and CD4 T follicular helper cell collaboration promotes anti-tumor CD8 T cell responses. *Cell* **2021,** *184* (25), 6101-6118 e13.
30. Wieland, A.; Patel, M. R.; Cardenas, M. A.; Eberhardt, C. S.; Hudson, W. H.; Obeng, R. C.; Griffith, C. C.; Wang, X.; Chen, Z. G.; Kissick, H. T.; Saba, N. F.; Ahmed, R., Defining HPV-specific B cell responses in patients with head and neck cancer. *Nature* **2020**.
31. Chaurio, R. A.; Anadon, C. M.; Lee Costich, T.; Payne, K. K.; Biswas, S.; Harro, C. M.; Moran, C.; Ortiz, A. C.; Cortina, C.; Rigolizzo, K. E.; Sprenger, K. B.; Mine, J. A.; Innamarato, P.; Mandal, G.; Powers, J. J.; Martin, A.; Wang, Z.; Mehta, S.; Perez, B. A.; Li, R.; Robinson, J.; Kroeger, J. L.; Curiel, T. J.; Yu, X.; Rodriguez, P. C.; Conejo-Garcia, J. R., TGF-β-mediated silencing of genomic organizer SATB1 promotes Tfh cell differentiation and formation of intra-tumoral tertiary lymphoid structures. *Immunity* **2022,** *55* (1), 115-128.e9.
32. Overacre-Delgoffe, A. E.; Bumgarner, H. J.; Cillo, A. R.; Burr, A. H. P.; Tometich, J. T.; Bhattacharjee, A.; Bruno, T. C.; Vignali, D. A. A.; Hand, T. W., Microbiota-specific T follicular helper cells drive tertiary lymphoid structures and anti-tumor immunity against colorectal cancer. *Immunity* **2021,** *54* (12), 2812-2824.e4.
33. Graalmann, T.; Borst, K.; Manchanda, H.; Vaas, L.; Bruhn, M.; Graalmann, L.; Koster, M.; Verboom, M.; Hallensleben, M.; Guzman, C. A.; Sutter, G.; Schmidt, R. E.; Witte, T.; Kalinke, U., B cell depletion impairs vaccination-induced CD8(+) T cell responses in a type I interferon-dependent manner. *Ann Rheum Dis* **2021,** *80* (12), 1537-1544.
34. Guo, L.; Kapur, R.; Aslam, R.; Speck, E. R.; Zufferey, A.; Zhao, Y.; Kim, M.; Lazarus, A. H.; Ni, H.; Semple, J. W., CD20+ B-cell depletion therapy suppresses murine CD8+ T-cell-mediated immune thrombocytopenia. *Blood* **2016,** *127* (6), 735-8.
35. Klarquist, J.; Cross, E. W.; Thompson, S. B.; Willett, B.; Aldridge, D. L.; Caffrey-Carr, A. K.; Xu, Z.; Hunter, C. A.; Getahun, A.; Kedl, R. M., B cells promote CD8 T cell primary and memory responses to subunit vaccines. *Cell Rep* **2021,** *36* (8), 109591.
36. Tanchot, C.; Rocha, B., CD8 and B cell memory: same strategy, same signals. *Nat Immunol* **2003,** *4* (5), 431-2.
37. Ossendorp, F.; Mengede, E.; Camps, M.; Filius, R.; Melief, C. J., Specific T helper cell requirement for optimal induction of cytotoxic T lymphocytes against major histocompatibility complex class II negative tumors. *J Exp Med* **1998,** *187* (5), 693-702.
38. Aubert, R. D.; Kamphorst, A. O.; Sarkar, S.; Vezys, V.; Ha, S. J.; Barber, D. L.; Ye, L.; Sharpe, A. H.; Freeman, G. J.; Ahmed, R., Antigen-specific CD4 T-cell help rescues exhausted CD8 T cells during chronic viral infection. *Proc Natl Acad Sci U S A* **2011,** *108* (52), 21182-7.
39. Janssen, E. M.; Lemmens, E. E.; Wolfe, T.; Christen, U.; von Herrath, M. G.; Schoenberger, S. P., CD4+ T cells are required for secondary expansion and memory in CD8+ T lymphocytes. *Nature* **2003,** *421* (6925), 852-6.
40. Laidlaw, B. J.; Craft, J. E.; Kaech, S. M., The multifaceted role of CD4(+) T cells in CD8(+) T cell memory. *Nat Rev Immunol* **2016,** *16* (2), 102-11.
41. Novy, P.; Quigley, M.; Huang, X.; Yang, Y., CD4 T cells are required for CD8 T cell survival during both primary and memory recall responses. *J Immunol* **2007,** *179* (12), 8243-51.
42. Kreiter, S.; Vormehr, M.; van de Roemer, N.; Diken, M.; Lower, M.; Diekmann, J.; Boegel, S.; Schrors, B.; Vascotto, F.; Castle, J. C.; Tadmor, A. D.; Schoenberger, S. P.; Huber, C.; Tureci, O.; Sahin, U., Mutant MHC class II epitopes drive therapeutic immune responses to cancer. *Nature* **2015,** *520* (7549), 692-6.
43. Bousso, P., T-cell activation by dendritic cells in the lymph node: lessons from the movies. *Nature Reviews Immunology* **2008,** *8* (9), 675-684.

44. Kaumaya, P. T., B-cell epitope peptide cancer vaccines: a new paradigm for combination immunotherapies with novel checkpoint peptide vaccine. *Future Oncol* **2020,** *16* (23), 1767-1791.
45. Wagner, S.; Mullins, C. S.; Linnebacher, M., Colorectal cancer vaccines: Tumor-associated antigens vs neoantigens. *World J Gastroenterol* **2018,** *24* (48), 5418-5432.
46. Cui, C.; Wang, J.; Fagerberg, E.; Chen, P. M.; Connolly, K. A.; Damo, M.; Cheung, J. F.; Mao, T.; Askari, A. S.; Chen, S.; Fitzgerald, B.; Foster, G. G.; Eisenbarth, S. C.; Zhao, H.; Craft, J.; Joshi, N. S., Neoantigen-driven B cell and CD4 T follicular helper cell collaboration promotes anti-tumor CD8 T cell responses. *Cell* **2021,** *184* (25), 6101-6118.e13.
47. Parker, D. C., T cell-dependent B cell activation. *Annu Rev Immunol* **1993,** *11*, 331-60.
48. Chen, X.; Jensen, P. E., The role of B lymphocytes as antigen-presenting cells. *Arch Immunol Ther Exp (Warsz)* **2008,** *56* (2), 77-83.
49. Batista, F. D.; Harwood, N. E., The who, how and where of antigen presentation to B cells. *Nature Reviews Immunology* **2009,** *9* (1), 15-27.
50. Chattopadhyay, S.; Chen, J. Y.; Chen, H. W.; Hu, C. J., Nanoparticle Vaccines Adopting Virus-like Features for Enhanced Immune Potentiation. *Nanotheranostics* **2017,** *1* (3), 244-260.
51. Bachmann, M. F.; Jennings, G. T., Vaccine delivery: a matter of size, geometry, kinetics and molecular patterns. *Nat Rev Immunol* **2010,** *10* (11), 787-96.
52. Spohn, G.; Bachmann, M. F., Exploiting viral properties for the rational design of modern vaccines. *Expert Rev Vaccines* **2008,** *7* (1), 43-54.
53. Somiya, M.; Liu, Q.; Kuroda, S., Current Progress of Virus-mimicking Nanocarriers for Drug Delivery. *Nanotheranostics* **2017,** *1* (4), 415-429.
54. Poh, C. M.; Carissimo, G.; Wang, B.; Amrun, S. N.; Lee, C. Y.; Chee, R. S.; Fong, S. W.; Yeo, N. K.; Lee, W. H.; Torres-Ruesta, A.; Leo, Y. S.; Chen, M. I.; Tan, S. Y.; Chai, L. Y. A.; Kalimuddin, S.; Kheng, S. S. G.; Thien, S. Y.; Young, B. E.; Lye, D. C.; Hanson, B. J.; Wang, C. I.; Renia, L.; Ng, L. F. P., Two linear epitopes on the SARS-CoV-2 spike protein that elicit neutralising antibodies in COVID-19 patients. *Nature communications* **2020,** *11* (1), 2806.
55. Amrun, S. N.; Lee, C. Y.; Lee, B.; Fong, S. W.; Young, B. E.; Chee, R. S.; Yeo, N. K.; Torres-Ruesta, A.; Carissimo, G.; Poh, C. M.; Chang, Z. W.; Tay, M. Z.; Chan, Y. H.; Chen, M. I.; Low, J. G.; Tambyah, P. A.; Kalimuddin, S.; Pada, S.; Tan, S. Y.; Sun, L. J.; Leo, Y. S.; Lye, D. C.; Renia, L.; Ng, L. F. P., Linear B-cell epitopes in the spike and nucleocapsid proteins as markers of SARS-CoV-2 exposure and disease severity. *EBioMedicine* **2020,** *58*, 102911.
56. Borst, J.; Ahrends, T.; Bąbała, N.; Melief, C. J. M.; Kastenmüller, W., CD4(+) T cell help in cancer immunology and immunotherapy. *Nat Rev Immunol* **2018,** *18* (10), 635-647.
57. Griss, J.; Bauer, W.; Wagner, C.; Simon, M.; Chen, M.; Grabmeier-Pfistershammer, K.; Maurer-Granofszky, M.; Roka, F.; Penz, T.; Bock, C.; Zhang, G.; Herlyn, M.; Glatz, K.; Läubli, H.; Mertz, K. D.; Petzelbauer, P.; Wiesner, T.; Hartl, M.; Pickl, W. F.; Somasundaram, R.; Steinberger, P.; Wagner, S. N., B cells sustain inflammation and predict response to immune checkpoint blockade in human melanoma. *Nature communications* **2019,** *10* (1), 4186.
58. Gu-Trantien, C.; Migliori, E.; Buisseret, L.; de Wind, A.; Brohée, S.; Garaud, S.; Noël, G.; Dang Chi, V. L.; Lodewyckx, J. N.; Naveaux, C.; Duvillier, H.; Goriely, S.; Larsimont, D.; Willard-Gallo, K., CXCL13-producing TFH cells link immune suppression and adaptive memory in human breast cancer. *JCI Insight* **2017,** *2* (11).
59. Garaud, S.; Buisseret, L.; Solinas, C.; Gu-Trantien, C.; de Wind, A.; Van den Eynden, G.; Naveaux, C.; Lodewyckx, J. N.; Boisson, A.; Duvillier, H.; Craciun, L.; Ameye, L.; Veys, I.; Paesmans, M.; Larsimont, D.; Piccart-Gebhart, M.; Willard-Gallo, K., Tumor infiltrating B-cells signal functional humoral immune responses in breast cancer. *JCI insight* **2019,** *5* (18).

60. Gu-Trantien, C.; Loi, S.; Garaud, S.; Equeter, C.; Libin, M.; de Wind, A.; Ravoet, M.; Le Buanec, H.; Sibille, C.; Manfouo-Foutsop, G.; Veys, I.; Haibe-Kains, B.; Singhal, S. K.; Michiels, S.; Rothé, F.; Salgado, R.; Duvillier, H.; Ignatiadis, M.; Desmedt, C.; Bron, D.; Larsimont, D.; Piccart, M.; Sotiriou, C.; Willard-Gallo, K., CD4+ follicular helper T cell infiltration predicts breast cancer survival. *The Journal of clinical investigation* **2013,** *123* (7), 2873-92.
61. Germain, C.; Gnjatic, S.; Tamzalit, F.; Knockaert, S.; Remark, R.; Goc, J.; Lepelley, A.; Becht, E.; Katsahian, S.; Bizouard, G.; Validire, P.; Damotte, D.; Alifano, M.; Magdeleinat, P.; Cremer, I.; Teillaud, J. L.; Fridman, W. H.; Sautès-Fridman, C.; Dieu-Nosjean, M. C., Presence of B cells in tertiary lymphoid structures is associated with a protective immunity in patients with lung cancer. *American journal of respiratory and critical care medicine* **2014,** *189* (7), 832-44.
62. Wieland, A.; Patel, M. R.; Cardenas, M. A.; Eberhardt, C. S.; Hudson, W. H.; Obeng, R. C.; Griffith, C. C.; Wang, X.; Chen, Z. G.; Kissick, H. T.; Saba, N. F.; Ahmed, R., Defining HPV-specific B cell responses in patients with head and neck cancer. *Nature* **2021,** *597* (7875), 274-278.
63. Cillo, A. R.; Kürten, C. H. L.; Tabib, T.; Qi, Z.; Onkar, S.; Wang, T.; Liu, A.; Duvvuri, U.; Kim, S.; Soose, R. J.; Oesterreich, S.; Chen, W.; Lafyatis, R.; Bruno, T. C.; Ferris, R. L.; Vignali, D. A. A., Immune Landscape of Viral- and Carcinogen-Driven Head and Neck Cancer. *Immunity* **2020,** *52* (1), 183-199.e9.
64. Whittington, P. J.; Radkevich-Brown, O.; Jacob, J. B.; Jones, R. F.; Weise, A. M.; Wei, W. Z., Her-2 DNA versus cell vaccine: immunogenicity and anti-tumor activity. *Cancer Immunol Immunother* **2009,** *58* (5), 759-67.
65. Li, J.; Byrne, K. T.; Yan, F.; Yamazoe, T.; Chen, Z.; Baslan, T.; Richman, L. P.; Lin, J. H.; Sun, Y. H.; Rech, A. J.; Balli, D.; Hay, C. A.; Sela, Y.; Merrell, A. J.; Liudahl, S. M.; Gordon, N.; Norgard, R. J.; Yuan, S.; Yu, S.; Chao, T.; Ye, S.; Eisinger-Mathason, T. S. K.; Faryabi, R. B.; Tobias, J. W.; Lowe, S. W.; Coussens, L. M.; Wherry, E. J.; Vonderheide, R. H.; Stanger, B. Z., Tumor Cell-Intrinsic Factors Underlie Heterogeneity of Immune Cell Infiltration and Response to Immunotherapy. *Immunity* **2018,** *49* (1), 178-193.e7.
66. Lutz, M. B.; Kukutsch, N.; Ogilvie, A. L.; Rössner, S.; Koch, F.; Romani, N.; Schuler, G., An advanced culture method for generating large quantities of highly pure dendritic cells from mouse bone marrow. *Journal of immunological methods* **1999,** *223* (1), 77-92.
67. Song, Y.; Bugada, L.; Li, R.; Hu, H.; Zhang, L.; Li, C.; Yuan, H.; Rajanayake, K. K.; Truchan, N. A.; Wen, F.; Gao, W.; Sun, D., Albumin nanoparticle containing a PI3Kγ inhibitor and paclitaxel in combination with α-PD1 induces tumor remission of breast cancer in mice. *Sci Transl Med* **2022,** *14* (643), eabl3649.
68. Chen, H. W.; Ren, X. Q.; Paholak, H. L. J.; Burnett, J.; Ni, F.; Fang, X. L.; Sun, D. X., Facile Fabrication of Near-Infrared-Resonant and Magnetic Resonance Imaging-Capable Nanomediators for Photothermal Therapy. *Acs Appl Mater Inter* **2015,** *7* (23), 12814-12823.
69. Clauson, R. M.; Chen, M.; Scheetz, L. M.; Berg, B.; Chertok, B., Size-Controlled Iron Oxide Nanoplatforms with Lipidoid-Stabilized Shells for Efficient Magnetic Resonance Imaging-Trackable Lymph Node Targeting and High-Capacity Biomolecule Display. *ACS Appl Mater Interfaces* **2018,** *10* (24), 20281-20295.
70. Udenfriend, S.; Stein, S.; Böhlen, P.; Dairman, W.; Leimgruber, W.; Weigele, M., Fluorescamine: a reagent for assay of amino acids, peptides, proteins, and primary amines in the picomole range. *Science (New York, N.Y.)* **1972,** *178* (4063), 871-2.
71. Veneziano, R.; Moyer, T. J.; Stone, M. B.; Wamhoff, E. C.; Read, B. J.; Mukherjee, S.; Shepherd, T. R.; Das, J.; Schief, W. R.; Irvine, D. J.; Bathe, M., Role of nanoscale antigen organization on B-cell activation probed using DNA origami. *Nat Nanotechnol* **2020,** *15* (8), 716-723.
72. Franz, B.; May, K. F., Jr.; Dranoff, G.; Wucherpfennig, K., Ex vivo characterization and isolation of rare memory B cells with antigen tetramers. *Blood* **2011,** *118* (2), 348-57.

73. DiPiazza, A. T.; Leist, S. R.; Abiona, O. M.; Moliva, J. I.; Werner, A.; Minai, M.; Nagata, B. M.; Bock, K. W.; Phung, E.; Schäfer, A.; Dinnon, K. H., 3rd; Chang, L. A.; Loomis, R. J.; Boyoglu-Barnum, S.; Alvarado, G. S.; Sullivan, N. J.; Edwards, D. K.; Morabito, K. M.; Mascola, J. R.; Carfi, A.; Corbett, K. S.; Moore, I. N.; Baric, R. S.; Graham, B. S.; Ruckwardt, T. J., COVID-19 vaccine mRNA-1273 elicits a protective immune profile in mice that is not associated with vaccine-enhanced disease upon SARS-CoV-2 challenge. *Immunity* **2021,** *54* (8), 1869-1882.e6.
74. Reiss, S.; Baxter, A. E.; Cirelli, K. M.; Dan, J. M.; Morou, A.; Daigneault, A.; Brassard, N.; Silvestri, G.; Routy, J. P.; Havenar-Daughton, C.; Crotty, S.; Kaufmann, D. E., Comparative analysis of activation induced marker (AIM) assays for sensitive identification of antigen-specific CD4 T cells. *PloS one* **2017,** *12* (10), e0186998.
75. Mingueneau, M.; Krishnaswamy, S.; Spitzer, M. H.; Bendall, S. C.; Stone, E. L.; Hedrick, S. M.; Pe'er, D.; Mathis, D.; Nolan, G. P.; Benoist, C., Single-cell mass cytometry of TCR signaling: amplification of small initial differences results in low ERK activation in NOD mice. *Proceedings of the National Academy of Sciences of the United States of America* **2014,** *111* (46), 16466-71.
76. Billi, A. C.; Gharaee-Kermani, M.; Fullmer, J.; Tsoi, L. C.; Hill, B. D.; Gruszka, D.; Ludwig, J.; Xing, X.; Estadt, S.; Wolf, S. J.; Rizvi, S. M.; Berthier, C. C.; Hodgin, J. B.; Beamer, M. A.; Sarkar, M. K.; Liang, Y.; Uppala, R.; Shao, S.; Zeng, C.; Harms, P. W.; Verhaegen, M. E.; Voorhees, J. J.; Wen, F.; Ward, N. L.; Dlugosz, A. A.; Kahlenberg, J. M.; Gudjonsson, J. E., The female-biased factor VGLL3 drives cutaneous and systemic autoimmunity. *JCI Insight* **2019,** *4* (8).

# Chapter 4

# Dual Targeting of STING and PI3Kγ Eliminates Regulatory B Cells to Overcome STING Resistance for Pancreatic Cancer Immunotherapy


## 4.1 Abstract

The immune suppression in tumors and lymph nodes of pancreatic ductal adenocarcinoma (PDAC), regulated by suppressive myeloid cells and regulatory B (Breg) cells, hinders the effectiveness of immunotherapy. Although STING agonists activate myeloid cells to overcome immune suppression, it expands Breg cells, conferring STING resistance in PDAC. We discovered that blocking PI3Kγ during STING activation abolished IRF3 phosphorylation to eliminate Breg cells, while PI3Kγ inhibition sustained STING-induced IRF3 phosphorylation to preserve STING function in myeloid cells. Therefore, we developed a dual functional compound SH-273 and its albumin nanoformulation Nano-273, which stimulates STING to activate myeloid cells and inhibits PI3Kγ to eliminates Breg cells overcoming STING resistance. Nano-273 achieved systemic antitumor immunity through intravenous administration, which decreases Breg cells and remodels microenvironment in tumors and lymph nodes. Nano-273, combined with anti-PD-1, extended median survival of 200 days in transgenic KPC PDAC mice (KrasG12D-P53R172H-Cre), offering potential for PDAC treatment.


## 4.2 Introduction

Pancreatic ductal adenocarcinoma (PDAC), the deadliest cancer type, has only an 12% five-year survival rate, underscoring a critical need for more effective treatments[1]. The only two available first-line therapeutic regimens for pancreatic cancer are FOLFIRINOX (leucovorin, fluorouracil, irinotecan, and oxaliplatin) and a combination of Abraxane (an albumin-based nanoparticle of paclitaxel) with gemcitabine. However, these treatments offer limited efficacy[2-4]. Notably, while immunotherapies targeting PD-1/PD-L1 have shown remarkable success in various other cancer types, their effectiveness in PDAC patients remains minimal[5,6].

The immunosuppressive microenvironment in both tumors and lymph nodes of PDAC presents a significant challenge to the efficacy of immunotherapy. The myeloid cell-driven immune suppression, such as tumor-associated macrophages (TAMs), myeloid-derived suppressor cells (MDSCs) and inactivate dendritic cells (DCs), is well-established[6,7].Yet, the immune suppression by regulatory B (Breg) cells has only recently been recognized[8-11]. Recent studies demonstrate that PDAC has significantly high Breg cell populations, exacerbating immune suppression[8,9] and contributing to negative patient outcomes during PDAC immunotherapy[8-10].

However, current immunomodulators to counter immune suppression primarily focus on targeting myeloid cells[6,12], without effectively regulating Breg cells[7,13]. For instance, STING agonist, as one of the most effective immunomodulators, overcomes myeloid cell-driven immune suppression by stimulating type I interferon signaling[14], but STING agonist simultaneously expands suppressive Breg cells[11], which represents an intrinsic resistance mechanism in PDAC[13]. More importantly, the opposite effect of STING agonist in myeloid cells and in Breg cells depends on the same pathway through IRF3 phosphorylation[11]. In myeloid cells, STING activation increases IRF3 phosphorylation promoting type I interferon expression. This repolarizes TAMs into the M1 phenotype and stimulates dendritic cells (DCs) to activate cytotoxic CD8+ T cells[14]. However, in Breg cells, STING-induced IRF3 phosphorylation promotes IL-35 and IL-10 gene expression, which expands Breg cells for immune suppression[8,11,15]. Therefore, there is a pressing need to develop strategies to overcome the immune suppression in PDAC by simultaneously activating myeloid cells and eliminating Breg cells in both tumors and lymph nodes.

In this study, we discovered that blocking PI3Kγ during STING activation abolished IRF3 phosphorylation in B cells, thus decreasing Breg cells, while sustaining IRF3 phosphorylation in myeloid cells to preserve STING function. Based on the finding, we developed a dual functional compound SH-273 by stimulating STING and inhibiting PI3Kγ, which preserves STING function to activate myeloid cells and eliminates Breg cells to overcome STING resistance. To achieve systemic antitumor immunity, we prepared albumin nanoformulation of SH-273 (Nano-273) for intravenous administration to achieve systemic antitumor immunity by decreasing Breg cells and remodeling microenvironment in tumors and lymph nodes[11], a goal not attainable through local intratumorally injection of STING agonists[13,14]. The in vivo efficacy of Nano-273 was evaluated in transgenic pancreatic cancer mouse model (KPC, KrasG12D, P53R172H, Pdx1-Cre) to extend median survival of 200 days, where no toxicity was observed at therapeutic dose regimen. Single-cell analysis and flow cytometry was used to evaluate Nano-273 to remodel microenvironment and eliminate Breg cells. These data suggest that Nano-273 is a promising candidate for

pancreatic cancer immunotherapy, by eliminating Breg cells to overcome STING resistance and counteract suppressive microenvironment in both tumors and lymph nodes.

### 4.3 Results

#### STING agonists expand Breg cells in PDAC Mice

Recent studies suggest that immunosuppression in PDAC is mediated by both immune suppressive regulatory B cells and myeloid cells [6,7,11-13]. To validate the presence of Breg cells in PDAC mouse model, we analyzed their frequency in tumors and lymph nodes of KPC (KrasG12D, P53R172H, Pdx1-Cre) transgenic mice, which spontaneously develop pancreatic adenocarcinoma in comparison with normal C57BL/6 mice. Our results revealed a significant increase in both IL35+ and IL10+ Breg cell frequencies in the tumor, lymph nodes of KPC mice compared to normal mice. Specifically, Breg cell frequencies were 4.6 and 36.2 times higher in KPC mouse tumors (10.2% and 19.9%) than in pancreatic tissues of normal mice (2.2% and 0.55%), 32.4 and 310 times higher in KPC mouse lymph nodes (22% and 18.6%) than in normal lymph nodes (0.68% and 0.06%). (**Figure 4.1a, 4.1b**). Additionally, a high level of M2 macrophages was also observed in the tumor, lymph nodes, and spleen of PDAC mice (**Figure S1**).

Recent studies also suggest that STING agonists further expand Breg cells, contributing to intrinsic STING resistance in PDAC[8,11,15]. To confirm these, we evaluated the in vivo effects of two STING agonists, cGAMP and diABZi, in C57BL/6 mice implanted with PDAC KPC 6422 cells. Following five doses of STING agonists administered either intratumorally (it) or intravenously (iv), in combination with anti-PD-1, we observed minimal tumor growth inhibition (**Figure 4.1c**). Both intratumorally and intravenously administrations of STING agonists further expanded $IL35^+$ and $IL10^+$ Breg cells in tumor tissues and lymph nodes **(Figure 4.1d and 4.1e)**. This persistence of high level Breg cells may explain the limited efficacy of STING agonists combined with anti-PD-1 in KPC mice, which underscores the importance of eliminating Breg cells to overcome STING resistance in PDAC.

#### Blocking PI3Kγ abolished STING-induced IRF3 phosphorylation in B cells, while PI3Kγ inhibition sustained STING-induced IRF3 phosphorylation in myeloid cells.

To understand the expressions of STING and PI3Kγ in different tissues and immune cells, we first used western blot to detect their protein levels. The data showed that STING is present in tissues including tumor and lymph nodes of KPC mice, normal pancreas and normal lymph nodes in

C57BL/6 mice, as well as different immune cells including B cells, bone marrow derived macrophages (BMDM), bone marrow derived dendritic cells (BMDM) in both KPC mice and normal mice (**Figure 4.2a, 4.2b**), In comparison, PI3Kγ is also expressed in tumor and lymph node, as well as different immune cells. (**Figure 4.2a, 4.2b**).

STING activation triggers IRF3 phosphorylation in myeloid cells, enhancing type I interferon expression, while in B cells, IRF3 phosphorylation boosts IL-10 and IL-35 expression, expands B regulatory (Breg) cells[8,11,15]. To investigate effect of PI3Kγ inhibition on STING-induced IRF3 phosphorylation across cell types, we used western blot to analyze IRF3 phosphorylation in the presence/absence of PI3Kγ inhibitor (IPI-549) and STING agonist (MSA-2) in B cells, Bone Marrow derived dendritic cell (BMDC) and bone marrow derived macrophage (BMDM) from KPC mice, and THP-1 hSTING$^{HAQ}$ monocyte cell line, as well as CD4 T cells. STING activation by MSA-2 indeed increased IRF3 phosphorylation in B cells and myeloid cells (BMDC, BMDM, and THP-1 hSTING$^{HAQ}$) (**Figure 4.2c**), consistent with previous report[11]. Surprisingly, PI3Kγ inhibition by IPI-549 completely abolished STING-induced IRF3 phosphorylation in B cells, but it sustained STING-induced IRF3 phosphorylation in myeloid cells (**Figure 4.2c**). These phenomena are not observed in CD4 T cells (**Figure 4.2c**).

**Blocking PI3Kγ eliminated STING-induced Breg cells expansion, while PI3Kγ inhibition preserved STING induced myeloid cell activation.**

To further analyze how did PI3Kγ inhibition alter Breg cell populations, we used flow cytometry to monitor IL-35+ and IL-10+ Breg cells in the splenocytes isolated from KPC and STING knockout mice (Tmem173$^{-/-}$), treated with or without the STING agonist MSA-2 and the PI3Kγ inhibitor IPI-549 in vitro. The data showed that STING agonist (MSA-2) treatment significantly increased IL-35$^{+}$ and IL-10$^{+}$ Breg cells by 100 and 18-fold, but PI3Kγ inhibitor (IPI-549) completely eliminated these Breg cells (**Figure 4.2d and S2**). To confirm this effect is STING-dependent, we also monitored IL-35+ and IL-10+ Breg cells in the splenocytes from STING knockout mice (Tmem173$^{-/-}$ mice) under treatment of STING agonist (MSA-2) and PI3Kγ inhibitor (IPI-549). The data showed that neither MSA-2 nor IPI-549 has any effect on IL-35$^{+}$ and IL-10$^{+}$ Breg cells in STING knockout mice (**Figure S3**), strongly suggesting STING dependence. Additionally, we found no significant induction of IL-35 and IL-10 in BMDCs, BMDMs, THP-1 cells, and CD4 T cells under similar treatment conditions (**Figure S4-S8**), suggesting that STING-induced IL-35 and IL-10 expressions are exclusively in B cells.

To investigate whether PI3Kγ inhibition would impact STING activation in myeloid cells, we measured STING induced type I interferon expression in BMDC, monocyte THP1 hSTING$^{R232}$, and THP-1-Blue$^{TM}$ ISG (hSTING$^{HAQ}$), and THP-1 hSTING$^{KO}$ cells. The data shows that STING agonist MSA-2 stimulated IFN-beta secretion in these STING positive cells but not in STING knockout cells, and PI3Kγ inhibition (IPI-549) sustained STING activation in these STING positive cells (**Figure 4.2e-4.2h**).

To study whether PI3Kγ inhibition would influence STING induced activation of myeloid cells, we measured dendritic cell activation and M1-macrophage polarization in BMDCs and BMDMs from KPC mice, as well as macrophage cell line RAW264.7 cells. The data showed that STING agonist (MSA-2) activated BMDCs (**Figure 4.2i and S9**) and BMDMs (**Figure 4.2j and S10**) as measured by CD86$^{+}$ populations, stimulated M1-macrophage polarization (**Figure 4.2k and S11**) and increased TNF-alpha secretion in macrophage RAW264.7 (**Figure 4.2l**). PI3Kγ inhibition preserved the STING induced activation in these myeloid cells (**Fig 4.2e-4.2l**).

In summary, our results suggest that PI3Kγ inhibition abolished STING-induced IRF3 phosphorylation in B cells, thereby eliminating Breg cell expansion. However, PI3Kγ inhibition sustained STING-induced IRF3 phosphorylation in myeloid cells, promoting type I interferon production and facilitating the activation of myeloid cells.

**Dual functional compound SH-273 and its albumin nanoformulation inhibit PI3Kγ to eliminates Breg cells and stimulate STING function to activate myeloid cells.**

To simultaneously activate STING and inhibit PI3Kγ, we developed a dual functional compound (SH-273), and encapsulated it into albumin nanoformulation Nano-273 for intravenous administration to achieve systemic immunity **(Figure 4.3a)**. The synthesis of SH-273 is described in **Scheme 1**. The dual functional compound SH-273 stimulated STING activity (IC50 29.6 nM) in THP-1 Blue ISG cells (STING reporter) (**Figure S12**) and inhibited PI3Kγ (IC50 20.2 nM) (**Figure S13**). SH-273 abolished the STING-induced IRF3 phosphorylation in B cells from splenocytes of KPC PDAC mice (**Figure 4.3b**). SH-273 eliminated STING-induced expansion of IL35$^{+}$ and IL10$^{+}$ Breg cells in the splenocytes from KPC mice (**Figure 4.3c**). As a control, SH-273 did not show such effect in the splenic B cells from STING knockout mice (Tmem173$^{-/-}$), suggesting SH-273 effect is indeed STING dependent (**Figure S14**). In contrast, SH-273 sustained activity to stimulate IRF3 phosphorylation in myeloid cells, and thus SH-273 preserved STING function to activate these myeloid cells (**Figure S12**)

In order to achieve systemic immunity, we prepared an albumin nanoformulation of SH-273 (Nano-273) for intravenous administration and effective delivery to tumor and lymph nodes[11]. Nano-273 showed a uniform morphology with an average hydrodynamic diameter of 135 nm, a polydispersity index (PDI) of 0.095, maintaining stable even after 1000-fold dilution (**Figure 4.3a and S15a**). Nano-273 showed effective delivery to pancreatic tumors and lymph nodes compared to SH-273 in transgenic KPC PDAC mice (**Figure S15b**). Additionally, 2D and 3D confocal imaging showed that albumin nanoformulation of fluorescent dye delivered more and penetrate deeper into tumor tissue and tumor organoids from KPC PDAC mice than free fluorescent dye (**Figure S16-S18**). Furthermore, 2D confocal imaging revealed albumin nanoformulation of fluorescent dye delivered more and deeper into lymph nodes of KPC PDAC mice than free fluorescent dye (**Figure S19)**. 3D confocal imaging showed albumin nanoformulation of fluorescent dye penetrated deep into the lymph nodes with accumulation in the macrophages and B cells (**Figure S20**).

**Nano-273 extended median survival to 200 days in KPC PDAC mice through activating systemic immunity.**

To assess the in vivo efficacy of Nano-273, We tested Nano-273 in combination with anti-PD1 in transgenic KPC PDAC mice with spontaneous pancreatic tumors. The data showed that the combination of Nano-273 and anti-PD-1 extended median survival to 200 days compared to control group (median survival at 120 days). MSA-2 combined with anti-PD-1 slightly extended median survival to 146 days. Neither the anti-PD-1 antibody alone nor combined with the albumin nanoformulation of paclitaxel (Nano-P) significantly improved median survival of KPC PDAC mice. (**Figure 4.4a).** Nano-273 combined with anti-PD-1 showed superior efficacy in KPC mice compared to other treatment groups **(Figure S21**), which includes combination of IPI549 and MSA2, Nano-P and IPI549. At the endpoint of the study, we also examined the metastasis in the lung, liver, spleen, and kidney tissues. Notably, Nano-273 substantially decreased tumor metastasis and local invasion to lung (**Figure 4.4b**).

In addition, we also tested the Nano-273's efficacy in xenograft model using KPC 6422 cells in C57BL/6 mice. Both Nano-273 and SH-273, in combination with anti-PD-1 antibody, significantly delayed tumor growth compared to the MSA-2, IPI-549, and control groups, with Nano-273 demonstrating superior efficacy over free SH-273 (**Figure 4.4c and S22**).

In order to evaluate the systemic anticancer immunity of Nano-273 through intravenous administration, we compared the anticancer efficacy of Nano-273 via intravenous (iv),

subcutaneous (sc), or intratumorally (it) injections, to inhibit bilaterally inoculated KPC 6422 cells in C57BL/6 mice. Intratumorally injections of Nano-273 only suppressed local tumor growth, but had minimal inhibition to the tumor at the distal site. This phenomenon is confirmed in clinical studies that local intra-tumor injection of STING agonists only generated local tumor inhibition but did not have much effects on distal tumors or metastasis.[13,14,16-18] This highlights the importance of using STING agonists systematically to induce systemic immunity. Indeed, our data showed that both intravenous and subcutaneous injections of Nano-273 elicited robust systemic immune responses, significantly reducing tumor burden at both local and distal sites (**Figure 4.4d and S23**).

To investigate how systemic delivery of Nano-273 achieve systemic immunity in comparison with intratumoral injection, we used flow cytometry to analyze the M1-macrophage polarization in local, distal tumors and lymph nodes. The data showed that Nano-273 (iv and sc) significant increased M1 macrophages at distal tumors and lymph nodes, while intra-tumoral injection of Nano-273 did not increase M1-macrophage in either distal tumors or lymph nodes (**Figure 4.4e**). To confirm if systemic efficacy of Nano-273 indeed depends on the systemic immune cell trafficking, we used fingolimod (FTY-720) to inhibit lymphocyte egress from lymph nodes[19], which reversed effect of Nano-273 after iv administration (**Figure S24**). Fingolimod also decreased immune infiltration in distal tumor and reduced M1 macrophage in the lymph nodes and distal tumor sites (**Figure S25**). These data suggest that systemic delivery of Nano-273 achieve systemic immunity for its superior systemic anticancer efficacy in KPC PDAC mice.

Finally, to confirm if systemic delivery of Nano-273 will not cause toxicity in major organs, we performed extensive toxicity study using the same dose regimen as seen in the therapeutic studies (iv injection five doses of Nano-273 and SH273). No toxicity in the liver, kidney, and blood cells was observed as shown by liver enzymes (AST, GST), kidney function (BUN, creatinine) and blood cell counts (**Figure 4.4f**). Pathological staining of major organs (liver, kidney, spleen, lung, and heart) also did not show toxicity as indicated healthy tissue structures (**Figure S26**).

**Nano-273 eliminated STING-induced Breg cells expansion and remodeled immune microenvironment in tumor and lymph nodes for systemic anticancer immunity.**

To investigate how did Nano-273 remodel the tumor immune microenvironment, we first utilized flow cytometry to examine immune cell infiltration following the treatments in **Figure 4.4a**. Both Nano-273 and SH-273 significantly increased immune cell infiltration to tumors compared to STING agonist (MSA-2) or PI3Kγ inhibitor (IPI-549) alone (**Figure 4.5a**). Subsequently, we

employed single-cell RNA-sequencing (RNA-Seq) to analyze all immune cells in the tumor tissues post-treatments. Immune cell phenotypes were identified based on RNA expression levels and corroborated by TotalSeq™-C antibody surface staining (**Figure 4.5b and 4.5d**), which showed increased B and CD8 T cell populations. The data showed that both Nano-273 and SH-273 significantly decreased $IL35^+$ and $IL10^+$ Breg cells, while increased ICOSL+ B cell populations in tumors (**Figure 4.5c, 4.5e and S27**)[20]. In contrast, STING agonist (MSA-2) significantly increased $IL35^+$ and $IL10^+$ Breg cells in tumors (**Figure 4.5c, 4.5e and S27**), similar to literature reports[8,11,14].

To verify these findings in single cell RNA-seq, we further used flow cytometry to assess Breg cell frequencies in tumors, lymph nodes, and spleens post-treatment. The Nano-273 and SH-273 significantly decreased Breg cell frequencies by 1.8 to 7.8 -folds in tumors ($IL35^+$ Breg cell: 2.0% and 5.3%, $IL10^+$ Breg cell 1.2% and 3.1%), 10.5 to 510 -folds in lymph nodes ($IL35^+$ Breg cell: 0.01% and 0.2%; $IL10^+$ Breg cell: 0.03% and 0.2%) in comparison with MSA-2 and control groups in tumors ($IL35^+$ Breg cell: 15.6% and 9.6%; $IL10^+$ Breg cell: 9.3% and 5.7%), and in lymph nodes ($IL35^+$ Breg cell: 5.1% and 3.5%; $IL10^+$ Breg cell: 3.1% and 2.1%)(**Figure 4.5f**). Our results suggest that Nano-273 effectively eliminated STING-induced Breg cells expansion and remodeled immune microenvironment in both tumors and lymph nodes, thereby achieving systemic anticancer immunity.

#### 4.4 Discussion and Conclusion

The immunosuppressive microenvironment in the tumor and lymph nodes of PDAC presents a significant hurdle for the efficacy of immunotherapy.[6,7] Therefore, a variety of immune modulators targeting myeloid cell suppression have been developed[21-27], but they have shown only limited clinical success[16,28]. Recent research showed that the immune suppression in PDAC's is significantly regulated by high number of regulatory B cells in both tumors and lymphatic systems[8,9,11]. A well-known immune modulator, STING agonist, could activates myeloid cells, but unfortunately expands Breg cells in tumors and lymph nodes, contributing to therapeutic resistance[7,11,13,21-24].

In this study, we discovered that the PI3Kγ inhibition during STING activation abolished IRF3 phosphorylation in B cells, effectively eliminated Breg cells, but PI3Kγ inhibition sustained IRF3 phosphorylation and thereby preserved STING activation in myeloid cells. Based on this finding, we developed a dual functional compound SH-273 to activate STING and inhibit PI3Kγ. SH-273 preserved STING function to activate myeloid cells and eliminated Breg cells to overcome STING

resistance. To achieve systemic antitumor immunity, we also prepared an albumin nanoformulation Nano-273 for safe intravenous administration and effective delivery to pancreatic tumors and lymph nodes in transgenic KPC PDAC mice. Impressively, when combined with anti-PD-1 therapy, Nano-273 extended the median survival to 200 days in transgenic KPC PDAC mice. In contrast, other clinically used treatments did not significantly improve survival, including the anti-PD1 antibody alone, anti-PD1 combined with albumin nanoformulation of paclitaxel (nab-paclitaxel), and STING agonist MSA-2 with anti-PD1. Subsequent immune profiling using single cell RNA-seq and flow cytometry confirmed that Nano-273 markedly reduced Breg cell frequency and significantly remodeled the immune microenvironment than other treatment groups.

This study provides a novel and more effective strategy to overcome immune suppressive environment in both tumors and lymph nodes in PDAC tumors by simultaneously targeting myeloid cells and Breg cells. While the role of myeloid cells in immune suppression of PDAC is well-established, the significant impact of Breg cells has only recently been recognized[8-11]. Bhalchandra et al. found an increased Breg cells in primary human PDAC tissues from 56 patients compared to adjacent normal tissues[8]. Their findings revealed a negative relationship between Breg cells abundance in tumors and PDAC prognosis, but positive correlation between plasma cell numbers and PDAC prognosis. Similarly, Li et al. reported that STING agonist significantly increased the frequency of Breg cells in the pancreatic cancer mouse model[11]. Our study corroborates these findings, showing elevated Breg cells in PDAC mouse tumors relative to normal pancreatic tissue (**Figure 4.1 and 4.5**), and we also confirmed that STING agonists increased Breg cells in PDAC (**Figure 4.2 and 4.5**). This underscores the role of Breg cells in PDAC immune suppression and intrinsic resistance to STING agonists. Crucially, our research demonstrates that blocking PI3Kγ during STING activation eliminated STING-induced Breg cell expansion and significantly enhanced the effectiveness of immunotherapy in PDAC. Our data shows that Nano-273 markedly reduced $IL35^+$ and $IL10^+$ Breg frequency in tumor to less than 2% and 1.2%, compared to 15.6% and 9.3% in the group treated with a STING agonist, and 9.6% and 5.7% in the control group. Furthermore, Nano-273 triggered a more robust activation of the tumor immune microenvironment, evidenced by increased immune cell infiltration into tumors, and heightened frequencies of CD8 T cells, and M1 macrophages, compared to treatments with STING agonist, PI3Kγ inhibitor, or the control group.

While previous studies have emphasized the critical role of Breg cells in PDAC immune suppression, the specific signaling pathway to overcome Breg cell expansion during STING activation was not well-defined. Our research reveals that inhibiting PI3Kγ decreased IRF3

phosphorylation in B cells, hindering the expression of IL-35 and IL-10, thereby eliminating Breg cells, while it sustained IRF3 phosphorylation in myeloid cells, thus preserved STING activation for Type-I interferon production (**Figure 4.2**). This suggests the divergent effects of PI3K during STING activation in Breg and myeloid cells[8,11]. PI3Kγ is mainly recognized for its role in regulating macrophage repolarization from M2 to M1 phenotype.[29,30] PI3Kγ has also been reported to be expressed in B cells[31-34]. However, its function in B cells has been less understood.[34,35] Our study presents a novel mechanism and potential therapeutic application for PI3Kγ inhibition in regulating Breg cells as a strategy in pancreatic cancer immunotherapy.

Furthermore, while clinical trials commonly employ local intra-tumoral injections of STING agonists due to the limited pharmacokinetic properties of these agents, the local intra-tumor injection of STING agonist often fails to induce a systemic anticancer immunity[13,14,16-18]. And thus the local injection of STING agonist mainly shows anticancer efficacy in local tumors but does not exhibit strong anticancer efficacy in distal tumors or metastasis. Additionally, intra-tumoral injections are not feasible for many cancers in clinical setting, including pancreatic cancer. Therefore, developing an effective systemic delivery for STING agonists has become a critical objective to achieve systemic anticancer immunity to improve their clinical efficacy[17,36,37]. In our study, we utilized albumin nanoformulation of SH-273 for safe intravenous administration and effective delivery to pancreatic tumors and lymph nodes. Clinically, albumin nanoformulation of paclitaxel (Abraxane®) has been approved as the first-line therapy in pancreatic cancer patients benefited from its superior efficacy compared to traditional solvent-based Taxol®[38]. Our findings show that intravenous administration of Nano-273 displayed low toxicity and effectively combatted both local and distal tumors (**Figure 4.4**). Our previous research has also shown that albumin nanoformulations of immune modulators enhance the drug delivery to tumors and lymph nodes, thereby overcoming immune suppression in both tumors and lymphatic system[11]. Nano-273 exhibited greater accumulation in both tumors and lymph nodes compared to the solvent-based formulation (**Figure S15b, S16-S20**).

In conclusion, our dual functional compound SH-273, by stimulating STING and inhibiting PI3Kγ, preserves STING function in myeloid cells and eliminates Breg cells to overcome STING resistance. Nano-273 achieved systemic antitumor immunity through intravenous administration, which decreases Breg cells and remodels microenvironment in tumors and lymph nodes. Nano-273, combined with anti-PD-1, extended median survival of 200 days in transgenic KPC PDAC mice (KrasG12D-P53R172H-Cre), offering potential for PDAC treatment.

#### 4.5 Methods

### Animal experiments

All animal experiments were conducted according to protocols approved by the University of Michigan Committee on Use and Care of Animals (UCUCA). Animals were maintained under pathogen-free conditions, in temperature- and humidity-controlled housing, with free access to food and water, under a 12-hour light-dark rhythm at the unit for laboratory animal medicine (ULAM), part of the University of Michigan medical school office of research. CD1 and C57BL/6 mice were obtained from The Jackson Laboratories. The KPC (LSL-KrasG12D/+;LSL-Trp53R172H/+;Pdx-1-Cre) transgenic mice were bred, genotyped and maintained by ULAM following reference[39]. Tumor experiments by xenograft implanting were performed using 6-week-old male wild-type C57BL/6 mice. Endpoints for anti-tumor efficacy studies were determined using the End-Stage Illness Scoring System, mice receiving an End-Stage Illness Score greater than 6 were euthanized by CO2 asphyxiation.

### Cells

All cells were maintained at 37 °C in a 5% CO2/95% air atmosphere and approximately 85% relative humidity. Primary B-cells, CD4 T cells and splenocytes were cultured in RPMI-1640 media supplemented with 10% fetal bovine serum, 2-Mercaptoethanol (50 μM) and 1% pen/strep. THP-1-Blue™ ISG, THP-1 hSTING$^{KO}$ and THP-1 hSTING$^{R232}$ cells were cultured in RPMI 1640 supplemented with 2 mM L-glutamine, 25 mM HEPES, 10% heat-inactivated fetal bovine serum, 100 μg/mL normocin and 1% pen/strep. Bone marrow-derived dendritic cells (BMDCs) and bone marrow-derived macrophages (BMDMs) were isolated from mouse bone marrow cells and cultured following previously reported protocols[40,41]. RAW264.7 macrophages were cultured in complete RPMI-1640 media supplemented with 10% fetal bovine serum, 1% L-glutamine, 1% MEM nonessential amino acid solution, 1% sodium pyruvate and 1% pen/strep. KPC 6422 cells obtained from kerafast were cultured in DMEM supplemented with 10% fetal bovine serum, Glutamax and 1% pen/strep[42].

### Analyze Breg cells and macrophages in various tissues and assess the effectiveness of STING agonist in pancreatic cancer mouse models

To analyze Breg cells and macrophage proportions, lymph node, tumor, and spleen tissues from KPC (LSL-Kras G12D, LSL-P53R172H, Pdx1-cre) transgenic mice were harvested and prepared

for single-cell suspension. CD45, CD4, CD19, IL35, and IL10 were used to identify regulatory B cells by flow cytometry. Similarly, CD45, CD11b, F4/80, CD80, and CD206 were used to identify M1 and M2 macrophages. To evaluate the in vivo efficacy of the STING agonists, 6-week-old C57BL/6 male mice were subcutaneously inoculated at the right flank with 5*10^5 KPC 6422 cells/mouse. DiABZi (20 μg/mouse for intratumorally injection and 1.5 mg/kg for intravenous injection) and 2'3'-cGAMP (10 μg/mouse for intratumorally injection) were administrated 5 days post tumor inoculation, every 3 days for a total of 5 times. Tumor volumes were calculated as volume = (width)^2 × length/2.

**Western blot analysis of STING and PI3Kγ**

Lymph node, pancreas and tumor were harvest from C57BL/6 mice or transgenic KPC mice. Proteins were immediately extracted post-harvest and digestion for western blot analysis. B cells were isolated from splenocytes of C57BL/6 mice or transgenic KPC mice using the STEMCELL EasySep™ mouse B cell isolation kit. Bone marrow-derived dendritic cells (BMDCs) and bone marrow-derived macrophages (BMDMs) were isolated from bone marrow cells of C57BL/6 mice or transgenic KPC mice and cultured following previously reported protocols[40,41]. Proteins were collected following cell lysis, sonication, and centrifugation for western blot analysis.

**Study the role of PI3Kγ in STING activation in different immune cells**

B and CD4+ T cells were isolated from the spleen using the STEMCELL EasySep™ mouse B cell isolation kit and EasySep™ mouse CD4+ T cell isolation kit, respectively. To investigate the phosphorylation of IRF3, B cells (pre-treated with 5 μg/mL anti-IgM), CD4+ T cells, BMDCs, BMDMs, and THP-1-Blue™ ISG cells were seeded in 12-well plates at a density of 3*10^6 cells/well and incubated with or without MSA-2 (5 μg/mL) and with or without IPI-549 (17 μM). Proteins were analyzed by western blot analysis after cell collection and lysis. IL35 or IL10 expressions were analyzed by flow cytometry after cell collection and staining with anti-EBI3 and anti-IL10 antibodies. For STING activation in BMDCs, BMDMs, THP-1 cell lines, and RAW264.7 cells, the cells were treated with or without 10 μM of MSA-2 and with or without 10 μM of IPI-549. Supernatants were collected for cytokine measurement via ELISA. BMDCs were collected and stained with CD80 and CD86 for activation analysis by flow cytometry. BMDMs and RAW264.7 cells were collected and stained with CD80 or CD86 to access M1 polarization ratios by flow cytometry.

**Synthesis of SH-273, preparation of albumin nanoformulation of SH-273, and test of their cellular and binding activity.**

Synthesis of SH-273 is described in **Scheme 1**. Starting material compound **1** was cyclized with methyl thioglycolate to afford **2**. Then, condensation between **2** and amine gave **3** which was brominated with NBS to produce **4**. Sequential oxidation of **4** by NMO and PCC produced **6** followed by deprotection to furnish intermediate **7.**[43]

Starting material compound **8**, (S)-2-amino-N-(1-(8-ethynyl-1-oxo-2-phenyl-1,2-dihydroisoquinolin-3-yl)ethyl)pyrazolo[1,5-a]pyrimidine-3-carboxamide reacted with 2-azidoethanol in $CH_2Cl_2$ with CuI.A-21 catalyst to afford intermediate **9**. The reaction mixture was sonicated for 1h and stirred at room temperature overnight. Upon completion of the reaction, the catalyst was removed by filtration using $CH_2Cl_2$ and the solvent was evaporated under vacuum.

The solution of intermediate **9** (66.9 mg, 0.125 mmol), **7** (44 mg, 0.13 mmol), HATU (71.3 mg, 0.187 mmol), DIPEA (24.2 mg, 0.187 mmol), and DMAP (15 mg, 0.125 mmol) in DMF (1 mL) was stirred at room temperature for 38 h. Upon completion of the reaction, the mixture was concentrated to yield SH-273, which was then purified using column chromatography (20:1 ethyl acetate/methanol) to provide the title compound **SH-273** (74.55 mg).

NMR of SH-273: $^1$H NMR (599 MHz, $CDCl_3$) δ 8.40 (dd, *J* = 6.7, 1.7 Hz, 1H), 8.36 (dd, *J* = 4.5, 1.6 Hz, 1H), 8.12 (s, 1H), 7.95 (s, 1H), 7.88 (d, *J* = 7.0 Hz, 1H), 7.78 (dd, *J* = 7.6, 1.4 Hz, 1H), 7.55 (t, *J* = 7.7 Hz, 1H), 7.43 (d, *J* = 8.9 Hz, 3H), 7.39 – 7.33 (m, 3H), 7.23 (s, 2H), 6.75 (dd, *J* = 6.8, 4.5 Hz, 1H), 6.62 (s, 1H), 5.53 (s, 2H), 4.72 (t, *J* = 6.9 Hz, 1H), 4.57 – 4.49 (m, 2H), 4.43 (t, *J* = 5.2 Hz, 2H), 3.92 (s, 6H), 3.73 – 3.67 (m, 1H), 3.68 – 3.60 (m, 2H), 3.11 (dd, *J* = 7.5, 4.3 Hz, 1H), 2.73 (s, 3H), 2.48 (t, *J* = 6.5 Hz, 2H), 1.40 (dd, *J* = 6.9, 5.0 Hz, 4H), 1.35 (dd, *J* = 9.4, 6.7 Hz, 4H).

Albumin nano formulation of SH-273 (Nano-273) was then prepared followed previously established protocol[11]. Briefly, SH-273 (10 - 12 mg) was dissolved in 1mL of chloroform and then mixed with mouse albumin solution (100 mg/20 mL) to generate a milky emulsion using a rotor-stator homogenizer. This emulsion was processed through five to six cycles at 26,000 psi in a high-pressure homogenizer (Nano DeBEE) at 4°C. Subsequently, the organic solvent was removed using a rotary evaporator at 25°C. The Nano-273 suspension was then filtered (0.22 μm), lyophilized, and stored at −20°C. Size distribution and morphology were assessed using dynamic light scattering and transmission electron microscopy (TEM).

The cellular IC50 of SH-273 was measured using THP-1-Blue™ ISG cells. THP-1-Blue™ ISG cells were seeded in a 96-well plate with a density of 1*10^5 cells/well and incubated with different concentrations of MSA-2 and Nano-273 for 24 hrs at 37 °C. Cell media were then collected, mixed, and incubated with QUANTI-Blue™ solution. SEAP levels were subsequently measured using Synergy 2 microplate reader (Biotek) at 620 nm in absorbance mode. B cells (pre-treated with 5 μg/mL anti-IgM) and Bone marrow dendritic cells were seeded in a 12-well plate at a density of 3*10^6 cells/well and incubated with SH-273 (17 μM). Proteins were analyzed by western blotting after cell collection and lysis. For IL35 or IL10 expression analysis, cells were collected and stained with anti-EBI3 and anti-IL10 antibodies for flow cytometry.

PI3Kγ binding affinity was evaluated using PI3Kγ (p110γ/PIK3R5) assay kit from BPS Bioscience, following the provided protocol. Inhibitors were prepared at 5X concentration in an aqueous solution at various concentrations. The PI3Kγ enzyme was diluted to ~4 ng/μl with 2.5x Kinase assay buffer. Reaction components were added sequentially: 5 μl of PI3K lipid substrate, 5 μl of inhibitor or inhibitor buffer, 5 μl of 12.5 μM ATP, and 10 μl of diluted PI3Kγ. Between each addition, the plate was shaken for 1 minute to ensure thorough mixing. After a 40-minute reaction, 25 μl of ADP-Glo reagent was added to each well. The plate was covered with aluminum foil and incubated at room temperature for 45 minutes. Subsequently, 50 μl of Kinase Detection reagent was added to each well, followed by another 30-minute incubation at room temperature, again covered with aluminum foil. Luminescence was measured using a microplate reader.

**Pharmacokinetics and toxicity of SH-273 and Nano-273 in mice**

To investigate the pharmacokinetics of SH-273 and Nano-273, KPC transgenic mice (approximately 100 days old with spontaneous tumors) were divided into two groups (n = 9) and treated with SH-273 (i.v. 17.6 μmol/kg) or Nano-273 (i.v. 17.6 μmol/kg). Tissue samples (plasma, liver, tumor, lymph nodes) were collected at 0.5, 2, and 7 hours post-administration, processed, and analyzed. SH-273 concentrations were measured by LC-MS using An AB SCIEX QTRAP 5500 mass spectrometer with a Turbo V electrospray ionization source (Applied Biosystems) coupled to a Shimadzu LC-20AD HPLC system, was used for the quantification. HPLC separation was performed on a waters XBridge® C18 3.5 μm, 5 cm x 2.1 mm column (Waters Corporation). Mobile phase A (water containing 0.1% formic acid) was first kept at 95% for 0.8 min, then decreased to 1% during 1.2 min, and maintained for 1.5 min, returned to 5% B (acetonitrile containing 0.1% formic acid) and maintained for 2 min. The flow rate was 400 μL/min. Positive ion MS/MS was conducted to detect SH273. The mass spectrometric conditions were set as

follows: source temperature, 500°C; curtain gas (CUR), 30 psi; ion spray voltage, 5500 V; ion source gas 1 (GS1), 60 psi; ion source gas 2 (GS2), 40 psi; collision gas (CAD), high; entrance potential (EP), 10 eV; collision energy (CE), 45 eV. The MS/MS transition 853.2 > 648.1 was used to detect SH273, and a dwell time of 50 ms was used for the transition. And the second transition 473 > 431.1 was used for the internal standard Clofazimine (CFZ). Data acquisition and quantitation were performed using Analyst software (Applied Biosystems). To determine the SH273 in mice plasma, 140 μL of internal standard solution (CFZ 50 ng/mL in Acetonitrile) and 30 μL of acetonitrile were added into 30 μL of plasma samples. The mixture was vortexed for 10 min and centrifuged at 3500 rpm for 10 min. Then, the supernatant was transferred to the autosampler vials for LC–MS/MS analysis. tissue samples were homogenized (Precellys tissue homogenizer, Bertin Technologies) with the addition of 20% Acetonitrile-water solution with a ratio of 5:1 volume (mL) to weight of tissue (g). Then, 140 μL of internal standard solution and 30 μL of acetonitrile were added into 30 μL of tissue homogenization samples for protein precipitation. The mixture was vortexed for 10 min and centrifuged at 3500 rpm for 10 min. The supernatant was transferred to the autosampler vials for LC–MS/MS analysis. Blank plasma and tissues, the samples from un-treated control groups, were used to exclude contamination or interference. The SH273 analytical curves were constructed with 12 nonzero standards spiked with blank plasma or tissue, by plotting the peak area ratio of SH273 to the internal standard versus the sample concentration. The concentration range evaluated was from 1 to 5000 ng/mL in plasma and tissues. All samples for calibration curve were made as the method mentioned above.

To study the in vivo toxicity, CD1 mice (6 weeks) were randomly assigned to two groups (n = 4) and administered with SH-273 (15 mg/kg) or Nano-273 (15 mg/kg) every three days for 5 times. Blood was collected on day 0, day 3, and day 15 following the initial dose for whole blood cell count. At day 15, plasma was collected for test of liver enzymes and kidney functions. At day 15, organs (heart, liver, spleen, lung and kidney) were harvest and collected for pathological staining. All blood cell count, liver enzymes, kidney functions and tissues pathological staining were conducted by ULAM.

**In vivo anti-tumor efficacy**

KPC transgenic mice were randomly assigned to various treatment groups (n = 10). Treatments started at 8 weeks of age, with doses administered weekly for a total of five times. The survival dates of the mice were documented either at the time of death or upon reaching the endpoint as defined by the End-Stage Illness Scoring System. Lung tissues were collected and underwent

pathological staining to analyze metastasis in KPC mice that reached the endpoint in each treatment group by ULAM. C57BL/6 male mice at 6 weeks of age were subcutaneously inoculated with 5*10^5 KPC 6422 cells at the right flank (**Figure 4c**) or both flanks (**Figure 4d**). MSA-2 (i.v. 34.0 μmol/kg) plus anti-PD-1 antibody (100 μg), IPI-549 (i.v. 18.9 μmol/kg) plus anti-PD-1 antibody (100 μg), SH-273 (i.v. 17.6 μmol/kg) plus anti-PD-1 antibody (100 μg) and Nano-273 (i.v. 17.6 μmol/kg) plus anti-PD-1 antibody (100 μg) were then administered to the mice 5 days post-tumor inoculation and repeated every 3 days for a total of five times. Tumor volumes were calculated as volume = (width)^2 × length/2.

**Immune profiling of lymph nodes and tumors after treatments in vivo by flow cytometry**

For in vivo M1 macrophage ratio measurements, lymph nodes and distal tumors were harvested and processed into single-cell suspensions 10 days following the final dosage. Markers CD45, CD11b, F4/80, CD80, and CD206 were used to identify M1 macrophages by flow cytometry. For in vivo Breg cell measurements, lymph nodes and tumors were harvested and processed into single-cell suspensions 10 days after the final dosage. CD45, CD4, CD19, IL35, and IL10 markers were used to identify regulatory B cells by flow cytometry.

**Single-cell RNA sequencing for immune fingerprints of tumors after treatments in vivo**

Tumor samples were harvested and dissociated into single-cell suspensions 9 days after the final dosage. Dead cells were excluded using a dead cell removal kit (Miltenyi Biotec). The single-cell suspensions were then stained with TotalSeq™-C Mouse antibody. These suspensions were subjected to final cell counting on a Countess II Automated Cell Counter (Thermo Fisher) and diluted to a concentration of 700-1000 nuclei/μL. We constructed 3′ single-nucleus libraries using the 10x Genomics Chromium Controller and followed the manufacturer's protocol for 3′ V3.1 chemistry with NextGEM Chip G reagents (10x Genomics). The final library quality was assessed using a TapeStation 4200 (Agilent), and the libraries were quantified by Kapa qPCR (Roche). Pooled libraries were subjected to 150 bp paired-end sequencing according to the manufacturer's protocol (Illumina NovaSeq 6000). Bcl2fastq2 Conversion Software (Illumina) was used to generate demultiplexed Fastq files, and a CellRanger Pipeline (10x Genomics) was used to align reads and generate count matrices.

**Immunofluorescence staining of tumor and lymph node**

For immunofluorescence staining, tumor and lymph node tissues from transgenic KPC mice were harvested 5 hours post-intravenous administration of fluorescent dye (50 mg/kg). The tissues

were immediately fixed in 1% paraformaldehyde for 1 hour, followed by immersion in 30% sucrose in 0.1% NaN3 in PBS overnight. Subsequently, tissues were embedded in optical coherence tomography (OCT) compound and snap-frozen in a CO2(s)+EtOH bath. Tissue sections of 15 μm were prepared and air-dried for 0.5 hours prior to staining. The sections were incubated with a blocking solution for 1 hour, followed by staining solution overnight at 4°C. Slides were then mounted with VECTASHIELD® Mounting Medium (lymph node) and ProLong™ Diamond Antifade Mountant with DAPI (tumor) for confocal imaging. F4/80 (Alexa Fluor 594) was used to stain macrophages at tumor. B220 (Brilliant Violet 421), CD 3 (Alexa Fluor 488) and F4/80 (Alexa Fluor 647) were used to stain B cells, T cells and macrophages at lymph node, respectively.

**3D imaging of in vivo lymph node and tumor distribution**

Tumors and lymph nodes were collected 5 hours after intravenous administration of fluorescent dye (50 mg/kg). Harvested tissues were immediately processed following iDisco protocol for clearing and staining of antibodies. For tumor immune fluorescence staining, F4/80 (Alexa Fluor 594) and B220 (Brilliant Violet 421) were validated and used. For lymph node immune fluorescence staining, B220 (Brilliant Violet 421), F4/80 (Alexa Fluor 594) and CD 3 (Alexa Fluor 488) were validated and used. Subsequent 3D imaging of the tumors and lymph nodes was performed using Zeiss Light Sheet 7 and Nikon N-SIM Super resolution + A1R Confocal microscopes, respectively.

*Sample pretreatment with methanol*

1. Dehydrate with methanol/H2O series: 20%, 40%, 60%, 80%, 100%; 1h each.
2. Wash further with 100% methanol for 1h and then chill the sample at 4°c.
3. Overnight incubation, with shaking, in 66% DCM / 33% Methanol at room temperature.
4. Wash twice in 100% Methanol at room temperature, and then chill the sample at 4°C.
5. Bleach in chilled fresh 5%H2O2 in methanol (1 volume 30% H2O2 to 5 volumes MeOH), overnight at 4°C.
6. Rehydrate with methanol/H2O series: 80%, 60%, 40%, 20%, PBS; 1h each at room temperature.
7. Wash in PTx.2 1hr for two times at room temperature.

*Immunolabeling*

1. Incubate samples in permeabilization solution, 37°C, **n**/2 days (max. 2 days)
2. Block in blocking solution, 37 °C, **n**/2 days (max. 2 days).
3. Incubate with primary antibody in PTwH/5%DMSO/3% donkey serum, 37°C, **n** days.

4. Wash in PTwH for 4-5 times until the next day.

*Clearing*

1. Dehydrate in methanol/H2O series: 20%, 40%, 60%, 80%, 100%, 100%; 1 hour each at room temperature.
2. 3 hours incubation, with shaking, in 66% DCM / 33% methanol at room temperature.
3. Incubate in 100% DCM 15 minutes twice (with shaking) to wash the MeOH.
4. Incubate in dibenzyl ether (no shaking).

PTx.2 buffer (1 L): 100 mL PBS 10X, 2 mL TritonX-100.

PTwH buffer (1 L): 100 mL PBS 10X, 2 mL Tween-20, 1 mL Heparin stock solution (10 mg/mL).

Permeabilization solution (500 mL): 400 mL PTx.2 buffer, 11.5 g of glycine, 100 mL of DMSO.

Blocking solution (50 mL): 42 mL PTx.2 buffer, 3 mL of donkey serum, 5 mL of DMSO.

### 4.6 Figures

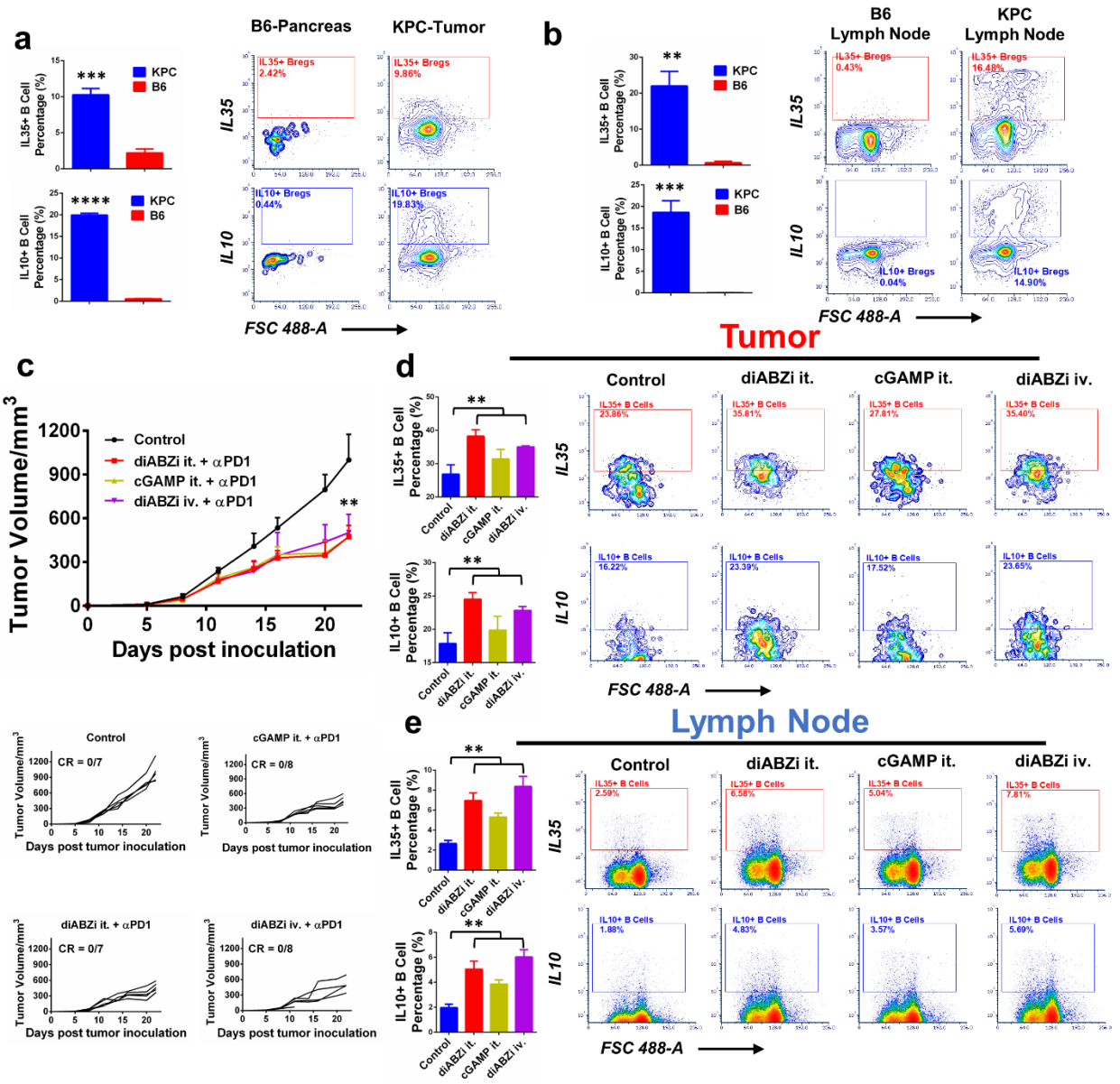


**Figure 4.1. STING agonists expand Breg cells in PDAC Mice.** Quantification and representative flow cytometry analysis of IL35$^+$ and IL10$^+$ Breg cells in KPC mice pancreatic tumor (**a**) and lymph node (**b**) in KPC mice and C57BL/6 mice. Data for quantification are shown as mean ± SD, n = 3. (**c**) Antitumor efficacy of STING agonists in C57BL/6 mice inoculated with pancreatic tumor (KPC 6422 cell line). Average tumor volumes changes after treatment with PBS (control), diABZi (intratumorally injection, 20 ug/mouse) plus anti-PD-1 antibody (100 μg), cGAMP (intratumorally injection 10 ug/mouse) plus anti-PD-1 antibody (100 μg), and diABZi (intravenous injection 1.5 mg/kg) plus anti-PD-1 antibody (100 μg). The data represents the mean ± SD; n = 5. Quantification and representative flow cytometry analysis of IL35$^+$ and IL10$^+$ Breg cells in tumor (**d**) and lymph node (**e**) from mice inoculated with KPC 6422 cell in **Figure 1c**. Statistical comparisons are based on one-way ANOVA, followed by post hoc Tukey's

pairwise comparisons or by Student's unpaired T-test. The asterisks denote statistical significance at the level of * $p < 0.05$, ** $p < 0.01$, *** $p < 0.001$, **** $p < 0.0001$. ANOVA, analysis of variance; SD, standard deviation. For (**c**), Statistical comparisons are compared between STING agonists groups with control group.

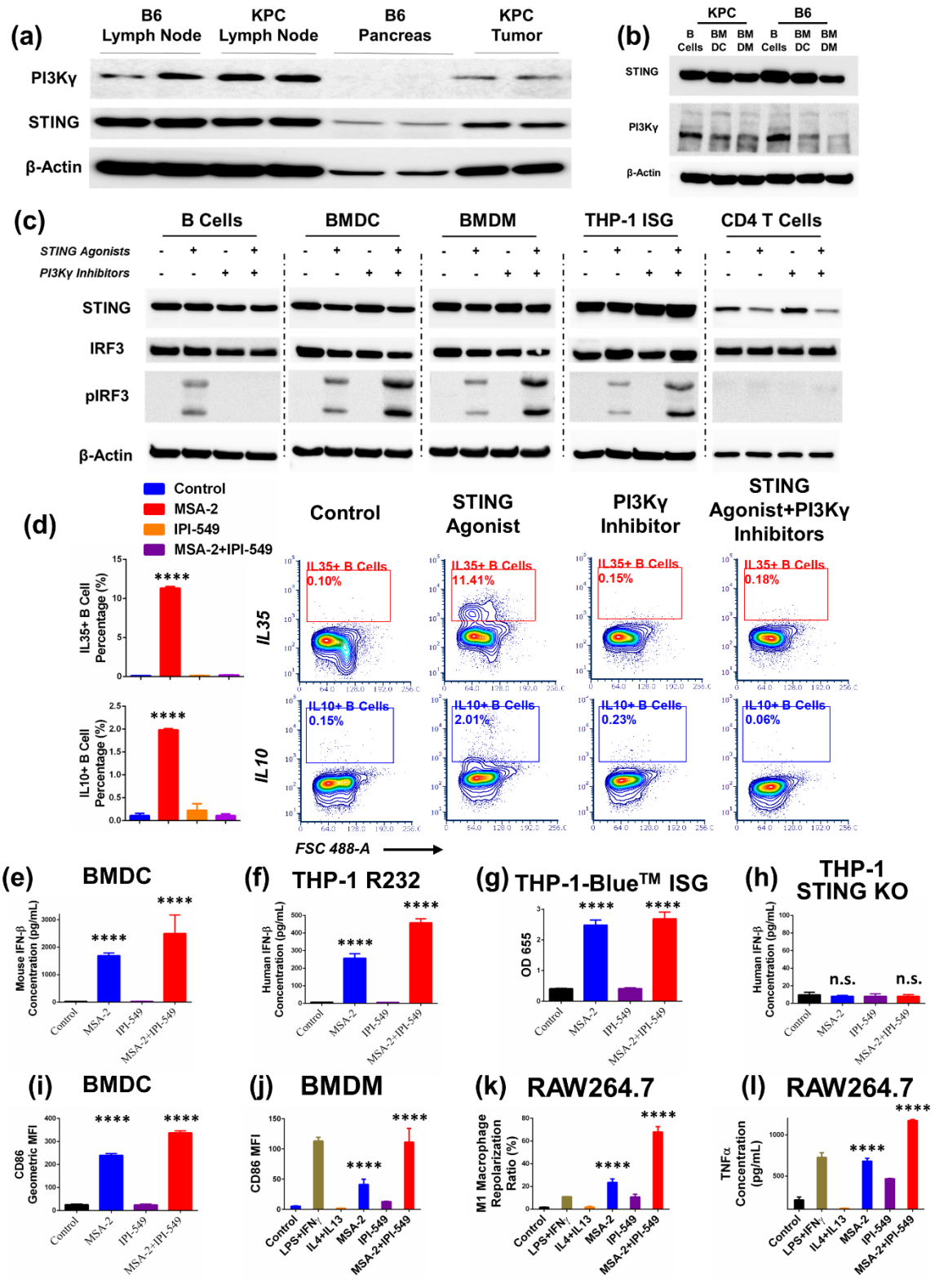


**Figure 4.2. PI3Kγ inhibition abolished STING-induced IRF3 phosphorylation to eliminate STING-induced Breg cells expansion, while PI3Kγ inhibition sustained STING-induced IRF3 phosphorylation to preserve STING function in myeloid cells.**

(**a**) PI3Kγ and STING expression at lymph node and pancreatic tumor from KPC mice compared to C57BL/6 mice. (**b**) PI3Kγ and STING expression at B cell, bone marrow derived dendritic cells and bone marrow derived macrophages from KPC mice and C57BL/6 mice. (**c**) Phosphorylation of IRF3 at splenic B cells, bone marrow derived dendritic cells (BMDCs), bone marrow derived macrophages (BMDMs) and CD4 T cells derived from KPC mice and THP-1 hSTING$^{HAQ}$ cells after treatments with or without MSA-2 or IPI-549. (**d**) Quantification and representative flow cytometry analysis of IL35$^{+}$ and IL10$^{+}$ Breg cells (from KPC spleen) after treatments with or without MSA-2 or IPI-549. (**e**) Quantification of mouse Interferon-β concentration of bone marrow derived dendritic cells (BMDCs) derived from C57BL/6 mice after treatments with or without MSA-2 or IPI-549. (**f, g**) Quantification of human Interferon-β concentration from THP-1 R232 hSTING$^{R232}$ after treatments with or without MSA-2 or IPI-549. (**g**) Quantification of STING activation by reporter assay from THP1-Blue$^{TM}$ ISG by measuring optical density at 655 nm after treatments with or without MSA-2 or IPI-549. (**h**) Quantification of human Interferon-β concentration from THP-1 hSTING$^{KO}$ after treatments with or without MSA-2 or IPI-549. (**i, j**) Quantification of CD86 geometric mean fluorescent intensity of bone marrow derived dendritic cells (BMDCs) bone marrow derived macrophages (BMDMs) derived from C57BL/6 mice after treatments with or without MSA-2 or IPI-549. (**k**) Quantification of RAW264.7 M1 polarization ratios after treatments with or without MSA-2 or IPI-549. (**l**) Quantification of TNF-α concentration from RAW264.7 after treatments with or without MSA-2 or IPI-549. Data for quantification are shown as mean ± SD, n = 3. Statistical comparisons are based on one-way ANOVA, followed by post hoc Tukey's pairwise comparisons or by Student's unpaired T-test. The asterisks denote statistical significance at the level of **** $p < 0.0001$. ANOVA, analysis of variance; SD, standard deviation; n.s., no statistical significance. For (**d**) statistical comparisons are conducted between MSA-2 group with other groups. For (**e-l**), statistical comparisons are conducted between MSA-2 and MSA-2+IPI-549 groups with control group.

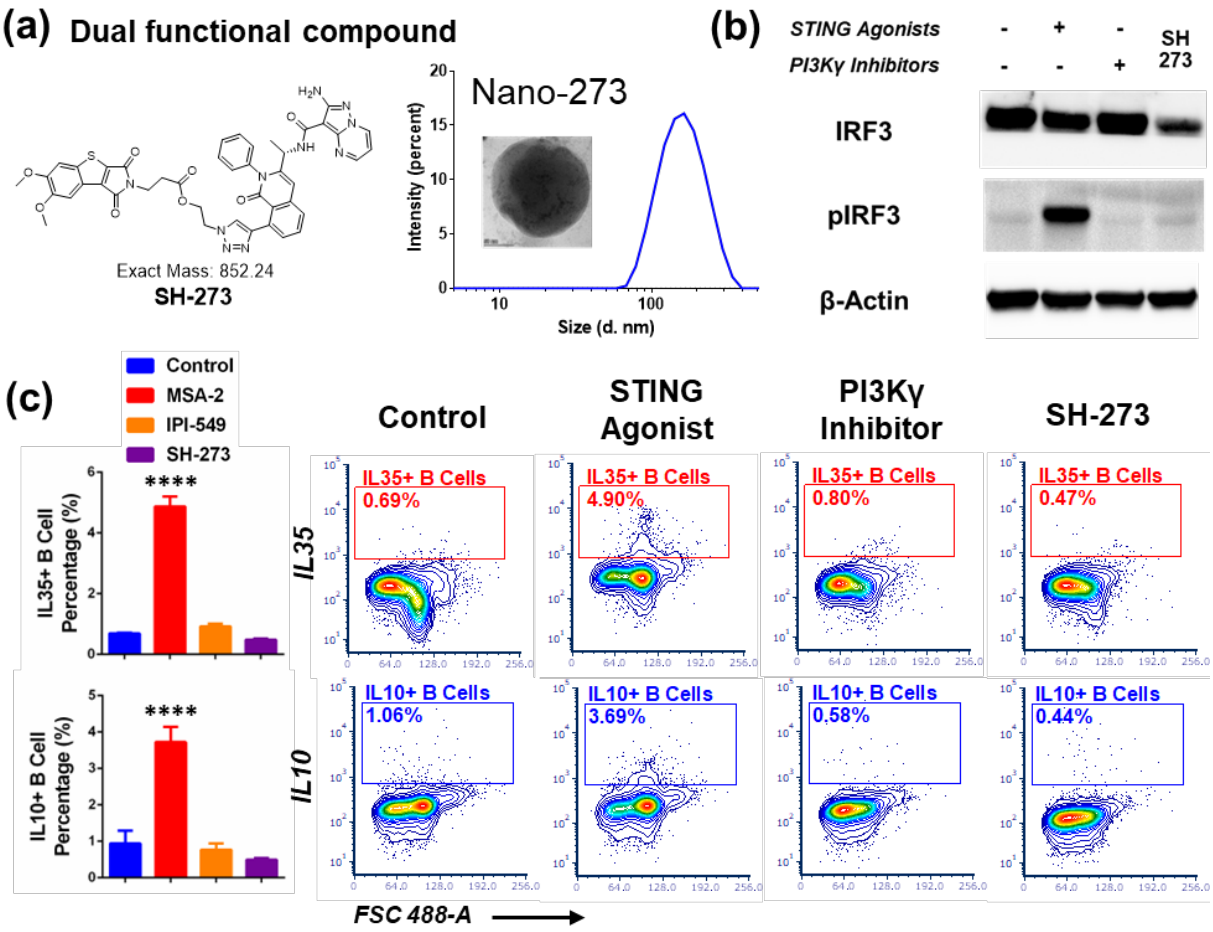


**Figure 4.3. Dual functional compound SH-273 and its albumin nanoformulation eliminate Breg cells through abolishing STING-induced IRF3 phosphorylation.** (**a**) Molecular structure of dual functional compound SH-273. Dynamic Light Scattering (DLS) size distribution of SH-273 albumin nano formulation (Nano-273). Insert image is Transmission electron microscopy (TEM) imaging of Nano-273. (**b**) Phosphorylation of IRF3 at splenic B cells derived from KPC PDAC mice after treatments with MSA-2, IPI-549 or SH-273, respectively. (**c**) Quantification and representative flow cytometry analysis of $IL35^{+}$ and $IL10^{+}$ Breg cells (from KPC spleen) after treatments with MSA-2, IPI-549 or SH-273, respectively. Data for quantification are shown as mean ± SD, n = 3. Statistical comparisons are based on one-way ANOVA, followed by post hoc Tukey's pairwise comparisons or by Student's unpaired T-test. The asterisks denote statistical significance at the level of **** $p < 0.0001$. ANOVA, analysis of variance; SD, standard deviation. For (**c**) statistical comparisons are conducted between MSA-2 group with other groups.

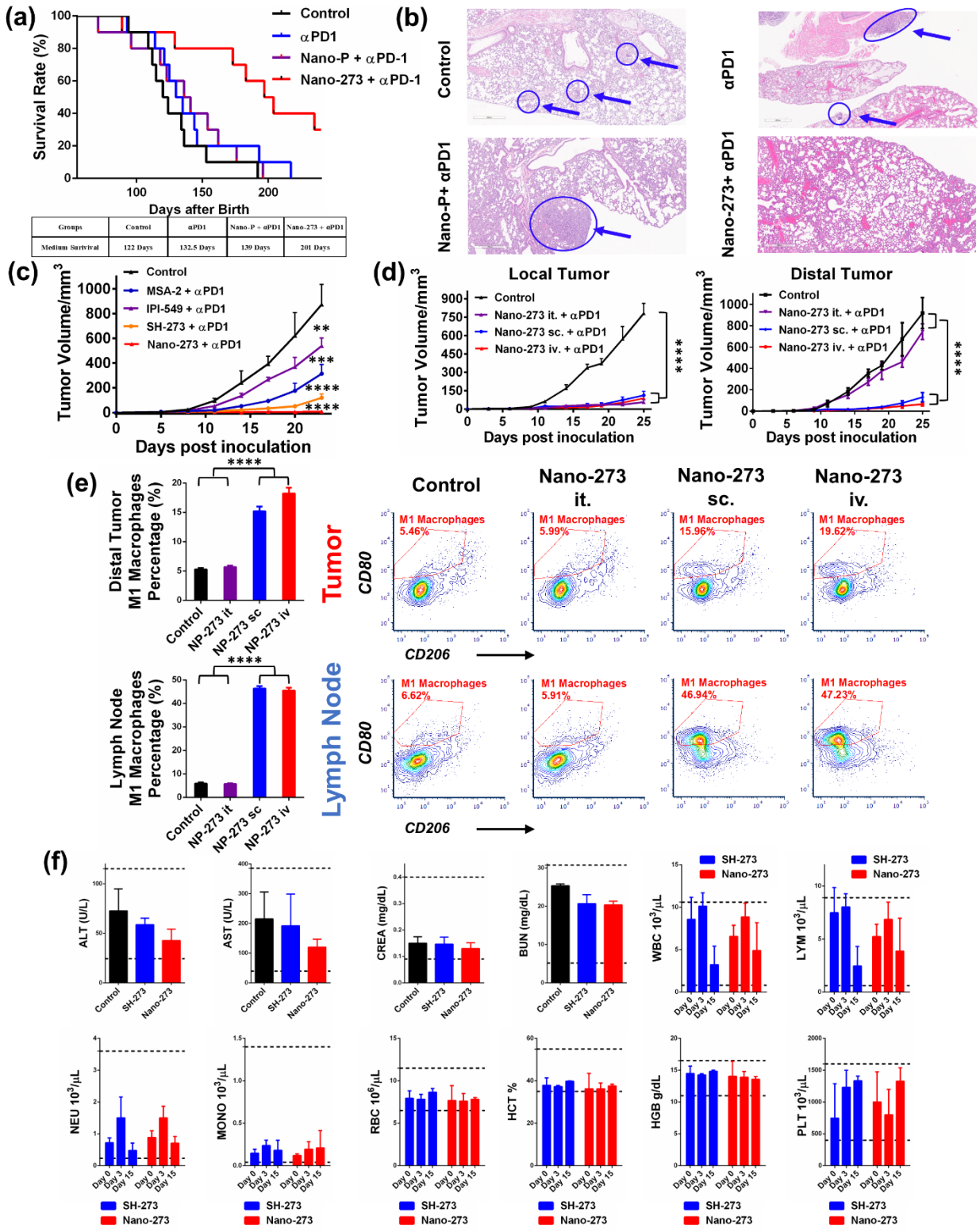


**Figure 4.4. Nano-273 extended median survival to 200 days in KPC PDAC mice via activating systemic immunity without exhibiting toxicity.** (**a**) Antitumor efficacy in transgenic KPC (LSL-KrasG12D, LSL-Trp53R172H/+, Pdx1cre/+) PDAC mice with

different treatments. Survival rate of KPC mice after treatment with PBS (control), anti-PD-1 antibody (100 μg), Paclitaxel in albumin nano formulation (intravenous injection, 11.7 μmol/kg) plus anti-PD-1 antibody (100 μg) and Nano-273 (i.v. 17.6 μmol/kg) plus anti-PD-1 antibody (100 μg). n = 10 for each group. (**b**) Pathological staining of lung tissues from (**a**) to evaluate pancreatic cancer metastasis or invasion. Blue arrows and circles indicated metastasis or invasion foci. (**c**) Antitumor efficacy in C57BL/6 mice inoculated with KPC 6422 tumor after different treatments. Average tumor volume after treatment with PBS (control), MSA-2 (i.v. 34.0 μmol/kg) plus anti-PD-1 antibody (100 μg), IPI-549 (i.v. 18.9 μmol/kg) plus anti-PD-1 antibody (100 μg), SH-273 (i.v. 17.6 μmol/kg) plus anti-PD-1 antibody (100 μg) and Nano-273 (i.v. 17.6 μmol/kg) plus anti-PD-1 antibody (100 μg). The data represents the mean ± SD; n = 5. (**d**) Antitumor efficacy in C57BL/6 mice inoculated with KPC 6422 tumor with Nano-273 treatment in different administration routes. Average tumor volume of KPC pancreatic cancer mice after treatment with PBS (control) and Nano-273 (17.6 μmol/kg) after intratumorally (i.t), subcutaneous (s.c.) and intravenous (i.v.) injection, respectively plus anti-PD-1 antibody (100 μg). Local tumor is referred to the tumor with intra-tumor injection or near s.c. injection site. Distal tumor is referred to no intra-tumor injection or far from s.c. injection site. The data represents the mean ± SD; n = 5. (**e**) Quantification and representative flow cytometry analysis of M1 macrophage ratios at distal tumor and lymph node after treatments from (**c**). The data represents the mean ± SD; n = 3. (**f**) Liver enzymes, kidney function, and blood cell counts in CD1 mice after treatments with SH-273 and Nano-273 every 3 days for 5 doses (17.6 μmol/kg) through intravenous injection. The data represents the mean ± SD; n = 3. Statistical comparisons are based on one-way ANOVA, followed by post hoc Tukey's pairwise comparisons or by Student's unpaired T-test. The asterisks denote statistical significance at the level of * $p < 0.05$, ** $p < 0.01$, *** $p < 0.001$, **** $p < 0.0001$. ANOVA, analysis of variance; SD, standard deviation. For (**c**) statistical comparisons are conducted between treatment groups with control. Statistical comparisons in (**f**) showed no statistical significance.

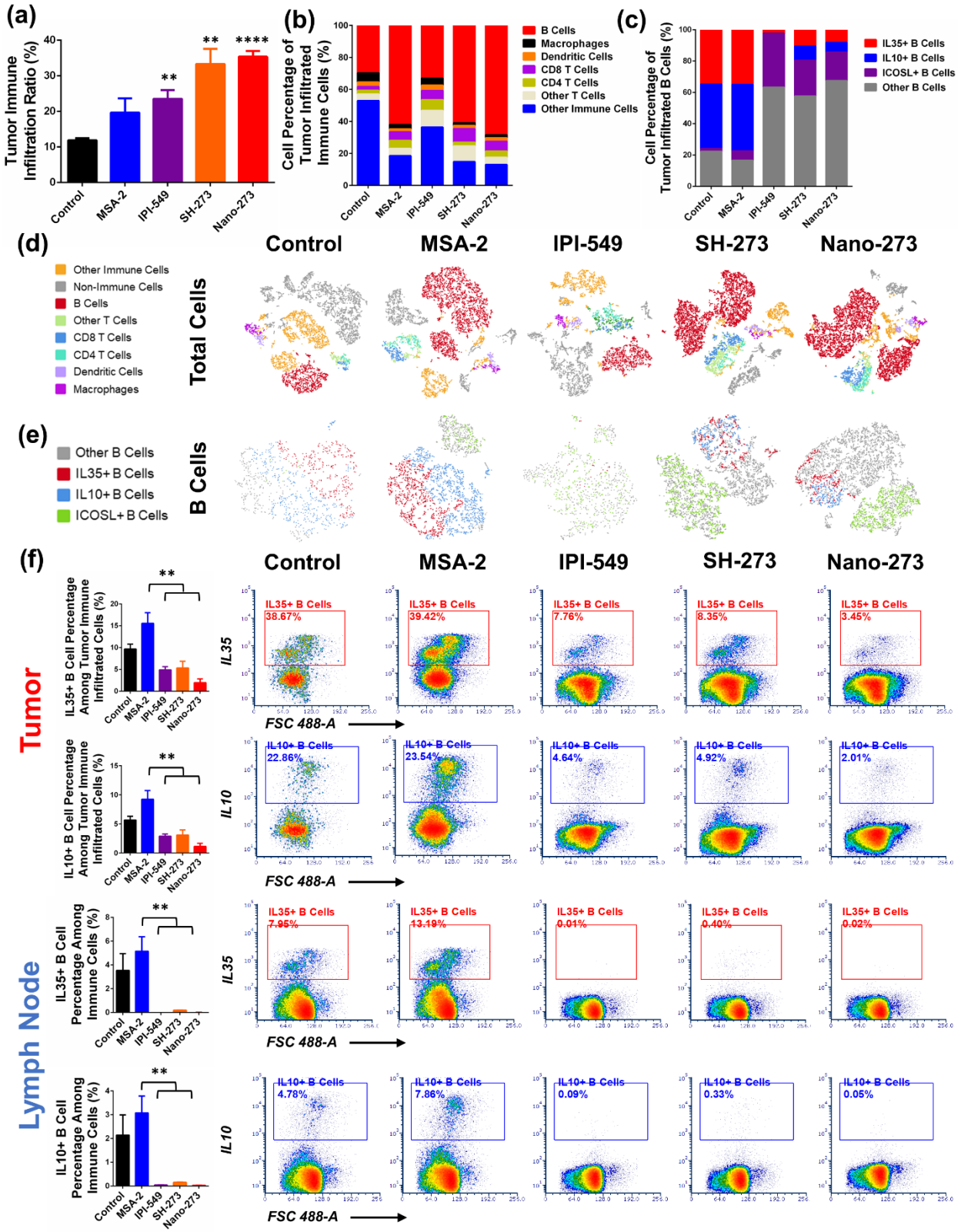


**Figure 4.5. Nano-273 eliminated STING-induced Breg cells expansion and remodeled the immune microenvironment in tumor and lymph nodes for systemic**

**anticancer immunity.** (**a**) Quantification of tumor immune infiltration by flow cytometry from the residual tumors of the mice at 10 days after final dose in **Figure 4c.** (**b**) Different immune cell populations among tumor infiltrating immune cells by single cell RNA-seq analysis from anti-tumor efficacy study in mice at 9 days after final dose in **Figure 4c**. (**c**) Percentage of different subpopulations of B cells among total B cells by single cell RNA-seq analysis. (**d, e**) t-distributed Stochastic Neighbor Embedding (t-SNE) plots of tumor-infiltrating immune cells and B cells by single cell RNA-seq analysis from mice in anti-tumor efficacy study at **Figure 4c**. (**f**) Quantification and representative flow cytometry analysis of $IL35^+$ and $IL10^+$ Breg cells at tumor and lymph node in mice from anti-tumor efficacy study at **Figure 4c**. Statistical comparisons are based on one-way ANOVA, followed by post hoc Tukey's pairwise comparisons or by Student's unpaired T-test. The asterisks denote statistical significance at the level of ** $p < 0.01$, **** $p < 0.0001$. ANOVA, analysis of variance; SD, standard deviation. For (**a**) statistical comparisons are conducted between treatment groups with control.

### 4.7 Bibliography


1 Siegel, R. L., Miller, K. D. & Jemal, A. Cancer statistics, 2020. *CA Cancer J Clin* **70**, 7-30, doi:10.3322/caac.21590 (2020).

2 Conroy, T. *et al.* FOLFIRINOX versus gemcitabine for metastatic pancreatic cancer. *N Engl J Med* **364**, 1817-1825, doi:10.1056/NEJMoa1011923 (2011).

3 Von Hoff, D. D. *et al.* Gemcitabine plus nab-paclitaxel is an active regimen in patients with advanced pancreatic cancer: a phase I/II trial. *J Clin Oncol* **29**, 4548-4554, doi:10.1200/JCO.2011.36.5742 (2011).

4 Bear, A. S., Vonderheide, R. H. & O'Hara, M. H. Challenges and Opportunities for Pancreatic Cancer Immunotherapy. *Cancer Cell* **38**, 788-802, doi:10.1016/j.ccell.2020.08.004 (2020).

5 Macherla, S. *et al.* Emerging Role of Immune Checkpoint Blockade in Pancreatic Cancer. *Int J Mol Sci* **19**, 3505, doi:10.3390/ijms19113505 (2018).

6 Leinwand, J. & Miller, G. Regulation and modulation of antitumor immunity in pancreatic cancer. *Nature Immunology* **21**, 1152-1159, doi:10.1038/s41590-020-0761-y (2020).

7 Ho, W. J., Jaffee, E. M. & Zheng, L. The tumour microenvironment in pancreatic cancer — clinical challenges and opportunities. *Nature Reviews Clinical Oncology* **17**, 527-540, doi:10.1038/s41571-020-0363-5 (2020).

8 Mirlekar, B. *et al.* Balance between immunoregulatory B cells and plasma cells drives pancreatic tumor immunity. *Cell Rep Med* **3**, 100744, doi:10.1016/j.xcrm.2022.100744 (2022).

9 Senturk, Z. N., Akdag, I., Deniz, B. & Sayi-Yazgan, A. Pancreatic cancer: Emerging field of regulatory B-cell-targeted immunotherapies. *Front Immunol* **14**, 1152551, doi:10.3389/fimmu.2023.1152551 (2023).

10 Tong, D.-N. *et al.* Characterization of B cell-mediated PD-1/PD-L1 interaction in pancreatic cancer patients. *Clinical and Experimental Pharmacology and Physiology* **47**, 1342-1349, doi:https://doi.org/10.1111/1440-1681.13317 (2020).

11 Li, S. *et al.* STING-induced regulatory B cells compromise NK function in cancer immunity. *Nature* **610**, 373-380, doi:10.1038/s41586-022-05254-3 (2022).

12 Balachandran, V. P., Beatty, G. L. & Dougan, S. K. Broadening the Impact of Immunotherapy to Pancreatic Cancer: Challenges and Opportunities. *Gastroenterology* **156**, 2056-2072, doi:https://doi.org/10.1053/j.gastro.2018.12.038 (2019).
13 Chamma, H., Vila, I. K., Taffoni, C., Turtoi, A. & Laguette, N. Activation of STING in the pancreatic tumor microenvironment: A novel therapeutic opportunity. *Cancer Letters* **538**, 215694, doi:https://doi.org/10.1016/j.canlet.2022.215694 (2022).
14 Le Naour, J., Zitvogel, L., Galluzzi, L., Vacchelli, E. & Kroemer, G. Trial watch: STING agonists in cancer therapy. *OncoImmunology* **9**, 1777624, doi:10.1080/2162402X.2020.1777624 (2020).
15 Wang, Y., Geller, A. E. & Yan, J. Unexpected Breg-NK crosstalk in STING agonist therapy. *Cellular & Molecular Immunology* **19**, 1330-1332, doi:10.1038/s41423-022-00952-4 (2022).
16 Vanpouille-Box, C., Hoffmann, J. A. & Galluzzi, L. Pharmacological modulation of nucleic acid sensors — therapeutic potential and persisting obstacles. *Nature Reviews Drug Discovery* **18**, 845-867, doi:10.1038/s41573-019-0043-2 (2019).
17 Jneid, B. *et al.* Selective STING stimulation in dendritic cells primes antitumor T cell responses. *Science Immunology* **8**, eabn6612 (2023).
18 Sun, X., Zhou, X., Lei, Y. L. & Moon, J. J. Unlocking the promise of systemic STING agonist for cancer immunotherapy. *Journal of Controlled Release* **357**, 417-421, doi:https://doi.org/10.1016/j.jconrel.2023.03.047 (2023).
19 Brinkmann, V. *et al.* Fingolimod (FTY720): discovery and development of an oral drug to treat multiple sclerosis. *Nature reviews. Drug discovery* **9**, 883-897, doi:10.1038/nrd3248 (2010).
20 Lu, Y. *et al.* Complement Signals Determine Opposite Effects of B Cells in Chemotherapy-Induced Immunity. *Cell* **180**, 1081-1097.e1024, doi:10.1016/j.cell.2020.02.015 (2020).
21 Sun, L., Wu, J., Du, F., Chen, X. & Chen, Z. J. Cyclic GMP-AMP Synthase Is a Cytosolic DNA Sensor That Activates the Type I Interferon Pathway. *Science* **339**, 786-791, doi:doi:10.1126/science.1232458 (2013).
22 Ishikawa, H., Ma, Z. & Barber, G. N. STING regulates intracellular DNA-mediated, type I interferon-dependent innate immunity. *Nature* **461**, 788-792, doi:10.1038/nature08476 (2009).
23 Barber, G. N. STING: infection, inflammation and cancer. *Nature Reviews Immunology* **15**, 760-770, doi:10.1038/nri3921 (2015).
24 Hopfner, K.-P. & Hornung, V. Molecular mechanisms and cellular functions of cGAS–STING signalling. *Nature Reviews Molecular Cell Biology* **21**, 501-521, doi:10.1038/s41580-020-0244-x (2020).
25 Pan, B.-S. *et al.* An orally available non-nucleotide STING agonist with antitumor activity. *Science* **369**, eaba6098, doi:doi:10.1126/science.aba6098 (2020).
26 DeNardo, D. G., Andreu, P. & Coussens, L. M. Interactions between lymphocytes and myeloid cells regulate pro-versus anti-tumor immunity. *Cancer and Metastasis Reviews* **29**, 309-316 (2010).
27 Xiong, J., Wang, H. & Wang, Q. Suppressive myeloid cells shape the tumor immune microenvironment. *Advanced Biology* **5**, 1900311 (2021).
28 Mantovani, A., Allavena, P., Marchesi, F. & Garlanda, C. Macrophages as tools and targets in cancer therapy. *Nature Reviews Drug Discovery* **21**, 799-820 (2022).
29 Kaneda, M. M. *et al.* PI3Kγ is a molecular switch that controls immune suppression. *Nature* **539**, 437-442, doi:10.1038/nature19834 (2016).
30 De Henau, O. *et al.* Overcoming resistance to checkpoint blockade therapy by targeting PI3Kγ in myeloid cells. *Nature* **539**, 443-447, doi:10.1038/nature20554 (2016).

31 Werner, M., Hobeika, E. & Jumaa, H. Role of PI3K in the generation and survival of B cells. *Immunol Rev* **237**, 55-71, doi:10.1111/j.1600-065X.2010.00934.x (2010).
32 Olayinka-Adefemi, F., Hou, S. & Marshall, A. J. Dual inhibition of phosphoinositide 3-kinases delta and gamma reduces chronic B cell activation and autoantibody production in a mouse model of lupus. *Front Immunol* **14**, 1115244, doi:10.3389/fimmu.2023.1115244 (2023).
33 Lucas, C. L., Chandra, A., Nejentsev, S., Condliffe, A. M. & Okkenhaug, K. PI3Kδ and primary immunodeficiencies. *Nature Reviews Immunology* **16**, 702-714, doi:10.1038/nri.2016.93 (2016).
34 Beer-Hammer, S. *et al.* The catalytic PI3K isoforms p110γ and p110δ contribute to B cell development and maintenance, transformation, and proliferation. *Journal of Leukocyte Biology* **87**, 1083-1095, doi:10.1189/jlb.0809585 (2010).
35 Lanahan, S. M., Wymann, M. P. & Lucas, C. L. The role of PI3Kgamma in the immune system: new insights and translational implications. *Nat Rev Immunol* **22**, 687-700, doi:10.1038/s41577-022-00701-8 (2022).
36 Chin, E. N. *et al.* Antitumor activity of a systemic STING-activating non-nucleotide cGAMP mimetic. *Science* **369**, 993-999, doi:doi:10.1126/science.abb4255 (2020).
37 Guo, J. & Huang, L. Nanodelivery of cGAS-STING activators for tumor immunotherapy. *Trends in Pharmacological Sciences* (2022).
38 Spada, A., Emami, J., Tuszynski, J. A. & Lavasanifar, A. The Uniqueness of Albumin as a Carrier in Nanodrug Delivery. *Molecular Pharmaceutics* **18**, 1862-1894, doi:10.1021/acs.molpharmaceut.1c00046 (2021).
39 Lee, J. W., Komar, C. A., Bengsch, F., Graham, K. & Beatty, G. L. Genetically Engineered Mouse Models of Pancreatic Cancer: The KPC Model (LSL-Kras(G12D/+) ;LSL-Trp53(R172H/+) ;Pdx-1-Cre), Its Variants, and Their Application in Immuno-oncology Drug Discovery. *Current protocols in pharmacology* **73**, 14.39.11-14.39.20, doi:10.1002/cpph.2 (2016).
40 Lutz, M. B. *et al.* An advanced culture method for generating large quantities of highly pure dendritic cells from mouse bone marrow. *Journal of immunological methods* **223**, 77-92, doi:10.1016/s0022-1759(98)00204-x (1999).
41 Song, Y. *et al.* Albumin nanoparticle containing a PI3Kγ inhibitor and paclitaxel in combination with α-PD1 induces tumor remission of breast cancer in mice. *Sci Transl Med* **14**, eabl3649, doi:10.1126/scitranslmed.abl3649 (2022).
42 Li, J. *et al.* Tumor Cell-Intrinsic Factors Underlie Heterogeneity of Immune Cell Infiltration and Response to Immunotherapy. *Immunity* **49**, 178-193.e177, doi:10.1016/j.immuni.2018.06.006 (2018).
43 Hong-Yi Zhao, Z. L., Shuai Mao, Meilin Wang, Miao He, Bo Wen, Wei Gao, Duxin Sun. Discovery of an oral tricyclic STING agonist with superior pharmacokinetic properties and potent in vivo efficacy. *Journal of Medicinal Chemistry* (2024).

# Chapter 5

# Conclusions

Humoral responses elicited by B cells that produce pathogen specific antibodies to provide protection against foreign infections. However, B cells are highly heterogeneous in their phenotypes and functions in immune system. The antitumor immunity by B cells goes beyond antibody related functions. In this research, we focused on two opposite aspects of B cells functions in antitumor immunity, a) antigen presenting function of B cells, which establishes collaborations with CD4 T cells to promote B/CD4 T cells crosstalk for antitumor immune responses, and b) regulatory function of B cell that mediate the immune suppression in lymph node and tumor, led to resistance to STING agonist in immunotherapy. We developed two strategies to modulate B cell immunity to enhance cancer immunotherapy. a) we engineered an antigen cluster nanocarrier (ACN) with viral mimicry antigen topography. These properties of ACN achieved optimal lymphoid delivery and B cell receptor binding/crosslinking. ACN facilitates optimal recognition, internalization and presentation of antigens by B cells to CD4 T cells. We also developed a SARS-CoV-2 B epitope-guided neoantigen cancer vaccine strategy, where a viral B epitope on ACN induced robust SARS-CoV-2 specific B cells uptake and presentation of tumor neoantigen to CD4 T cells. This vaccination strategy induced strong SARS-CoV-2 specific B cells and tumor antigen specific CD4 T cell crosstalk, germinal center B and follicular T helper cell responses and tumor specific CD4 and CD8 T cell activations. b) we developed a strategy to overcome B reg cells mediated immune suppression by dual targeting of PI3Kγ and STING. PI3Kγ inhibition in B cells during STING activation can eliminate regulatory B cells, while preserving the STING activation in myeloid cells. This novel finding provided a foundation by combining PI3Kγ inhibition with STING activation to overcome the immune suppression of regulatory B cells and myeloid cells in pancreatic cancer. Therefore, we developed a dual functional compound (SH-273) in albumin nanoformulation (Nano-273) activating STING and inhibiting PI3Kγ to eliminate regulatory B cells and stimulate myeloid cells. Nano-273 remodeled suppressive immune microenvironment in lymph node and tumor and overcame STING resistance. Combination of

Nano-273 and anti-PD-1 achieved superior efficacy to extend medium survival of 200 days in transgenic pancreatic cancer mice (KPC).

To design a vaccine nanocarrier to facilitate crosslink with B cell receptor (BCR) (chapter 2), three key features are critical. a) optimal size (less than 200 nm) helps the vaccine efficiently penetrate the lymph nodes and directly engage with B cells. b) optimal antigen density comparable to immunogenic viruses that displayed on the nanoparticle surface to induce robust B cell activation. c) repetitive antigen cluster structure with optimal distance between clusters is crucial for efficient crosslinking with the BCR, which triggers effective internalization of the antigen, decreases the threshold required to activate the BCR, and overcomes tolerance in antitumor B cell immunity. We successfully synthesized an antigen cluster nanovaccine (ACN) with 45 nm size and antigen cluster structure to display optimal density of antigens on the surface of each cluster to feature crosslink with BCR and subsequent B cell internalization. Significant BCR crosslink and B/CD4 T cell crosstalk were observed compared to other nonviral like nanocarrier in in vitro studies. Robust in vivo germinal center (GC) B cells and T follicular helper (Tfh) cells responses and remodel of tumor immune microenvironment were observed in mouse models. ACNVax combined with anti-PD-1 achieved long-term tumor remission in mouse HER2+ breast cancer model.

To efficiently promote B cell antigen presentation mediated B/CD4 T cell crosstalk (chapter 3), an optimal B cell epitope is essential. However, all current peptides/mRNA neoantigen cancer vaccines designed to activate antitumor CD4/CD8 T cell immunity through dendritic cell (DC)/macrophage mediated antigen presentation are unable to promote B/CD4 T cell collaboration. Most current neoantigen cancer vaccines only contain CD4/CD8 T cell epitopes, without B cell epitopes, could not promote B cell-mediated antigen presentation for B/CD4 T cell crosstalk. These vaccines cannot be taken up by B cells in a specific manner for antigen presentation (without B cell epitope binding to B cell receptor on B cells). Previous B cell cancer vaccines used tumor associated B cell antigen (TAA), such as HER-2, VEGF, and EGFR, but they mainly focused on activating B cells for antibody production against tumor. Antibody production alone by B cell vaccine is unlikely to achieve durable anticancer immunity since antibody treatments have only shown short-term efficacy in preclinical and clinical studies. Besides, TAA derived from intrinsic protein which expressed widely in normal tissues could induce immune tolerance that compromises B/CD4 T cell collaboration and antitumor CD8 T cell immune response. Therefore, we developed SARS-CoV-2 epitope-guided neoantigen cancer vaccine, which combined SARS-CoV-2 B epitopes with tumor CD4/CD8 T neoantigens, to promote B/CD4 T cell collaboration between SARS-CoV-2 specific B cell and tumor neoantigen specific CD4 T

cells. In vitro and in vivo studies indicated that SARS-CoV-2 B epitope efficiently promotes B/CD4 T cell crosstalk, GC B and Tfh cell responses, proliferation of antigen specific CD4/CD8 T cells and achieved superior antitumor efficacy. SARS-CoV-2 B epitope strategy was further adapted to mRNA platform where SARS-CoV-2 B epitopes were conjugated on the surface of lipid nanoparticle with mRNA neoantigen inside to activate robust B/CD4 T cell crosstalk and improve antitumor efficacy.

To overcome the immune suppression and STING resistance in lymph node and tumor at pancreatic cancer (chapter 4), optimal treatment to remove regulatory B cells (Bregs) is critical. We discovered that blocking PI3Kγ during STING activation abolished IRF3 phosphorylation in B cells, thus decreasing Bregs. Blocking PI3Kγ will maintain IRF3 phosphorylation in myeloid cells to preserve STING activation and type-I interferon expression. We developed a dual functional compound SH-273 to inhibit PI3Kγ in B cells during STING activation to eliminate Bregs induction. SH-273 sustains the STING activation in myeloid cells to secret type-I interferon and initiate antitumor immune responses. To achieve systemic immunity, we also prepared an albumin nanoformulation of SH-273 (Nano-273) to deliver compound to target tissues. Nano-273 showed preferentially deliver to lymph node and tumor compared to solvent-based compound and lower distribution in liver, which may help reduce the toxicity from systemic administration. Nano-273 eliminates Bregs in lymph and tumor in vivo, stimulates robust antitumor immune responses. Combination of Nano-273 and anti-PD-1 extended median survival to 200 days in transgenic KPC mouse model. Nano-273 provided a promising treatment for pancreatic cancer patients by eliminating Bregs and remodel immune suppression.

# Appendix A

## Supporting Information from Chapter 2

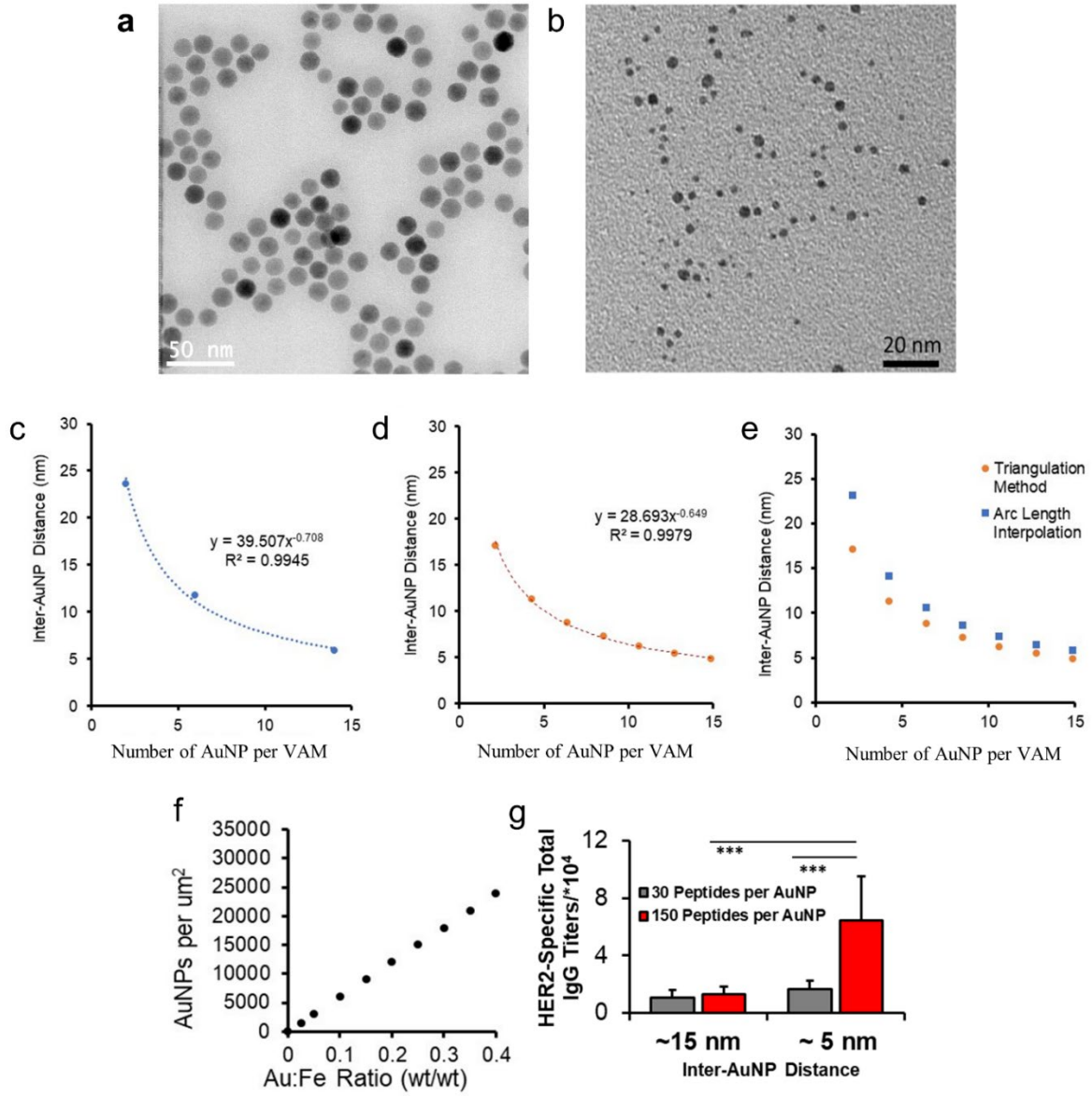


**Figure 2.S1 Characterizations of ACNVax**. (**a**) Representative scanning transmission electron microscopy (STEM) bright-field (BF) image of the core component of ACN, poly(siloxane)- and

poly (ethylene glycol)-containing di-block copolymer polymer-coated iron-oxide nanoparticle (IONP-Polymer); scale-bar: 50 nm. (**b**) Representative transmission electron microscopy (TEM) BF image of the surface component of gold nanoparticles (AuNP); scale-bar: 20 nm. (**c-e**) Modeling of inter-AuNP distance on antigen-clustered nanoparticle (ACN) surfaces. (**c**) Power function curve fit model based on the arc length between 2 (central angle: 180º), 6 (central angle: 90º) and 14 AuNPs (central angle: 45º) homogeneously distributed in 3D space around an IONP-Polymer core with 15 nm diameter. (**d**) Power function curve fit model based on the triangulation methodology described above. (**e**) Overlay comparison of both modeling strategies for inter-AuNP distance (nm). (**f**) AuNP density on ACN at different ratios between Au and Fe. (**g**) Quantification of antigen-specific IgG antibodies by ELISA after immunizations by ACNVax with different antigen cluster distances (5 or 15 nm) and different localized antigen densities (~30 and ~150 peptides/AuNPs). BALB/c mice were immunized at days 0 and 14, and antigen titers were detected at day 24; data represent the mean ± SD, n = 5. Statistical comparisons are based on one-way ANOVA, followed by post hoc Tukey's pairwise comparisons. The asterisks denote statistical significance at the level of *** $p < 0.001$. ANOVA, analysis of variance; SD, standard deviation.

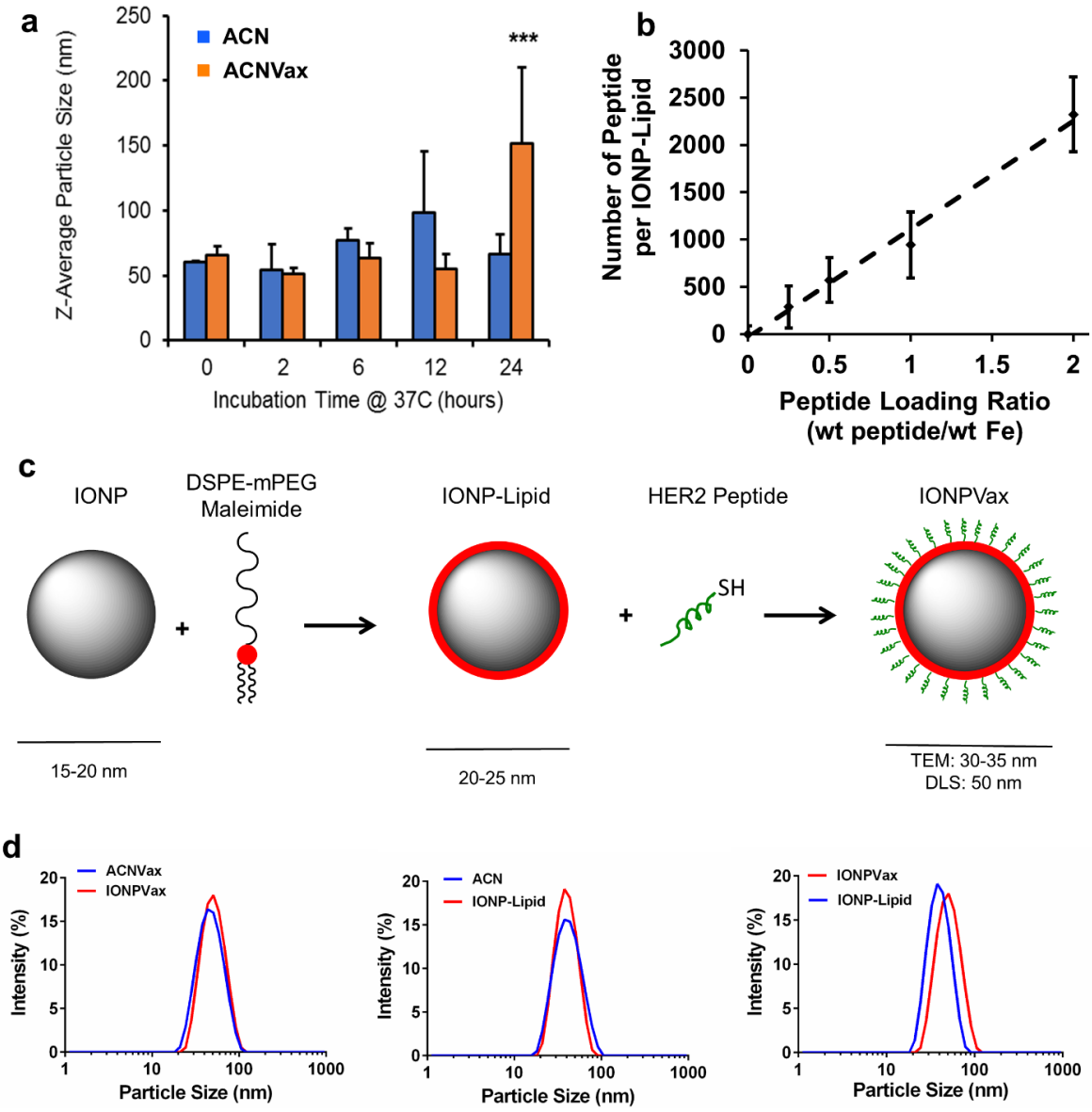


**Figure 2.S2 Characterizations of ACNVax and IONPVax.** (**a**) Serum stability study of ACN and HER2 epitope coated ACNVax in 50% FBS/PBS at 37ºC as determined by Z-average particle size (nm) as determined by dynamic light scattering; data represent mean ± SD, n = 3. (**b**) Peptide loading at the surface of IONP-Lipid at different peptide to IONP ratio. (**c**) Schematic representation of step-wise formulation of peptide functionalized lipid-coated iron-oxide nanoparticles (IONP-Lipid) by the (1) coating of iron-oxide nanoparticles with maleimide activated DSPE-mPEG phospholipids followed by the (2) conjugation of terminal cysteine-modified HER2 peptide to IONP via non-reducing thiol-directed chemistry. (**d**) Representative volume-weighted particle size distributions: ACN, lipid-coated iron-oxide nanoparticles (IONP-Lipid), ACNVax and HER2 epitope coated IONP-Lipid (IONPVax). Statistical comparisons are based on one-way ANOVA, followed by post hoc Tukey's pairwise comparisons. The asterisks denote statistical significance at the level of *** $p < 0.001$. ANOVA, analysis of variance; SD, standard deviation.

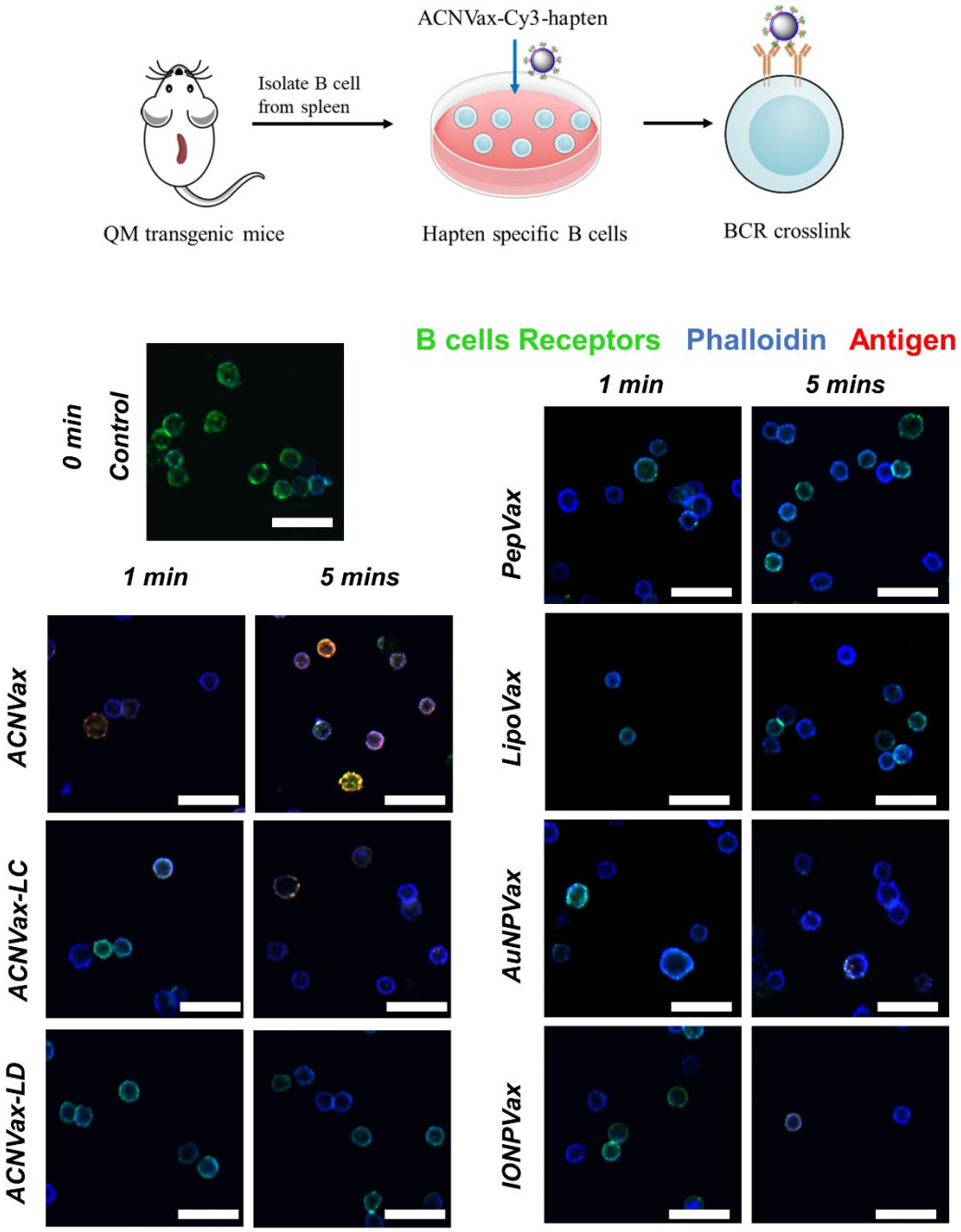


**Figure 2.S3 ACNVax crosslinked with B cell receptor.** Confocal image of Cy3 and hapten labeled ACNVax (red, 20 nM antigens) binding/crosslinking (yellow) with B cell receptor (antibody staining, green) in hapten-specific B cells from QM mice splenocytes, in comparison with other control groups (20 nM antigens): soluble Cy3 and hapten labeled B/CD4 antigen (PepVax), Cy3 and hapten labeled IONPVax, Cy3 and hapten labeled AuNPVax, Cy3 and hapten labeled lipoVax, Cy3 and hapten labeled ACNVax with longer distance (~15 nm) between clusters (ACNVax-LC) and Cy3 and hapten labeled ACNVax with low density of antigen (2% of peptide loading, ACNVax-LD). Blue, phalloidin stain of actin filaments; green, B cell receptor staining

using Alexa Fluor 488-AffiniPure Fab Fragment Goat Anti-Mouse IgM (μ Chain Specific) antibody; red: Cy3 and hapten-labeled CD4/B epitope. The scale bar is 10 μm.

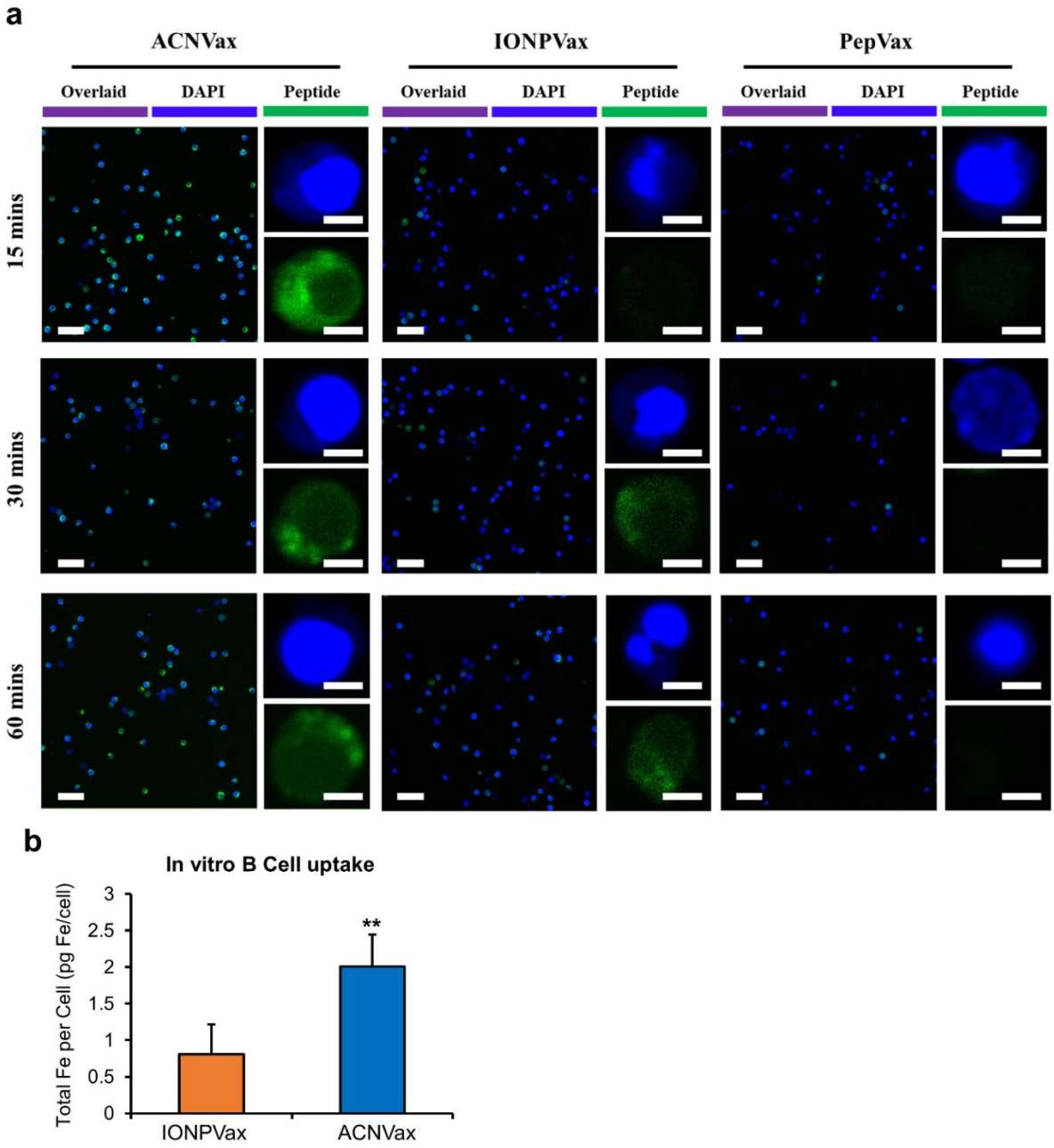


**Figure 2.S4 ACNVax enhanced antigen uptake by B cells.** (**a**) Confocal image of ACNVax, IONPVax and PepVax uptake by B cells. Peptides are labeled by EDFITC. Nuclei are stained by DAPI. Incubation time points are 15 min, 30 mins and 60 mins. Scale bar for large images is 25 nm, for zoom in images are 2.5 nm. (**b**) Quantification of in-vitro cell uptake of nanoparticles in murine primary B-cells by ICP-MS quantification of total Fe standardized by cell count (pg Fe per cell). B-cells are identified as $B220^{+}$; data represent mean ± SD, n = 3. Data for quantification are shown as mean ± SD, n = 3. Statistical comparisons are based on one-way ANOVA, followed by post hoc Tukey's pairwise comparisons or by Student's unpaired T-test. The asterisks denote

statistical significance at the level of * $p < 0.05$, ** $p < 0.01$. ANOVA, analysis of variance; SD, standard deviation.

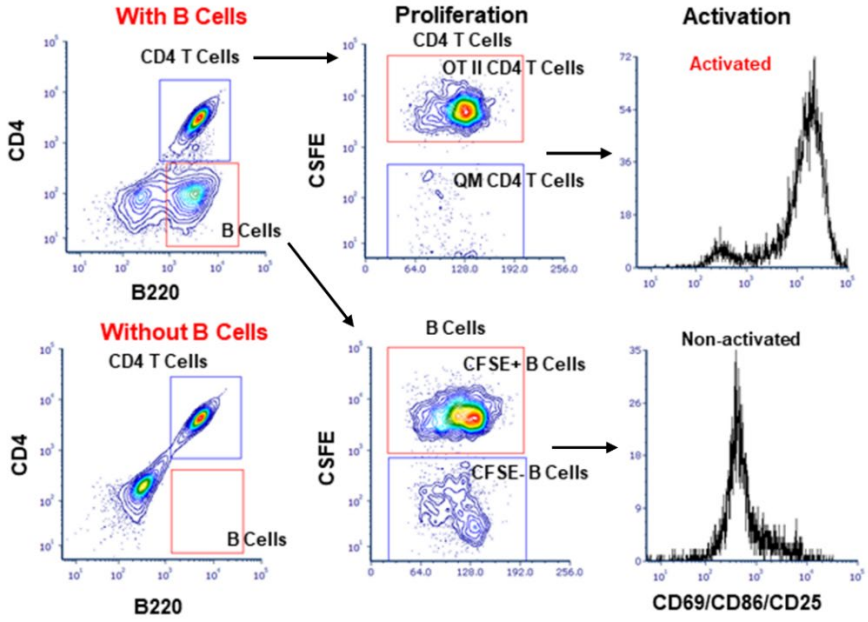


**Figure 2.S5 Gating strategy for flow cytometry analysis of B cell-antigen-presentation-mediated B/CD 4 T cell crosstalk by ACNVAX** (**Figure 2, Figure S5-S12**). All CD4 T cells from OT-II mice and part of B cells from QM mice are labeled with CFSE tracker for proliferation observations. CD69 and CD86 are used as markers for CD4 T cell activation, CD69 and CD25 are used as markers for B cell activation.

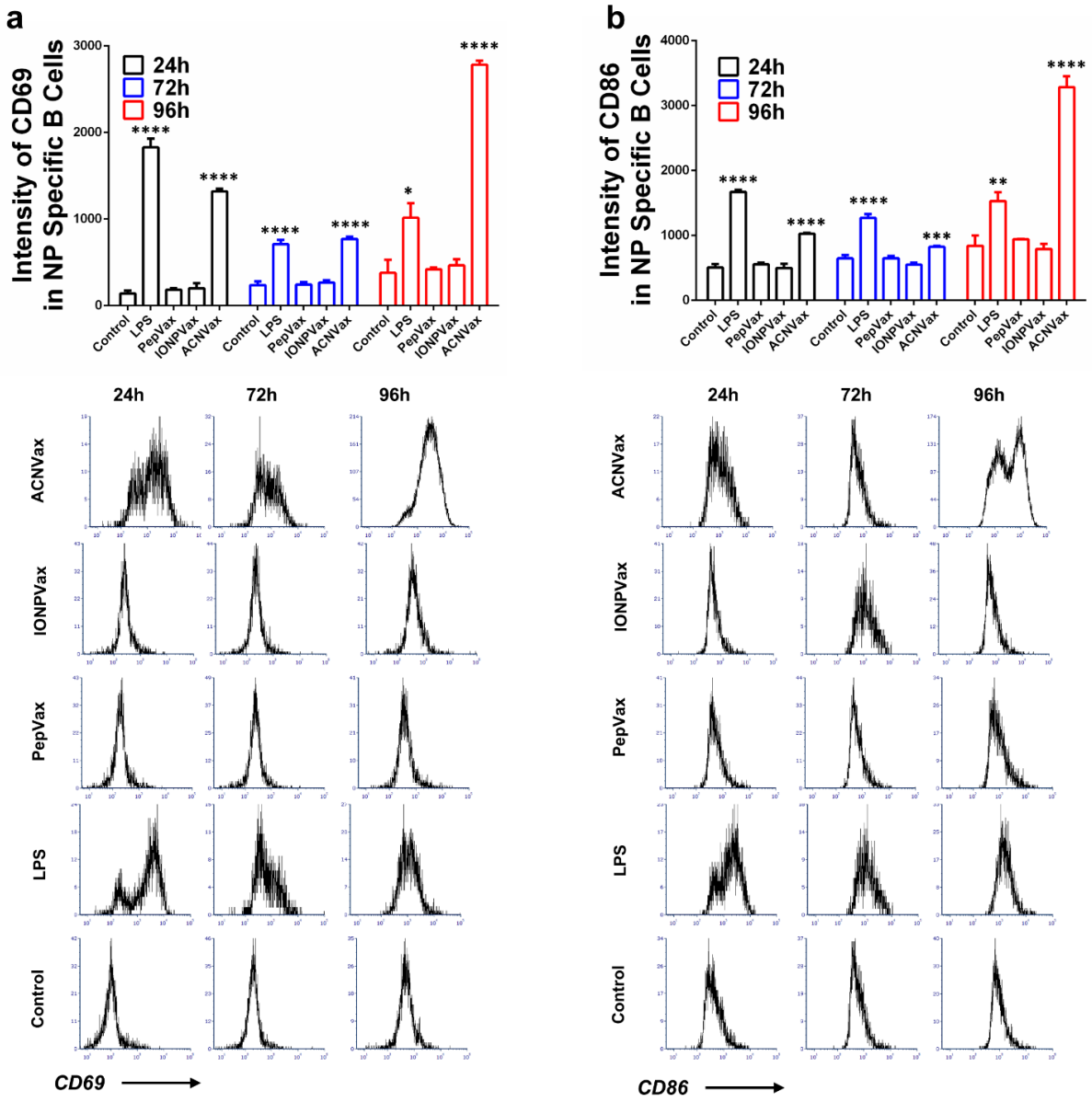


**Figure 2.S6 ACNVAX induced activation of antigen-specific B cells.** Hapten-specific B cell activations were measured from 24h to 96h by increase of intensity of CD69 (**a**) and CD86 (**b**) markers. ACN with HER2-CD4/B antigen-Hapten and OT-II CD4 epitope was incubated with splenocytes from QM mice (part of B cells labeled with CFSE), and OT-II specific CD4 T cells (labeled with CFSE) from splenocytes of OT-II transgenic mice. IONP and free antigen peptides with the same antigens as ACNVax group were used as controls. Data for quantification are shown as mean ± SD, n = 3. Statistical comparisons are based on one-way ANOVA, followed by post hoc Tukey's pairwise comparisons or by Student's unpaired T-test. The asterisks denote statistical significance at the level of * $p < 0.05$, ** $p < 0.01$, *** $p < 0.001$, **** $p < 0.0001$. ANOVA, analysis of variance; SD, standard deviation; n.s., no statistical significance.

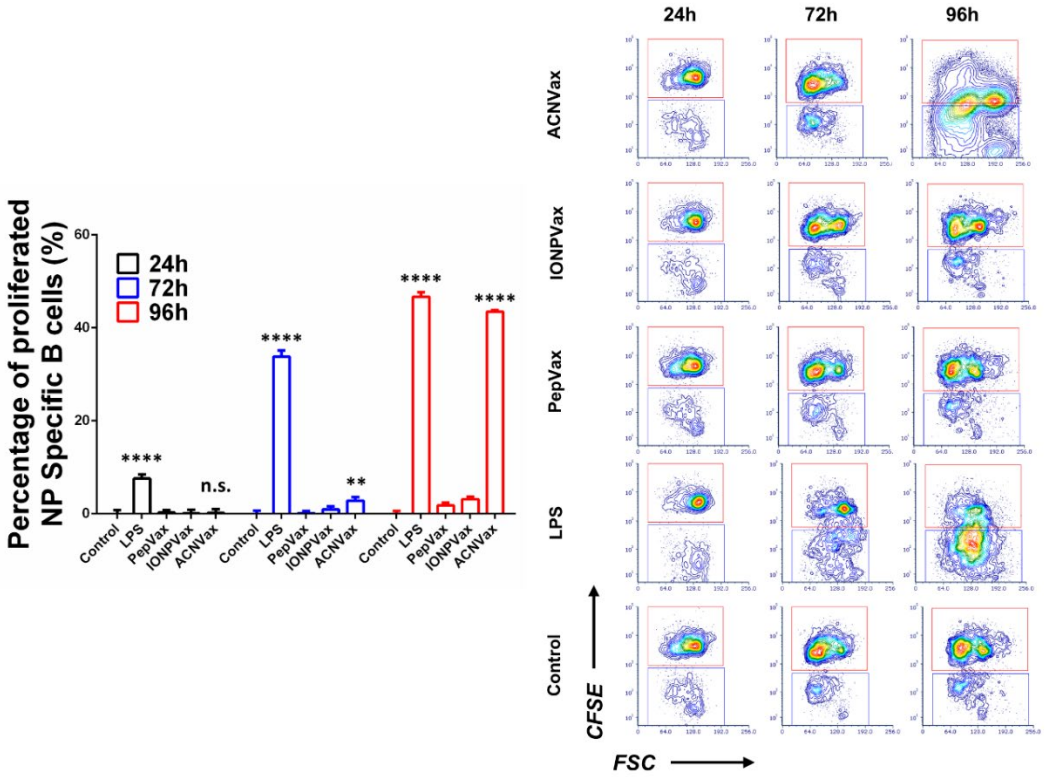


**Figure 2.S7 ACNVax induced proliferation of antigen-specific B cells.** Representative flow cytometry analysis and quantification of Hapten-specific B cell proliferation by measuring the percentage of decreased $CFSE^{+}$ QM B cells compared to control. Data for quantification are shown as mean ± SD, n = 3. Statistical comparisons are conducted among ACNVax and LPS with other groups. Statistical comparisons are based on one-way ANOVA, followed by post hoc Tukey's pairwise comparisons or by Student's unpaired T-test. The asterisks denote statistical significance at the level of * $p < 0.05$, ** $p < 0.01$, *** $p < 0.001$, **** $p < 0.0001$. ANOVA, analysis of variance; SD, standard deviation; n.s., no statistical significance.

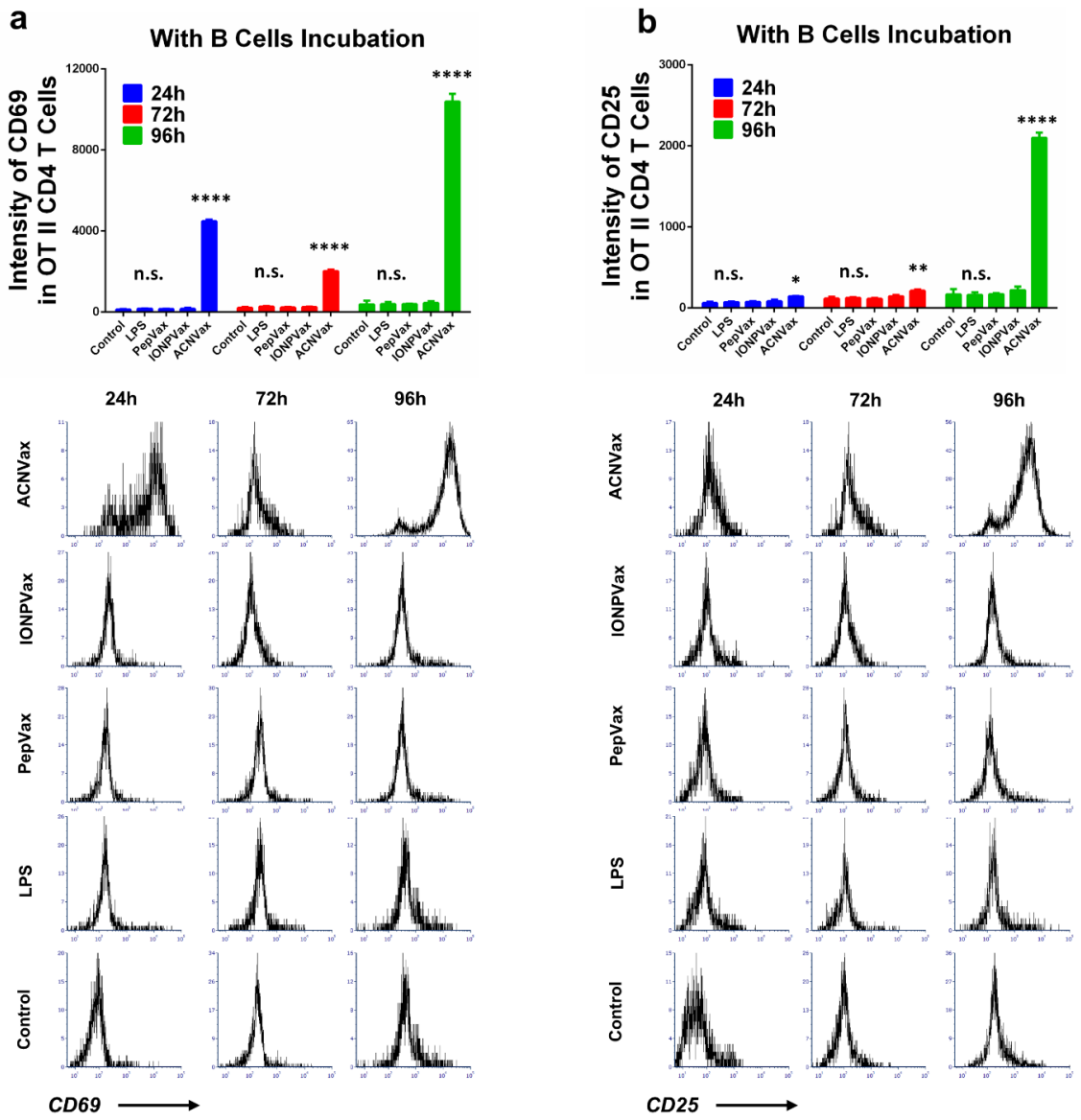


**Figure 2.S8 ACNVax induced activation of antigen-specific CD4 T cells.** Activation of CD4 T cell from OT-II mice with B cells incubation were measured from 24h to 96h after incubation by increase of intensity of CD69 (**a**) and CD25 (**b**) markers. ACN with HER2-CD4/B antigen-hapten and OT-II CD4 epitope was incubated with splenocytes from QM mice (part B cells labeled with CFSE), and OT-II specific CD4 T cells (labeled with CFSE) from splenocytes of OT-II transgenic mice. IONP and free antigen peptides with the same antigens as ACNVax group were used as controls. Data for quantification are shown as mean ± SD, n = 3. Statistical comparisons are conducted among ACNVax and LPS with other groups. Statistical comparisons are based on one-way ANOVA, followed by post hoc Tukey's pairwise comparisons or by Student's unpaired T-test. The asterisks denote statistical significance at the level of * $p < 0.05$, ** $p < 0.01$, *** $p < 0.001$, **** $p < 0.0001$. ANOVA, analysis of variance; SD, standard deviation; n.s., no statistical significance.

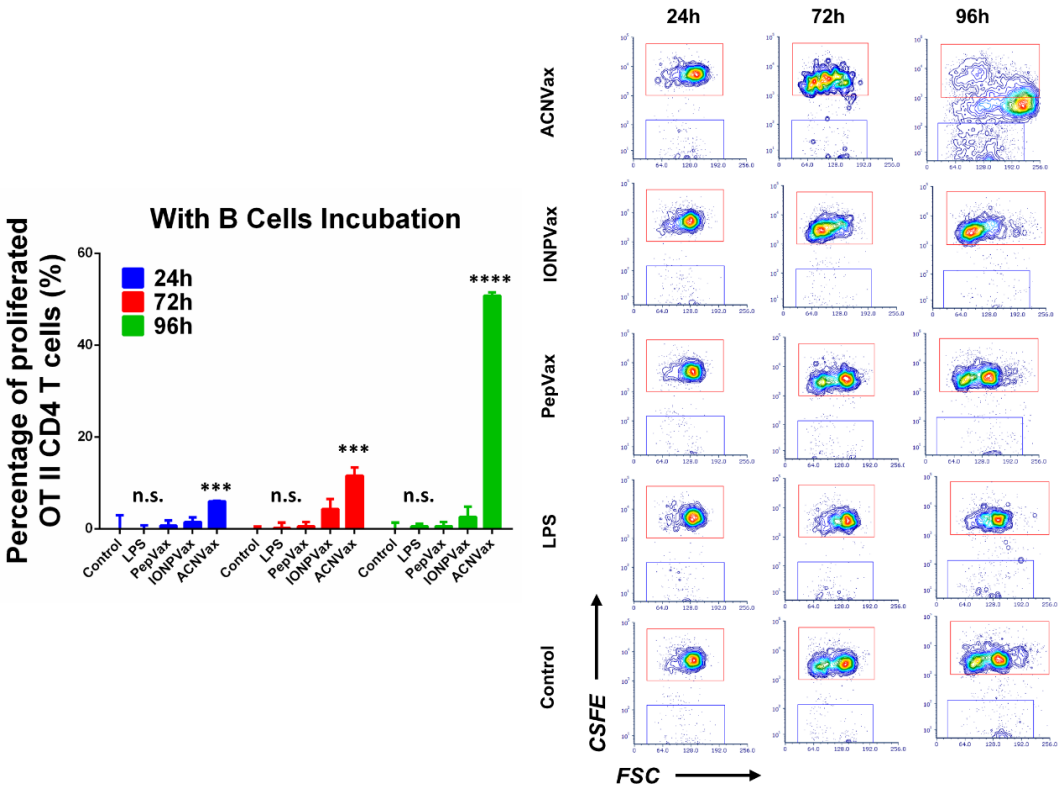


**Figure 2.S9 ACNVax induced proliferation of antigen-specific CD4 T cells.** Representative flow cytometry analysis and quantification of OT-II specific CD4 T cell proliferation with B cells incubation by measuring the percentage of decreased CFSE+ OT-II specific CD4 T cells compared to control. Data for quantification are shown as mean ± SD, n = 3. Statistical comparisons are conducted among ACNVax and LPS with other groups. Statistical comparisons are based on one-way ANOVA, followed by post hoc Tukey's pairwise comparisons or by Student's unpaired T-test. The asterisks denote statistical significance at the level of * $p < 0.05$, ** $p < 0.01$, *** $p < 0.001$, **** $p < 0.0001$. ANOVA, analysis of variance; SD, standard deviation; n.s., no statistical significance.

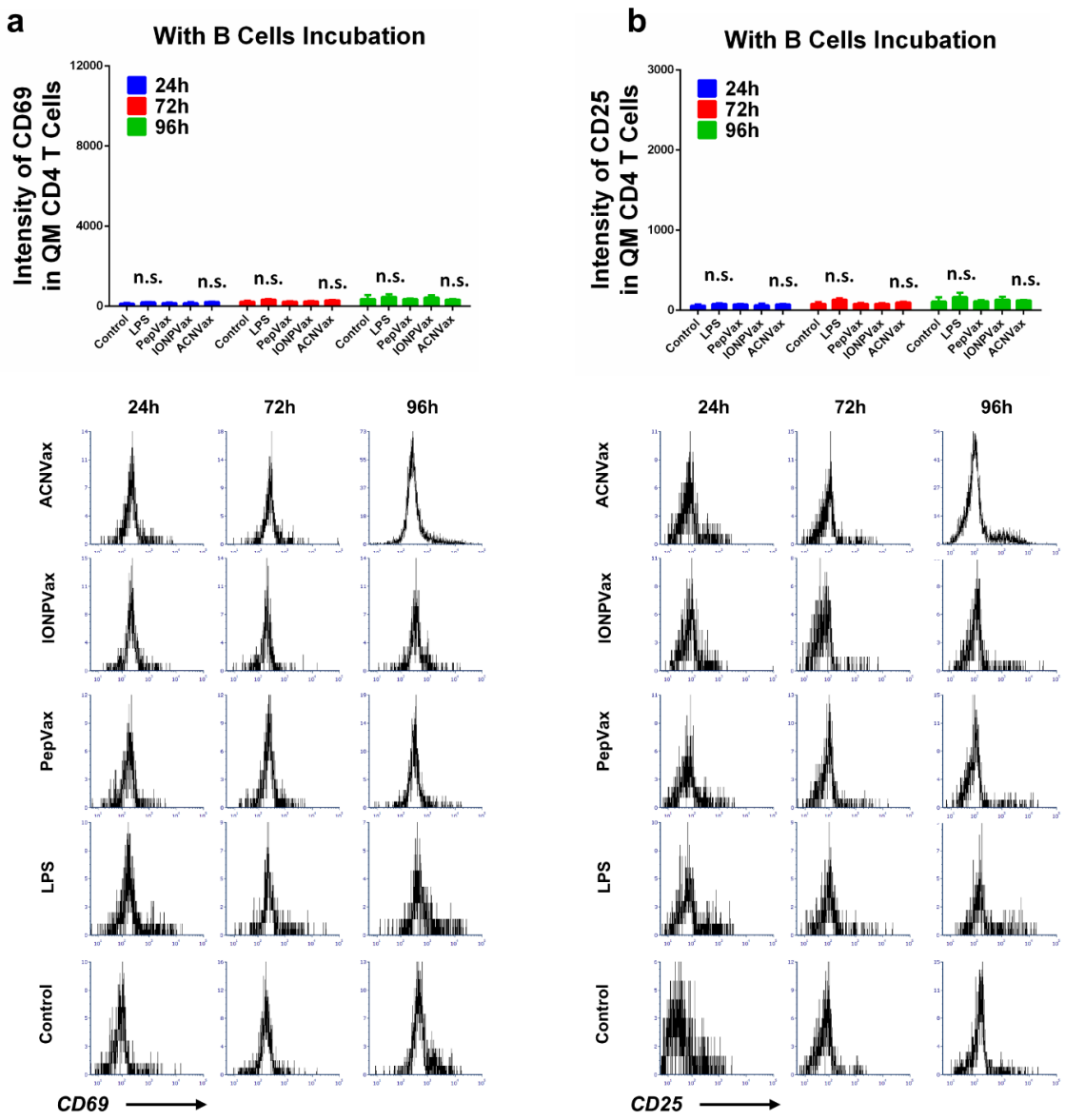


**Figure 2.S10 ACNVax did not induce activation of non-specific CD4 T cells.** Activation of CD4 T cell from QM mice with B cells incubation were measured from 24h to 96h after incubation by increase of intensity of CD69 (**a**) and CD25 (**b**) markers. ACN with HER2-CD4/B antigen-hapten and OT-II CD4 epitope was incubated with splenocytes from QM mice (part B cells labeled with CFSE), and OT-II specific CD4 T cells (labeled with CFSE) from splenocytes of OT-II transgenic mice. IONP and free antigen peptides with the same antigens as ACNVax group were used as controls. Data for quantification are shown as mean ± SD, n = 3. Statistical comparisons are conducted among ACNVax and LPS with other groups. Statistical comparisons are based on one-way ANOVA, followed by post hoc Tukey's pairwise comparisons or by Student's unpaired T-test. ANOVA, analysis of variance; SD, standard deviation; n.s., no statistical significance.

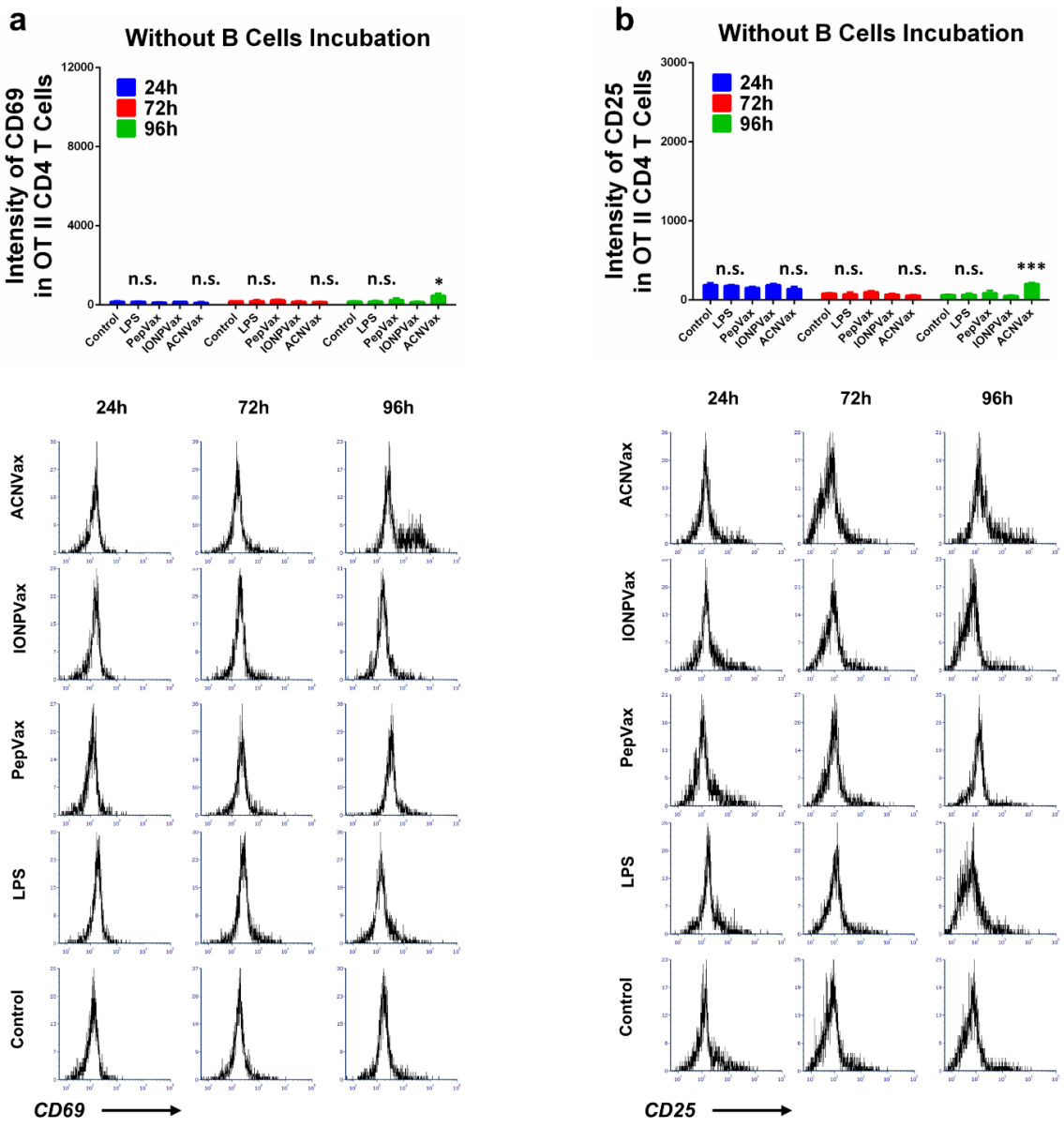


**Figure 2.S11 ACNVax did not induce activation of antigen-specific CD4 T cells after B cell depletion.** Activation of CD4 T cell from OT-II mice without B cells incubation were measured from 24h to 96h after incubation by increase of intensity of CD69 (**a**) and CD25 (**b**) markers. (**c**) Proliferation of CD4 T cell from OT-II mice without B cells were measured from 24h to 96h by CFSE marker. ACN with HER2-CD4/B antigen-Hapten and OT-II CD4 epitope was incubated with splenocytes from QM mice (B cell depleted through CD19 positive selection kit), and OT-II specific CD4 T cells (labeled with CFSE) from splenocytes of OT-II transgenic mice. IONP and free antigen peptides with the same antigens as ACNVax group were used as controls. Data for quantification are shown as mean ± SD, n = 3. Statistical comparisons are conducted among ACNVax and LPS with other groups. Statistical comparisons are based on one-way ANOVA, followed by post hoc Tukey's pairwise comparisons or by Student's unpaired T-test. The asterisks

denote statistical significance at the level of * $p < 0.05$, ** $p < 0.01$, *** $p < 0.001$. ANOVA, analysis of variance; SD, standard deviation; n.s., no statistical significance.

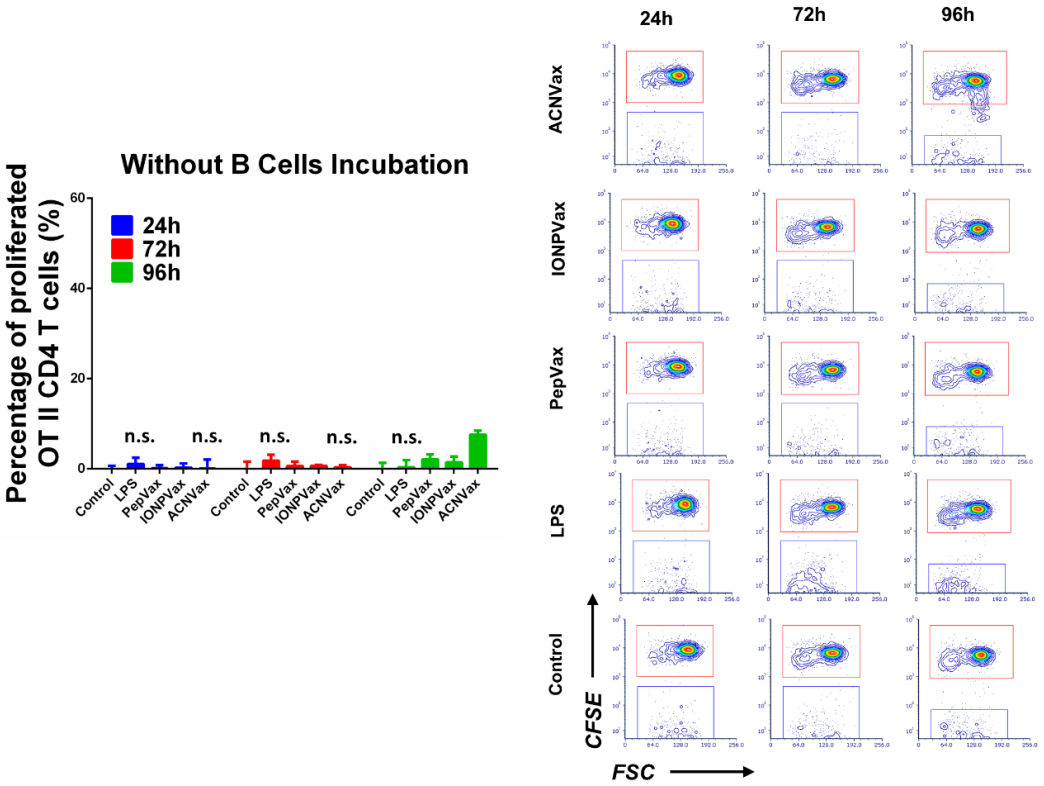


**Figure 2.S12 ACNVax did not induce proliferation of non-specific CD4 T cells after B cell depletion.** Representative flow cytometry analysis and quantification of OT-II CD4 T cell proliferation without B cells incubation by measuring the percentage of decreased CFSE+ OT II CD4 T cells compared to control. Data for quantification are shown as mean ± SD, n = 3. Statistical comparisons are conducted among ACNVax and LPS with other groups. Statistical comparisons are based on one-way ANOVA, followed by post hoc Tukey's pairwise comparisons or by Student's unpaired T-test. The asterisks denote statistical significance at the level of * $p < 0.05$, ** $p < 0.01$. ANOVA, analysis of variance; SD, standard deviation; n.s., no statistical significance.

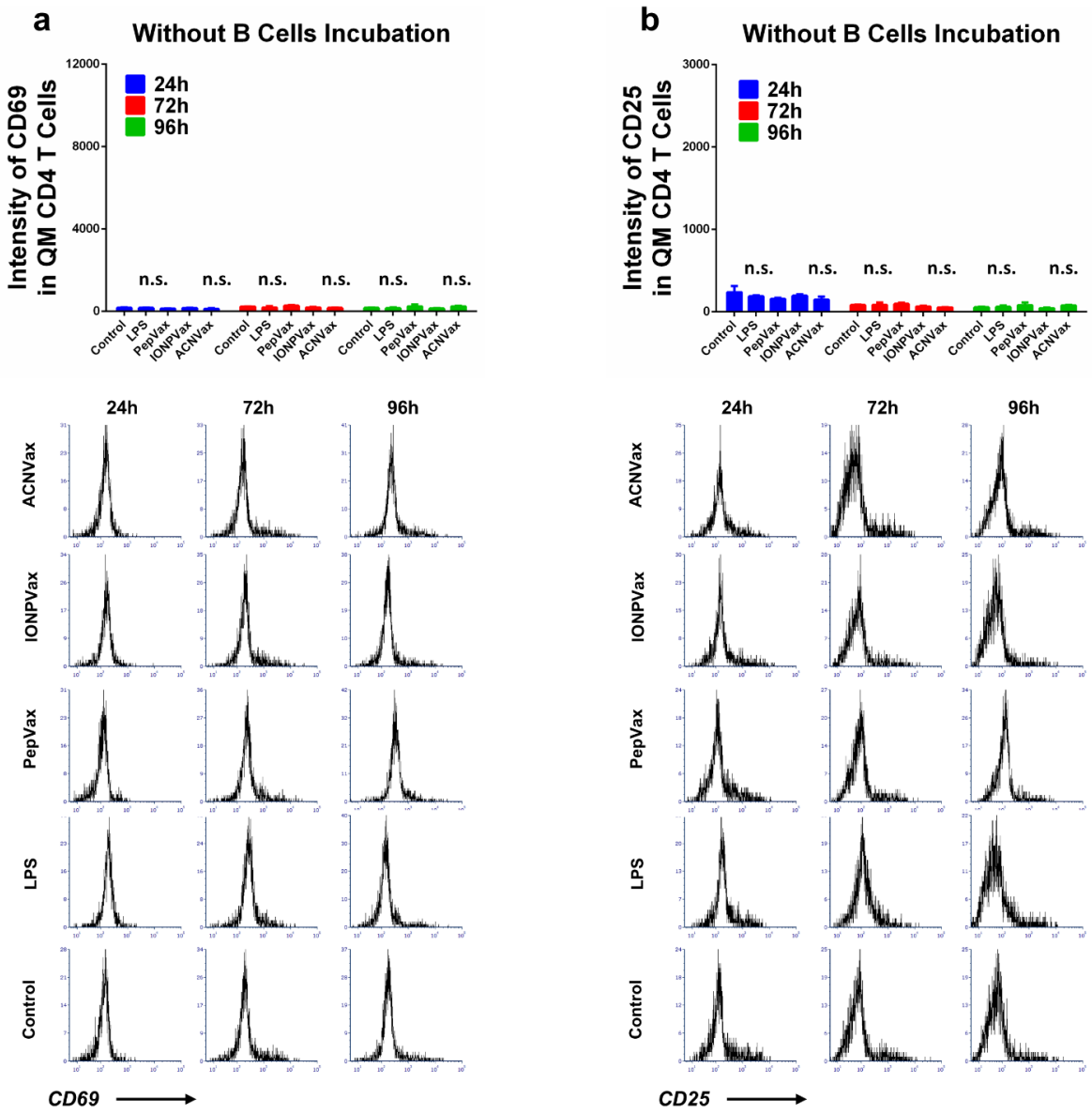


**Figure 2.S13 ACNVax did not induce activation of non-specific CD4 T cells after B cell depletion.** Activation of CD4 T cell from QM mice without B cells incubation were measured from 24h to 96h after incubation by increase of intensity of CD69 (**a**) and CD25 (**b**) markers. ACN with HER2-CD4/B antigen-Hapten and OT-II CD4 epitope was incubated with splenocytes from QM mice (B cell depleted through CD19 positive selection kit), and OT-II specific CD4 T cells (labeled with CFSE) from splenocytes of OT-II transgenic mice. IONP and free antigen peptides with the same antigens as ACNVax group were used as controls. Data for quantification are shown as mean ± SD, n = 3. Statistical comparisons are conducted among ACNVax and LPS with other groups. Statistical comparisons are based on one-way ANOVA, followed by post hoc Tukey's pairwise comparisons or by Student's unpaired T-test. ANOVA, analysis of variance; SD, standard deviation; n.s., no statistical significance.

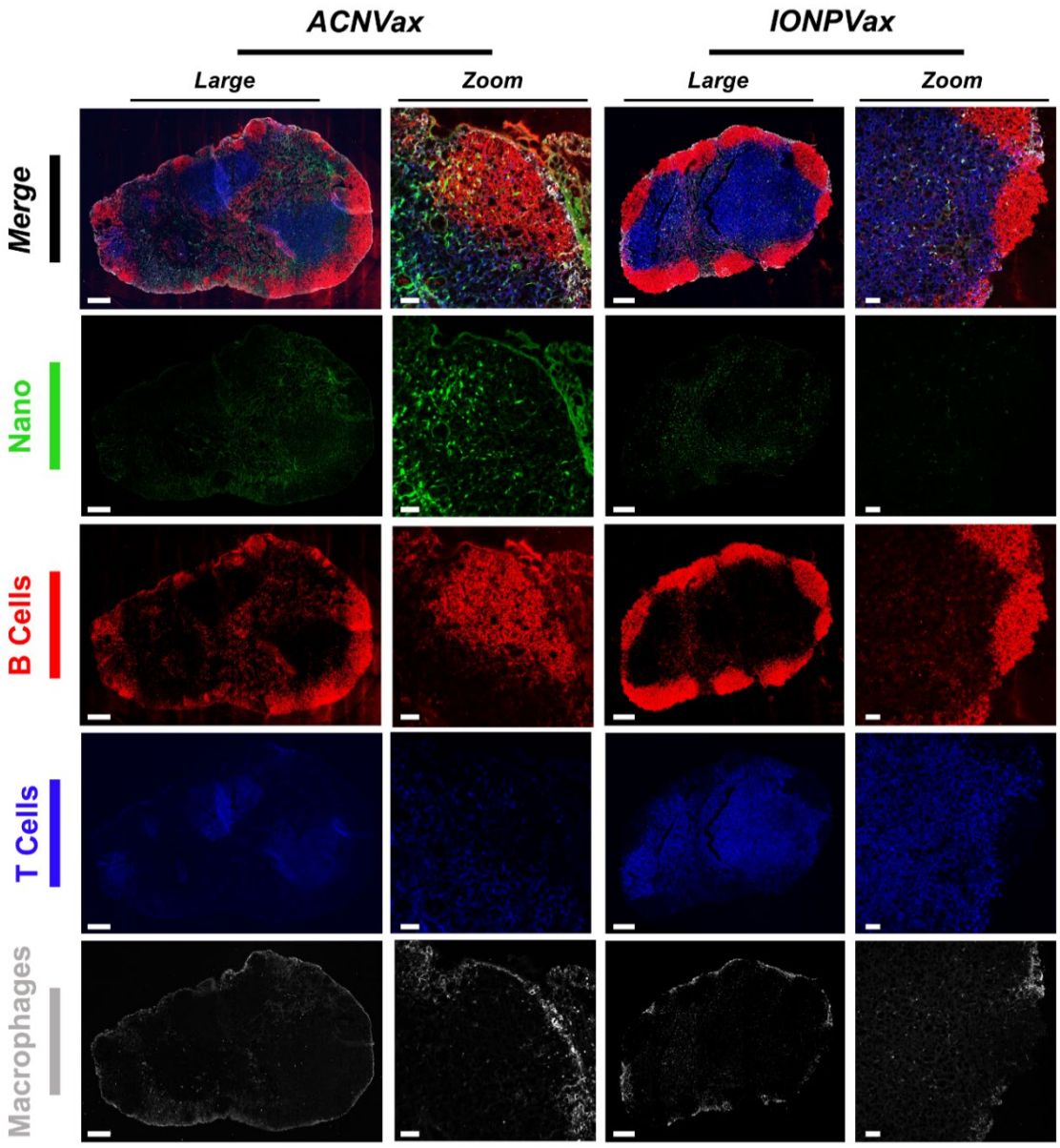


**Figure 2.S14 Confocal imaging of ACNVax and IONPVax lymph node distribution 12 hours after s.c injection in BALB/c mice.** EDFITC labeled HER2 B/CD4 epitope are used as antigen conjugated to ACN or IONP. Brilliant Violet 421 B220, Alexa Fluor® 594 CD 3 and Alexa Fluor® 647 CD169 were used for lymph node staining. Scale bar is 200 μm for whole lymph node imaging and 50 μm for magnified images. Green channels: Antigens; Red channel: B Cells; Blue channels: T cells; Gray channels: Macrophages.

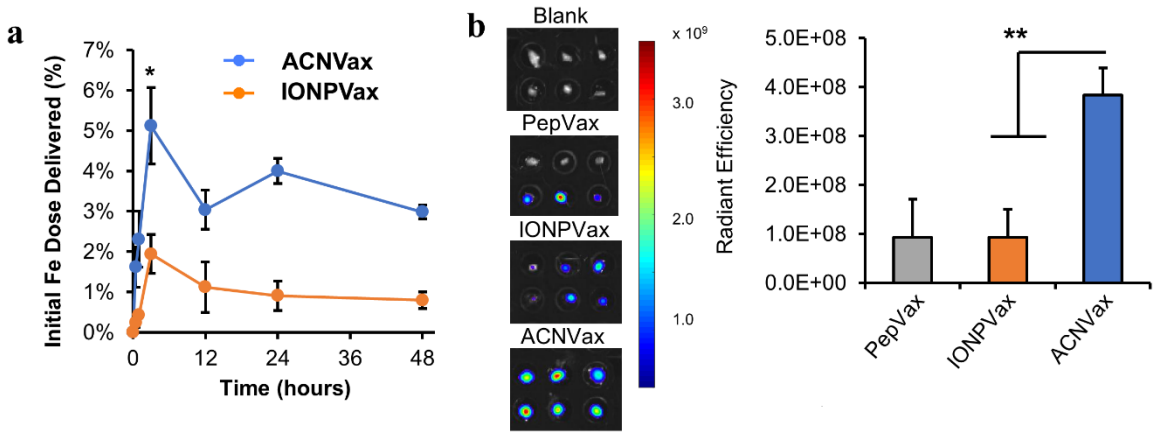


**Figure 2.S15 ACNVax enhanced delivery to lymph nodes.** (**a**) Quantification of ACNVax and IONPVax delivery to lymph nodes (popliteal + inguinal) ipsilateral to the administration site at designated time intervals represented as the percentage of initial iron-oxide delivered using ICP-MS; data represent mean ± SE, n = 3. (**b**) Representative ex-vivo IVIS fluorescence images and semi-quantitative analysis (popliteal (top) + inguinal (bottom)) of peptide delivery to lymph nodes acquired 3 hours after administration of PepVax-Cy5.5, IONPVax-Cy5.5 and ACNVax-Cy5.5 (Ex/Em = 675/720 nm, exposure = 0.5 s). The color bar represents mean radiant efficiency (p/s/cm2/sr)/(μW/cm2); data represent mean ± SD, n = 3. Statistical comparisons are based on one-way ANOVA, followed by post hoc Tukey's pairwise comparisons or by Student's unpaired T-test. The asterisks denote statistical significance at the level of * $p < 0.05$, ** $p < 0.01$. ANOVA, analysis of variance; SD, standard deviation.

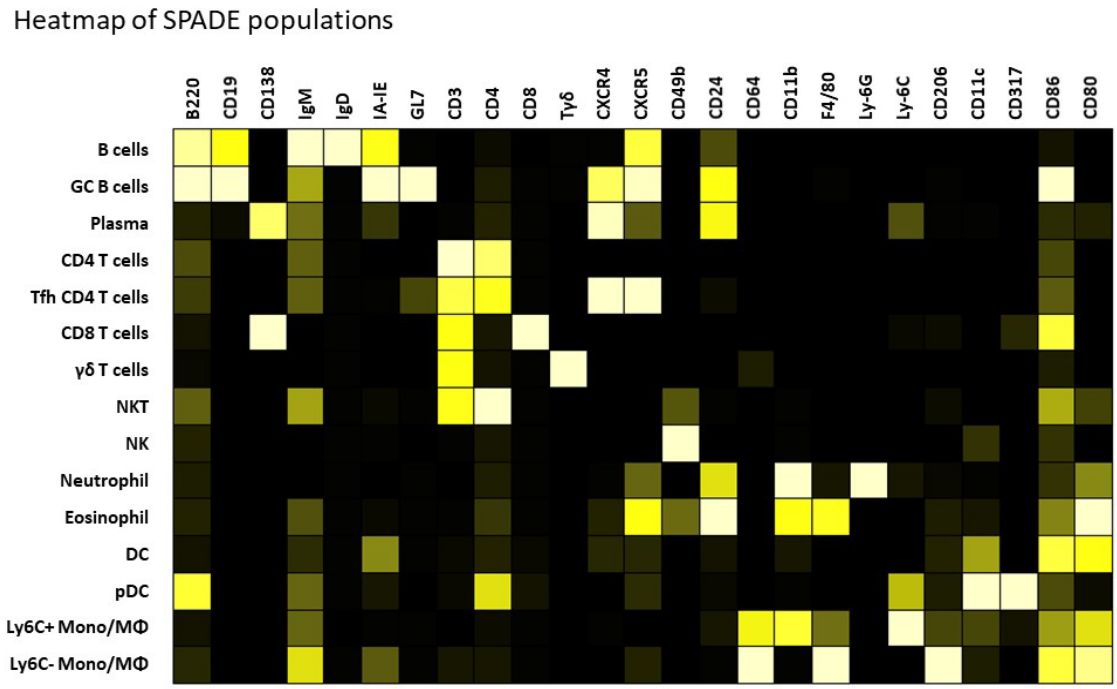


**Figure 2.S16 Heatmap showing marker expression of respective SPADE populations in lymph node and tumor**. The heatmap values were calculated by dividing the median intensity of the marker in the given population by the maximum median intensity of the marker in all the populations.

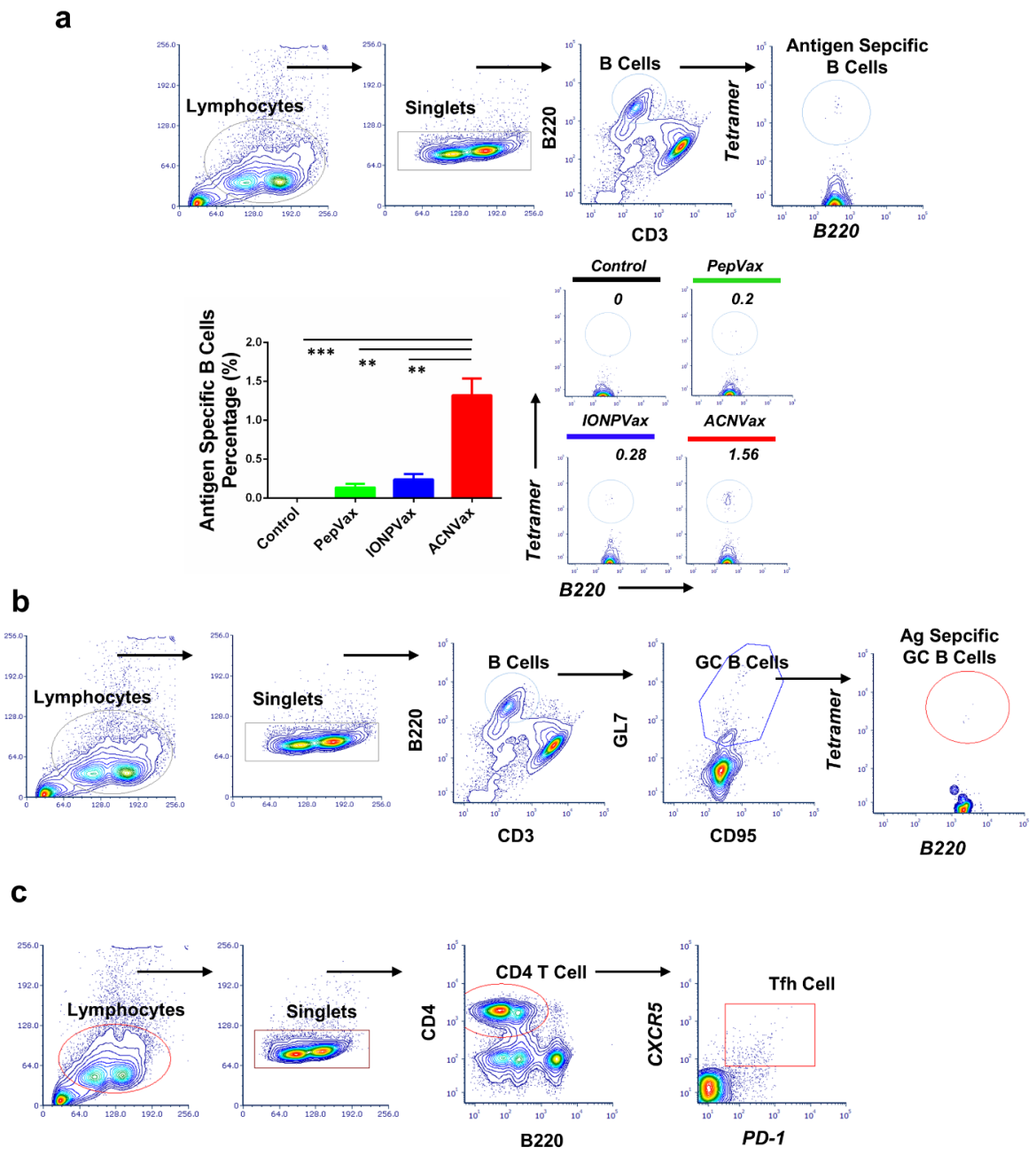


**Figure 2.S17 ACNVax induced GC B cells, antigen-specific GC B cells, and Tfh cells in the lymph nodes.** Flow cytometry monitored GC B cells, antigen-specific GC B cells and Tfh cells in the lymph nodes after three vaccinations in BALB/c mice using control (PBS), PepVax, ACNVax or IONPVax (14.6 nmol antigen and 13.9 nmol 2'3'-cGAMP as adjuvant) at days 0, 7, and 14, and analyzed at day 24. (**a**) Gating strategy and representative flow cytometry analysis and quantification of antigen specific B cells. $CD3^{-}B220^{+}tetramer^{+}$ were identified as antigen specific B cells. (**b**) Gating strategy of Germinal center B cells and Germinal center derived HER2-specific B-cells in lymph nodes using B-cell receptor tetramer staining. $CD3^{-}B220^{+}$ $CD95^{+}$ $GL\text{-}7^{+}$ populations were identified as GC B cells. (**c**) Gating strategy of Tfh cells. $B220^{-}CD4^{+}CXCR5^{+}PD\text{-}1^{+}$ populations were identified as Tfh cells. Data for quantification are shown as mean ± SD, n =

3. Statistical comparisons are based on one-way ANOVA, followed by post hoc Tukey's pairwise comparisons or by Student's unpaired T-test. The asterisks denote statistical significance at the level of * $p < 0.05$, ** $p < 0.01$, *** $p < 0.001$. ANOVA, analysis of variance; SD, standard deviation.

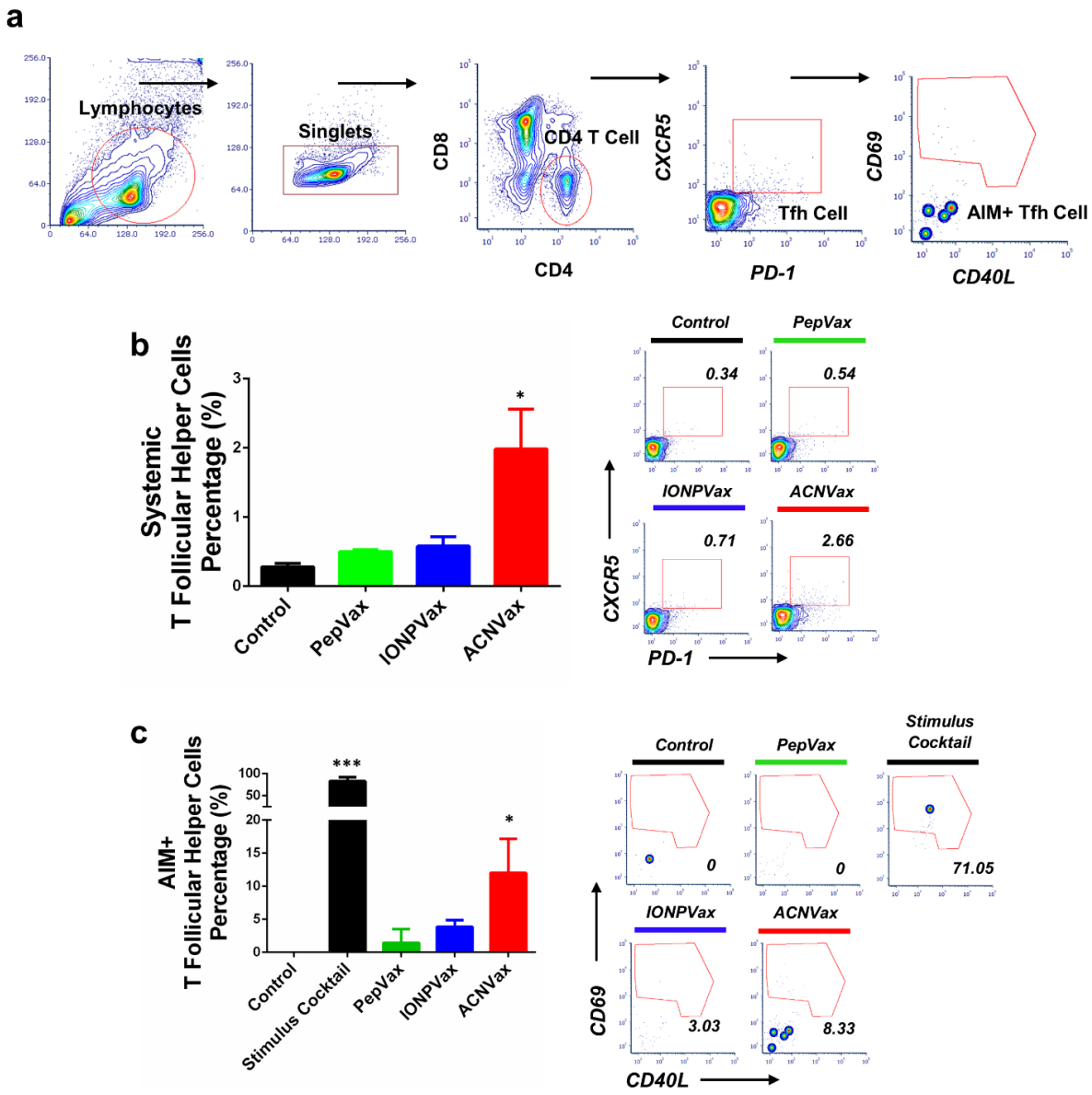


**Figure 2.S18 ACNVax induced Tfh and AIM+ Tfh in the spleen.** Flow cytometry monitored Tfh and AIM+ Tfh cells in the spleen after three vaccinations in BALB/c mice using control (PBS), PepVax, ACNVax or IONPVax (14.6 nmol antigen and 13.9 nmol 2'3'-cGAMP as adjuvant) at days 0, 7, and 14, and analyzed at day 24. Gating strategy (**a**) and representative flow cytometry analysis and quantification of Tfh (**b**) and AIM+ Tfh (**c**) cells. $B220^{-}CD4^{+}CXCR5^{+}PD\text{-}1^{+}$ populations were identified as Tfh cells. $CD69^{+}CD40L^{+/-}$ populations from Tfh cells were identified as $AIM^{+}$ Tfh cells. Data for quantification are shown as mean ± SD, n = 3. Statistical comparisons

are conducted among ACNVax with other groups. Statistical comparisons are based on one-way ANOVA, followed by post hoc Tukey's pairwise comparisons or by Student's unpaired T-test. The asterisks denote statistical significance at the level of * $p < 0.05$, ** $p < 0.01$, *** $p < 0.001$. ANOVA, analysis of variance; SD, standard deviation.

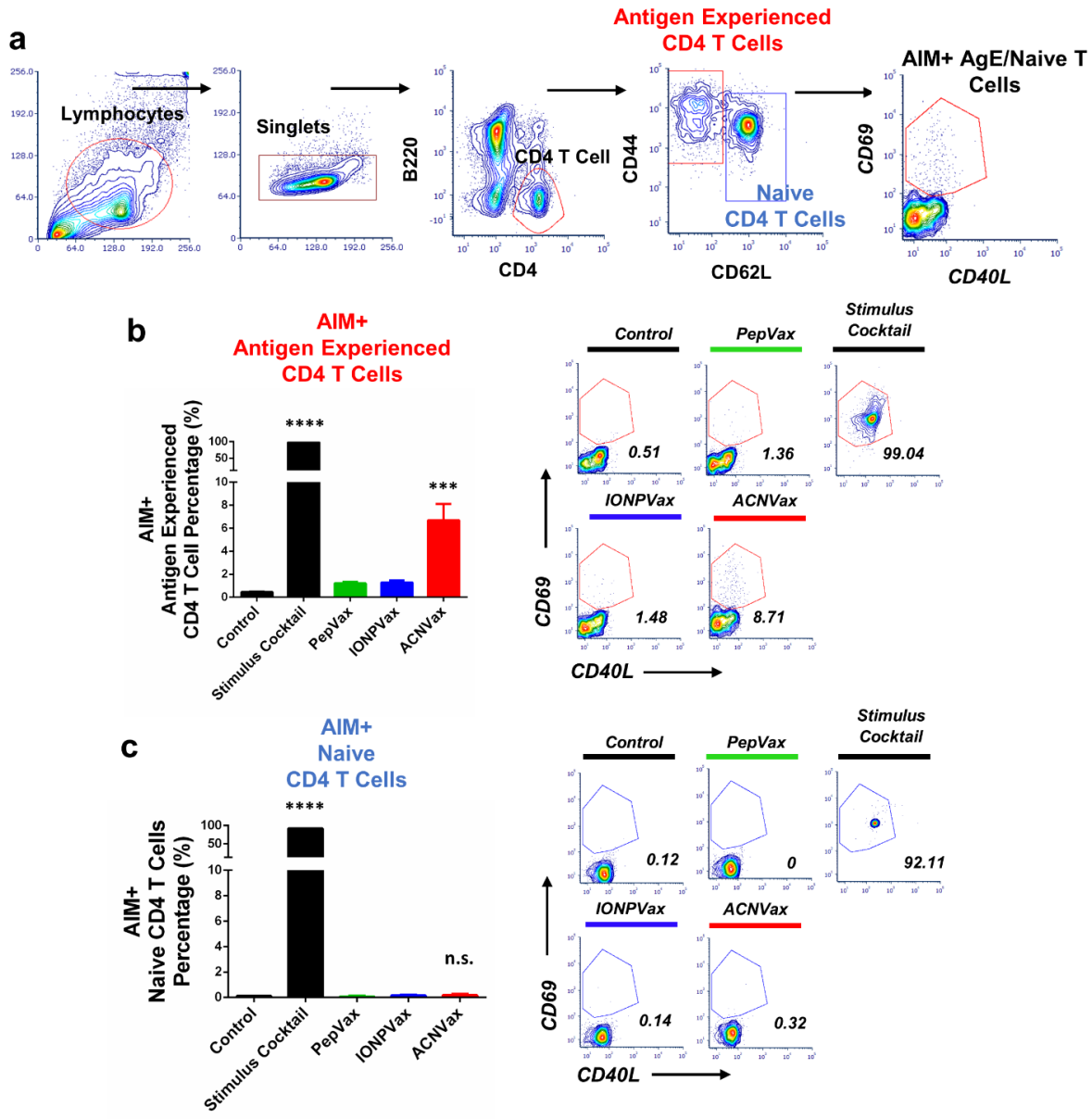


**Figure 2.S19 ACNVax induced AIM+ CD4 T cells.** Flow cytometry monitored AIM+ antigen experienced CD4 T and AIM+ naïve CD4 T cells in the spleen after three vaccinations in BALB/c mice using control (PBS), PepVax, ACNVax or IONPVax (14.6 nmol antigen and 13.9 nmol 2'3'-cGAMP as adjuvant) at days 0, 7, and 14, and analyzed at day 24. Gating strategy (**a**) and representative flow cytometry analysis and quantification of AIM+ antigen experienced CD4 T (**b**) and AIM+ naïve CD4 T cells (**c**). $B220^{-}CD4^{+}CD62L^{+}CD69^{+}CD40L^{+/-}$ populations were identified as $AIM^{+}$ antigen experienced CD4 T cells. $B220^{-}CD4^{+}CD62L^{-}$ $CD69^{+}CD40L^{+/-}$ populations were identified as AIM+ naïve CD4 T cells. Data for quantification are shown as mean ± SD, n = 3. Statistical comparisons are conducted among ACNVax with other groups. Statistical comparisons are based on one-way ANOVA, followed by post hoc Tukey's pairwise comparisons or by Student's unpaired T-test. The asterisks denote statistical significance at the level of * $p < 0.05$, ** $p < 0.01$, *** $p < 0.001$, **** $p < 0.0001$.

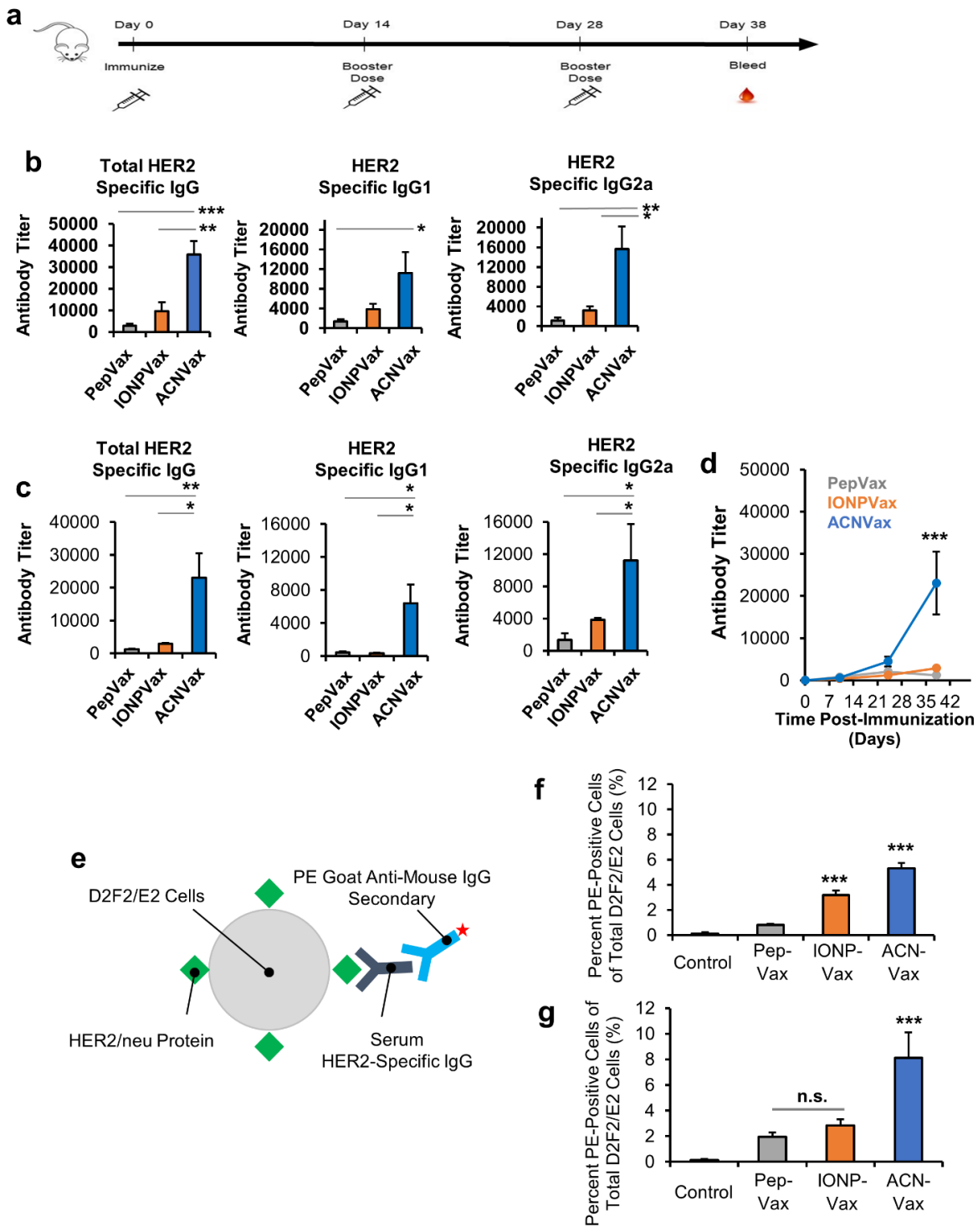


**Figure 2.S20 ACNVax induced production of HER2-specific antibody.** (**a**) Animal study immunization and analytical sampling timeline. (**b-d**) Quantification of antigen-specific IgG antibodies by indirect ELISA represented as antibody titer from serum collected 10 days after every immunization (day 10, day 24 and day 38) with either (**b**) 50 μg HER2 peptide (14.6 nmol) dose + 10 μg cGAMP or (**c,d**) 5 μg HER2 peptide dose + 10 μg cGAMP; data represent mean ±

SD, n = 5. (**e-g**) Antibody specificity binding to HER-2 positive (D2F2/E2) cell. (**e**) Schematic representation of the flow cytometry detection of anti-HER2 antibody binding specificity to D2F2/E2 cells using PE-labeled IgG secondary antibody detection. Anti-HER2 antibody binding specificity to D2F2/E2 cells of serum obtained from mice immunized with (**f**) 5 µg HER2 peptide dose + 10 µg cGAMP or (**g**) 50 µg HER2 peptide dose + 10 µg cGAMP; data represent mean ± SD, n = 3. Statistical comparisons are based on one-way ANOVA, followed by post hoc Tukey's pairwise comparisons. The asterisks denote statistical significance at the level of * p < 0.05, ** p < 0.01, *** p < 0.001. ANOVA, analysis of variance; SD, standard deviation; n.s., no statistical significance.

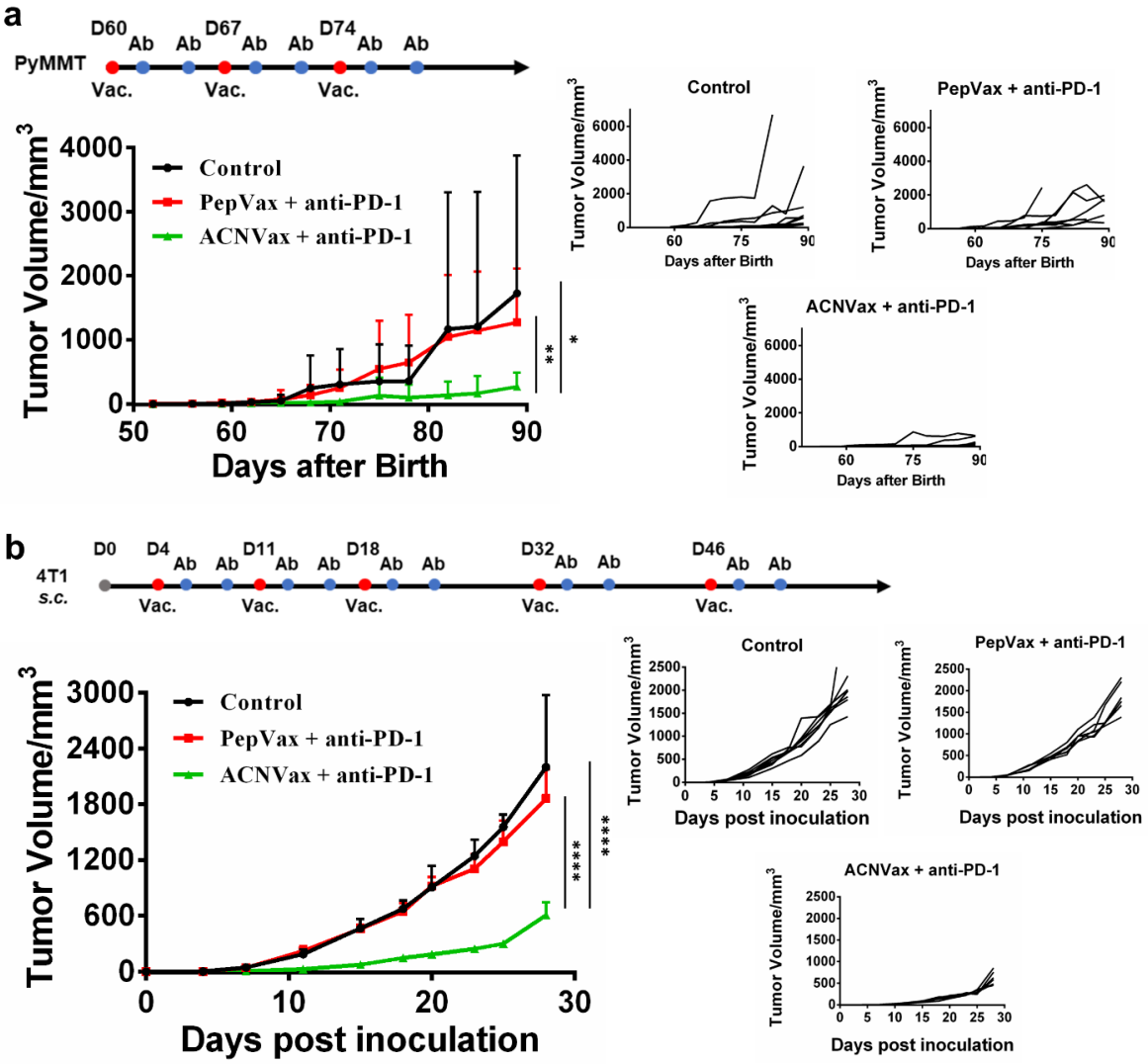


**Figure 2.S21 Antitumor efficacy of ACNVax on transgenic PyMT-MMTV breast cancer (a) and 4T1 xenograft breast cancer (b) models.** For each vaccine, we used 14.6 nmol epitopes with 13.9 nmol 2′3′-cGAMP as the adjuvant. Data represent the mean ± SD, n = 8 for all PyMT-MMTV groups, n=7 for the control, PepVax + anti-PD-1 and ACNVax + anti-PD-1 groups from

4T1 subcutaneous breast cancer model. Mouse HER2 epitope were used as antigen in the test: CDDDPESFDGNPSSGVAPLKPEHLQ (Mouse HER2 CD4/B cell epitope). Statistical comparisons are based on one-way ANOVA, followed by post hoc Tukey's pairwise comparisons. The asterisks denote statistical significance at the level of * $p < 0.05$, ** $p < 0.01$, *** $p < 0.001$, **** $p < 0.0001$. ANOVA, analysis of variance; SD, standard deviation; n.s., no statistical significance.

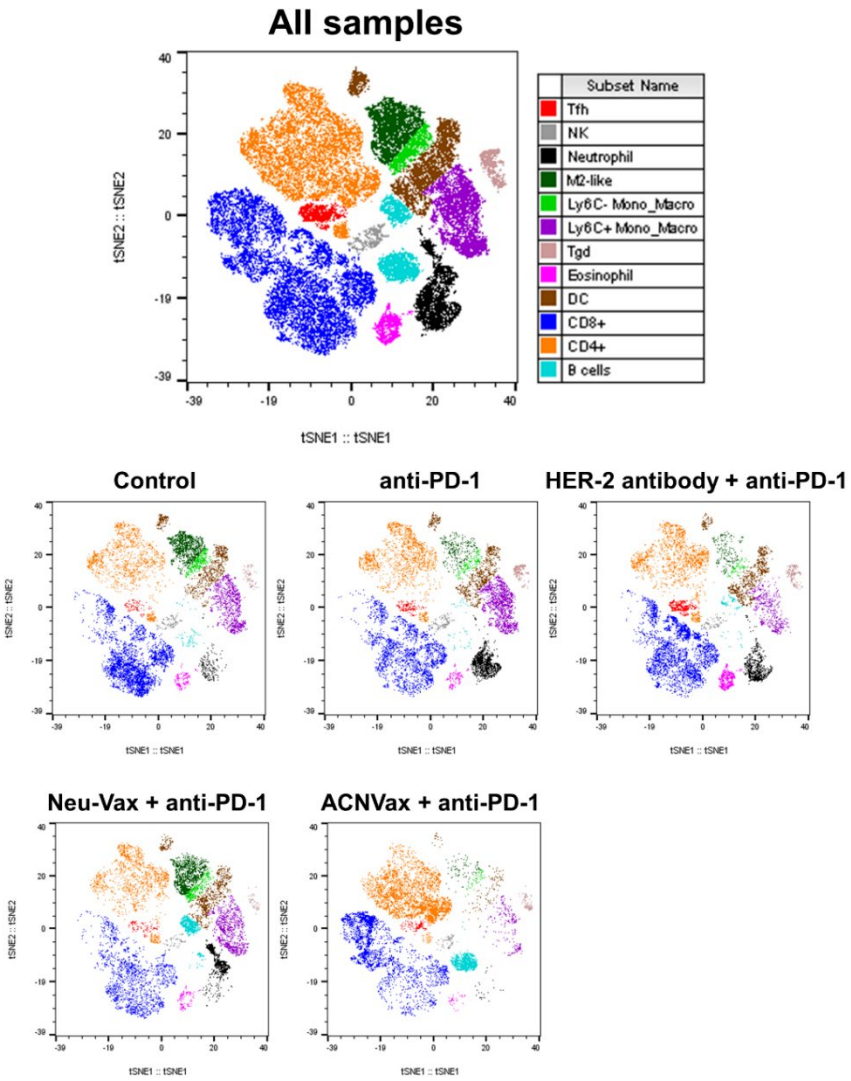


**Figure 2.S22** t-distributed stochastic neighbor embedding (TSNE) analysis of tumor infiltrating immune cells from CyTOF analysis results in Balb/c mice with HER2+ breast cancer by different treatment. Tumor samples were harvested and dissociated into single cell suspension 10 days after the second boost of vaccination. CyTOF antibody conjugation and data acquisition were done as previously described[1, 2]. CyTOF data analysis was performed as previously described[2]. All events were gated to remove noncellular events (negative for DNA intercalator), dead cells (negative for uptake of cisplatin) and doublets. viSNE analysis were performed using the Cytobank platform.

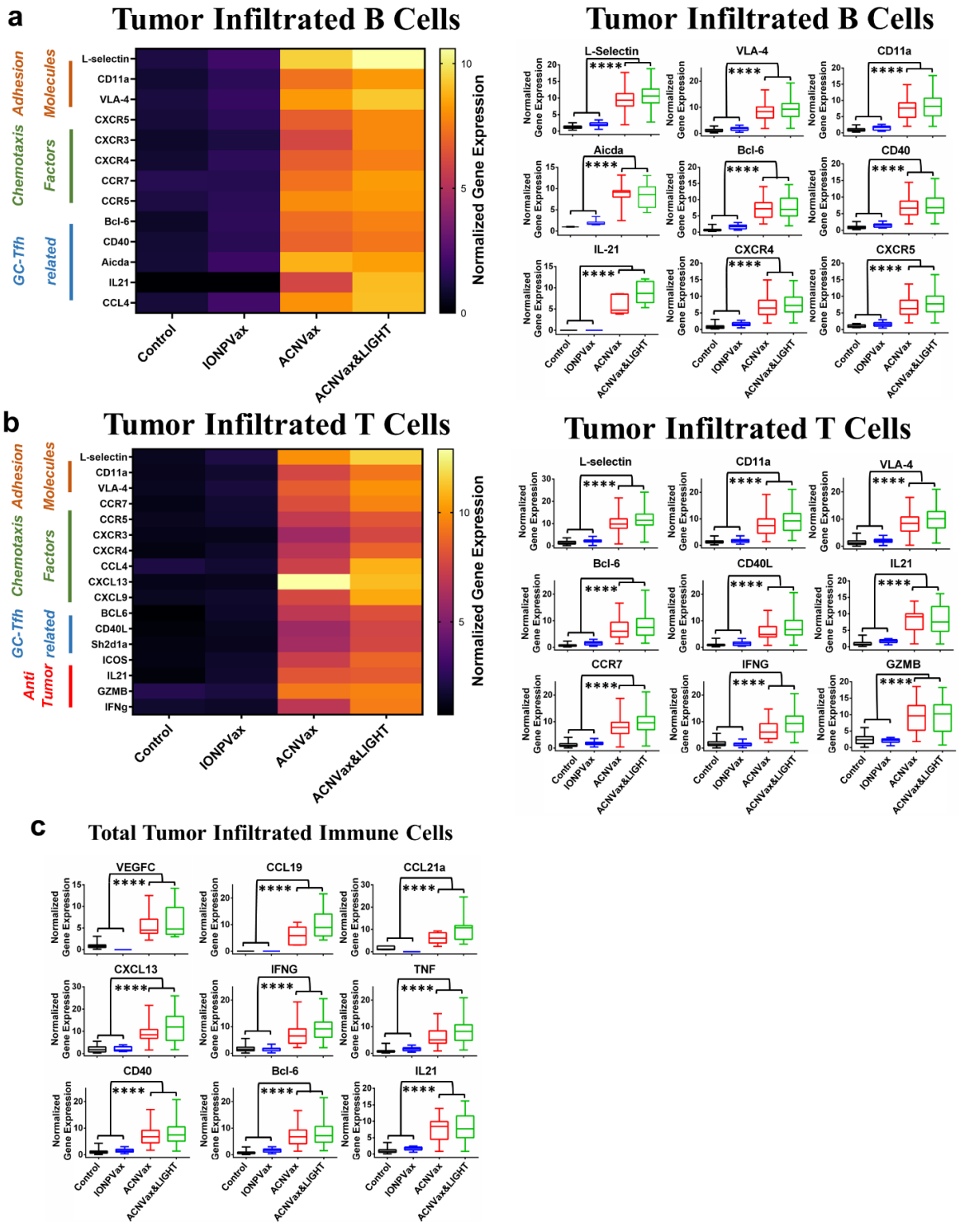


**Figure 2.S23 ACNVax induced various gene expression in tumor infiltrating B cells, T cells and total immune cells.** Heatmap and boxplots of selected gene expression levels in tumor infiltrated B cells (**a**), T cells (**b**) and total immune cells (**c**) from single-cell RNA sequencing. Statistical comparisons are based on one-way ANOVA, followed by post hoc Tukey's pairwise

comparisons. The asterisks denote statistical significance at the level of **** $p < 0.0001$. ANOVA, analysis of variance; SD, standard deviation.

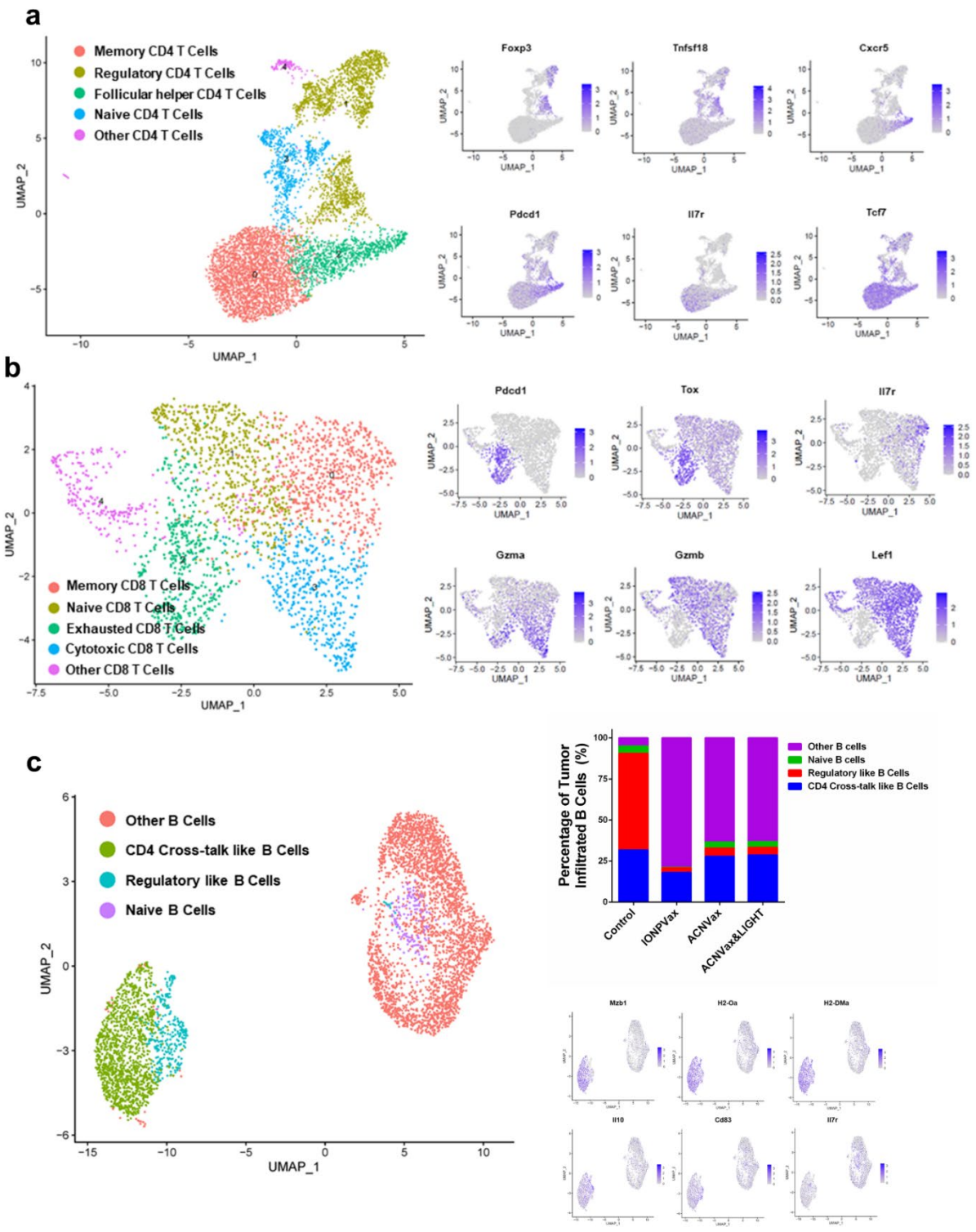


**Figure 2.S24 ACNVax induced various gene expressions in different sub-populations of CD4 T cells, CD8 T cells, and B cells.** Uniform manifold approximation and projection (UMAP) plot and signature genes of tumor infiltrated CD4 T (**a**) and CD8 T (**b**) cells. (**c**) UMAP plot with

signature genes and quantification of tumor infiltrated B cell subclusters from single-cell RNA sequencing.

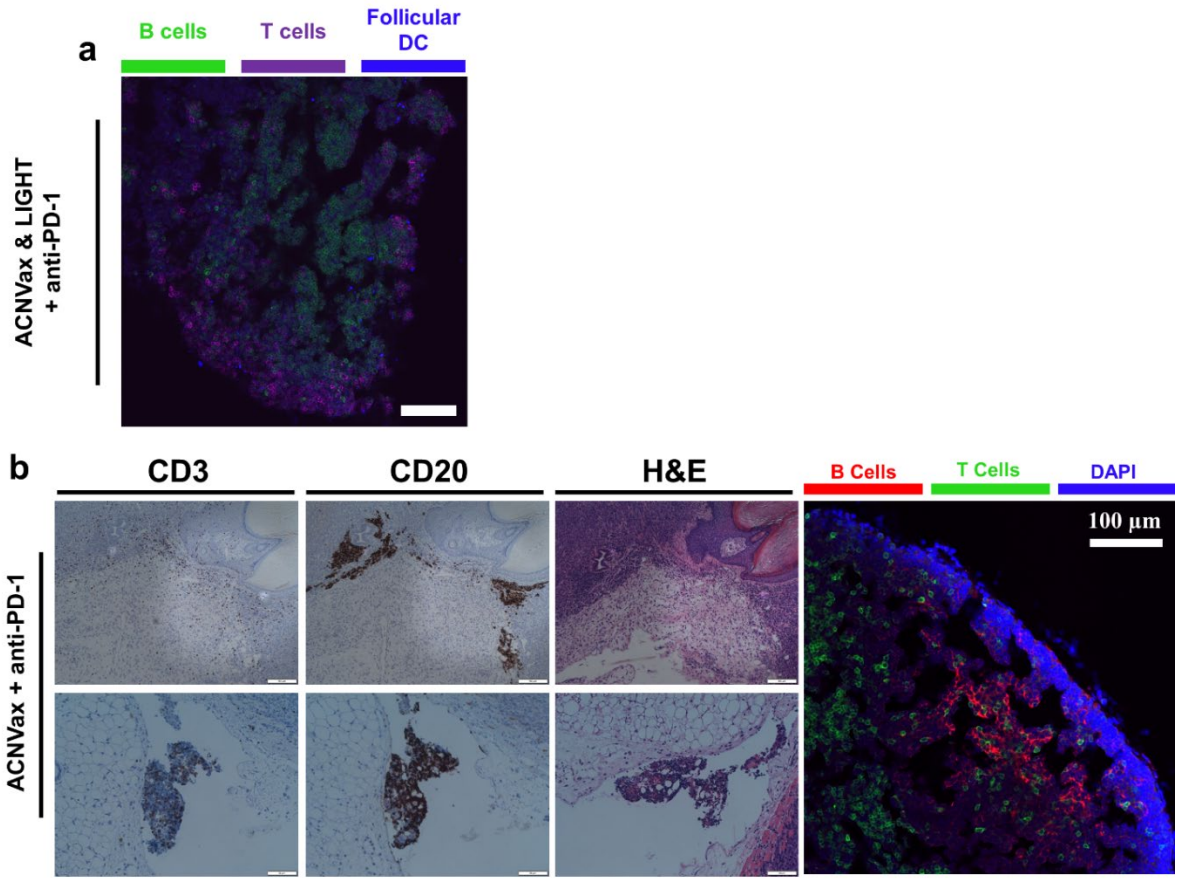


**Figure 2.S25 ACNVax increased tertiary lymphoid structure (TLS) formation.** (**a**) Confocal imaging and immunohistochemistry staining of tertiary lymphoid structures from mouse tumor samples in the ACNVax&LIGHT plus anti-PD-1 antibody group (14.6 nmol HER2 epitope, 13.9 nmol 2′3′-cGAMP, 50 ng LIGHT, 3 times every 7 days, 100 µg anti-PD-1 antibody biweekly for 3 weeks). Fluorescence immunostaining scale bar is 50 µm, immunohistochemistry staining scale bar is 100 µm. (**b**) Confocal imaging and immunohistochemistry staining of tertiary lymphoid structures from mice tumor from ACNVax plus anti-PD-1 immunized mice. Fluorescent immunostaining scale bar is 100 µm. Tumor tissues were harvested at the endpoint and immediately fixed in paraformaldehyde. For immunohistochemistry staining, antibodies are used to identify different populations of immune cells: B cells (CD20) and T cells (CD3). For fluorescent immunostaining, Alexa Fluor® 594 CD19 (B cells), FITC CD3 (T cells), Alexa Fluor® 647 anti-mouse CD21/CD35 (CR2/CR1) and DAPI Fluoromount-G® were used for confocal imaging. Immunohistochemistry staining scale bar is 100 µm.

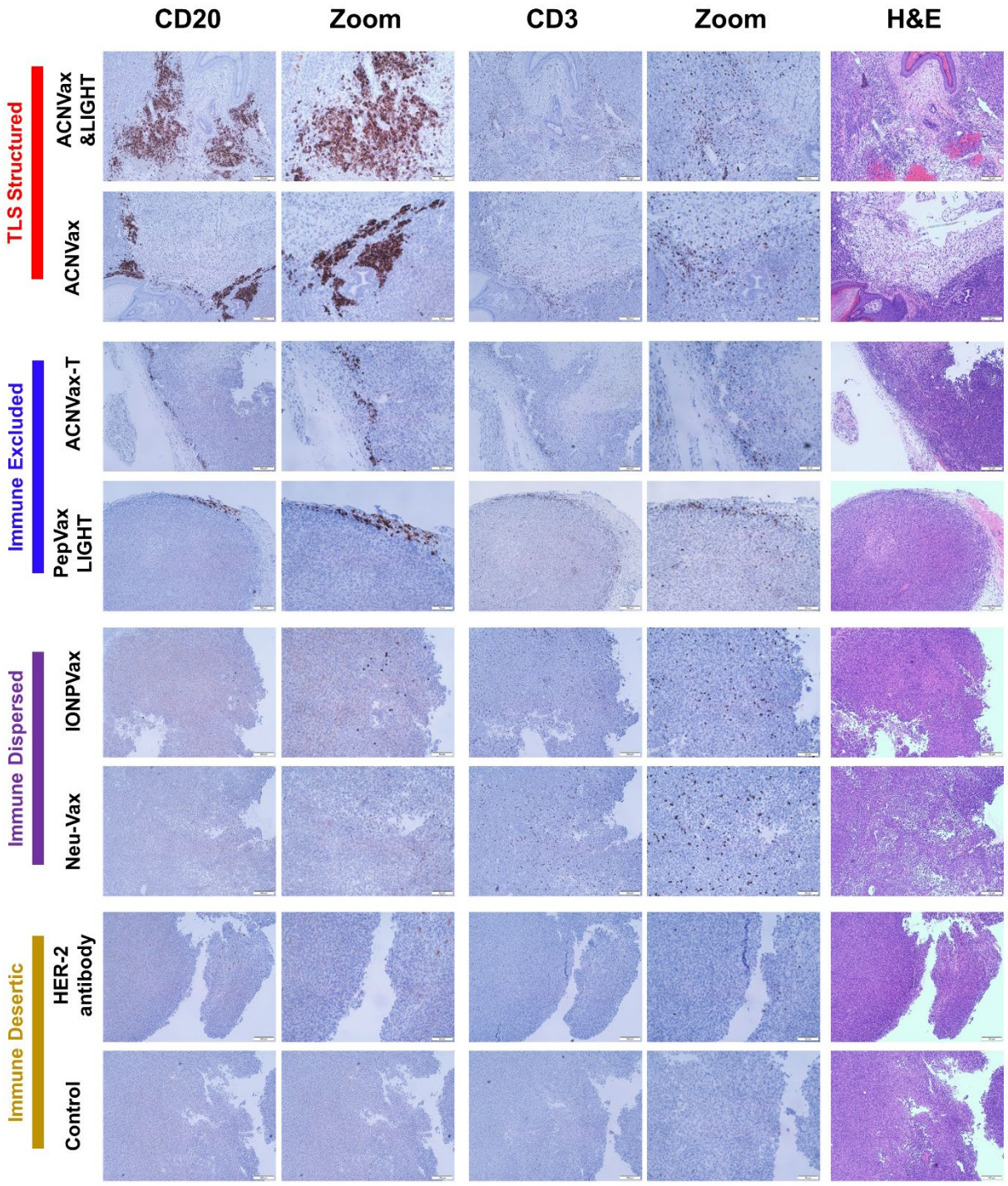


**Figure 2.S26 ACNVax induced tertiary lymphoid structure (TLS) formation in comparison with other groups.** (**a**) immunohistochemistry staining images of tumor samples different groups. Tumor tissues were harvested at the endpoint and immediately fixed in paraformaldehyde. For immunohistochemistry staining, antibodies are used to identify different populations of immune cells: B cells (CD20) and T cells (CD3). Immunohistochemistry staining scale bar is 100 μm.

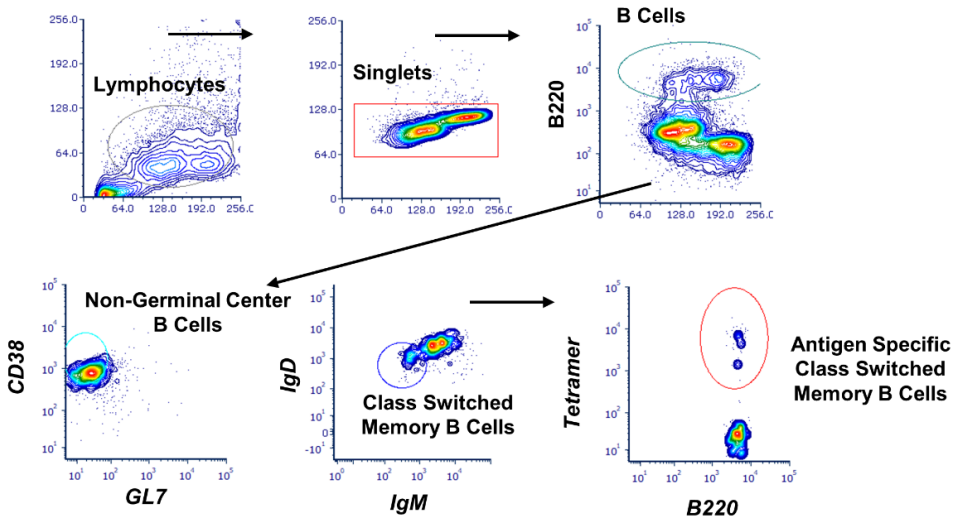


**Figure 2.S27 Gating strategy of class switched memory B cells and antigen specific class switched memory B cells from spleen, lymph node, bone marrow and peripheral blood of the mice in Figure 7a.** $B220^{+}$ $CD38^{+}$ $GL\text{-}7^{-}IgD^{-}IgM^{-}$ populations were identified as class switched memory B cells. HER2 tetramer positive class switched memory B cells were identified as antigen specific class switched memory B cells.

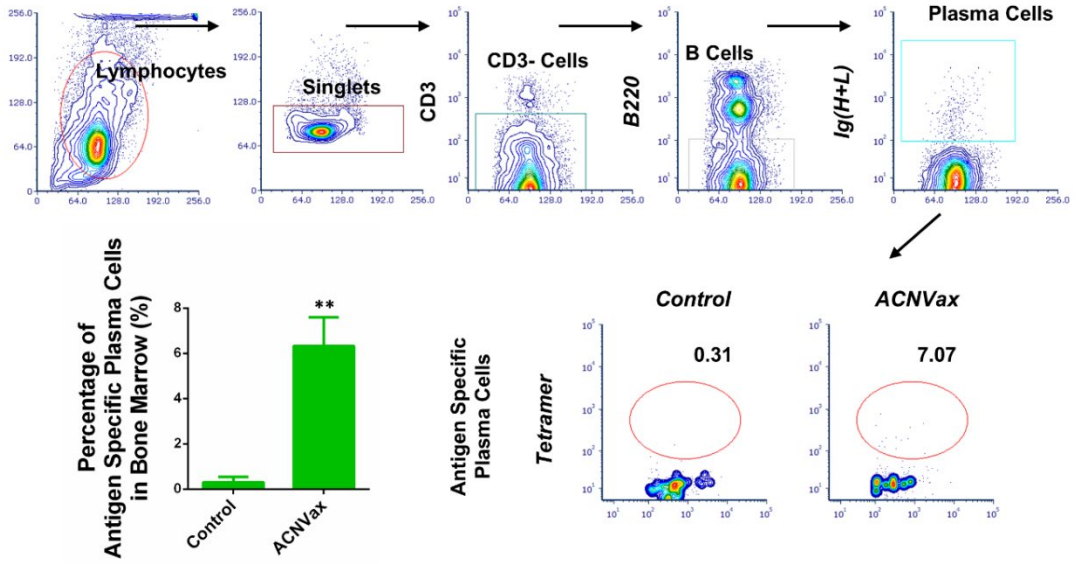


**Figure 2.S28 Gating strategy and representative flow cytometry analysis and quantification of antigen specific plasma cells from bone marrow of the mice in Figure 7a**. $CD3^{-}$ $B220^{low}Ig(H+L)^{+}tetramer^{+}$ were identified as antigen specific plasma cells. Data for quantification

are shown as mean ± SD, n = 3. Statistical comparisons are based on one-way ANOVA, followed by post hoc Tukey's pairwise comparisons or by Student's unpaired T-test. The asterisks denote statistical significance at the level of * $p < 0.05$, ** $p < 0.01$. ANOVA, analysis of variance; SD, standard deviation.

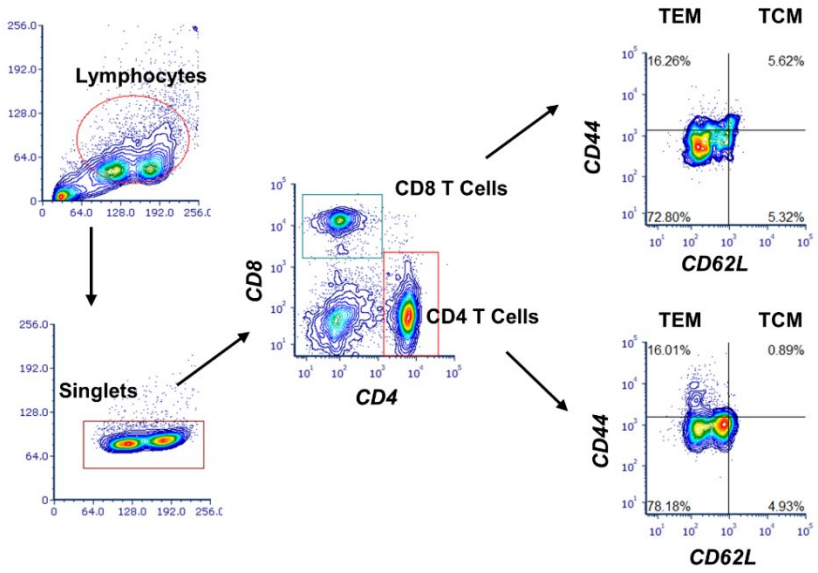


**Figure 2.S29 Gating strategy of CD4 T effector memory (TEM), CD4 T central memory (TCM) CD8 TEM and CD8 TCM cells from lymph node and peripheral blood of the mice in Figure 7a**. $CD8^-CD4^+$ $CD44^+$ $CD62L^-$ populations were identified as CD4 TEM cells, $CD8^-CD4^+$ $CD44^+$ $CD62L^+$ populations were identified as CD4 TCM cells. $CD4^-CD8^+$ $CD44^+$ $CD62L^-$ populations were identified as CD8 TEM cells, $CD4^-CD8^+$ $CD44^+$ $CD62L^+$ populations were identified as CD8 TCM cells.

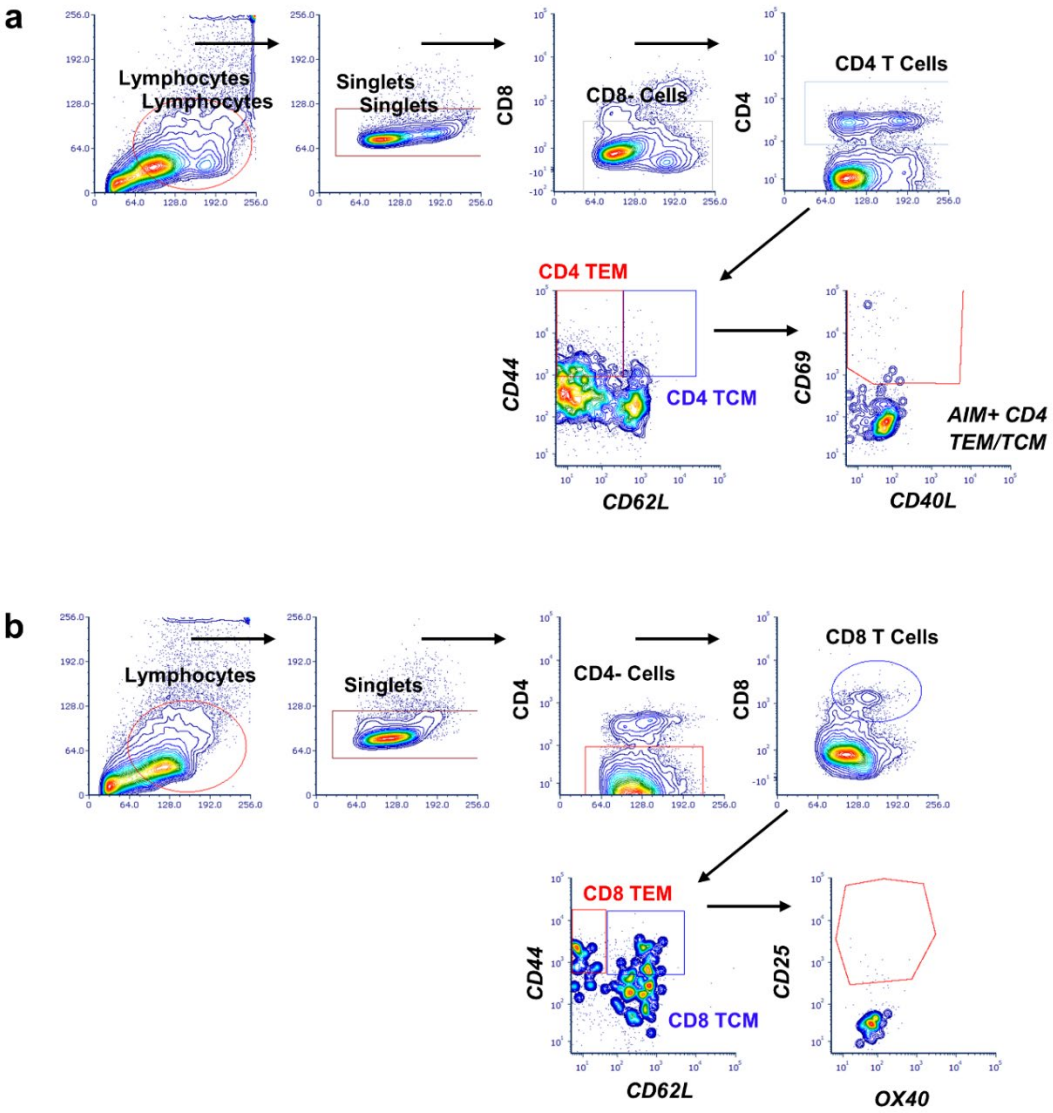


**Figure 2.S30 Gating strategy of activation-induced markers assay (AIM) for measuring antigen specific CD4 TEM/TCM cells (a) and CD8 TEM/TCM (b) from spleen of mice in Figure 7a.** $CD8^{-}CD4^{+}$ $CD44^{+}$ $CD62L^{-}$ populations were identified as CD4 TEM cells, $CD8^{-}CD4^{+}$ $CD44^{+}$ $CD62L^{+}$ populations were identified as CD4 TCM cells. $CD69^{+}CD40L^{+/-}$ populations from CD4 TEM/TCM cells were identified as $AIM^{+}$ CD4 TEM/TCM cells. $CD4^{-}CD8^{+}$ $CD44^{+}$ $CD62L^{-}$ populations were identified as CD8 TEM cells, $CD4^{-}CD8^{+}$ $CD44^{+}$ $CD62L^{+}$ populations were identified as CD8 TCM cells. $CD25^{+}OX40^{+/-}$ populations from CD8 TEM/TCM cells were identified as $AIM^{+}$ CD8 TEM/TCM cells.

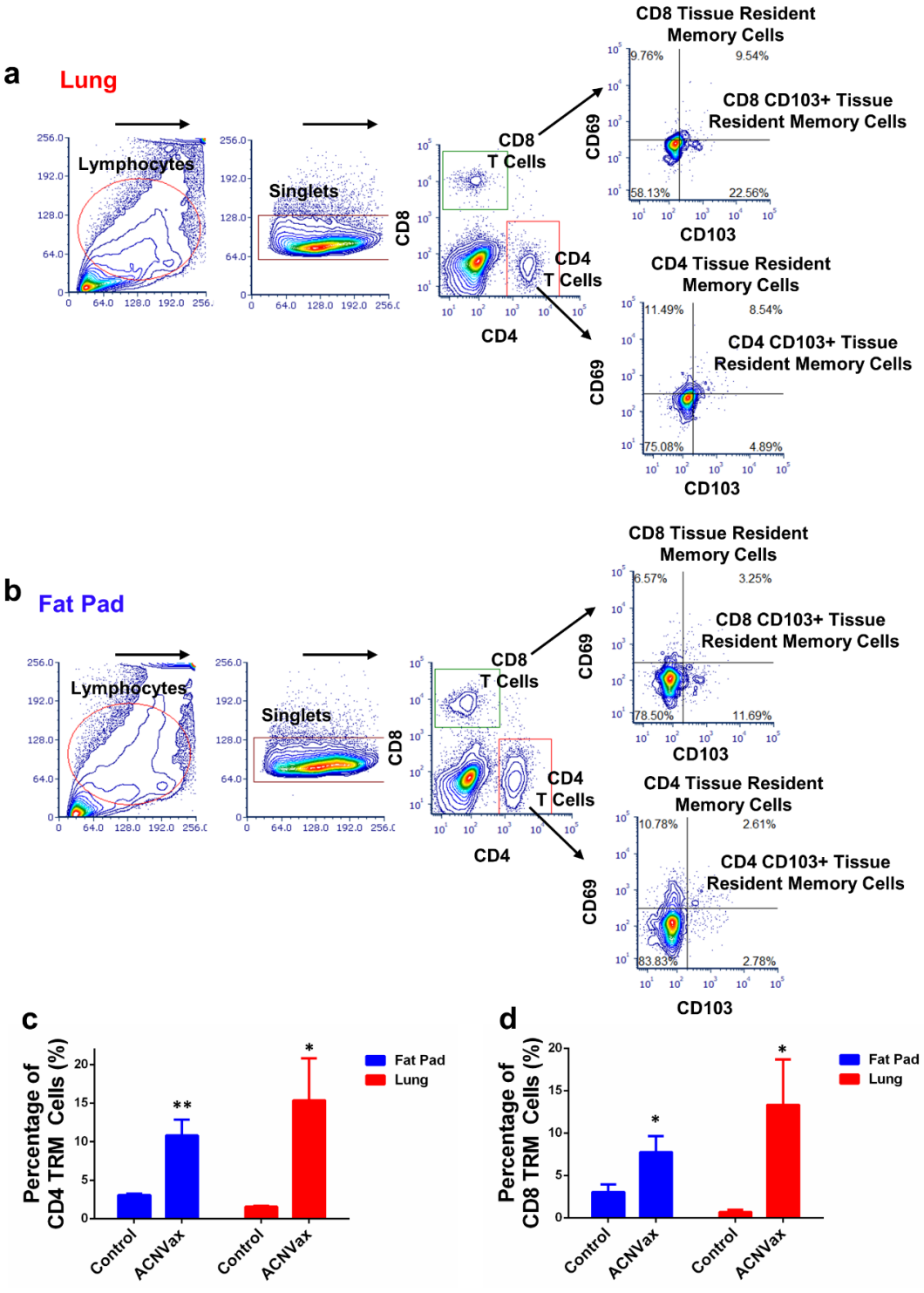


**Figure 2.S31 Gating strategy of flow cytometry analysis of CD4 Tissue resident memory T (TRM, c) and CD8 TRM (d) cells from Lung (a) and Fat pad (b).** Representative flow cytometry analysis and quantification of CD4 Tissue resident memory T (TRM, **c**) and CD8 TRM (**d**) cells from Lung (**a**) and Fat pad (**b**) of the mice in **Figure 6a**. $CD8^{-}CD4^{+}$ $CD69^{+}$ $CD103^{-/+}$ populations were identified as CD4 TRM cells. $CD4^{-}CD8^{+}$ $CD69^{+}$ $CD103^{-/+}$ populations were identified as CD8

TRM cells. Data for quantification are shown as mean ± SD, n = 3. Statistical comparisons are based on one-way ANOVA, followed by post hoc Tukey's pairwise comparisons or by Student's unpaired T-test. The asterisks denote statistical significance at the level of * $p < 0.05$, ** $p < 0.01$. ANOVA, analysis of variance; SD, standard deviation. Student's unpaired T-test. The asterisks denote statistical significance at the level of * $p < 0.05$, ** $p < 0.01$, *** $p < 0.001$, **** $p < 0.0001$. ANOVA, analysis of variance; SD, standard deviation.

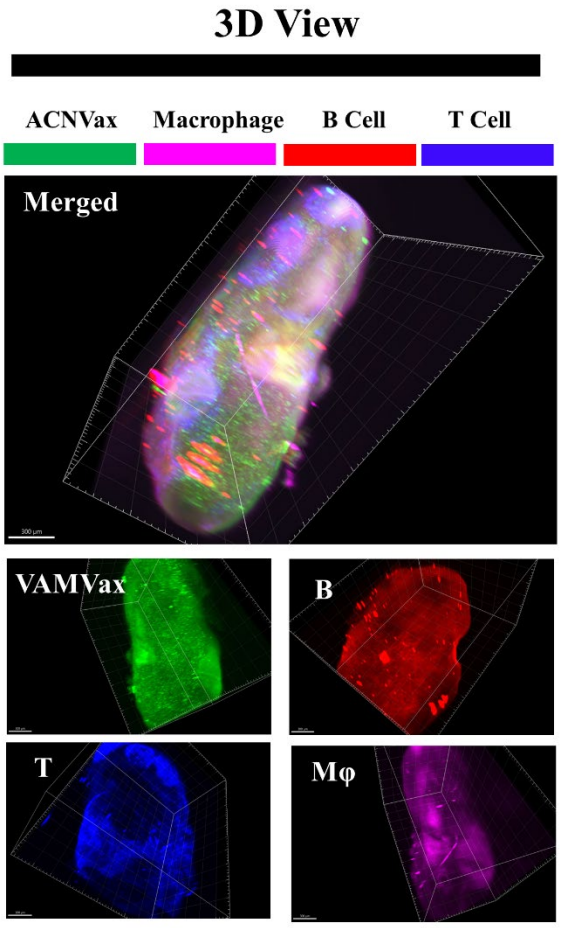


**Figure 2.S32 3D imaging of ACNVax lymph node distribution 12 hours after s.c injection in BALB/c mice.** EDFITC labeled HER2 B/CD4 epitope are used as antigen conjugated to ACN. Brilliant Violet 421 B220, Alexa Fluor® 594 CD 3 and Alexa Fluor® 647 CD169 were validated and used for lymph node immune fluorescence staining.

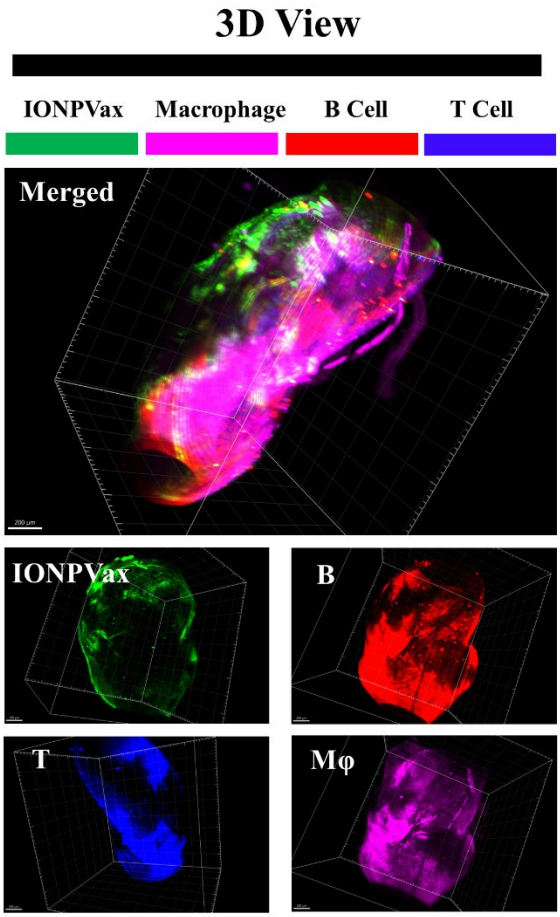


**Figure 2.S33 3D imaging of IONPVax lymph node distribution 12 hours after s.c injection in BALB/c mice.** EDFITC labeled HER2 B/CD4 epitope are used as antigen conjugated to IONP. Brilliant Violet 421 B220, Alexa Fluor® 594 CD 3 and Alexa Fluor® 647 CD169 were validated and used for lymph node immune fluorescence staining.

**Mathematical Modeling:**

*Gold Nanoparticle (AuNP) Loading per Viral antigen cluster mimicry nanovaccine (ACN)*

The extent of gold nanoparticle (AuNP) loading to Viral antigen cluster mimicry nanovaccine (ACN) surfaces was determined by ICP-MS determination of total elemental gold (Au) and iron (Fe) weights. These weights were then utilized to quantify total number spheres of a given element and particle size based on previously reported methods[3, 4]. The ratio of these experimental values was then interpreted as AuNPs per ACN, or the number of AuNPs per single IONP core.

Due to the crystalline structure of iron-oxide nanoparticles, it is possible to quantify the number of nanoparticles per unit Fe based on known particle size accordingly to previously establish

methodologies (**Table S1**)[3]. Using transmission electron microscopy (TEM), the exact particle size of iron-oxide nanoparticles was quantified using the ImageJ software. The particle size of the polymer-coated iron-oxide nanoparticle core of the ACN was 15 nm, while the particle size of the lipid-coated iron-oxide nanoparticle control was 30 nm. Based on the known unit cell volume of iron-oxide ($Fe_3O_4$) and quantified particle size, the number of nanoparticles per gram Fe was determined to be $1.5x10^{17}$ and $1.9x10^{16}$ for 15 nm and 30 nm cores, respectively (**Table S1**).

The number of gold nanoparticles per unit Au was quantified by two considerations. First, based on literature values reported[4], AuNPs with 3 nm diameters have 479 gold atoms per nanoparticle, which is 56% of the number of gold atoms per solid gold metallic colloids of the same diameter (835 gold atoms per nanoparticle). Therefore, by conversion from weight of Au to atoms of Au through Avogadro's Number it is possible to quantify the number of gold nanoparticle per unit Au. Quantification by this methodology revealed that number gold nanoparticle per gram Au was $6.38x10^{18}$ (**Table S2**). Second, based on literature values reported for the mass of a single AuNP for 2 nm, 5 nm and 10 nm particle size, the mass of a single 2 nm AuNP was interpolated based on curve fitting. Through curve fitting, the mass of a single 3 nm AuNP was determined to be $2.67x10^{19}$ grams or $3.67x10^{18}$ AuNPs per gram Au (**Table S2**). Notably, this quantified value matches those values reported for solid gold colloids based on 835 gold atoms per nanoparticle and therefore was not considered truly representative of our materials.

**Table 2.S1** Iron-oxide nanoparticle calculations. Quantification of total number of spheres per unit Fe and total surface area per unit Fe for 15-nm and 30-nm iron-oxide nanocrystal cores. Calculations were performed based on equations outlined previously[3].

| Description | Value |
|---|---|
| Unit cell volume of $Fe_3O_4$ | 0.5905 $nm^3$ |
| Fe atoms per unit $Fe_3O_4$ cell | 24 |
| Molecular weight of Fe | 55.85 g/mole |
| Avogadro's Number | $6.022 \times 10^{23}$ |
| Volume of 15 nm IONP core – single sphere | 1766 $nm^3$ |
| Volume of 30 nm IONP core – single sphere | 14130 $nm^3$ |
| Surface Area per Sphere - 15 nm IONP core | 707 $nm^2$ |
| Surface Area per Sphere - 30 nm IONP core | 2826 $nm^2$ |
| Number of Fe atoms per g Fe | $1.08 \times 10^{22}$ |
| Number of $Fe_3O_4$ unit cells per g Fe | $4.5 \times 10^{20}$ |
| Number of $Fe_3O_4$ unit cells per Single Sphere – 15 nm IONP core | 2944 |
| Number of $Fe_3O_4$ unit cells per Single Sphere – 30 nm IONP core | 23550 |
| Total Number of Spheres per g Fe – 15 nm IONP core | $1.5 \times 10^{17}$ |
| Total Number of Spheres per g Fe – 30 nm IONP core | $1.9 \times 10^{16}$ |
| Total Surface Area per g Fe – 15 nm IONP core | $1.1 \times 10^{20}$ $nm^2$ |
| Total Surface Area per g Fe – 30 nm IONP core | $2.7 \times 10^{20}$ $nm^2$ |

**Table 2.S2** Gold nanoparticle calculations. Quantification of total number of spheres per unit Au for 3 nm AuNPs

| Description | Value |
|---|---|
| Method 1 | |
| Density of Gold | 19.32 g/cm$^3$ |
| Atomic Number | 197 |
| Average # of Gold Atoms per AuNP (3 nm) | 479 |
| Number of AuNPs per g Fe (3 nm) | 6.38E+18 |
| Method 2 | |
| Mass of Single AuNP (g) | 2.67E-19 |
| Number of AuNPs per g Au (3 nm) | 3.67E+18 |

***Gold Nanoparticle Spatial Distribution –Inter-Nanoparticle Distance***

The distance between AuNPs on ACN surfaces was modeled based on two methodologies. The first technique was based on the arc length equation for a circle. If homogeneous distribution of AuNPs on a sphere is assumed, the loading of 2, 6 and 14 AuNPs on ACN surface will yield AuNPs in a single plane (circle) oriented at central angles equivalent to 180º, 90º and 45º, respectively. Using the arc length equation for a circle with radius 7.5 nm, 2, 6 and 14 AuNPs will be located 23.6, 11.8 and 5.9 nm apart, respectively. Plotting these three points and using a power function curve fitting model ($R^2$ = 0.99) allows for interpolations of inter-nanoparticle distances between 2-14 AuNPs per ACN surface (**Figure S1c-1e**, **Table S3**). The benefit of this technique is that it accounts for arc length and is not a straight-line distance calculation. However, this model represent AuNPs are single points and only has three points for the curve fitting model thereby limiting potential power and accuracy.

The second technique used to quantify inter-nanoparticle distance on ACN surfaces was based on a triangulation methodology. With the number of AuNPs per ACN surface known and assuming homogeneous distribution of AuNPs on a sphere around a single central focal point, AuNPs can be triangulated. For AuNP per ACN equal to or greater than 4, the number of triangles formed around a central focal point is 2n, where n is the number of AuNPs per ACN.

$$AuNP\ Triangles\ per\ IONP\ core\ = AuNP\ per\ IONP\ core \times 2$$

With the number of triangles determined, the surface occupied by a single triangle was quantified given the surface area of spherical ACN with 7.5 nm radius.

$$Surface\ Area\ per\ Triangle = \frac{Surface\ Area\ of\ IVLN}{Number\ of\ Triangles}$$

Assuming an equilateral triangle, the surface area of a single triangle can be used to determine the length of a side of the triangle, and therefore the distance between AuNPs represented as single points. By subtracting 2x the radius of the AuNPs, a better surface to surface contact distance can be interpreted (**Figure S1c-1e**, **Table S4**).

$$Distance\ between\ AuNPs = \sqrt{\frac{4\ \times Triangle\ Surface\ Area}{\sqrt{3}}} - (\ 2 \times AuNP\ radius)$$

The benefit of this technique is that does not rely on interpolation. However, this model is limited due to the reliance of straight-line distances between AuNPs.

**Table 2.S3** Inter-nanoparticle distance: Arc Length Interpolation Model. Interpolation data set for inter-AuNP distances based on AuNP per ACN determined by ICP-MS (**Figure 2.1c**) and the curve fitting model presented in **Figure 2.S1c-1e** ($y = 39.51x^{-.708}$, $R^2 = 0.99$).

| **Au/Fe Ratio (wt/wt)** | **AuNP per ACN** | **Inter-Nanoparticle Distance Arc Length (nm)** |
|---|---|---|
| 0.05 | 2.1 | 23.18 |
| 0.1 | 4.2 | 14.19 |
| 0.15 | 6.4 | 10.65 |
| 0.2 | 8.5 | 8.69 |

| | | |
|---|---|---|
| 0.25 | 10.6 | 7.42 |
| 0.3 | 12.7 | 6.52 |
| 0.35 | 14.9 | 5.84 |
| 0.4 | 17.0 | 5.32 |

**Table 2.S4** Inter-nanoparticle distance: Triangulation Model. Data set for inter-AuNP distances based on AuNP per ACN determined by ICP-MS (**Figure 1c**) and mathematic modeling presented above, and curve fitting model presented in **Figure S1c-1e** ($y = 28.69x^{-.649}$, $R^2 = 0.99$).

| **Au/Fe Ratio (wt/wt)** | **AuNP per ACN** | **Inter-Nanoparticle Distance Arc Length (nm)** |
|---|---|---|
| 0.05 | 2.1 | 17.10 |
| 0.1 | 4.2 | 11.36 |
| 0.15 | 6.4 | 8.82 |
| 0.2 | 8.5 | 7.30 |
| 0.25 | 10.6 | 6.27 |
| 0.3 | 12.7 | 5.50 |
| 0.35 | 14.9 | 4.91 |
| 0.4 | 17.0 | 4.43 |

**Table 2.S5** ACN material properties before and after peptide conjugation under saturating conditions.

| | ACN | ACNVax |
|---|---|---|
| **Particle Size (nm)** | **38 ± 3** | **44 ± 2** |
| **Polydispersity Index (PDI)** | **0.112 ± 0.04** | **0.087 ± 0.03** |
| **Zeta-Potential (mV)** | **-16 ± 4** | **-17 ± 1** |

**Table 2.S6** Lipid-coated IONP material properties before and after peptide conjugation under saturating conditions.

| | Lipid IONP | IONPVax |
|---|---|---|
| **Particle Size (nm)** | **38 ± 4** | **48 ± 5** |
| **Polydispersity Index (PDI)** | **0.068 ± 0.05** | **0.074 ± 0.02** |

**Table 2.S7** Heavy metal labeled antibody panel for CyTOF analysis in Lymph node (**Figure 3b**).

| Channel | Specificity | Clone | Vendor |
|---|---|---|---|
| 112Cd | CD19 | 6D5 | Life Technologies |
| 141Pr | IFNg | XMG1.2 | Biolegend |
| 142Nd | CD86 | GL-1 | Biolegend |
| 143Nd | CD80 | 16-10A1 | Biolegend |
| 144Nd | IgM | RMM-1 | Biolegend |
| 145Nd | CD4 | RM4-5 | Biolegend |
| 146Nd | CD45R (B220) | RA3-6B2 | Biolegend |

| | | | |
|---|---|---|---|
| 147Sm | CD206 | C068C2 | Biolegend |
| 148Nd | CD138 | 281-2 | Biolegend |
| 149Sm | CD8 | 53-6.7 | Biolegend |
| 150Nd | mPDCA-1 (CD317) | 129C1 | Biolegend |
| 151Eu | CD49b (DX5) | DX5 | Biolegend |
| 152Sm | Ly-6C | HK1.4 | Novus Biologicals |
| 153Eu | IFNb | 7F-D3 | Abcam |
| 154Sm | CD11c | N418 | Biolegend |
| 155Gd | IA-IE | M5/114.15.2 | Biolegend |
| 156Gd | CD25 | 3C7 | Biolegend |
| 158Gd | IgD | 11-26c-2a | Biolegend |
| 159Tb | Ly-6G | 1A8 | Biolegend |
| 160Gd | Il-4 | 11B11 | Biolegend |
| 161Dy | Il-17a | TC11-18H10.1 | Biolegend |
| 162Dy | TCRγδ | GL3 | Biolegend |
| 163Dy | CD64 | X54-5/7.1 | Biolegend |
| 164Dy | Il-10 | JES5-16E3 | Biolegend |
| 165Ho | CD115 | AFS98 | Biolegend |
| 166Er | CXCR5 | 614641 | Novus Biologicals |
| 167Er | FR4 | TH6 | Biolegend |
| 168Er | CD24 | M1/69 | Biolegend |
| 169Tm | CXCR4 | L276F12 | Biolegend |
| 170Er | CD62L | MEL-14 | Biolegend |

| | | | |
|---|---|---|---|
| 171Yb | CD44 | IM7 | Biolegend |
| 172Yb | CD11b | M1/70 | Fluidigm |
| 173Yb | PD-1 | RMP1-30 | Biolegend |
| 174Yb | GL7 | GL7 | Biolegend |
| 175Lu | F4/80 | BM8 | Biolegend |
| 176Yb | GmzB | GB11 | Abcam |
| 209Bi | CD3 | 145-2C11 | Biolegend |
| 89Y | mCD45 | 30-F11 | Fluidigm |
| 195Pt | Cisplatin | Live/Dead | Fluidigm |
| 191/193Ir | DNA Intercalator | DNA | Fluidigm |

**Table 2.S8** Murine HER-2 antibody (Murine 2C4) Amino Acids Sequences.

| | |
|---|---|
| Heavy Chain Variable Region | EVQLQQSGPELVKPGTSVKISCKASGFTFTDYTMDWVKQSHGKSLE WIGDVNPNSGGSIYNQRFKGKASLTVDRSSRIVYMELRSLTFEDTAV YYCARNLGPSFYFDYWGQGTTLTVSS |
| Heavy Chain Constant Region<br><br>(Mouse IgG2a) | AKTTAPSVYPLAPVCGDTTGSSVTLGCLVKGYFPEPVTLTWNSGSL SSGVHTFPAVLQSDLYTLSSVTVTSSTWPSQSITCNVAHPASSTKVD KKIEPRGPTIKPCPPCKCPAPNLLGGPSVFIFPPKIKDVLMISLSPIVTC VVVDVSEDDPDVQISWFVNNVEVHTAQTQTHREDYNSTLRVVSALP IQHQDWMSGKEFKCKVNNKDLPAPIERTISKPKGSVRAPQVYVLPP PEEEMTKKQVTLTCMVTDFMPEDIYVEWTNNGKTELNYKNTEPVLD SDGSYFMYSKLRVEKKNWVERNSYSCSVVHEGLHNHHTTKSFSRT PGK |
| Light Chain Variable Region | DTVMTQSHKIMSTSVGDRVSITCKASQDVSIGVAWYQQRPGQSPKL LIYSASYRYTGVPDRFTGSGSGTDFTFTISSVQAEDLAVYYCQQYYI YPYTFGGGTKLEIK |

| | |
|---|---|
| Light Chain Constant Region<br><br>(Mouse Ig Kappa) | RADAAPTVSIFPPSSEQLTSGGASVVCFLNNFYPKDINVKWKIDGSE<br>RQNGVLNSWTDQDSKDSTYSMSSTLTLTKDEYERHNSYTCEATHK<br>TSTSPIVKSFNRNEC |

**Table 2.S9** Heavy metal labeled antibody panel for CyTOF analysis in Tumor (**Figure 5a**).

| **Channel** | **Specificity** | **Clone** | **Vendor** |
|---|---|---|---|
| 112Cd | CD19 | 6D5 | Life Technologies |
| 141Pr | IFNg | XMG1.2 | Biolegend |
| 142Nd | CD86 | GL-1 | Biolegend |
| 143Nd | CD80 | 16-10A1 | Biolegend |
| 144Nd | Siglec-F | E50-2440 | BD Biosciencies |
| 145Nd | CD4 | RM4-5 | Biolegend |
| 146Nd | CD45R (B220) | RA3-6B2 | Biolegend |
| 147Sm | CD206 | C068C2 | Biolegend |
| 148Nd | CD138 | 281-2 | Biolegend |
| 149Sm | CD8 | 53-6.7 | Biolegend |
| 150Nd | mPDCA-1 (CD317) | 129C1 | Biolegend |
| 151Eu | CD49b (DX5) | DX5 | Biolegend |
| 152Sm | Ly-6C | HK1.4 | Novus Biologicals |
| 154Sm | CD11c | N418 | Biolegend |
| 155Gd | IA-IE | M5/114.15.2 | Biolegend |
| 156Gd | CD25 | 3C7 | Biolegend |
| 158Gd | TIM-3 | RMT3-23 | Biolegend |

| | | | |
|---|---|---|---|
| 159Tb | Ly-6G | 1A8 | Biolegend |
| 160Gd | Il-4 | 11B11 | Biolegend |
| 161Dy | Il-17a | TC11-18H10.1 | Biolegend |
| 162Dy | TCRγδ | GL3 | Biolegend |
| 163Dy | Il-17f | 316016 | Novus Biologicals |
| 164Dy | Il-10 | JES5-16E3 | Biolegend |
| 165Ho | CD115 | AFS98 | Biolegend |
| 166Er | CXCR5 | 614641 | Novus Biologicals |
| 167Er | FR4 | TH6 | Biolegend |
| 168Er | NOS2 | 5C1B52 | Biolegend |
| 169Tm | Ly-6A/E (Sca-1) | D7 | Biolegend |
| 170Er | CD62L | MEL-14 | Biolegend |
| 171Yb | CD44 | IM7 | Biolegend |
| 172Yb | CD11b | M1/70 | Fluidigm |
| 173Yb | PD-1 | RMP1-30 | Biolegend |
| 174Yb | CTLA-4 | UC10-4B9 | Biolegend |
| 175Lu | F4/80 | BM8 | Biolegend |
| 176Yb | GmzB | GB11 | Abcam |
| 209Bi | CD3 | 145-2C11 | Biolegend |
| 89Y | mCD45 | 30-F11 | Fluidigm |
| 195Pt | Cisplatin | Live/Dead | Fluidigm |
| 191/193Ir | DNA Intercalator | DNA | Fluidigm |

# Supporting Methods

## Preparation and characterization of different nanovaccine controls.

### AuNPVax

The synthesis of AuNP is the same as that in the preparation of ACN. AuNPs (2 nm) were synthesized by reacting sodium sulfide (Na2S) as the reducing reagent with gold in the form of chloroauric acid (HAuCl4). HER2 peptide was added to AuNPs following the same amount in the preparation of ACN in Milli-Q water and incubated overnight at 4 °C, and purified by magnetic separation overnight at 4 °C. AuNP-B/CD4 were imaged by STEM using a JEOL 2100F with a CEOS probe corrector.

### LipoVax

Liposome were prepared following the thin-film method[5]. DSPC (Avanti. Birmingham, Al), Cholesterol (Sigma-Aldrich, St. Louis, MO) and PEG2000-DSPE-MAL (Avanti. Birmingham, Al) were dissolved in chloroform at the weight ratio of 20:1:5 and dried under reduced pressure at 37 ºC until they formed a thin lipid film. The lipid film was hydrated with warm PBS, followed by sonication with a bath type sonicator. HER2 peptides were conjugated to PEG2000-DSPE-MAL on the surface of liposome via maleimide-thiol chemistry. HER2 peptide was added to liposome at a 5× weight ratio excess in Milli-Q water and incubated overnight at 4 °C, and purified either by magnetic separation overnight at 4 °C. The hydrodynamic particle size, polydispersity index and zeta potential were evaluated with a Malvern Zetasizer Nano-ZS in Milli-Q water at 25 °C.

### Confocal imaging for B Cell uptake *in-vitro*

ACNVax-EDFITC, IONPVax-EDFITC and PepVax-EDFITC peptide cellular uptakes were evaluated in primary B-cells isolated from murine spleens using an EasySep Mouse B-cell isolation kit. Cells were incubated with ACNVax-EDFITC, IONPVax-EDFITC and PepVax-EDFITC (25 μg/mL HER2-B/CD4 epitope) for 15 mins, 30 mins and 60 mins. Cells were then washed, fixed and plated onto eight-well glass chambers pretreated with 0.1% poly-l-lysine (LabTech II) on ice for at least 4 hours before confocal imaging.

### *In-vitro* B cell uptake

ACNVax and IONPVax cellular uptakes were evaluated in primary B-cells isolated from murine spleens using an EasySep Mouse B-cell isolation kit. Nanoparticle samples were incubated at 50 μg/mL Fe with cells for 18 hours in blank RPMI media at 37 °C, 5% $CO_2$/95% air atmosphere and

approximately 85% relative humidity. After 18 hours, cells were lifted by cell scraping and washed thrice with PBS. Following the wash steps, resulting cell pellets were re-suspended in 1 mL of PBS, cell counted and then digested in 1 mL aqua regia (1:3 molar ratio nitric acid: hydrochloric acid) for analysis by ICP-MS.

**Quantification of nanoparticle delivery to lymph nodes *in-vivo***

Mice were injected subcutaneously in the left hock with either IONP or ACN at a dose of 200 µg Fe per mouse. At the designated time intervals, mice were sacrificed and lymph nodes of interest were dissected for *ex-vivo* analysis. The extent of nanoparticle delivery to the lymph nodes was quantified using ICP-MS based on previously reported protocols[6].

**Quantification of peptide delivery to lymph nodes *in-vivo***

To facilitate quantification of peptide delivery to lymph nodes, lysine terminally modified HER2 peptides were chemically conjugated to sulfo-Cy5.5 NHS Ester. This conjugation was carried out at a 5-fold molar excess of sulfo-Cy5.5 NHS Ester to PepVax. IONPVax-Cy5.5 and ACNVax-Cy5.5 were subjected to Cy5.5 functionalization after initial peptide conjugation was completed to enable facile purification of excess fluorescent dye by magnetic separation. Subsequent to Cy5.5 functionalization, mice were injected as previously stated. After 3 hours, mice were sacrificed and lymph nodes of interest were dissected for *ex-vivo* analysis by IVIS imaging. IVIS imaging was utilized for semi-quantification of peptide delivery in terms of radiant efficiency.

**3D imaging of in vivo lymph node distribution**

To determine the ACNVax (conjugated to ED-FITC labeled HER2-B/CD4 peptide, 233.6 nmol HER2 epitope) distribution, lymph nodes were harvested 12 hours after subcutaneous dosing. Harvested tissues were immediately processed following iDisco protocol for clearing and staining of antibodies. Brilliant Violet 421 B220, Alexa Fluor® 594 CD 3 and Alexa Fluor® 647 CD169 were validated and used for lymph node immune fluorescence staining. 3D imaging was then conducted on Bruker MuVi SPIM.

*Sample Pretreatment with Methanol*

1. Dehydrate with methanol/H2O series: 20%, 40%, 60%, 80%, 100%; 1h each.

2. Wash further with 100% methanol for 1h and then chill the sample at 4°c.

3. Overnight incubation, with shaking, in 66% DCM / 33% Methanol at RT

4. Wash twice in 100% Methanol at RT, and then chill the sample at 4°c

5. Bleach in chilled fresh 5%H2O2 in methanol (1 volume 30% H2O2 to 5 volumes MeOH), overnight at 4°c.

6. Rehydrate with methanol/H2O series: 80%, 60%, 40%, 20%, PBS; 1h each at RT.

7. Wash in PTx.2 RT 1h x2 at RT.

*Immunolabeling*

1. Incubate samples in Permeabilization Solution, 37°C **n**/2 days (max. 2 days)

2. Block in Blocking Solution, 37 °, **n**/2 days (max. 2 days).

3. Incubate with primary antibody in PTwH/5%DMSO/3% Donkey Serum, 37°, n days.

4. Wash in PTwH for 4-5 times until the next day.

*Clearing*

1. Dehydrate in methanol/H2O series: 20%, 40%, 60%, 80%, 100%, 100%; 1hr each at RT. Can be left optionally overnight at RT at this point.

2. 3H incubation, with shaking, in 66% DCM / 33% Methanol at RT

3. Incubate in 100% DCM (Sigma 270997-12X100ML) 15 minutes twice (with shaking) to wash the MeOH.

4. Incubate in Dibenzyl Ether (DBE, Sigma 108014-1KG) (no shaking). The tube should be filled almost completely with DBE to prevent the air from oxidizing the sample. Before imaging, invert the tube a couple of time to finish mixing the solution.

**Supporting bibliography**

(1) Mingueneau, M.; Krishnaswamy, S.; Spitzer, M. H.; Bendall, S. C.; Stone, E. L.; Hedrick, S. M.; Pe'er, D.; Mathis, D.; Nolan, G. P.; Benoist, C. Single-cell mass cytometry of TCR signaling: amplification of small initial differences results in low ERK activation in NOD mice. *PNAS* **2014**, *111* (46), 16466-16471. DOI: 10.1073/pnas.1419337111.
(2) Billi, A. C.; Gharaee-Kermani, M.; Fullmer, J.; Tsoi, L. C.; Hill, B. D.; Gruszka, D.; Ludwig, J.; Xing, X.; Estadt, S.; Wolf, S. J.; et al. The female-biased factor VGLL3 drives cutaneous and systemic autoimmunity. *JCI Insight* **2019**, *4* (8). DOI: 10.1172/jci.insight.127291.

(3) Kokate, M.; Garadkar, K.; Gole, A. One pot synthesis of magnetite–silica nanocomposites: applications as tags, entrapment matrix and in water purification. *J Mater Chem A* **2013**, *1* (6), 2022-2029, 10.1039/C2TA00951J. DOI: 10.1039/C2TA00951J.
(4) Lu, Y.; Wang, L.; Chen, D.; Wang, G. Determination of the concentration and the average number of gold atoms in a gold nanoparticle by osmotic pressure. *Langmuir* **2012**, *28* (25), 9282-9287. DOI: 10.1021/la300893e.
(5) Wang, N.; Chen, M.; Wang, T. Liposomes used as a vaccine adjuvant-delivery system: From basics to clinical immunization. *J control release* **2019**, *303*, 130-150. DOI: 10.1016/j.jconrel.2019.04.025.
(6) Chertok, B.; Cole, A. J.; David, A. E.; Yang, V. C. Comparison of electron spin resonance spectroscopy and inductively-coupled plasma optical emission spectroscopy for biodistribution analysis of iron-oxide nanoparticles. *Mol pharmaceutics* **2010**, *7* (2), 375-385. DOI: 10.1021/mp900161h.

# Appendix B

## Supporting Information from Chapter 4

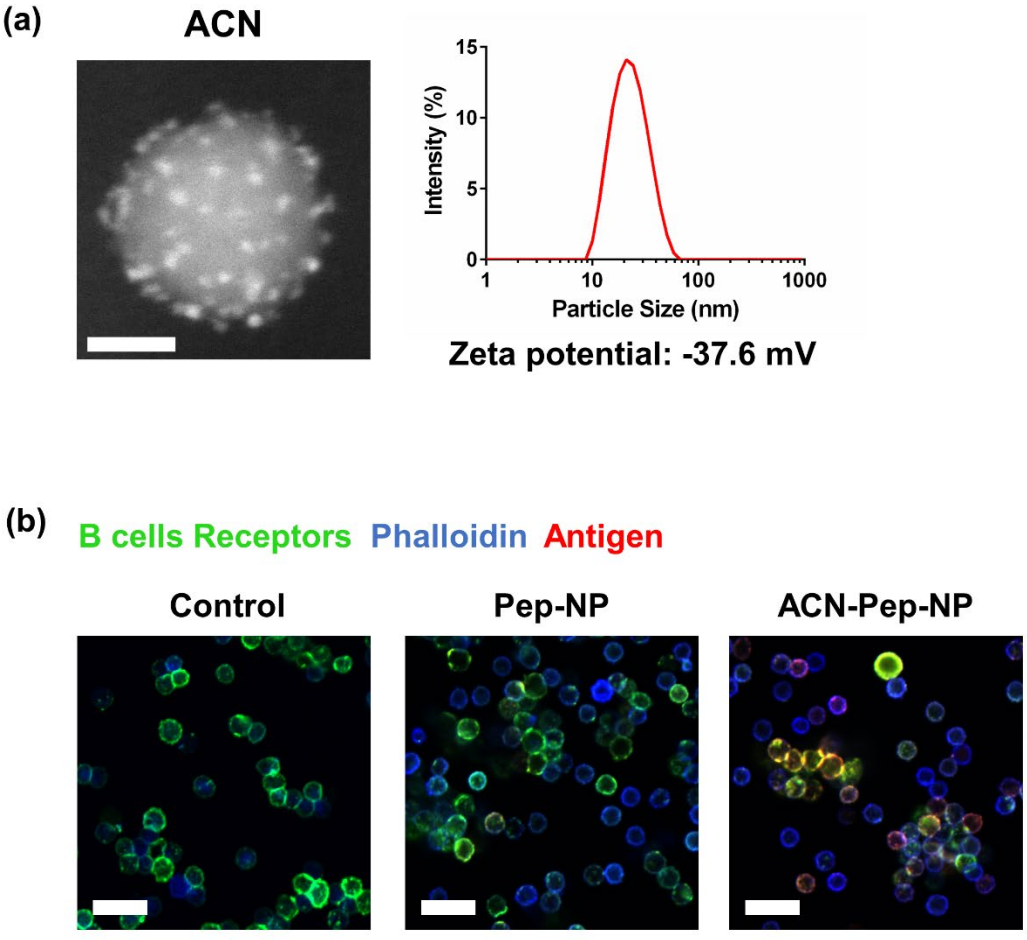


**Figure 3.S1** (**a**) Transmission electron microscopy (TEM) image of ACN. Scale bar is 10 µm. Representative volume-weighted particle size distribution of ACN. (**b**) Confocal image of Cy3 and hapten labeled ACN-Pep-NP (red) binding/crosslinking (yellow) with B cell receptor (antibody staining, green) in hapten-specific B cells from QM mice splenocytes, compared with Cy3 and hapten labeled CD4/B antigen (Pep-NP). Blue, phalloidin stain of actin filaments; green, B cell receptor staining using Alexa Fluor 488-

AffiniPure Fab Fragment Goat Anti-Mouse IgM (μ Chain Specific) antibody; red: Cy3-labeled CD4/B-hapten epitope. The scale bar is 20 μm.

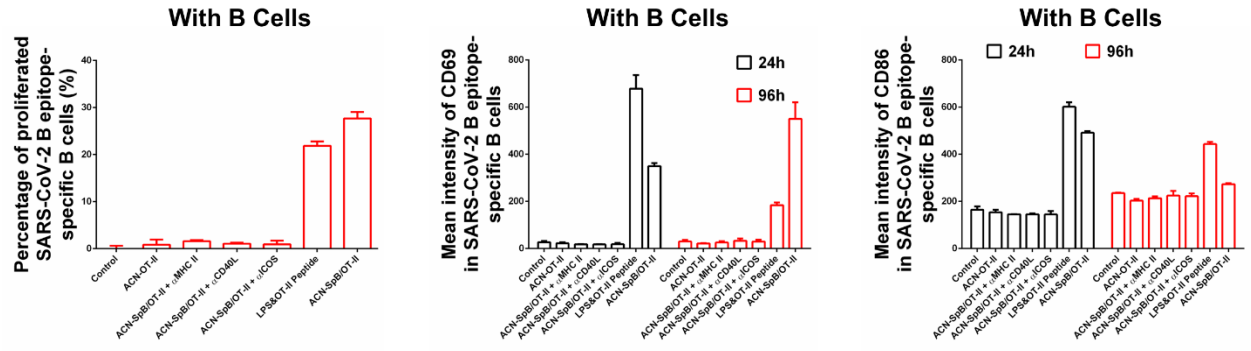


**Figure 3.S2** Flow cytometry quantification and representative analysis (96 h) of B cell proliferation from spike protein immunized mice, measured by the percentage of decrease in CFSE+ hapten-specific B cells compared to controls. Flow cytometry quantification and representative analysis (24 h and 96 h) of B cell from spike protein immunized mice activation by measuring geometric mean intensity of CD69 and CD86 markers. For αMHC-II, αICOS and αCD40L antibodies preincubation, all antibodies (20 μg/mL) were preincubated overnight with cells before antigen incubation.

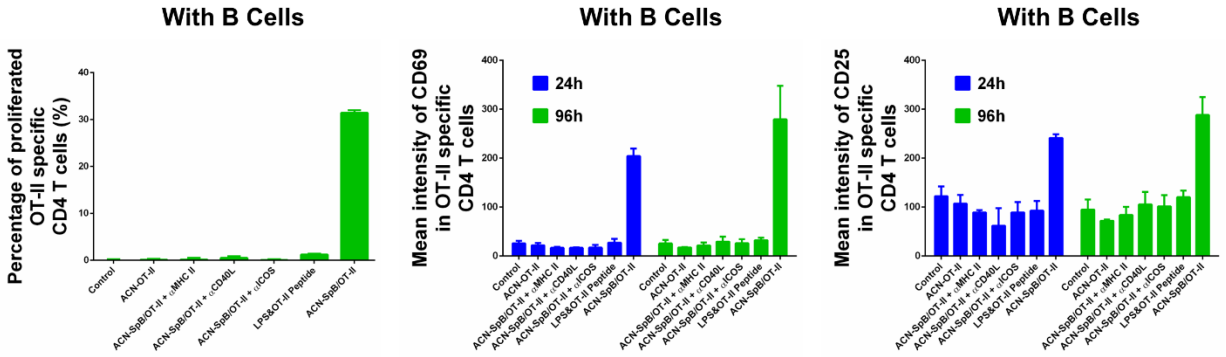


**Figure 3.S3** Flow cytometry quantification and representative analysis (96 h) of OT-II CD4 T cell proliferation, measured by the percentage of decrease in CFSE+ OT-II CD4 T cells compared to controls. Flow cytometry quantification and representative analysis (24 h and 96 h) of OT-II CD4 T cell activation by measuring geometric mean intensity of CD69 and CD25 markers. For αMHC-II, αICOS and αCD40L antibodies preincubation, all antibodies (20 μg/mL) were preincubated overnight with cells before antigen incubation.

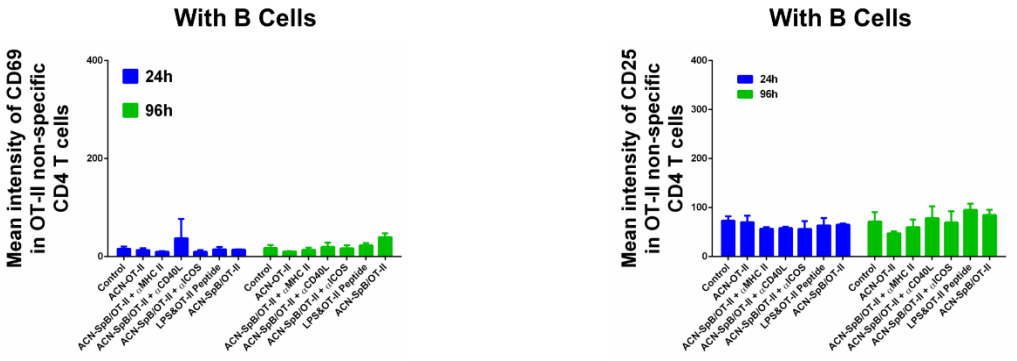


**Figure 3.S4** Flow cytometry quantification and representative analysis (24 h and 96 h) of CD4 T cell from spike protein immunized mice, activation by measuring geometric mean intensity of CD69 and CD25 markers. For αMHC-II, αICOS and αCD40L antibodies preincubation, all antibodies (20 μg/mL) were preincubated overnight with cells before antigen incubation.

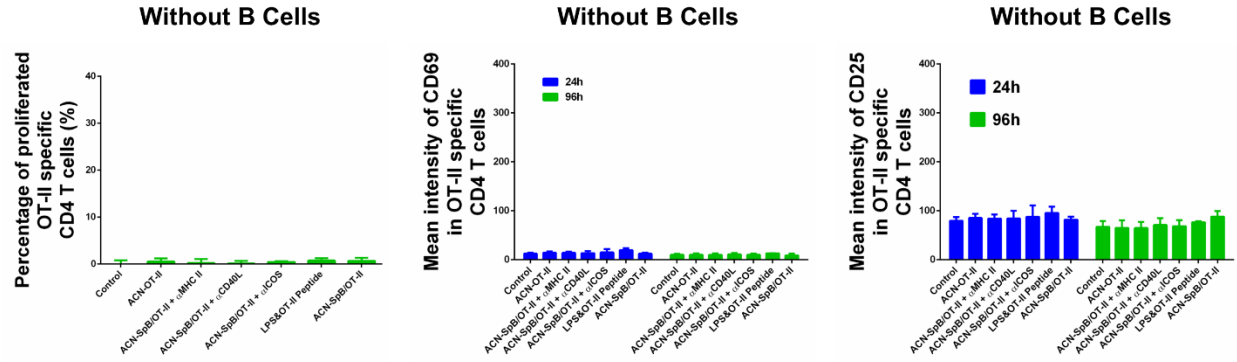


**Figure 3.S5** Flow cytometry quantification and representative analysis (96 h) of OT-II CD4 T cell proliferation without coincubation with B cells, measured by the percentage of decrease in CFSE+ OT-II CD4 T cells compared to controls. Flow cytometry quantification and representative analysis (24 h and 96 h) of OT-II CD4 T cell activation without coincubation with B cells by measuring geometric mean intensity of CD69 and CD25 markers. For αMHC-II, αICOS and αCD40L antibodies preincubation, all antibodies (20 μg/mL) were preincubated overnight with cells before antigen incubation.

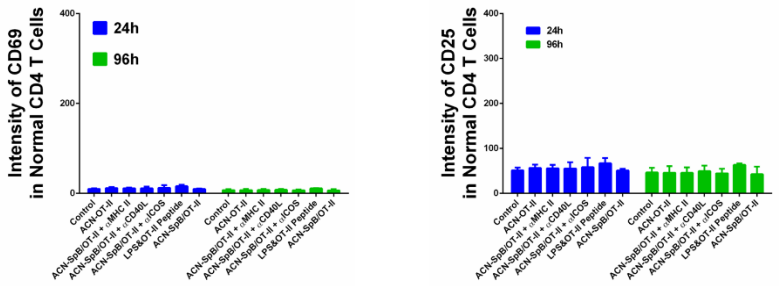


**Figure 3.S6** Flow cytometry quantification and representative analysis (24 h and 96 h) of CD4 T cell from spike protein immunized mice, activation without coincubation with B cells by measuring geometric mean intensity of CD69 and CD25 markers. For αMHC-II, αICOS and αCD40L antibodies preincubation, all antibodies (20 μg/mL) were preincubated overnight with cells before antigen incubation.

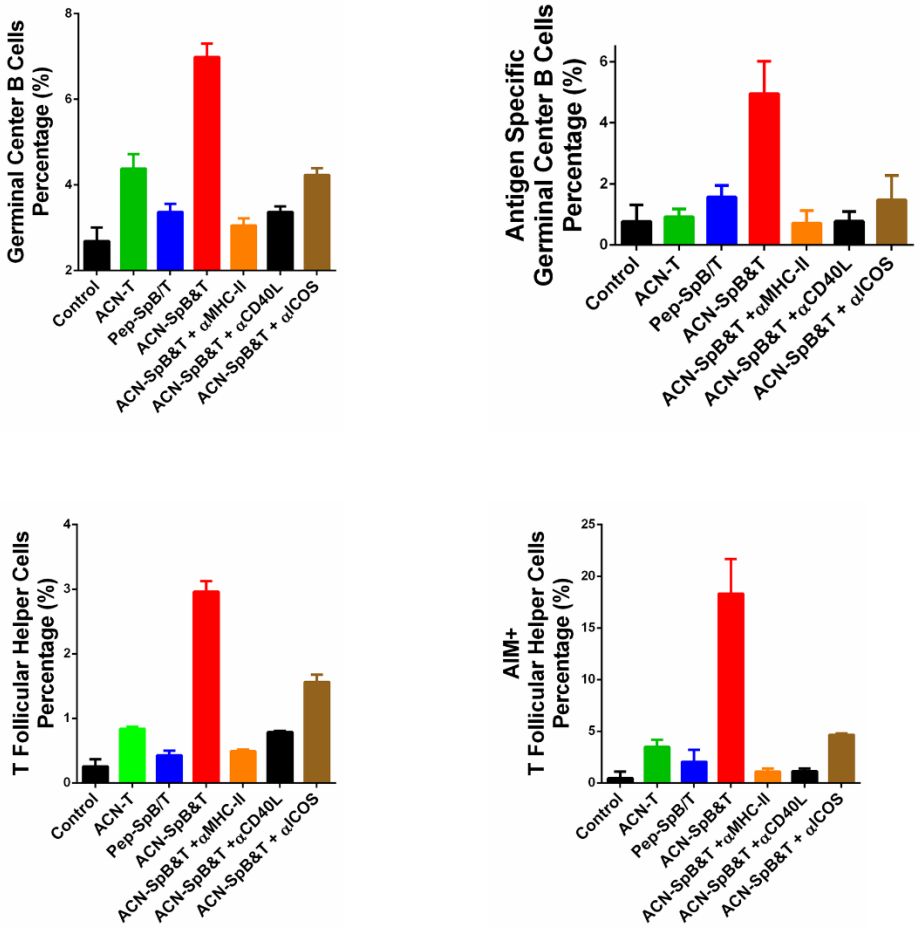


**Figure 3.S7** Flow cytometry quantification and representative analysis of germinal center (GC) B cells, antigen specific GC B cells, T follicular helper (Tfh) cells and activation-induced markers (AIM) positive Tfh cells in lymph nodes.

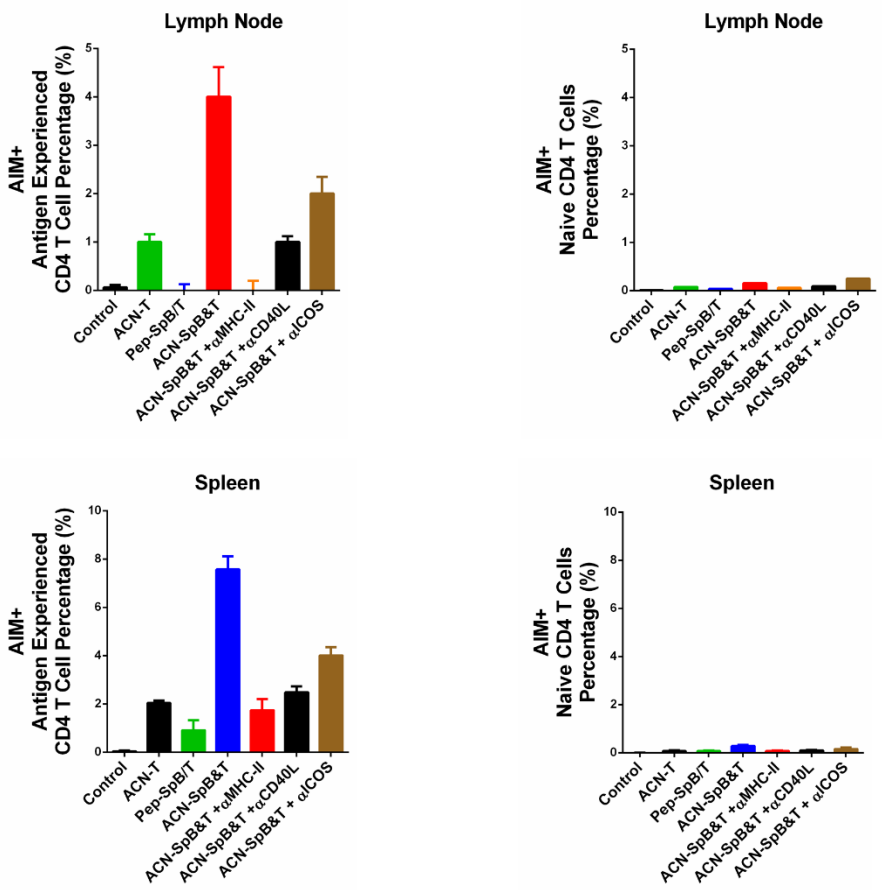


**Figure 3.S8** Flow cytometry quantification of activation-induced markers (AIM) positive antigen experienced cells and AIM$^+$ naive cells at lymph node (**h**) and spleen (**j**). CD69$^+$ CD40L$^{+/-}$ populations from Tfh cells were identified as AIM$^+$ Tfh cells. B220$^-$ CD4$^+$ CD62L$^+$ CD69$^+$ CD40L$^{+/-}$ populations were identified as AIM$^+$ antigen experienced CD4 T cells. B220$^-$ CD4$^+$ CD62L$^-$ CD69$^+$ CD40L$^{+/-}$ populations were identified as AIM$^+$ naïve CD4 T cells. Data for quantification are shown as mean ± SD, n = 3.

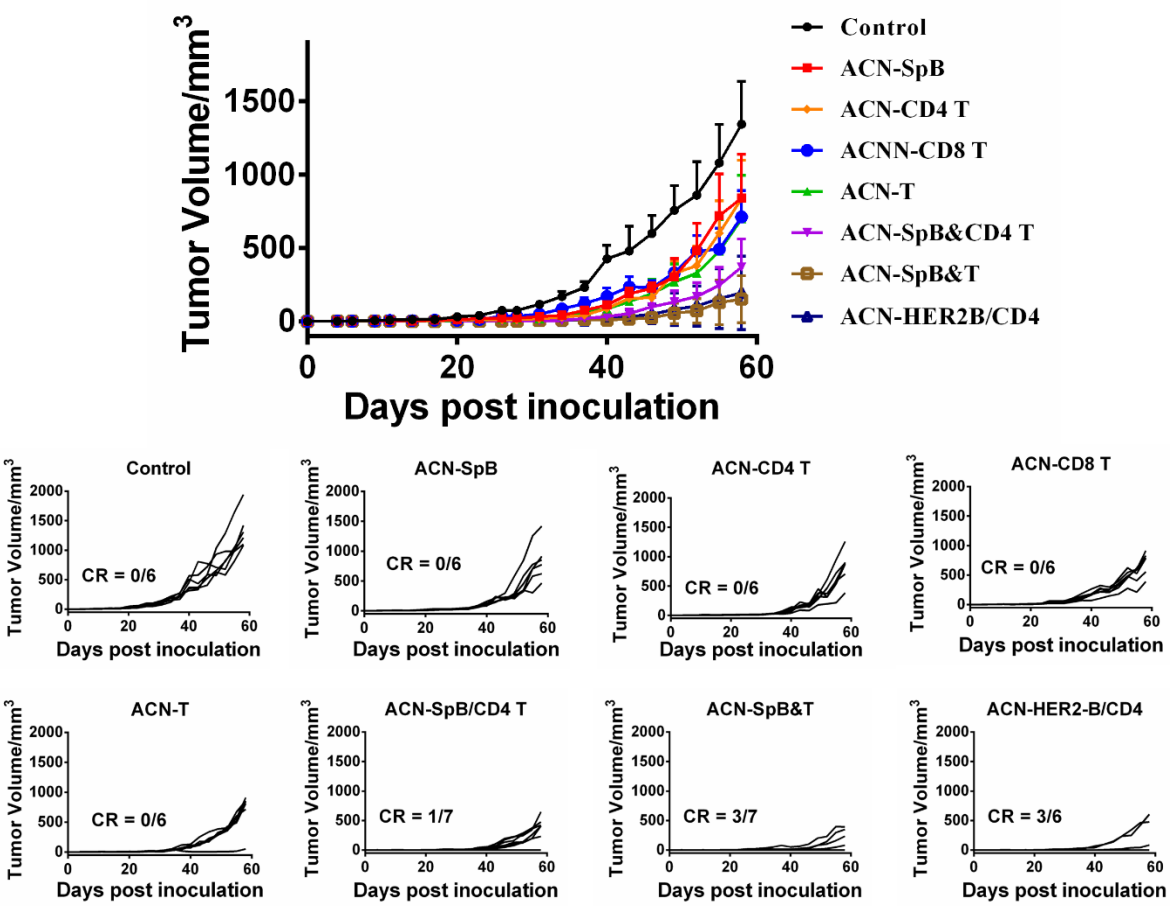


**Figure 3.S9** Antitumor efficacy of ACN with SARS-CoV-2 B epitope, HER2 CD4 T cell antigen, HER2 CD8 T cell antigen, HER2 CD4/8 T cell antigen, SARS-CoV-2 B epitope and HER2 CD4 T cell antigens, SARS-CoV-2 B epitope and HER2 CD4/8 T cell antigens or HER2 B and HER2 CD4/8 T cell antigens, respectively, in breast cancer model with D2E2F2 cells.

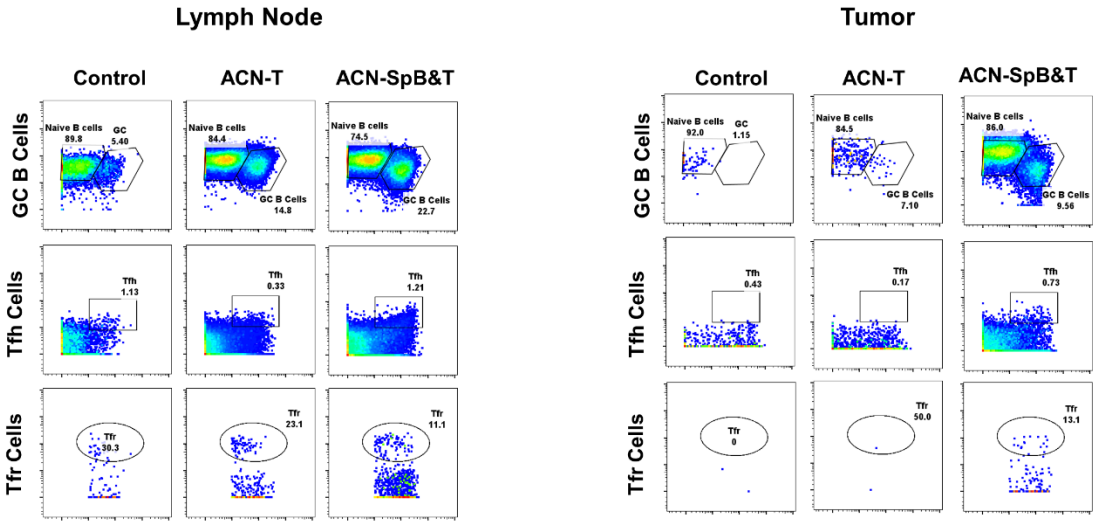


**Figure 3.S10** Cytometry by Time-of-Flight (CyTOF) analysis of the germinal center B, T follicular helper and follicular regulatory cells from lymph node and tumor samples of mice 10 days after different treatments from **Figure 3.2**.

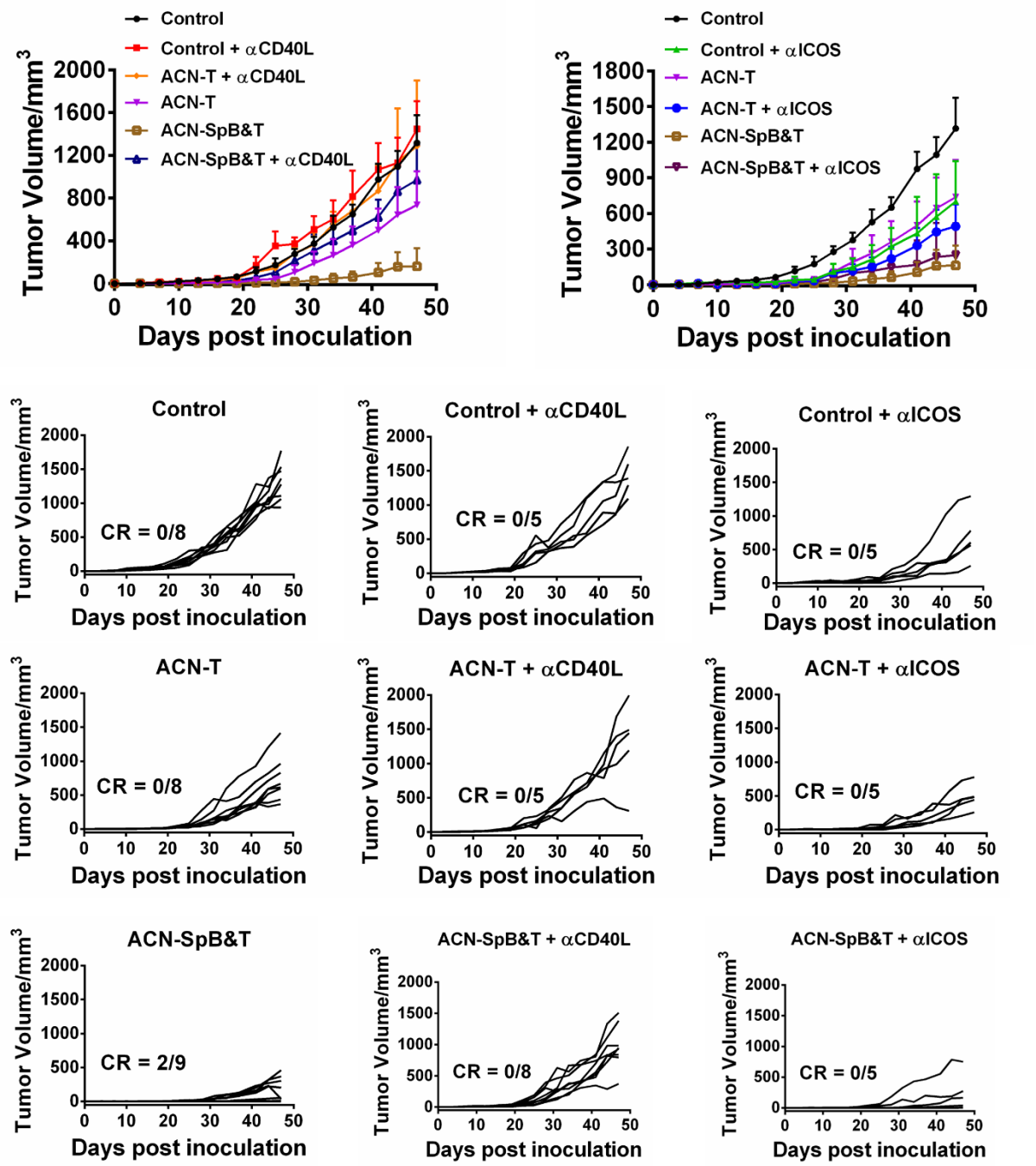


**Figure 3.S11** Antitumor efficacy of ACN with SARS-CoV-2 B epitope, HER2 CD4/8 T cell antigen, or SARS-CoV-2 B epitope and HER2 CD4/8 T cell antigens, respectively, in breast cancer model with D2E2F2 cells. For the αICOS (200 μg/mouse) or αCD40L (200 μg/mouse) antibodies blocking, antibody was intraperitoneal injected 10 days before vaccination, and then dosed 200 μg every three days.

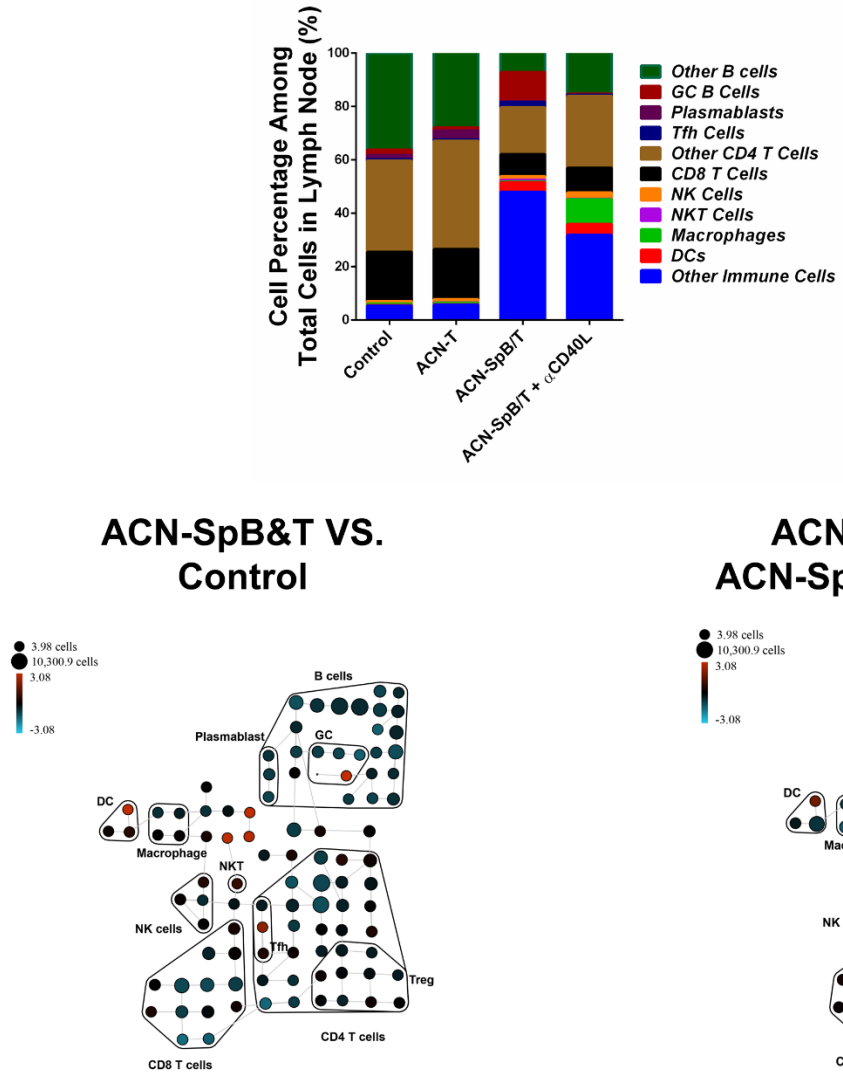


**Figure 3.S12** Cytometry by Time-of-Flight (CyTOF) analysis of the cell population from lymph node samples of mice 10 days after different treatments.

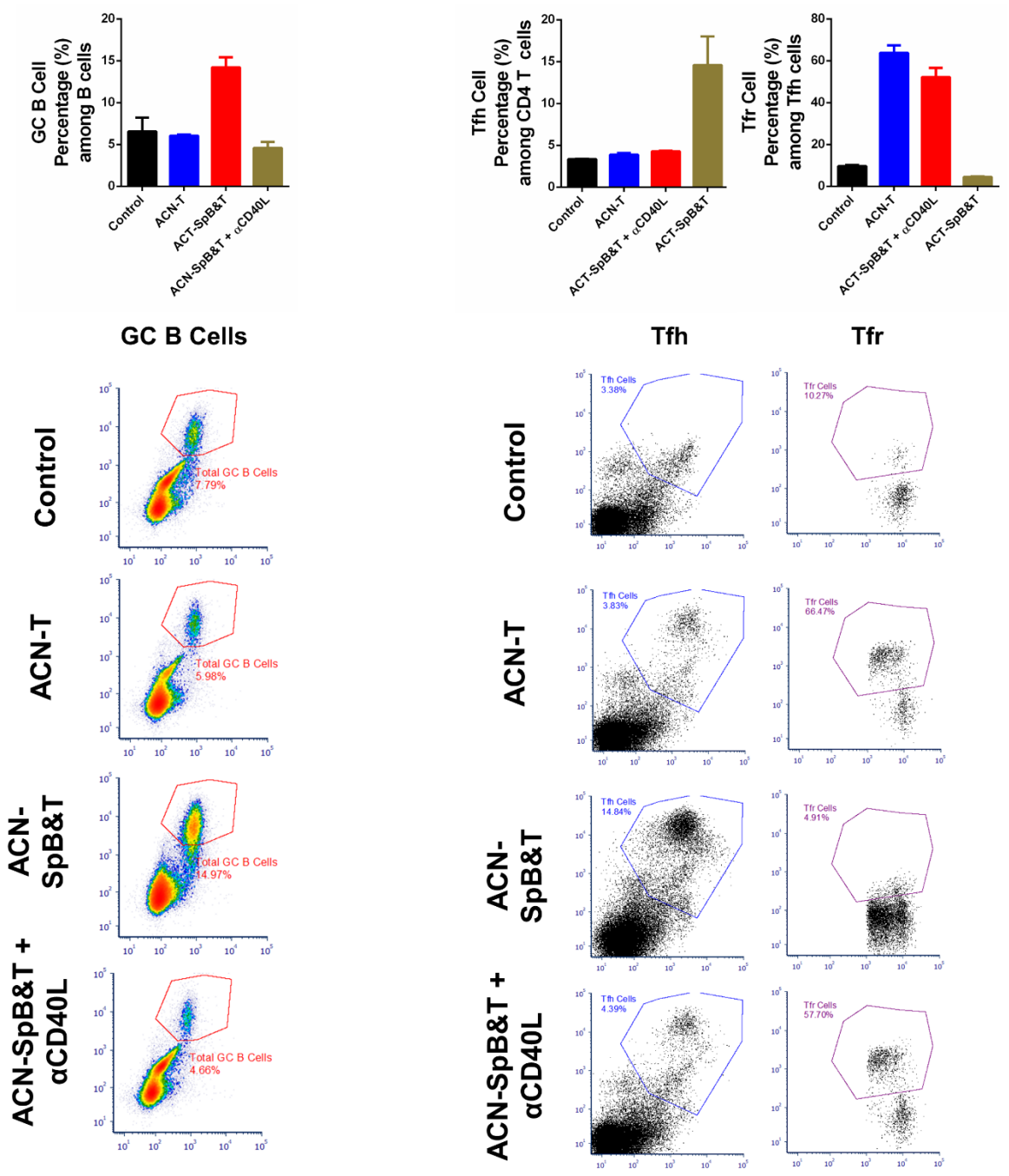


**Figure 3.S13** Flow cytometry quantification and representative analysis of GC B cells, Tfh cells and follicular regulatory cells from lymph node10 days after different treatments.

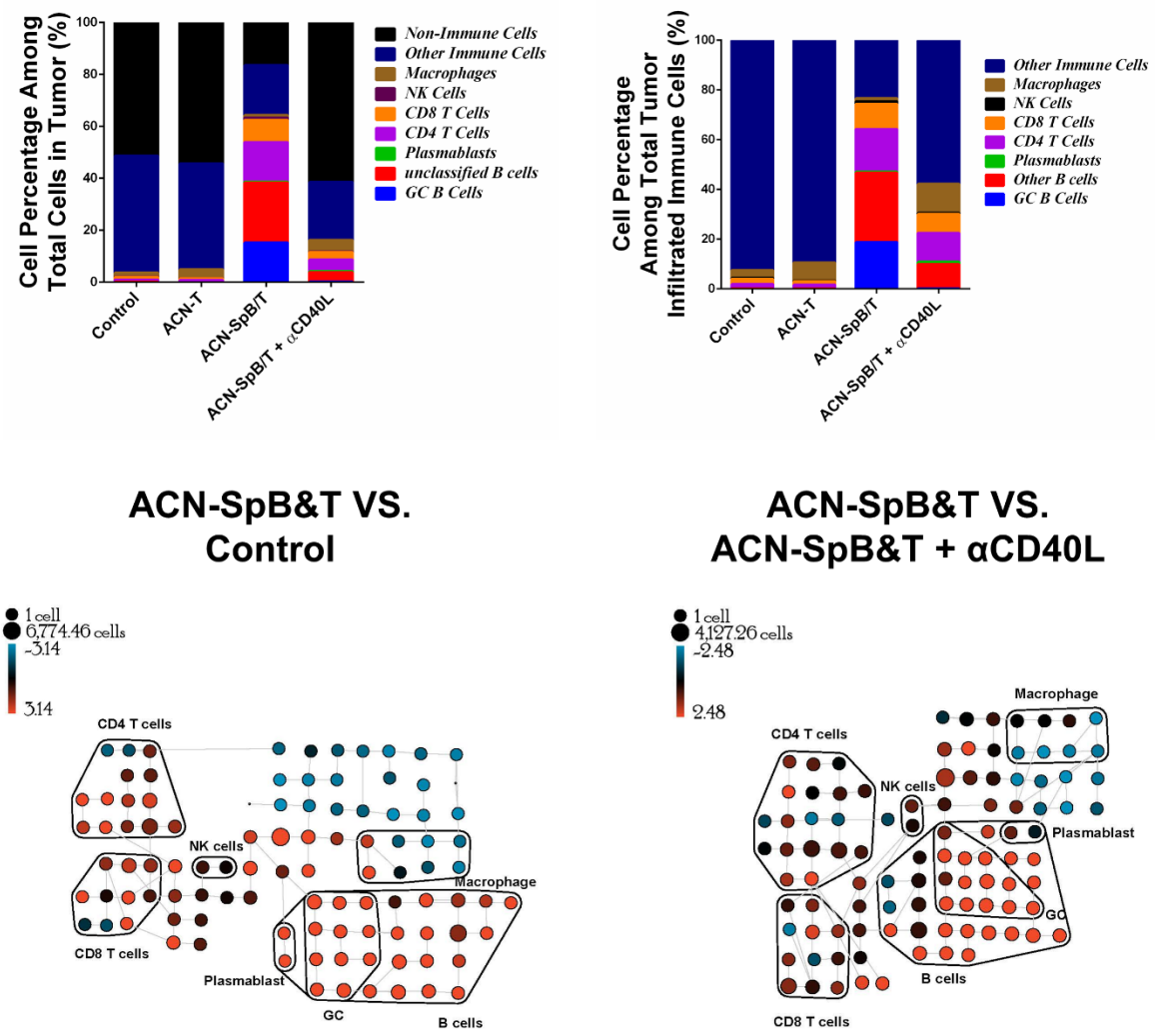


**Figure 3.S14** Cytometry by Time-of-Flight (CyTOF) analysis of the cell population from lymph node samples of mice 10 days after different treatments.

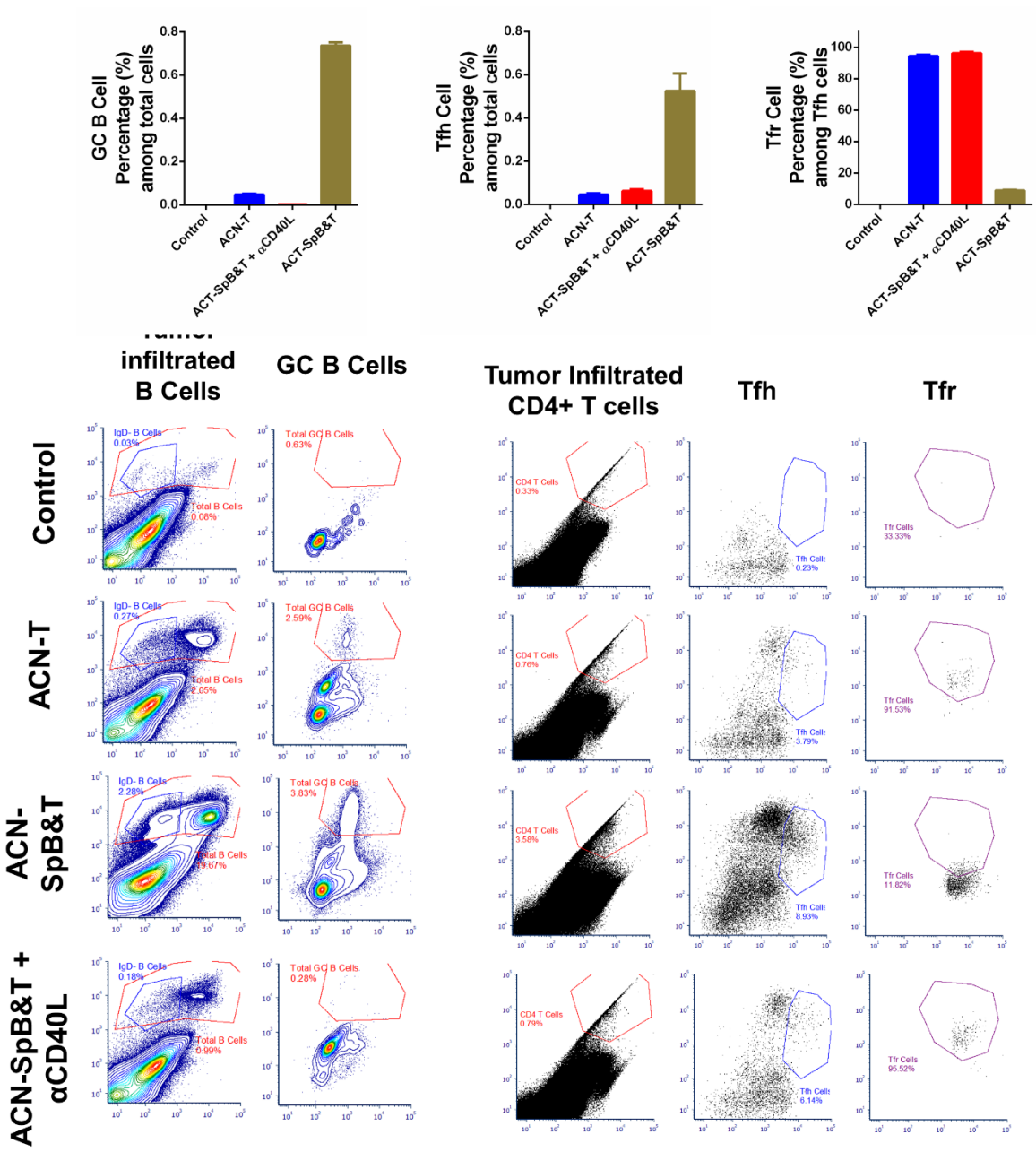


**Figure 3.S15** Flow cytometry quantification and representative analysis of GC B cells, Tfh cells and follicular regulatory cells from tumor 10 days after different treatments.

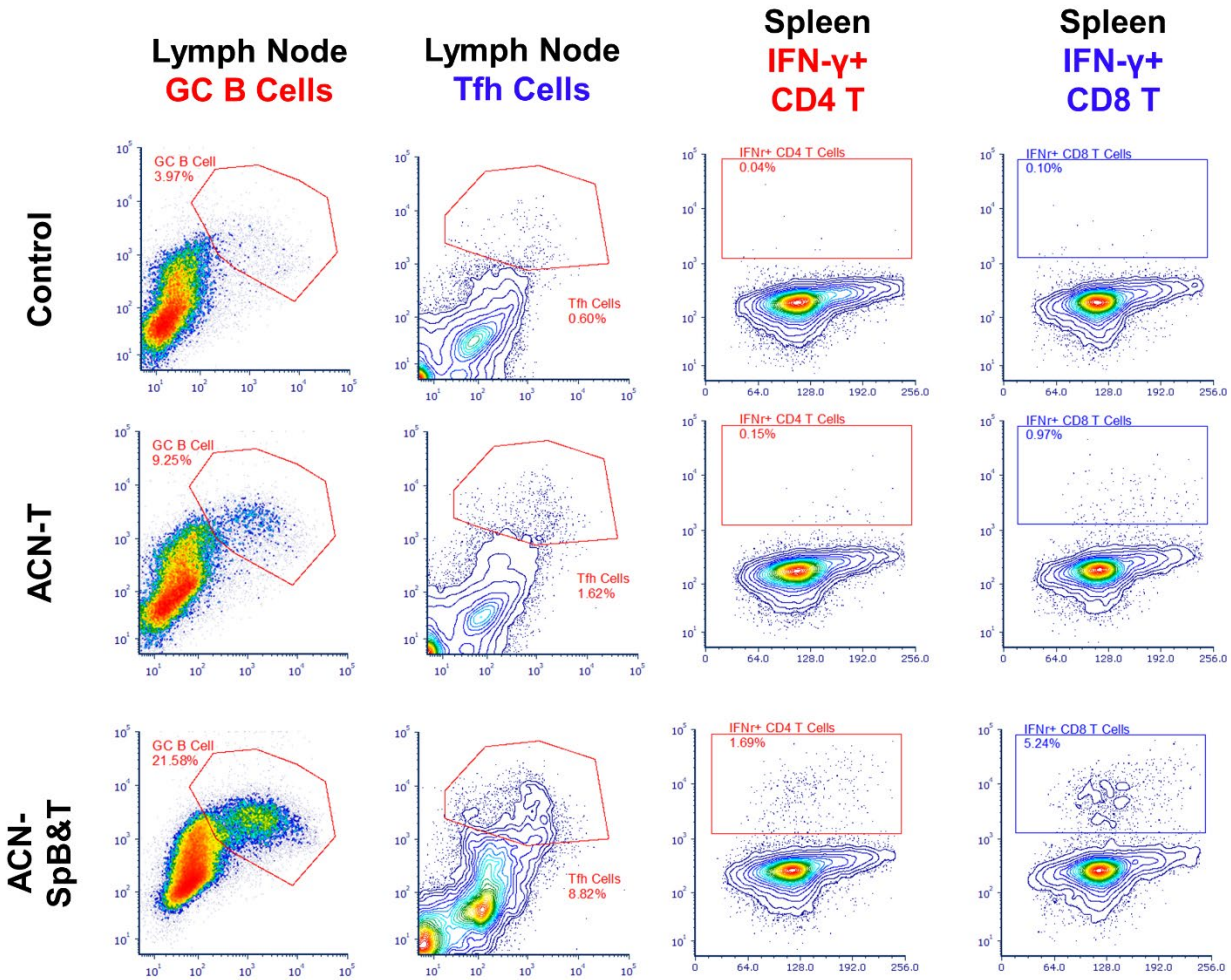


**Figure 3.S16** Flow cytometry quantification of GC B cells and Tfh cells from lymph node and antigen specific (IFN-γ+) CD4 T cells and antigen specific (IFN-γ+) CD8 T cells from tumor 5 days after the second booster vaccination from B16F10 model in **Figure 3.3**.

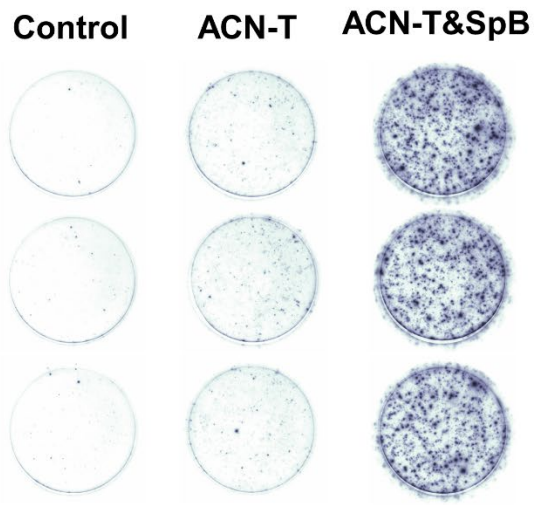


**Figure 3.S17** IFN-γ+ ELISPOT of splenocytes antitumor efficacy of B16F10 model from **Figure 3.3**.

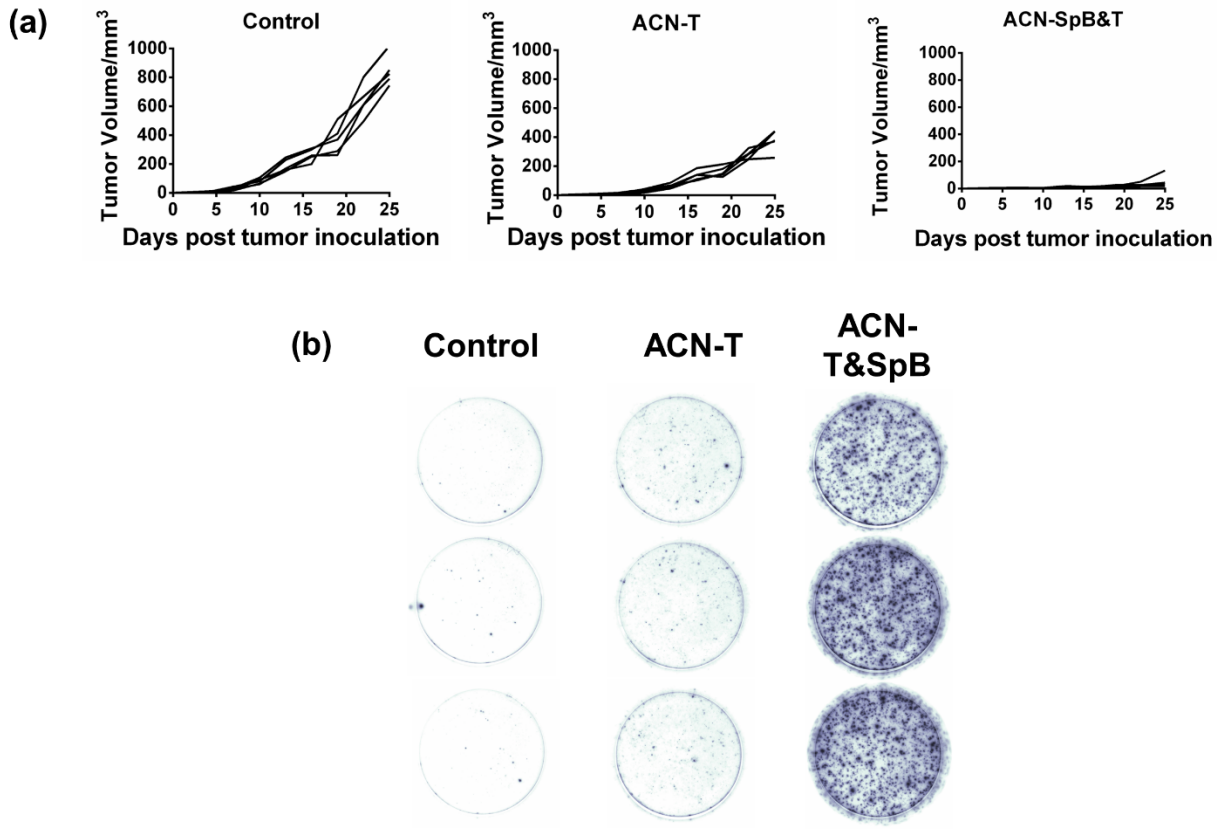


**Figure 3.S18** (**a**) Antitumor efficacy of ACN with SARS-CoV-2 B epitope and tumor T cell neoantigens compared with ACN with tumor T cell neoantigens in pancreatic cancer model with KPC 6422 cells. (**b**) IFN-γ+ ELISPOT of splenocytes antitumor efficacy of KPC model from **Figure 3.3**.

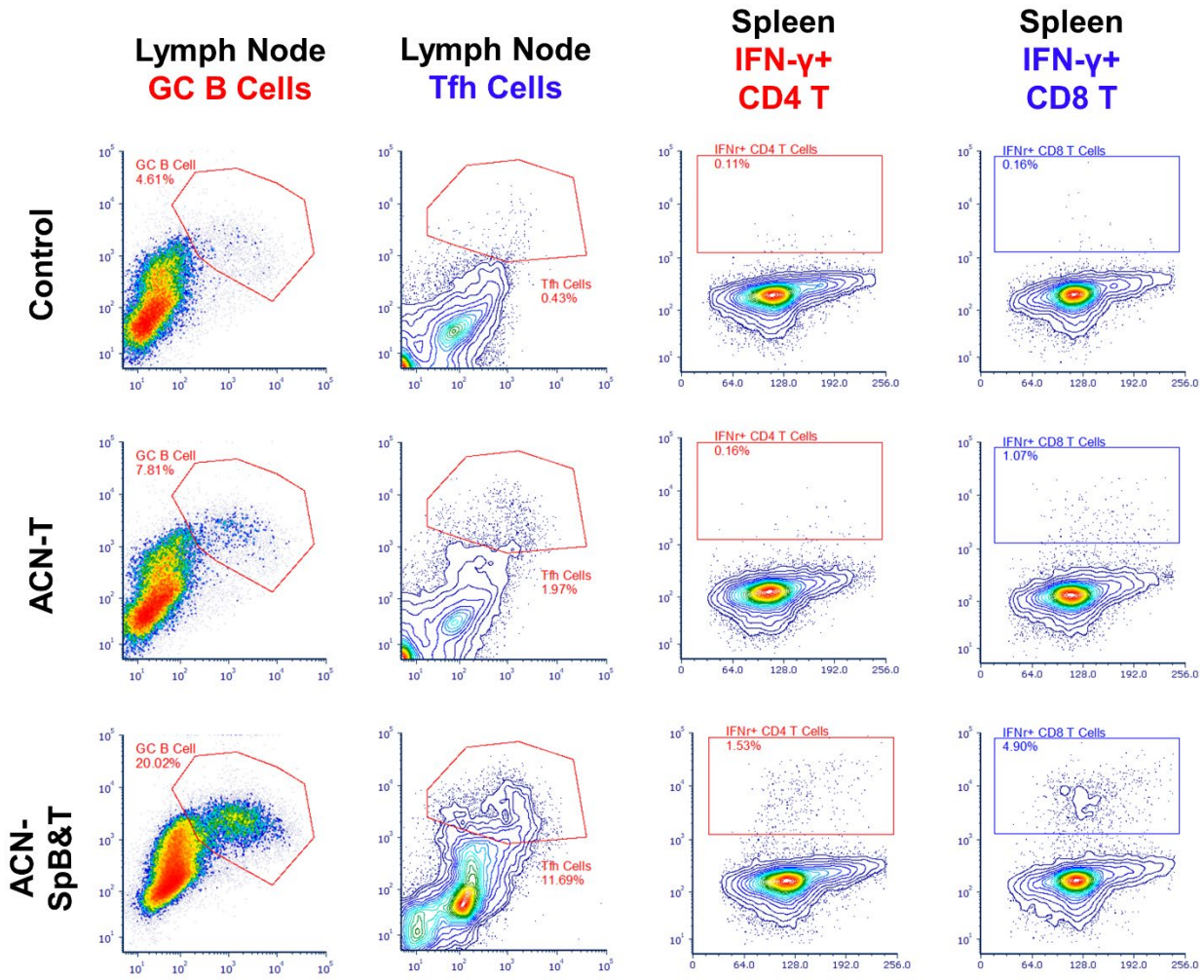


**Figure 3.S19** Flow cytometry quantification of GC B cells and Tfh cells from lymph node and antigen specific (IFN-γ+) CD4 T cells and antigen specific (IFN-γ+) CD8 T cells from tumor 5 days after the second booster vaccination from KPC model in **Figure 3.3**.

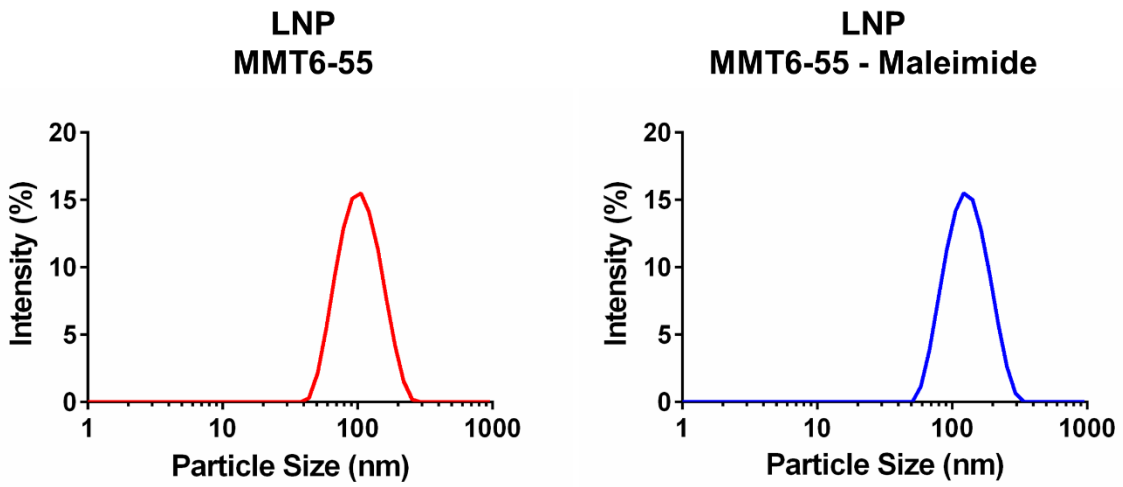


**Figure 3.S20** Volume-weighted particle size distribution of lipid nanoparticle formulated by ionizable lipid (MMT6-55), helper phospholipid (1,2-Distearoyl-sn-glycero-3-PC), cholesterol and PEG-lipid (DMG-PEG2000 or DMG-PEG2000-Maleimide) at predetermined molar ratios.

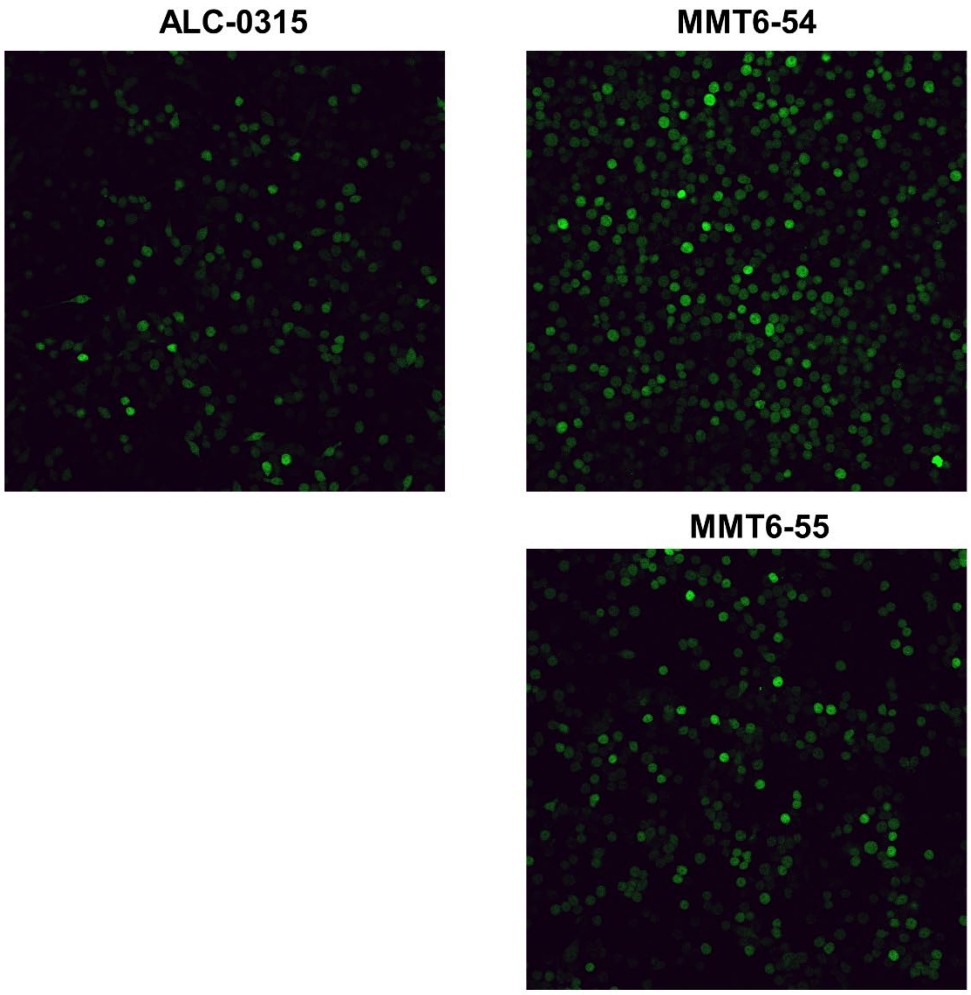


**Figure 3.S21** Enhanced green fluorescent protein (EGFP) expression of DC2.4 cells transfected by EGFP encoded mRNA encapsulated by different LNP formulations.

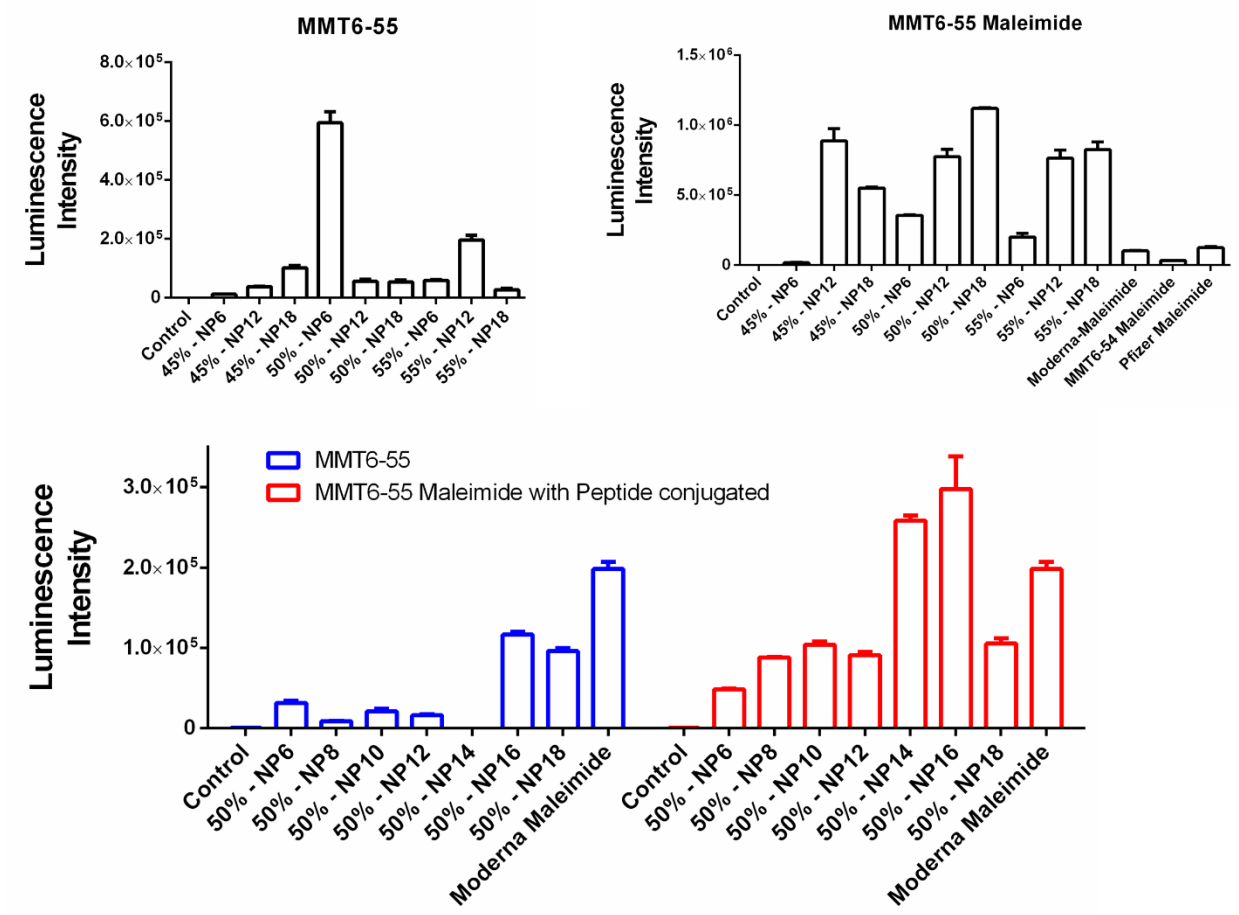


**Figure 3.S22** Firefly luciferase expression of DC2.4 cells transfected by firefly luciferase encoded mRNA encapsulated by different LNP formulations.

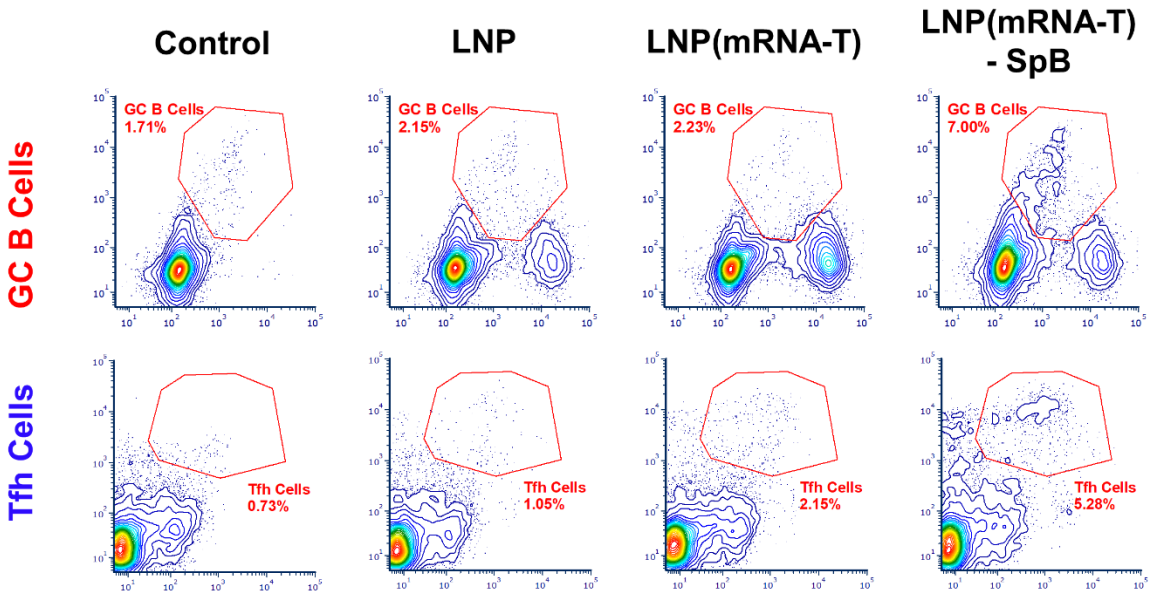


**Figure 3.S23** Flow cytometry quantification of GC B cells and Tfh cells from lymph node 6 days after the final vaccination from **Fig 3.3**.

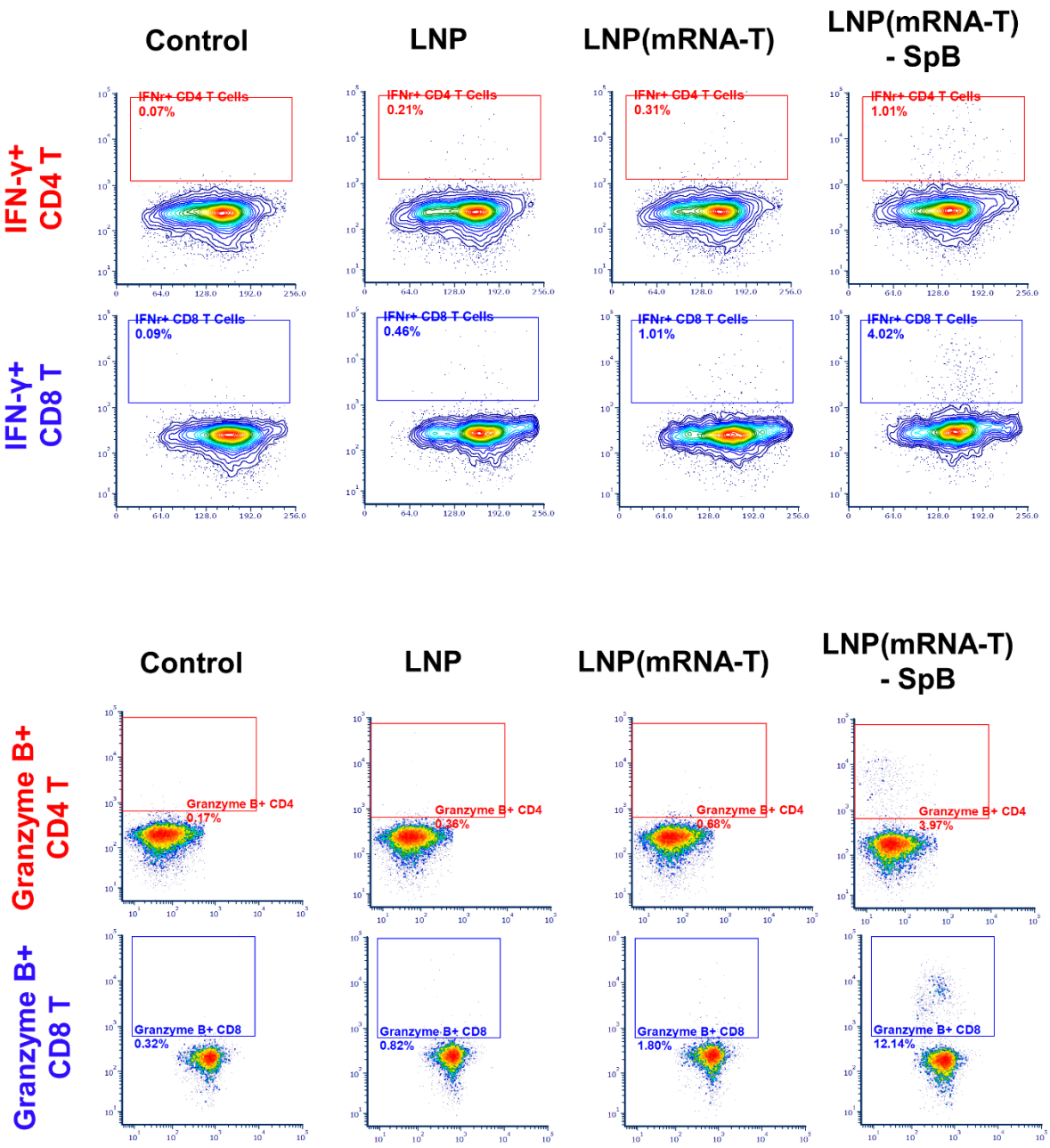


**Figure 3.S24** Flow cytometry quantification of antigen specific (IFN-γ+) CD4 T cells, antigen specific (IFN-γ+) CD8 T cells, Granzyme B+ CD4 T cells and Granzyme B+ CD8 T cells from lymph node 6 days after the final vaccination from **Figure 3.3**.

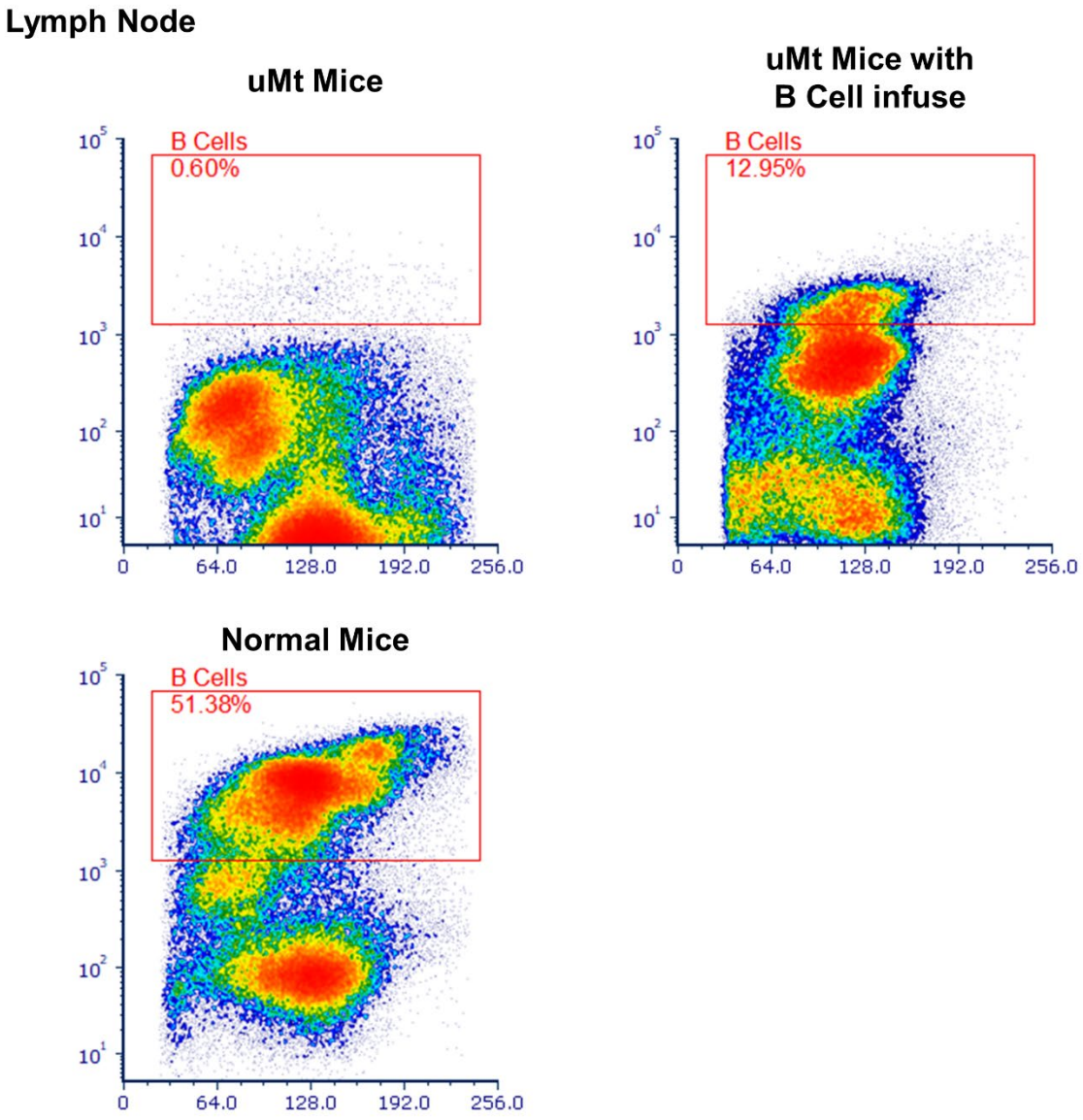


**Figure 3.S25** Flow cytometry analysis of B cells in lymph node from C57BL/6 and μMt mice.

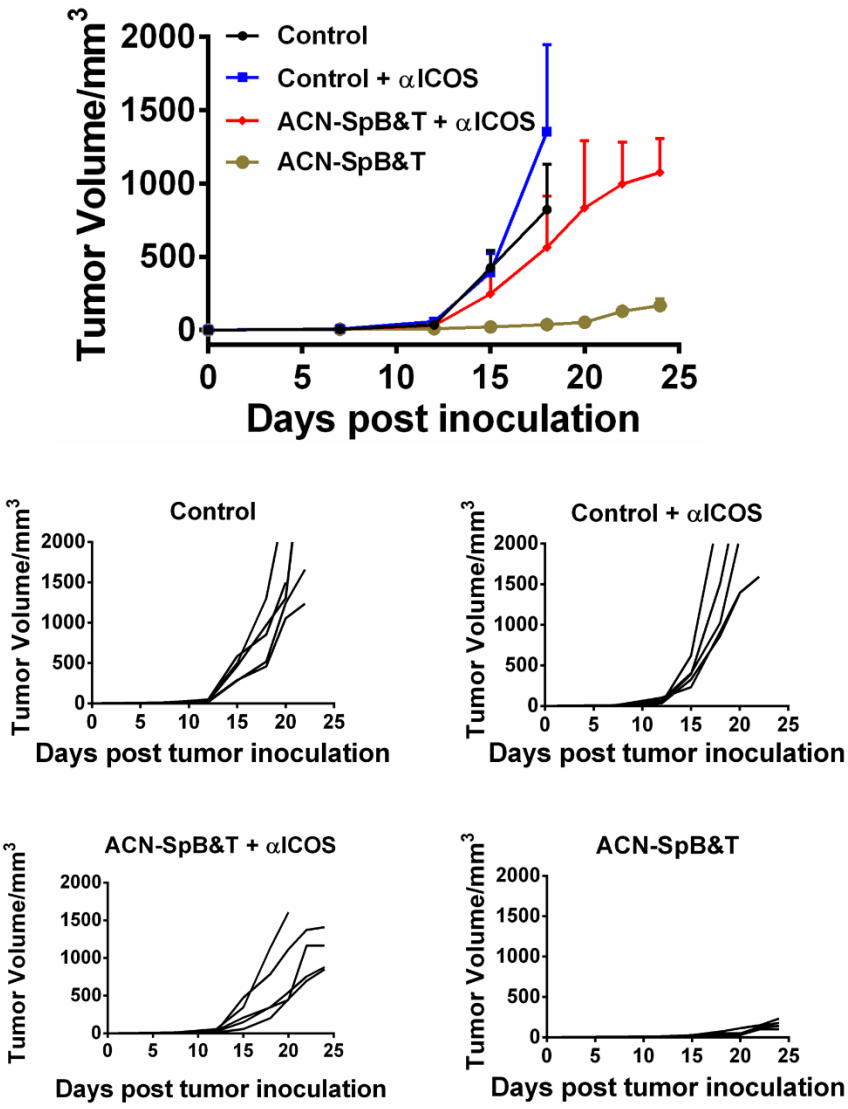


**Figure 3.S26** Antitumor efficacy of ACN with SARS-CoV-2 B epitope and tumor T cell neoantigens compared with ACN with tumor T cell neoantigens in melanoma model with B16-OVA cells. For the αICOS antibody (200 μg/mouse) blocking, antibody was intraperitoneal injected 10 days before vaccination, and then dosed 200 μg every three days.

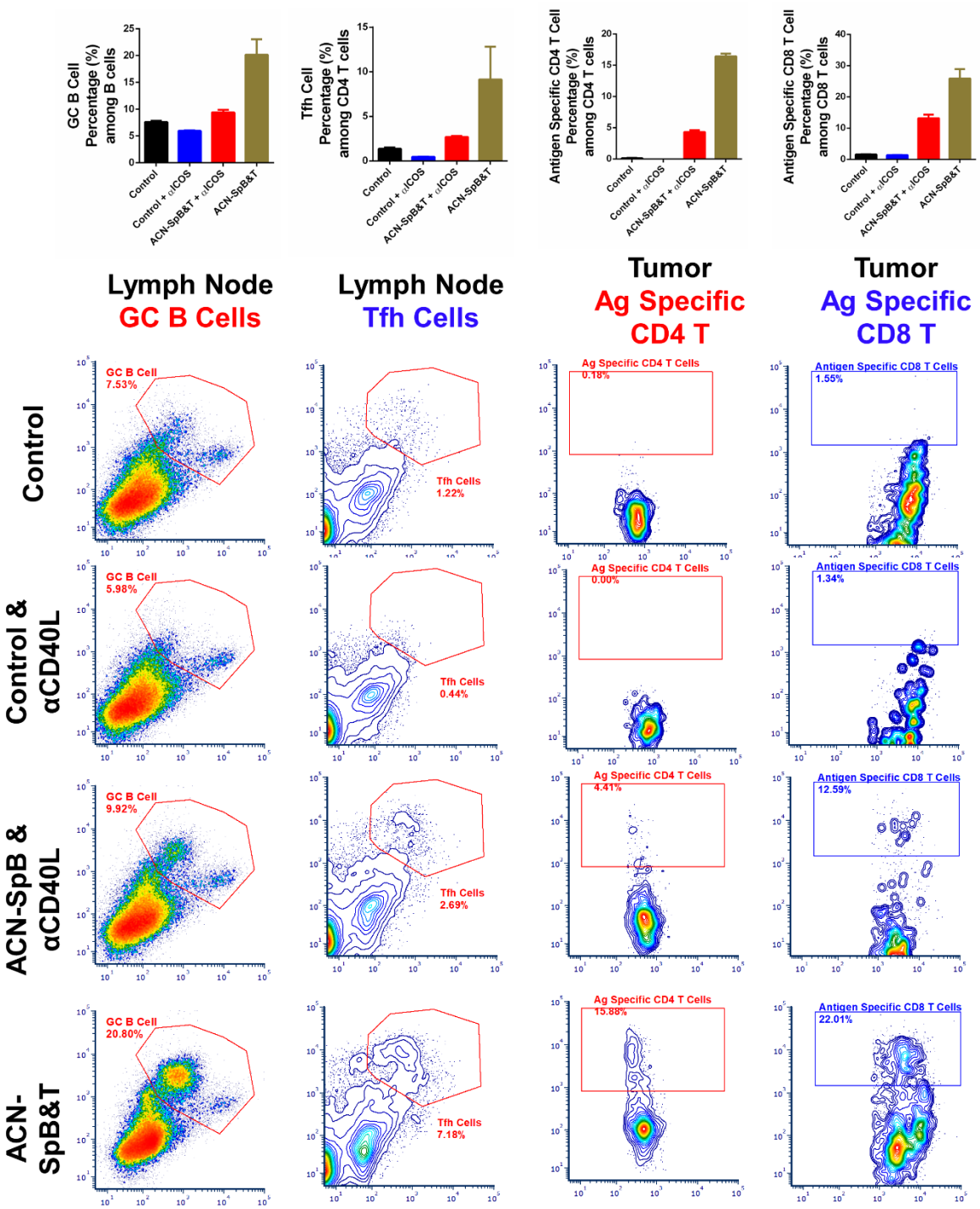


**Figure 3.S27** Flow cytometry quantification of GC B cells and Tfh cells from lymph node and antigen specific (IFN-γ+) CD4 T cells and antigen specific (IFN-γ+) CD8 T cells from tumor 6 days after the second booster vaccination from **Figure S26**.

# Appendix C

## Supporting Information from Chapter 4

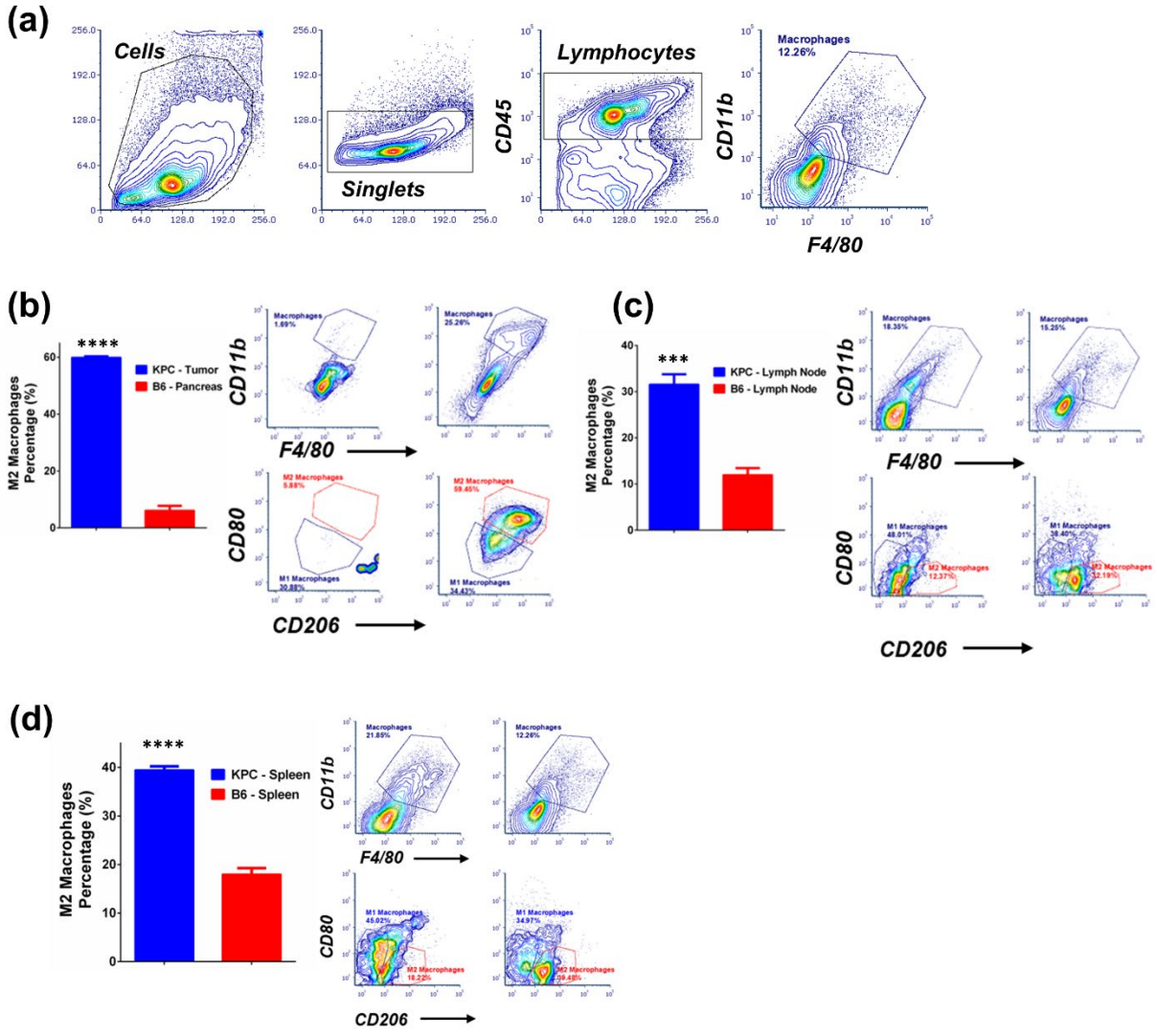


**Figure 4.S1** (**a**) Gating strategy for monitoring Macrophages. (**b-d**) Quantification and representative flow cytometry analysis of M1 and M2 macrophages in KPC mice pancreatic tumor and C57BL/6 mice pancreas tissues (**b**), KPC mice and C57BL/6 mice lymph node (**c**) and KPC mice and C57BL/6 mice spleen (**d**). Statistical comparisons are based on one-way ANOVA,

followed by post hoc Tukey's pairwise comparisons or by Student's unpaired T-test. The asterisks denote statistical significance at the level of * $p < 0.05$, ** $p < 0.01$, *** $p < 0.001$, **** $p < 0.0001$. ANOVA, analysis of variance; SD, standard deviation.

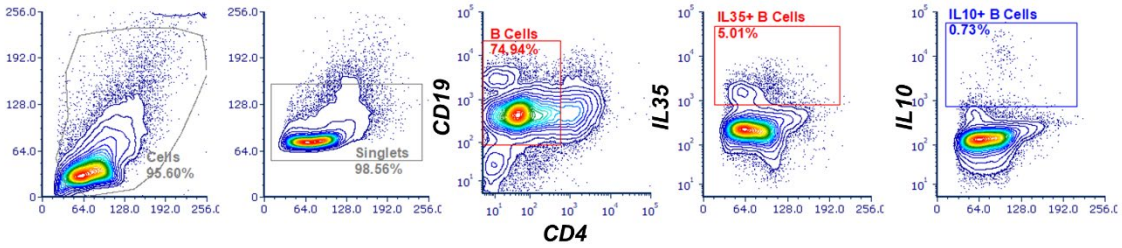


**Figure 4.S2** Gating strategy for identifying IL35$^{+}$ and IL10$^{+}$ Breg cells.

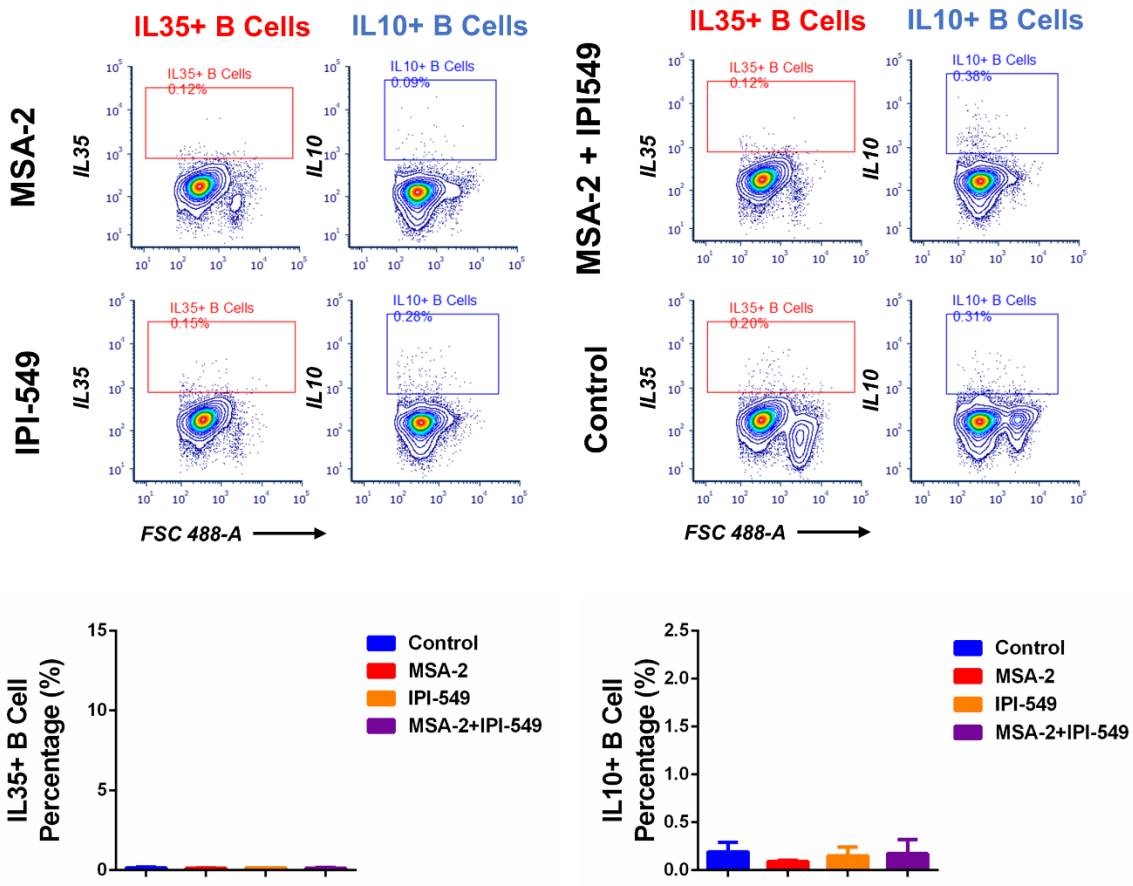


**Figure 4.S3** Quantification and representative flow cytometry analysis of IL35$^{+}$ and IL10$^{+}$ Breg cells (from STING knockout Tmem173$^{-/-}$ mice spleen) after treatments with or without MSA-2, with or without IPI-549. Statistical comparisons are based on one-way ANOVA, followed by post hoc Tukey's pairwise comparisons or by Student's unpaired T-test. The asterisks denote statistical significance at the level of * $p < 0.05$. No statistical significance across different groups. ANOVA, analysis of variance; SD, standard deviation.

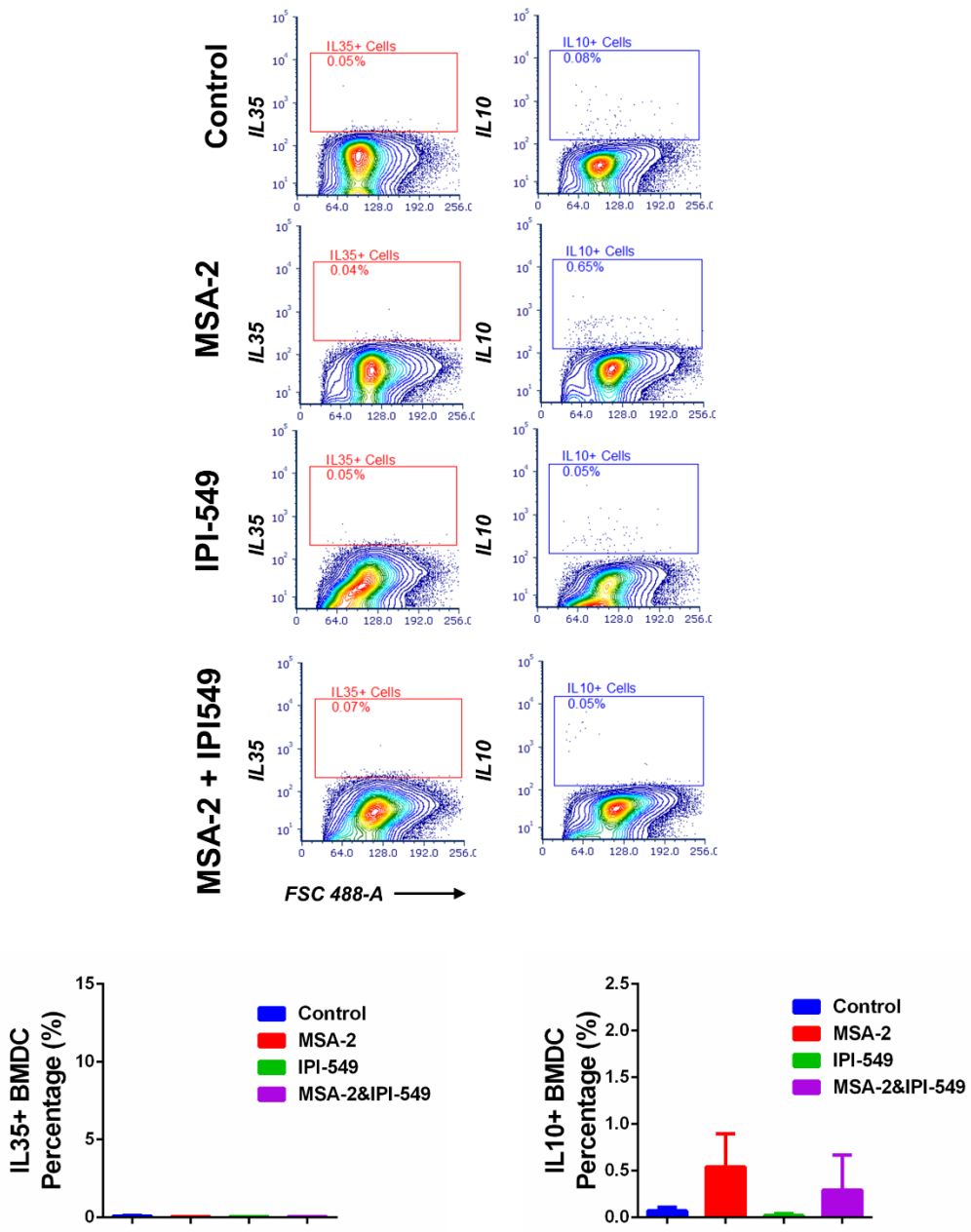


**Figure 4.S4** Quantification and representative flow cytometry analysis of IL35$^{+}$ and IL10$^{+}$ BMDC cells (from KPC mice) after treatments with or without MSA-2, with or without IPI-549. Statistical comparisons are based on one-way ANOVA, followed by post hoc Tukey's pairwise comparisons or by Student's unpaired T-test. The asterisks denote statistical significance at the level of * $p < 0.05$. No statistical significance across different groups. ANOVA, analysis of variance; SD, standard deviation.

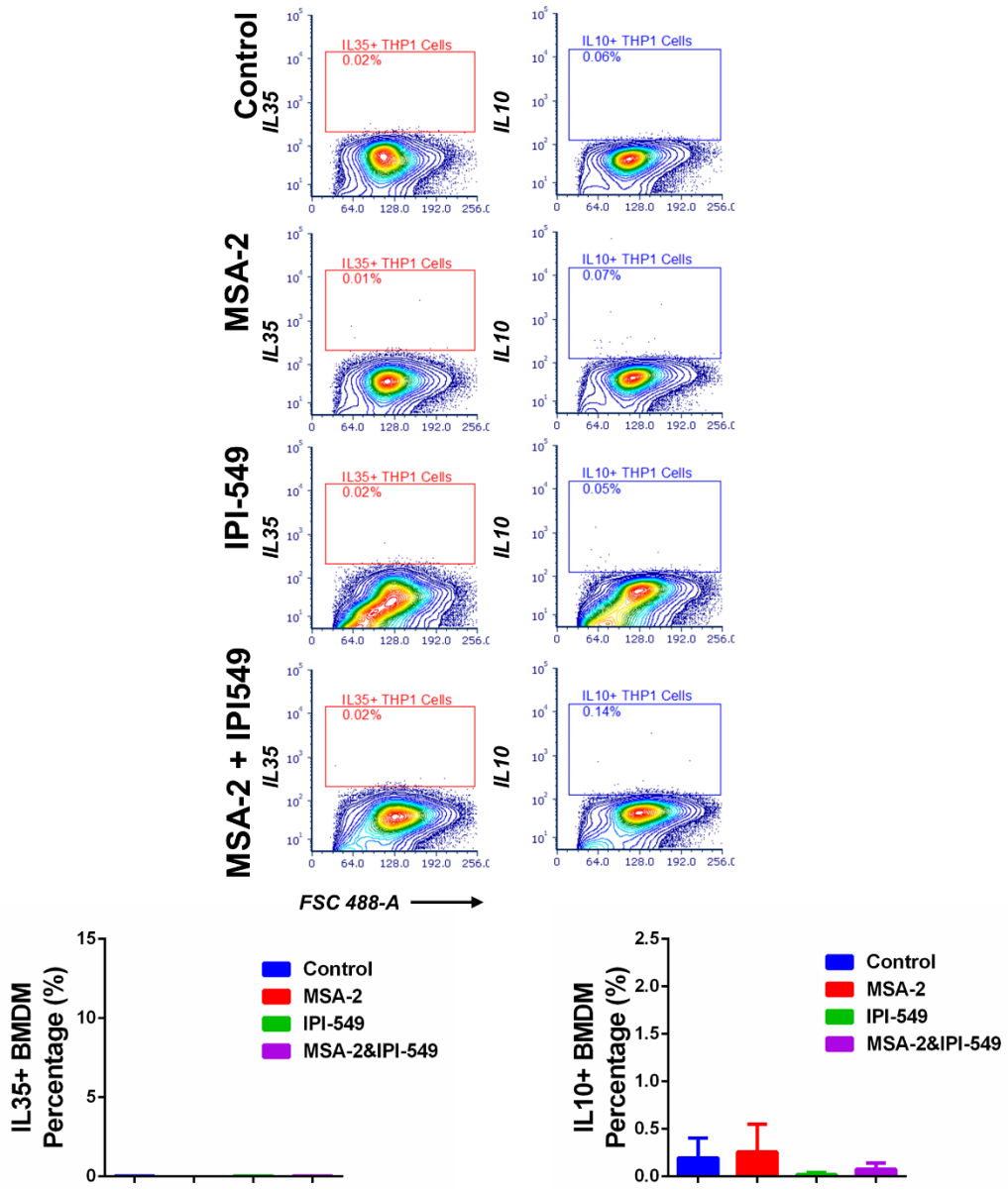


**Figure 4.S5** Quantification and representative flow cytometry analysis of IL35$^{+}$ and IL10$^{+}$ BMDM cells (from KPC mice) after treatments with or without MSA-2 and with or without IPI-549. Statistical comparisons are based on one-way ANOVA, followed by post hoc Tukey's pairwise comparisons or by Student's unpaired T-test. The asterisks denote statistical significance at the level of * $p < 0.05$. No statistical significance across different groups. ANOVA, analysis of variance; SD, standard deviation.

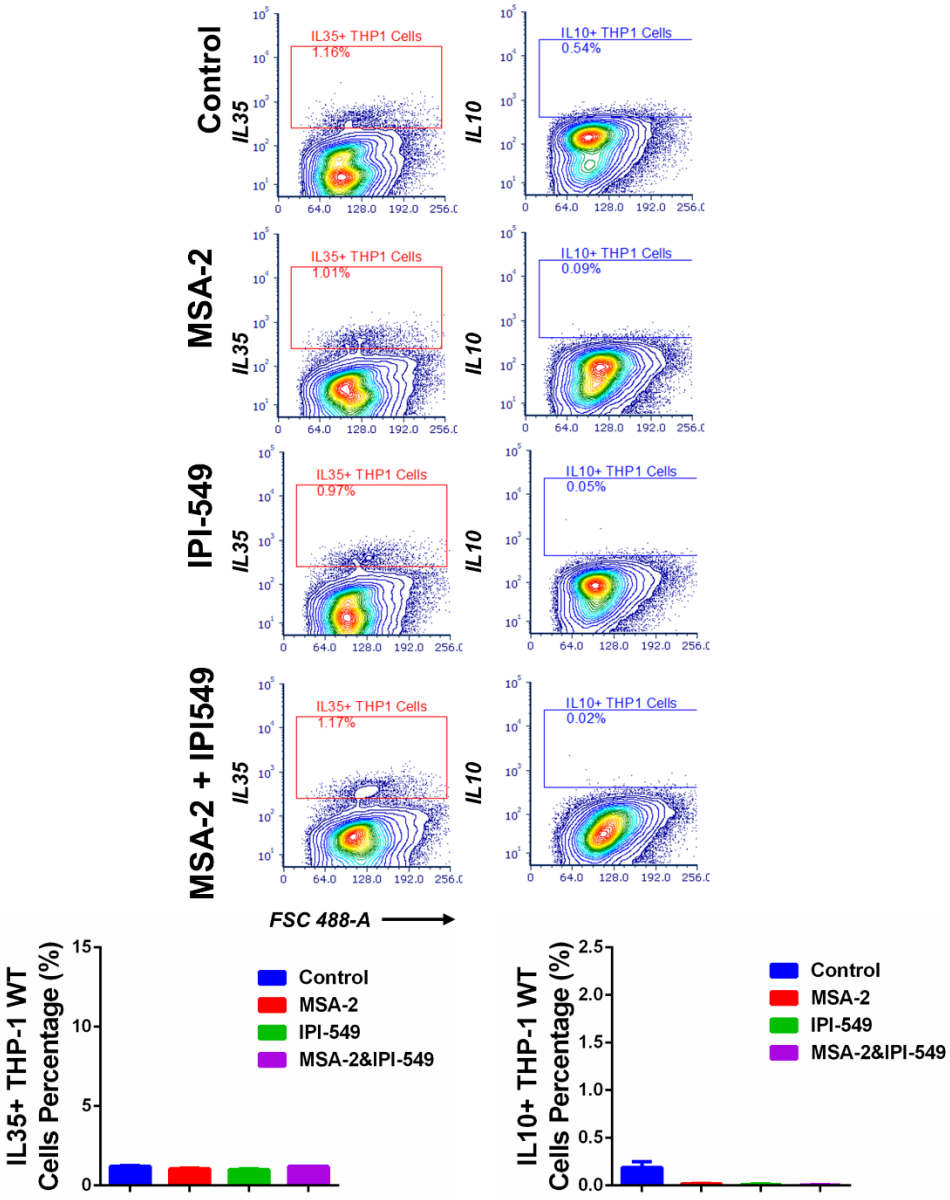


**Figure 4.S6** Quantification and representative flow cytometry analysis of IL35$^{+}$ and IL10$^{+}$ THP-1 hSTING$^{WT}$ cells after treatments with or without MSA-2, with or without IPI-549. Statistical comparisons are based on one-way ANOVA, followed by post hoc Tukey's pairwise comparisons or by Student's unpaired T-test. The asterisks denote statistical significance at the level of * $p < 0.05$. No statistical significance across different groups. ANOVA, analysis of variance; SD, standard deviation.

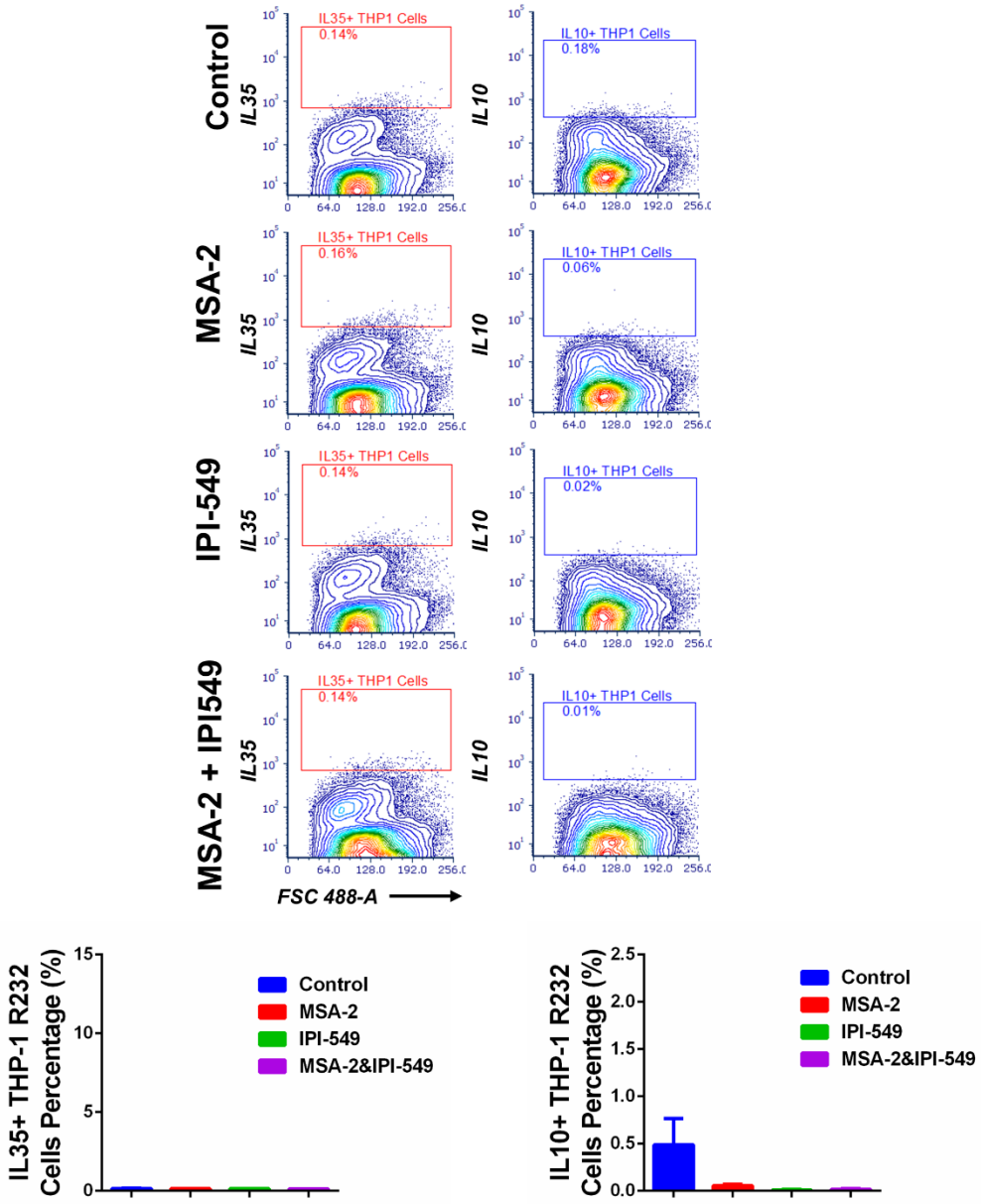


**Figure 4.S7** Quantification and representative flow cytometry analysis of IL35$^{+}$ and IL10$^{+}$ THP-1 hSTING$^{R232}$ cells after treatments with or without MSA-2, with or without IPI-549. Statistical comparisons are based on one-way ANOVA, followed by post hoc Tukey's pairwise comparisons or by Student's unpaired T-test. The asterisks denote statistical significance at the level of * $p < 0.05$. No statistical significance across different groups. ANOVA, analysis of variance; SD, standard deviation.

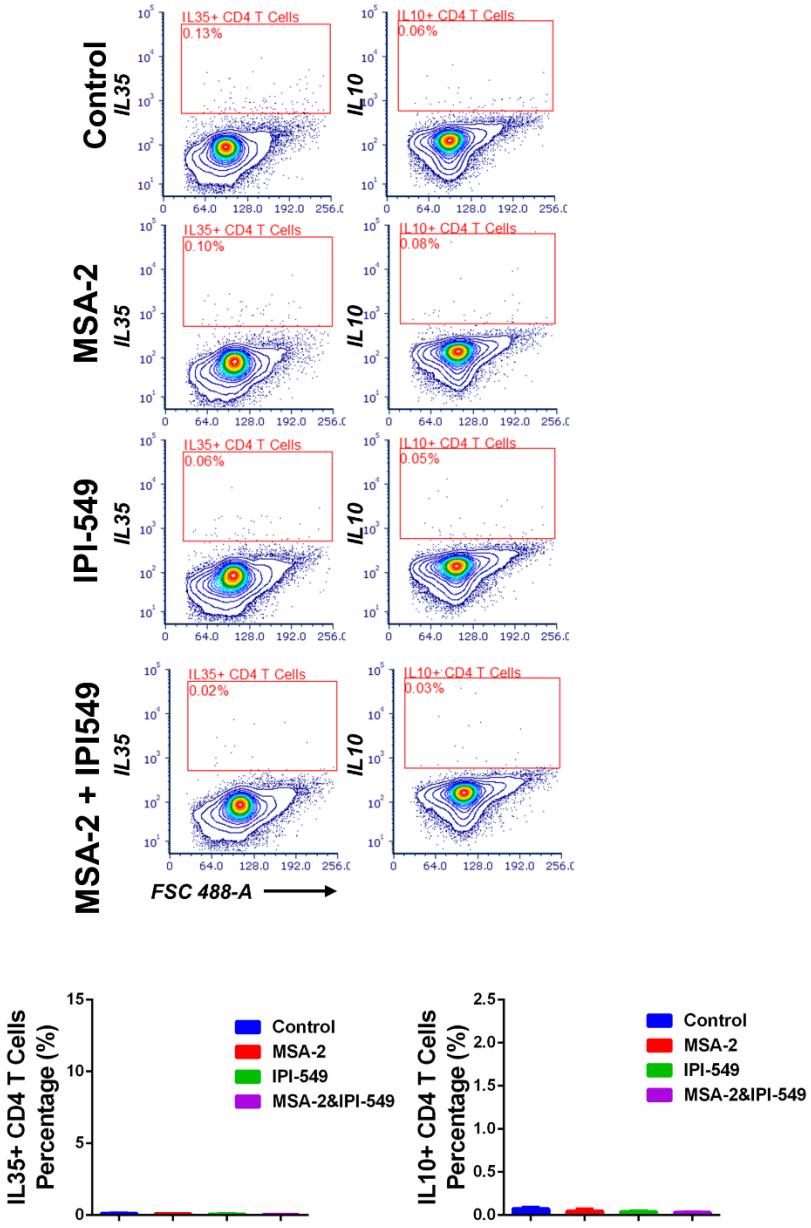


**Figure 4.S8** Quantification and representative flow cytometry analysis of IL35$^{+}$ and IL10$^{+}$ CD4 T cells (from KPC mice) after treatments with or without MSA-2, with or without IPI-549. Statistical comparisons are based on one-way ANOVA, followed by post hoc Tukey's pairwise comparisons or by Student's unpaired T-test. The asterisks denote statistical significance at the level of * $p < 0.05$. No statistical significance across different groups. ANOVA, analysis of variance; SD, standard deviation.

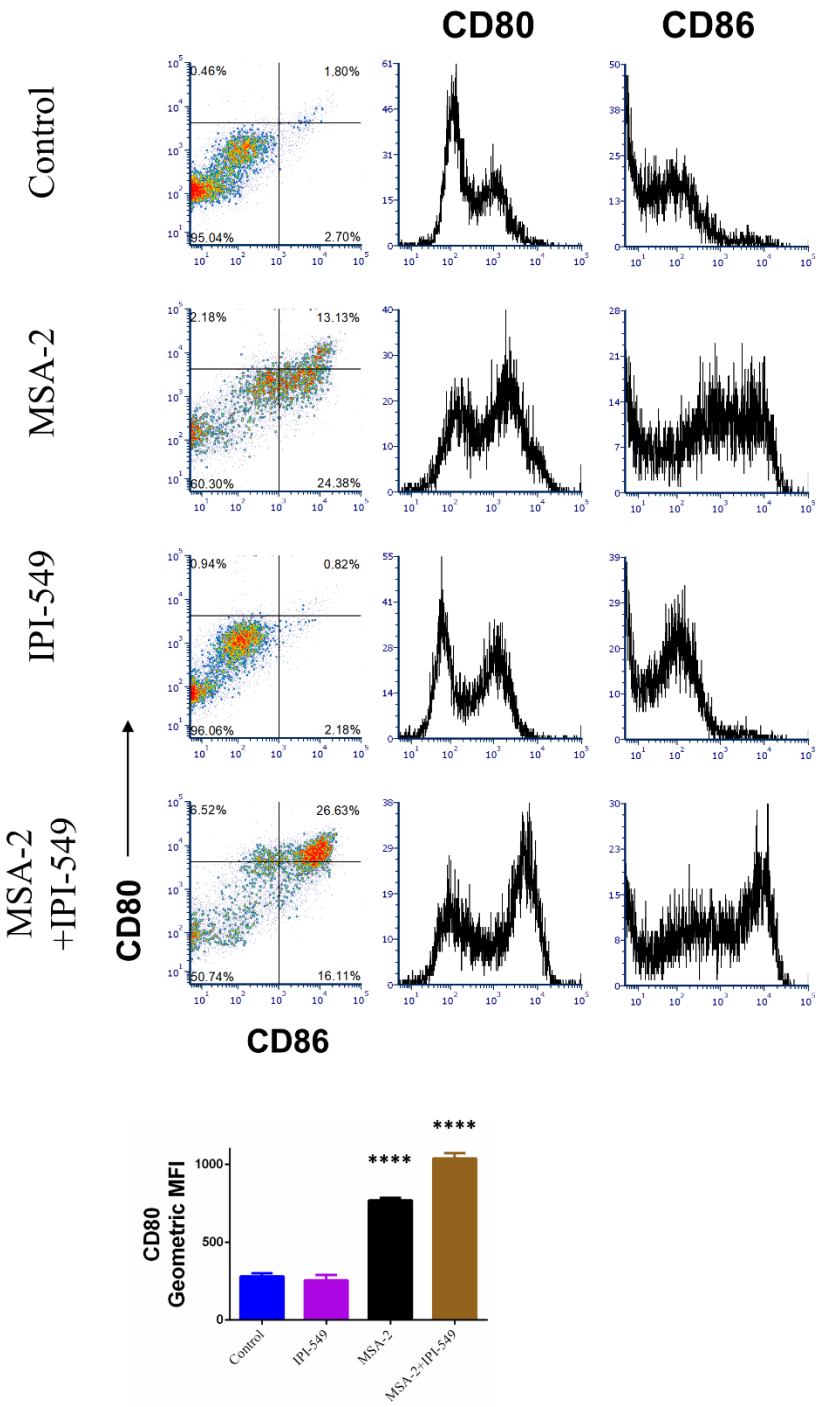


**Figure 4.S9** Quantification and representative flow cytometry analysis of CD80 and CD86 intensity of BMDC after treatments with or without MSA-2, with or without IPI-549. Statistical comparisons are based on one-way ANOVA, followed by post hoc Tukey's pairwise comparisons or by Student's unpaired T-test. The asterisks denote statistical significance at the level of **** $p < 0.0001$. ANOVA, analysis of variance; SD, standard deviation. statistical comparisons are conducted with control group.

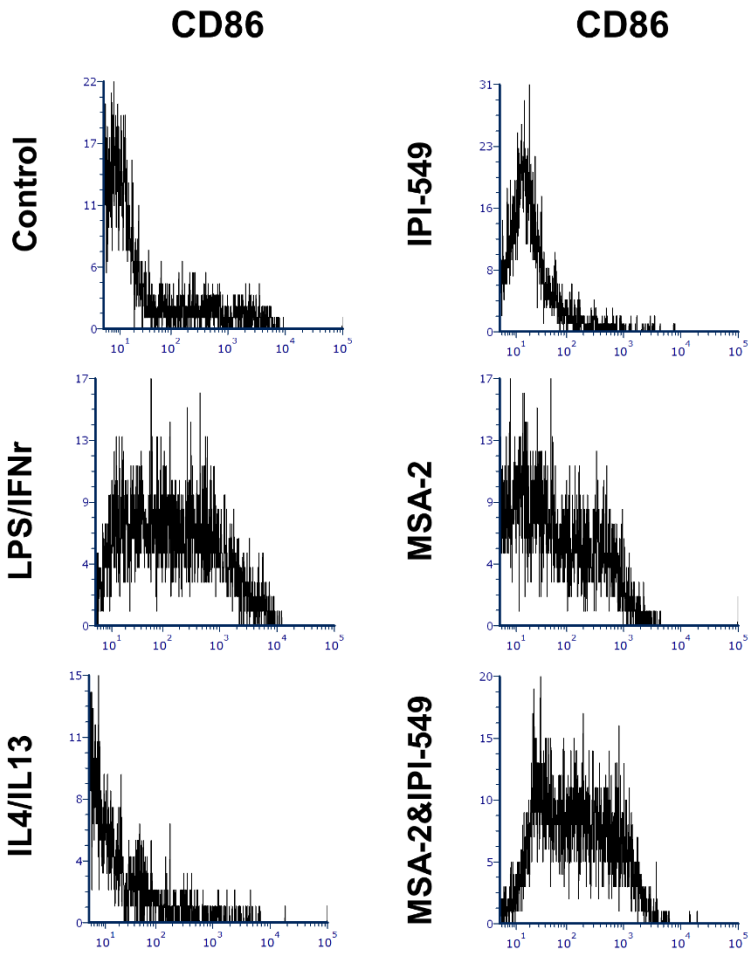


**Figure 4.S10** Quantification and representative flow cytometry analysis of CD86 intensity of BMDM after treatments with or without MSA-2, with or without IPI-549.

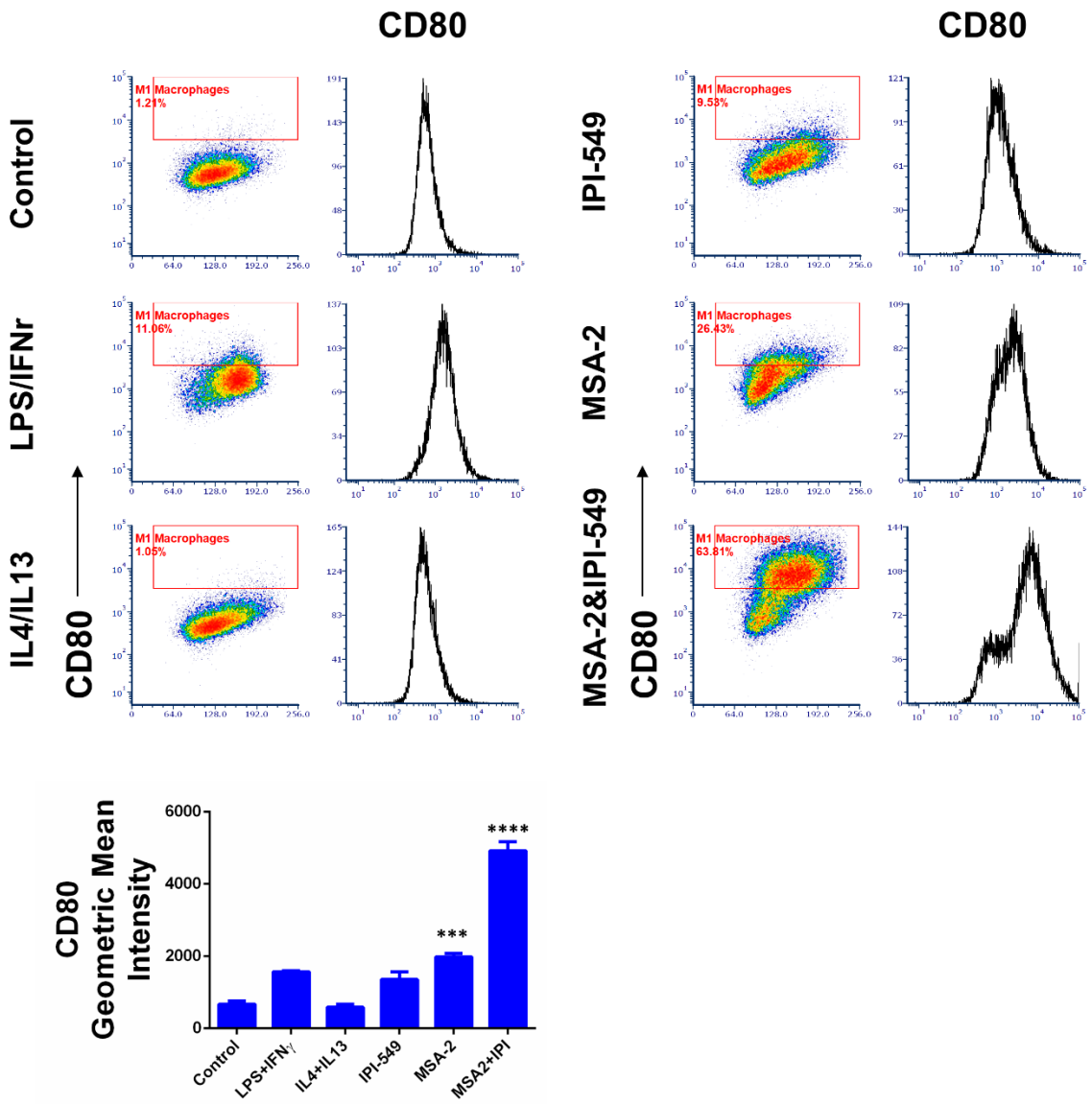


**Figure 4.S11** Quantification and representative flow cytometry analysis of M1 macrophage polarization of RAW264.7 by CD80 intensity after treatments with or without MSA-2, with or without IPI-549. Statistical comparisons are based on one-way ANOVA, followed by post hoc Tukey's pairwise comparisons or by Student's unpaired T-test. The asterisks denote statistical significance at the level of *** $p < 0.001$, **** $p < 0.0001$. ANOVA, analysis of variance; SD, standard deviation. statistical comparisons are conducted between MSA-2 and MSA-2+IPI-549 groups with control group.

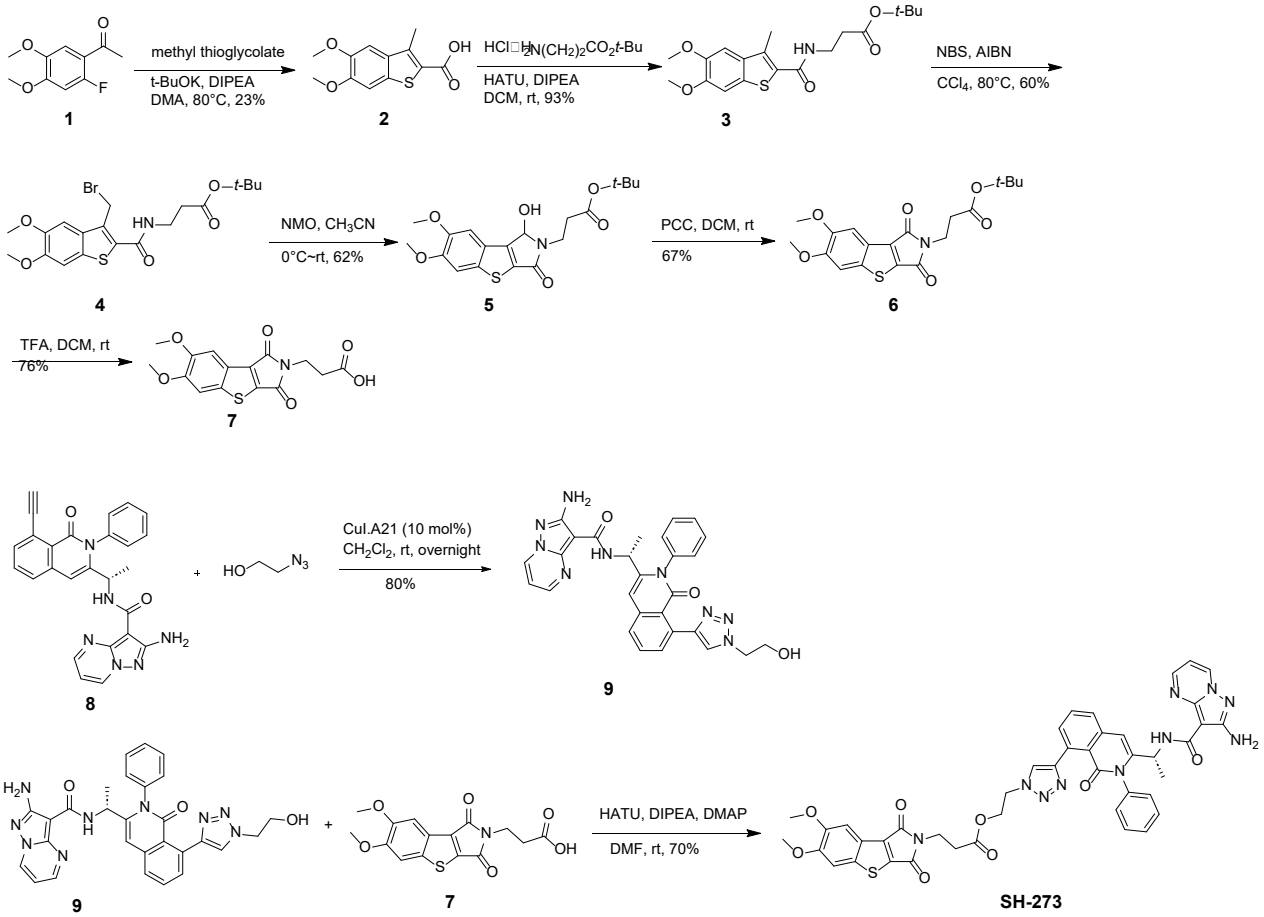
methyl thioglycolate
t-BuOK, DIPEA
DMA, 80°C, 23%
HCl·H2N(CH2)2CO2t-Bu
HATU, DIPEA
DCM, rt, 93%
NBS, AIBN
CCl4, 80°C, 60%
NMO, CH3CN
0°C~rt, 62%
PCC, DCM, rt
67%
TFA, DCM, rt
76%
CuI.A21 (10 mol%)
CH2Cl2, rt, overnight
80%
HATU, DIPEA, DMAP
DMF, rt, 70%
1
2
3
4
5
6
7
8
9
9
7
SH-273

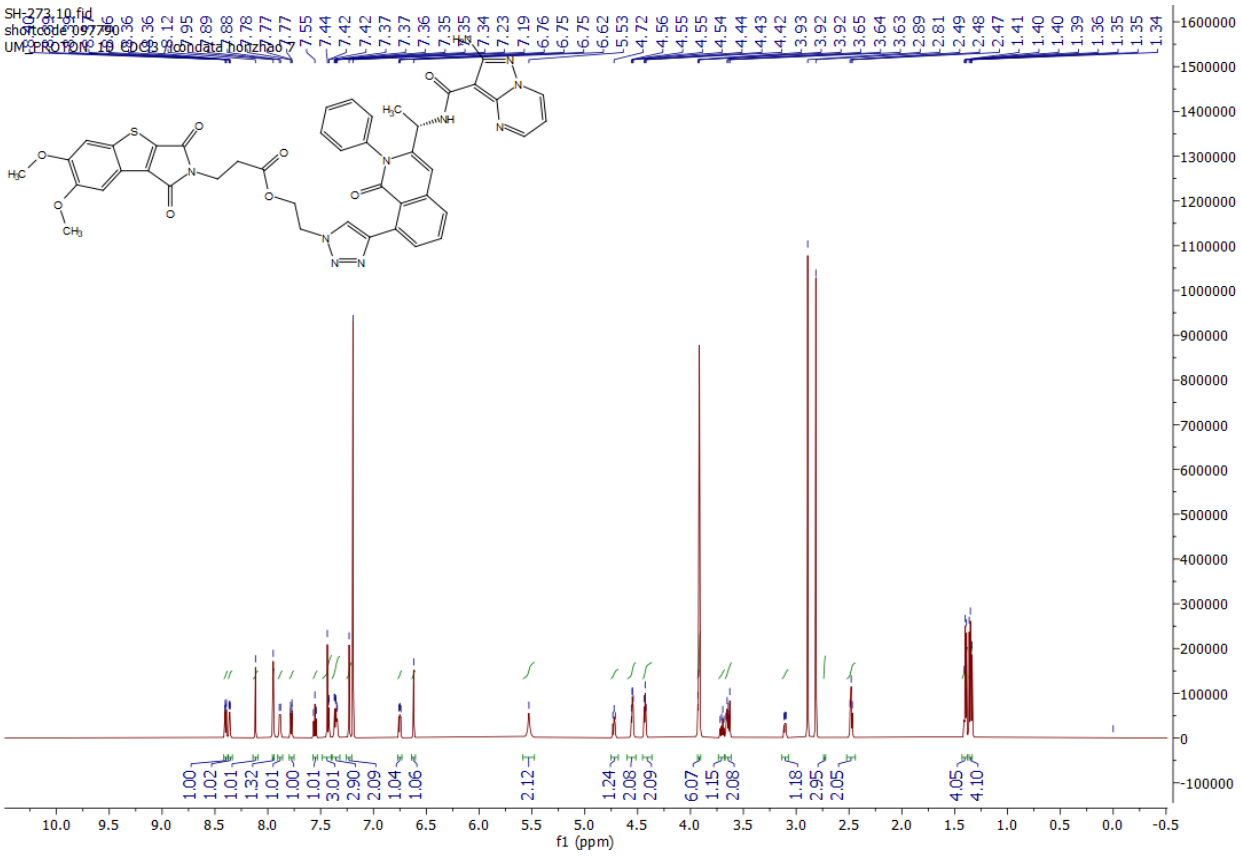


**Scheme 4.S1** Synthesis and NMR of SH-273

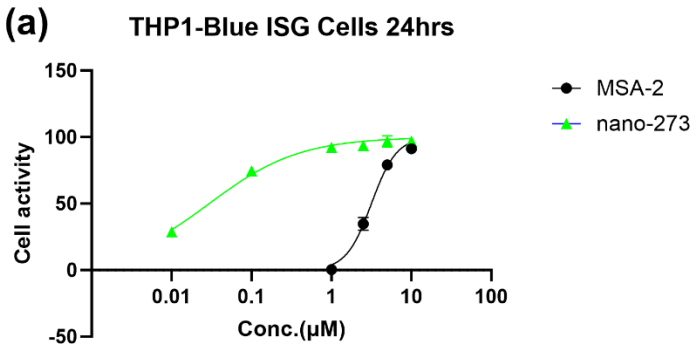


| Compounds: | MSA-2 | Nano-273 |
|---|---|---|
| IC50 (μM) | 3.166 | 0.02959 |

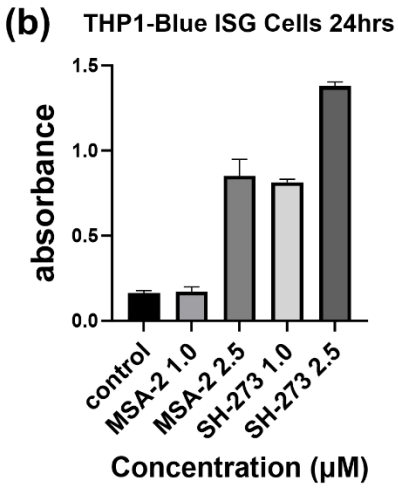


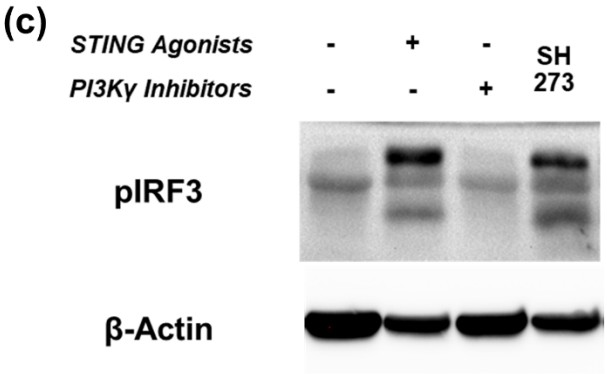


**Figure 4.S12** (**a**) Cellular IC50 of STING activation after MSA-2 or Nano-273 treatments in THP-1-Blue™ ISG cells. (**b**) Cellular STING activation after MSA-2 or SH-273 treatments in THP-1-Blue™ ISG cells. **(c)** Binding IC50 to PI3Kγ by SH-273 PI3Kγ motif and IPI-549. (**d**) Phosphorylation of IRF3 in bone marrow derived dendritic cells from KPC PDAC mice after treatments with MSA-2, IPI-549 or SH-273, respectively.

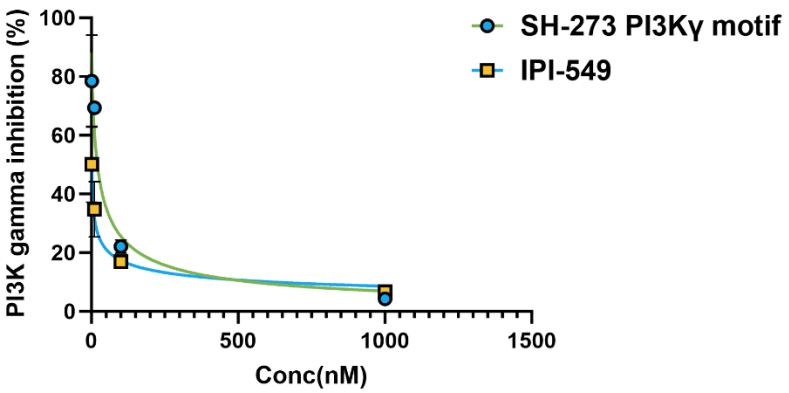


| compound | SH-273 PI3Kγ motif | IPI-549 |
|---|---|---|
| Gamma $IC_{50}$ (nM) | 20.24 | 1.19 |

**Figure 4.S13** Binding IC50 to PI3Kγ by SH-273 PI3Kγ motif and IPI-549.

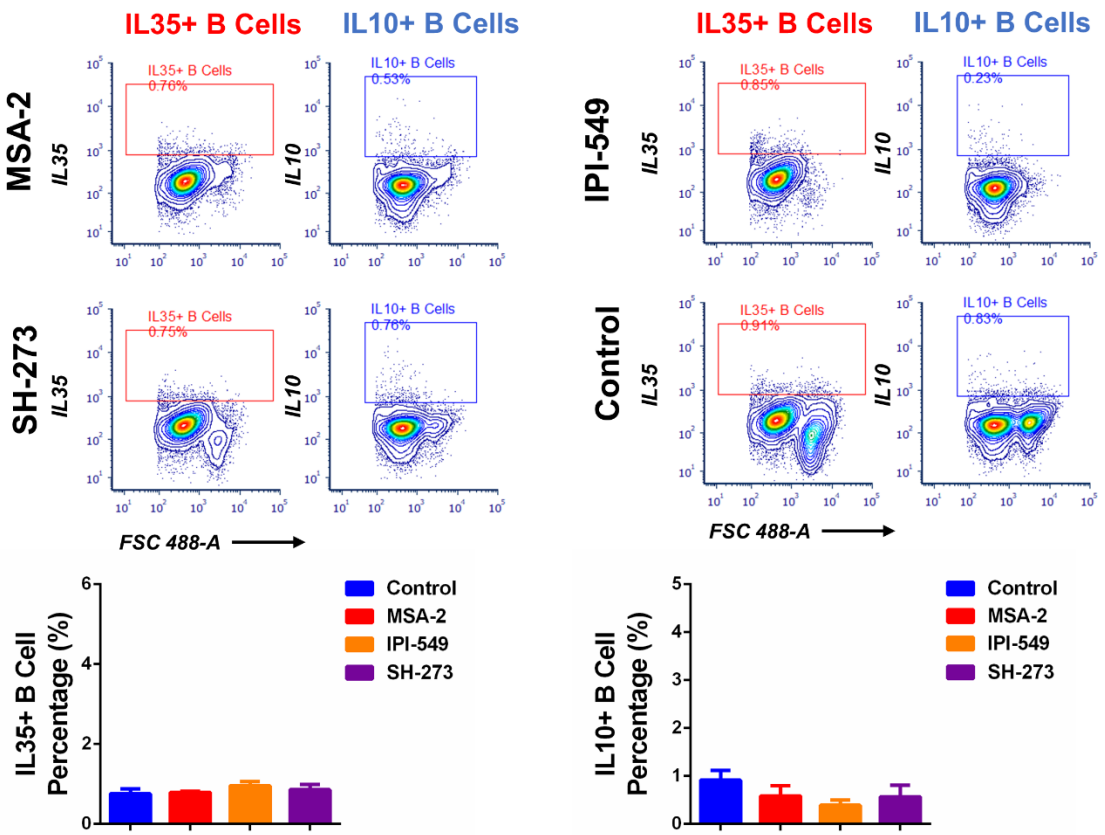


**Figure 4.S14** Quantification and representative flow cytometry analysis of IL35$^{+}$ and IL10$^{+}$ splenic B cells (from STING knockout Tmem173$^{-/-}$ mice) after treatments with or without MSA-2, with or without IPI-549, with or without SH-273. Statistical comparisons are based on one-way ANOVA, followed by post hoc Tukey's pairwise comparisons or by Student's unpaired T-test. The asterisks denote statistical significance at the level of * $p < 0.05$. No statistical significance across different groups. ANOVA, analysis of variance; SD, standard deviation.

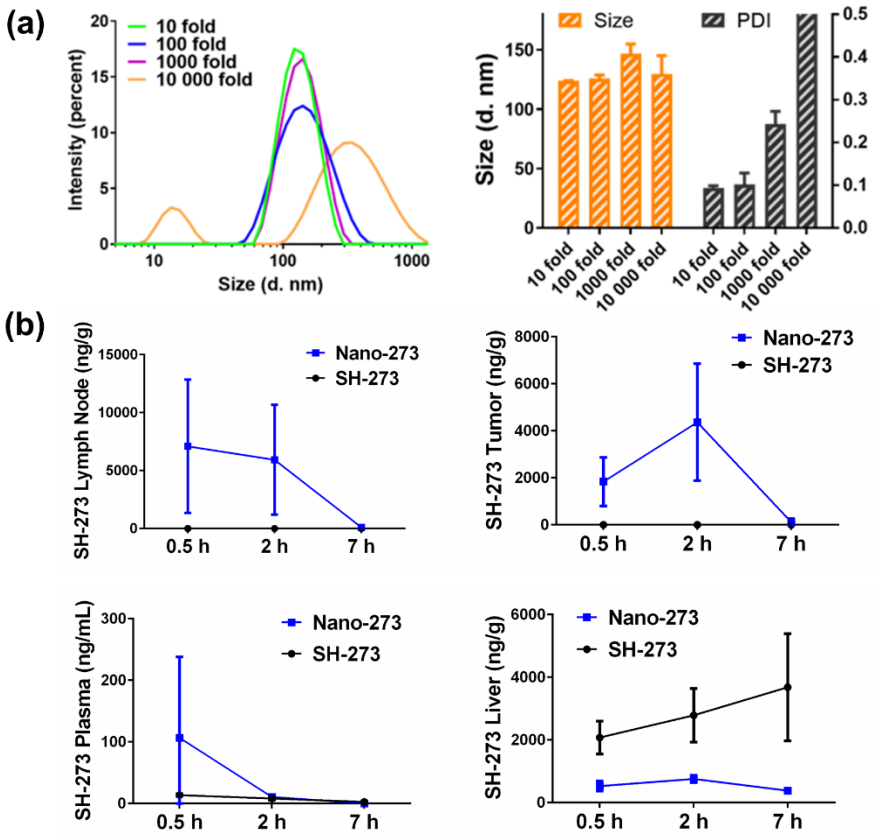


**Figure 4.S15 (a)** DLS size distribution and PDI of Nano-273 after 10-10000-fold dilution. **(b)** Pharmacokinetics and tissue distribution of Nano-273. SH-273 concentration in plasma, pancreatic tumor, lymph nodes, and liver after intravenous injection of SH-273 (17.6 μmol/kg) and Nano-273 (17.6 μmol/kg) in transgenic KPC PDAC mice.

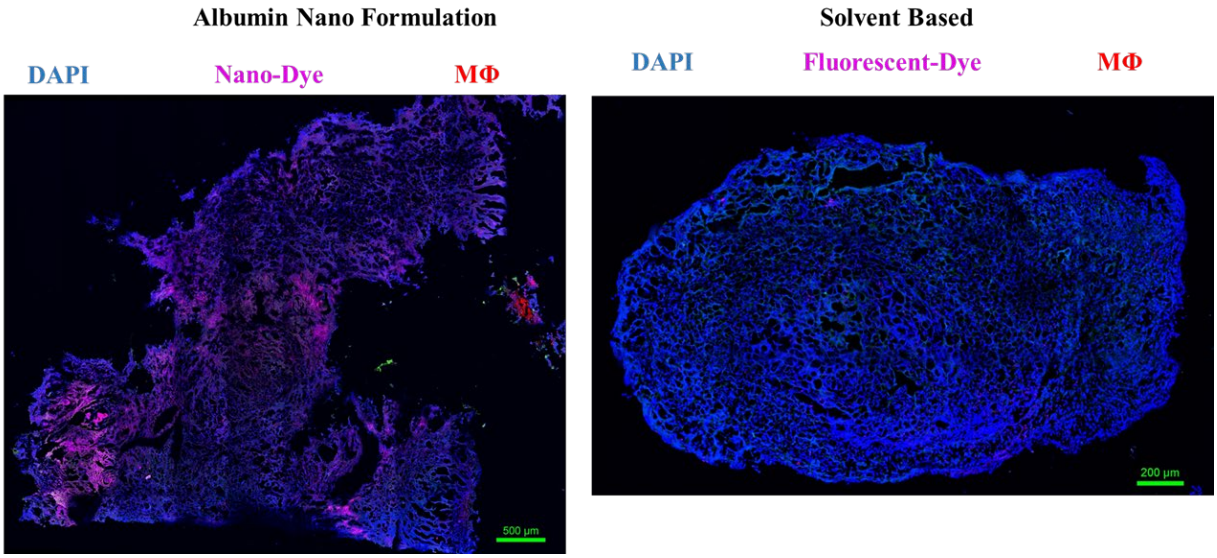


**Figure 4.S16** Confocal imaging of albumin nanoformulation and solvent based formulation in the tumor tissues from KPC mice. Tumor samples were collected 5 hours after intravenous injection of albumin nanoformulation of dual functional compound and fluorescent dye PTX-OG488 (red) or solvent based dual functional compound and PTX-OG488 (red) in KPC mice. The macrophages and nucleus were stained with F4/80 (red), and DAPI (blue). Scale bar, 500 µm.

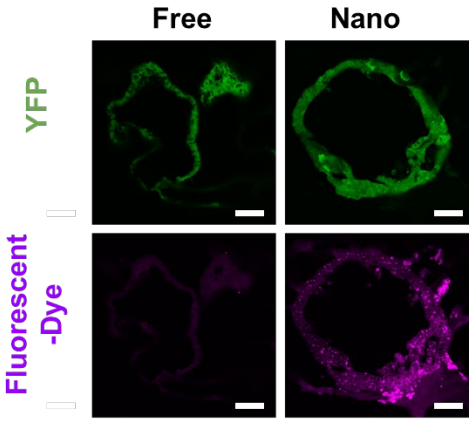


**Figure 4.S17** Confocal imaging of albumin nanoformulation and solvent based formulation of dual functional compound and fluorescent dye DID (magenta) or solvent based dual functional compound and DID in pancreatic tumor organoid derived from KPC mice. Scale bar is 100 µm.

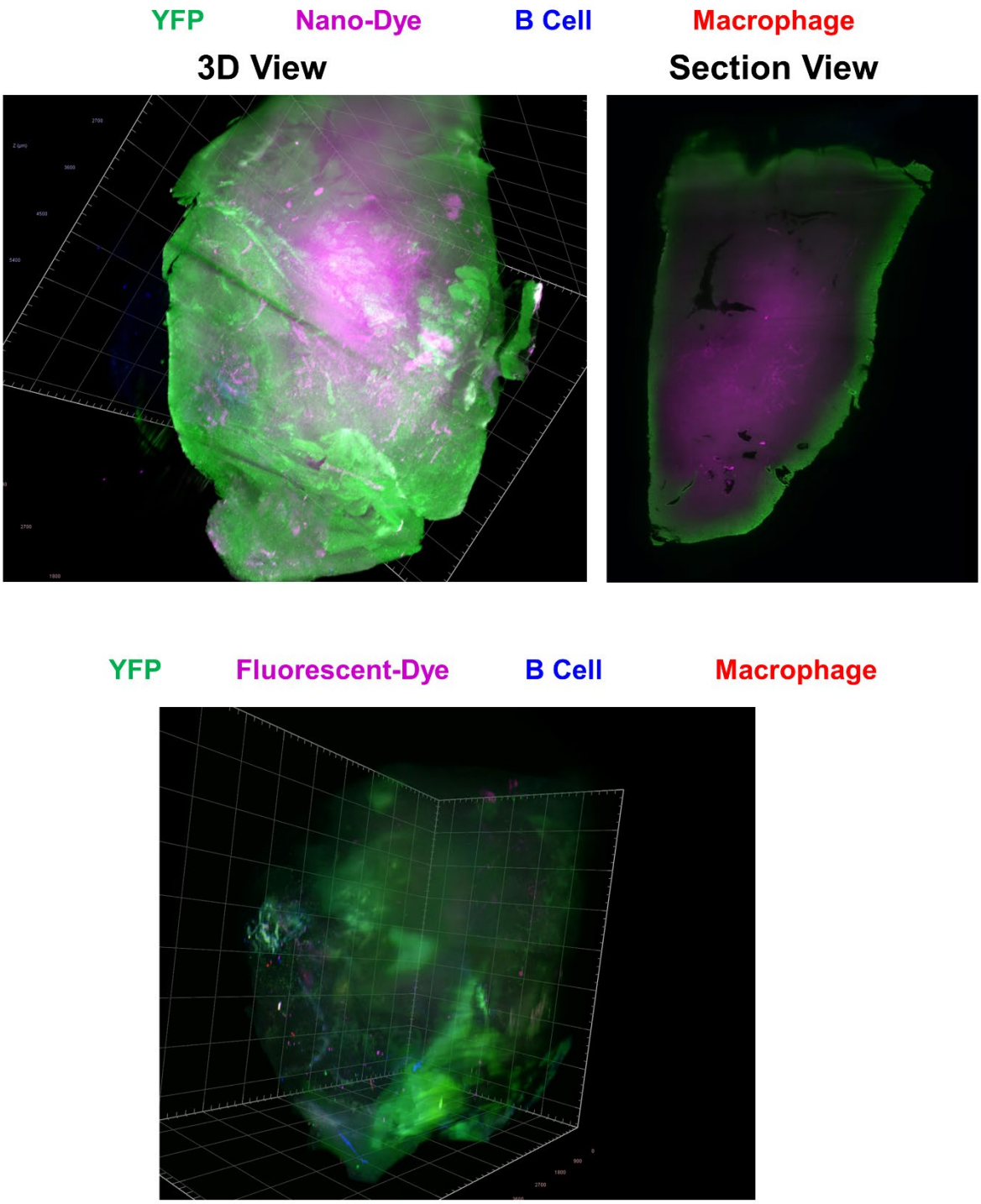


**Figure 4.S18** 3D imaging of albumin nanoformulation and solvent based formulation in the tumor tissues from KPC mice. Tumor samples were collected 5 hours after intravenous injection of albumin nanoformulation encapsulated with dual functional compound and fluorescent dye DID (magenta) or solvent based free dual functional compound and DID (magenta) in KPC mice. The macrophages, B cell, and nucleus were stained with F4/80 (red), YFP (green, tumor cells), and B220 (blue).

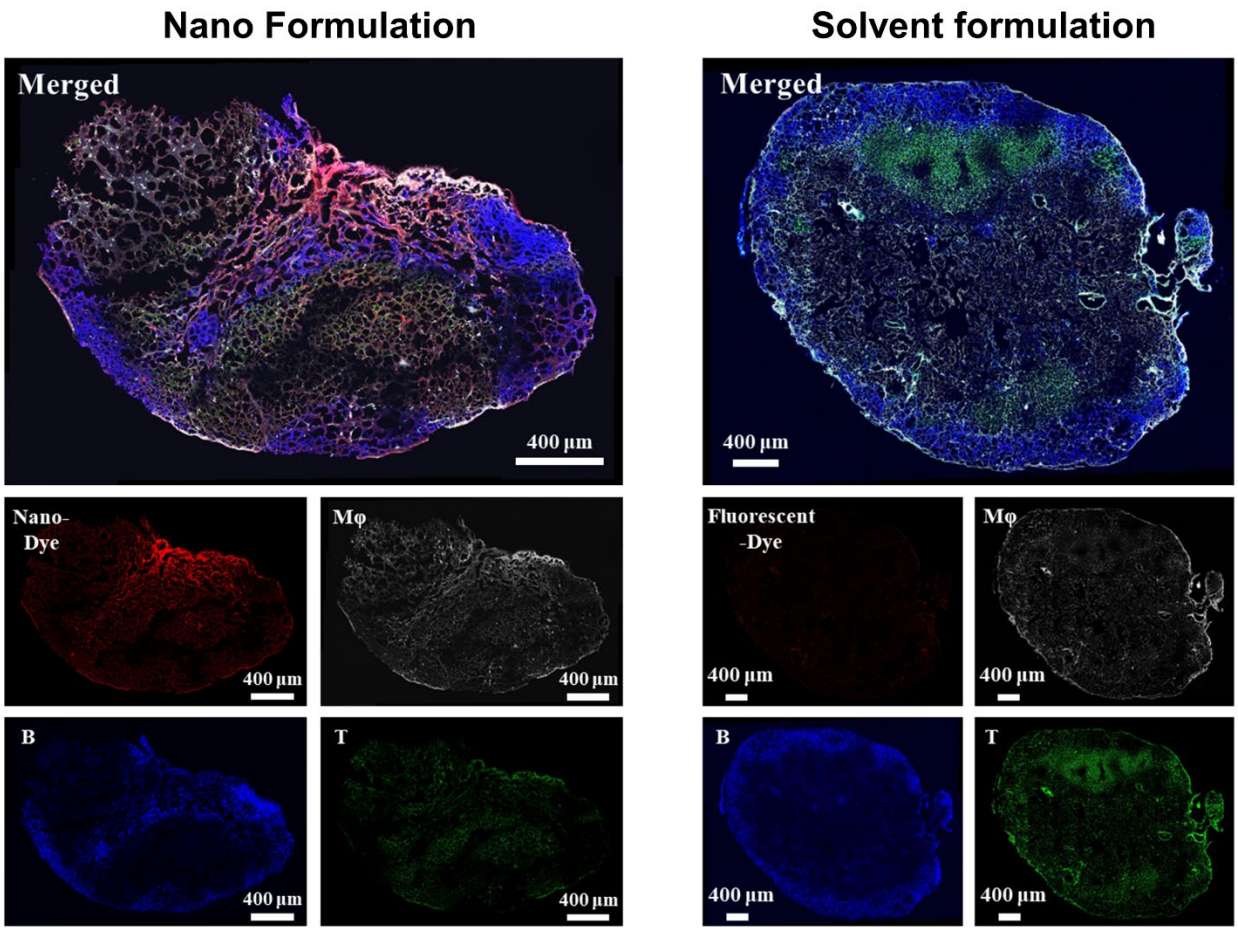


**Figure 4.S19** Confocal imaging of albumin nanoformulation and solvent based formulation in the lymph nodes from KPC mice. Lymph node samples were collected 5 hours after intravenous injection of albumin nanoformulation of dual functional compound and fluorescent dye PTX-OG488 (red) or solvent based dual functional compound and PTX-OG488 (red) in KPC mice. The macrophages, B cell and T cell were stained with F4/80 (white), B220 (blue), and CD3 (green).

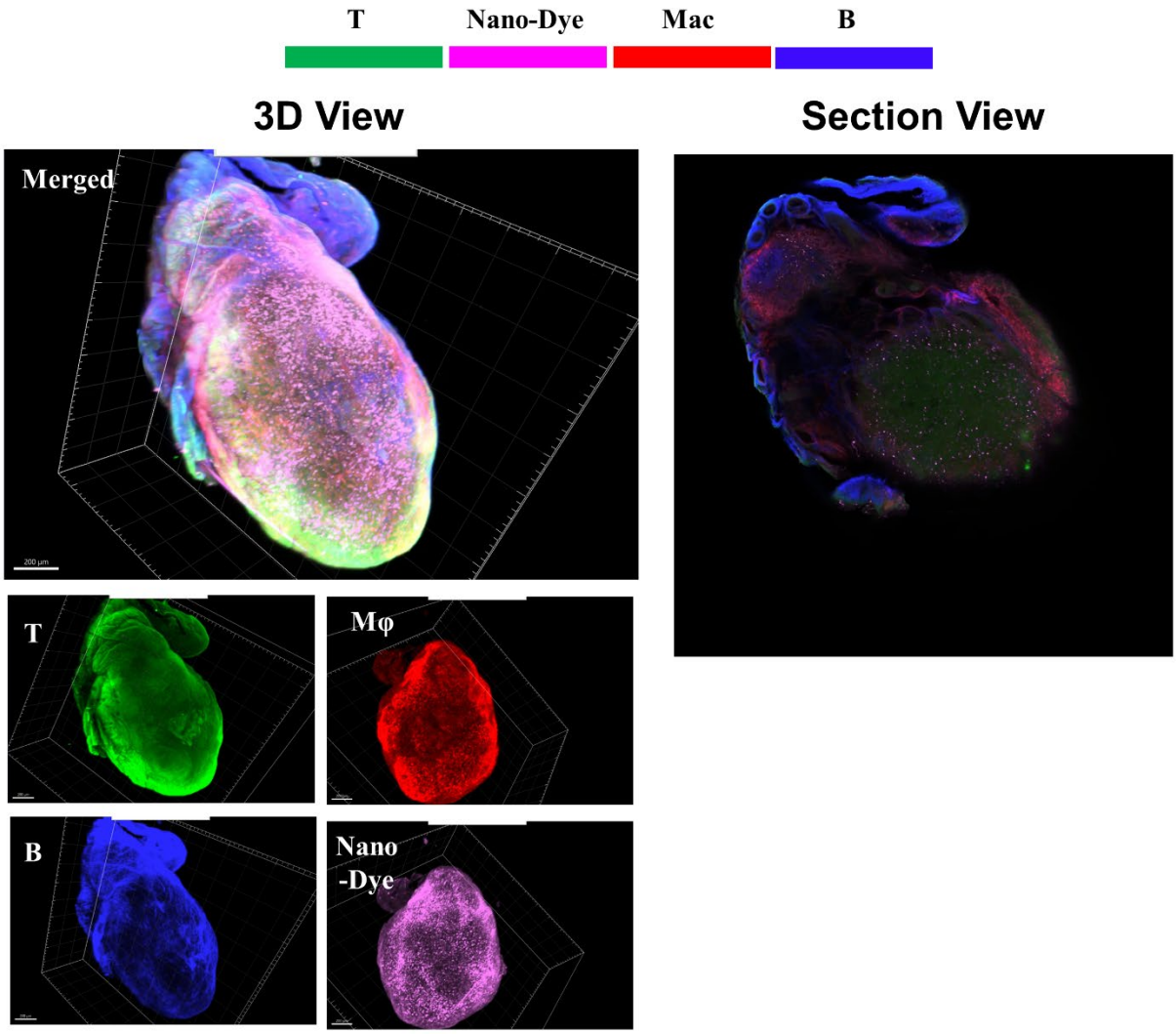


**Figure 4.S20** 3D imaging of albumin nanoformulation at lymph node from KPC mice. Lymph node samples were collected 5 hours after intravenous injection of albumin nanoformulation encapsulated with dual functional compound and fluorescent dye DID (magenta). The macrophages, B cell, and T cells were stained with F4/80 (red), B220 (blue), and CD3 (green).

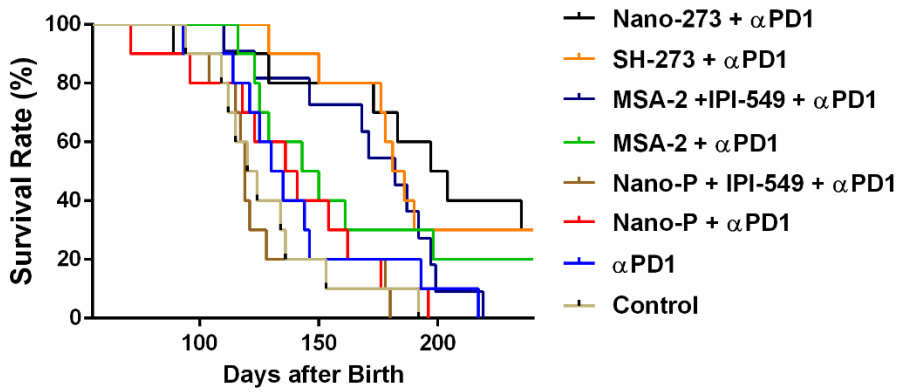


| Groups | Control | αPD1 | Nano-P + αPD1 | Nano-P + IPI-549(ip) + αPD1 | MSA-2 + αPD1 | MSA-2 + IPI-549 + αPD1 | SII-273 + αPD1 | Nano-273 + αPD1 |
|---|---|---|---|---|---|---|---|---|
| **Medium Surivival** | **122 Days** | **132.5 Days** | **139 Days** | **119 Days** | **146.5 Days** | **182 Days** | **183.5 Days** | **201 Days** |

**Figure 4.S21** Antitumor efficacy in transgenic KPC (LSL-KrasG12D, LSL-Trp53R172H, Pdx1cre/+) PDAC mice with different treatments. Survival rate of KPC mice after treatment with PBS (control), anti-PD-1 antibody (100 μg), Paclitaxel in albumin nano formulation (intravenous injection, 11.7 μmol/kg) plus anti-PD-1 antibody (100 μg), Paclitaxel in albumin nanoformulation (intravenous injection, 11.7 μmol/kg) and IPI-549 (intraperitoneal injection, 28.4 μmol/kg) plus anti-PD-1 antibody (100 μg), MSA-2 (intravenous injection, 34.0 μmol/kg) plus anti-PD-1 antibody (100 μg), MSA-2 (oral dose, 204 μmol/kg) and IPI-549 (oral dose, 28.4 μmol/kg) plus anti-PD-1 antibody (100 μg) and Nano-273 (intravenous injection, 17.6 μmol/kg) plus anti-PD-1 antibody (100 μg). n = 10 for each group.

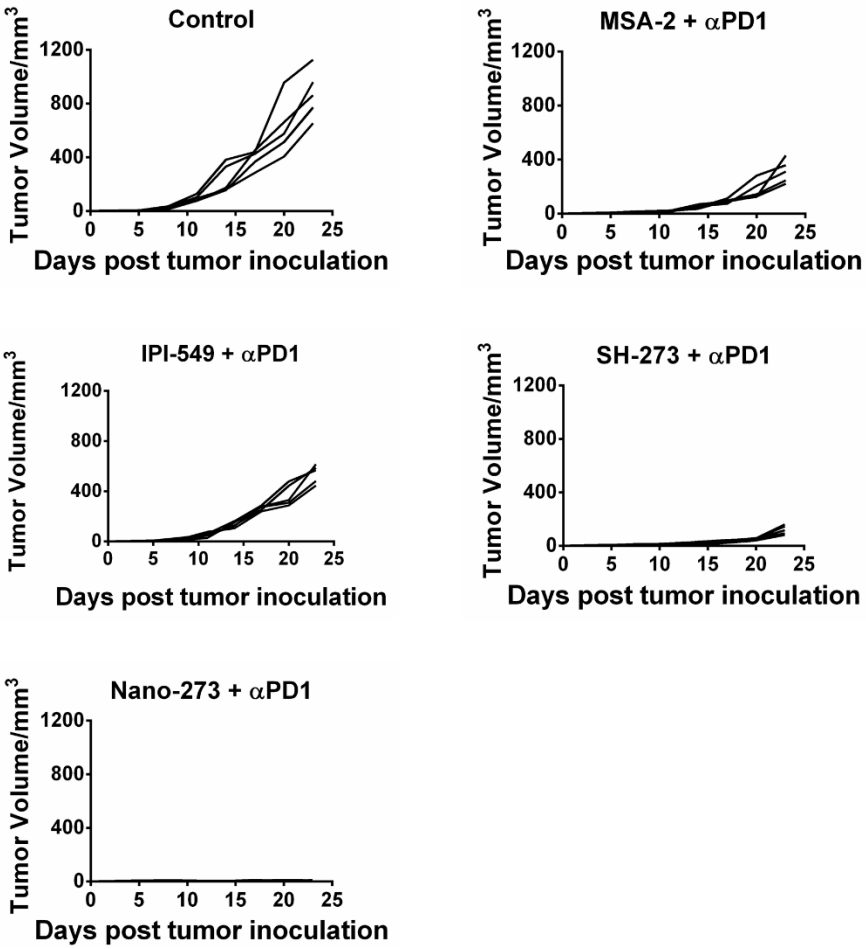


**Figure 4.S22** Antitumor efficacy in xenograft pancreatic cancer (KPC 6422 cell line) with different treatments. Individual tumor volume after treatment with PBS (control), MSA-2 (i.v. 34.0 μmol/kg) plus anti-PD-1 antibody (100 μg), IPI-549 (i.v. 18.9 μmol/kg) plus anti-PD-1 antibody (100 μg), SH-273 (i.v. 17.6 μmol/kg) plus anti-PD-1 antibody (100 μg) and Nano-273 (i.v. 17.6 μmol/kg) plus anti-PD-1 antibody (100 μg). n=5 mice in each group.

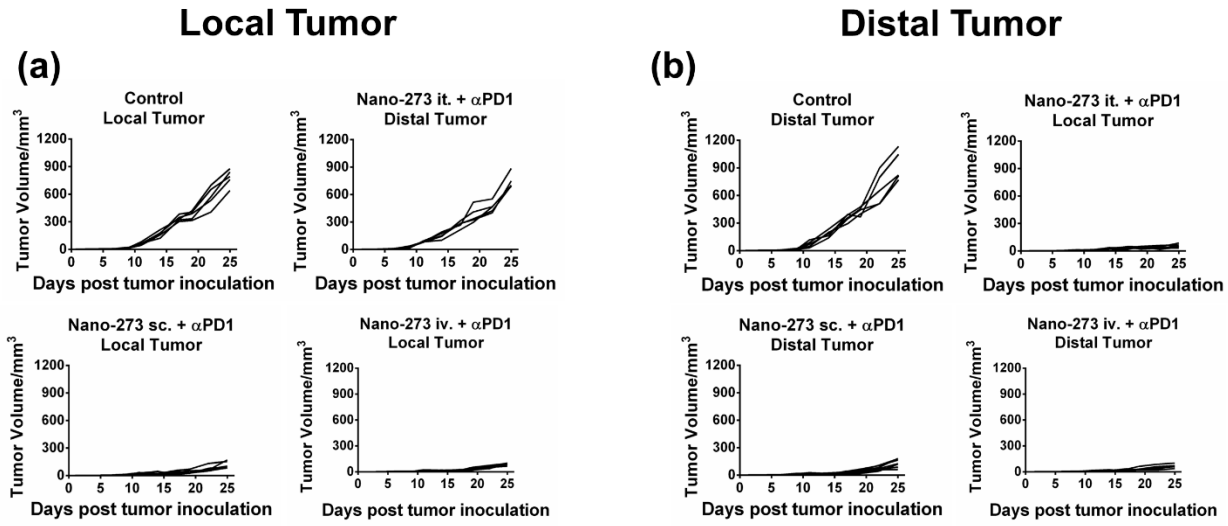


**Figure 4.S23** Antitumor efficacy for pancreatic cancer (KPC 6422 cell line) with Nano-273 treatment in different administration routes. Individual tumor volume after treatment with PBS (control) and Nano-273 (17.6 μmol/kg intratumorally, subcutaneously and intravenously injection, respectively) plus anti-PD-1 antibody (100 μg). n = 5 mice in each group.

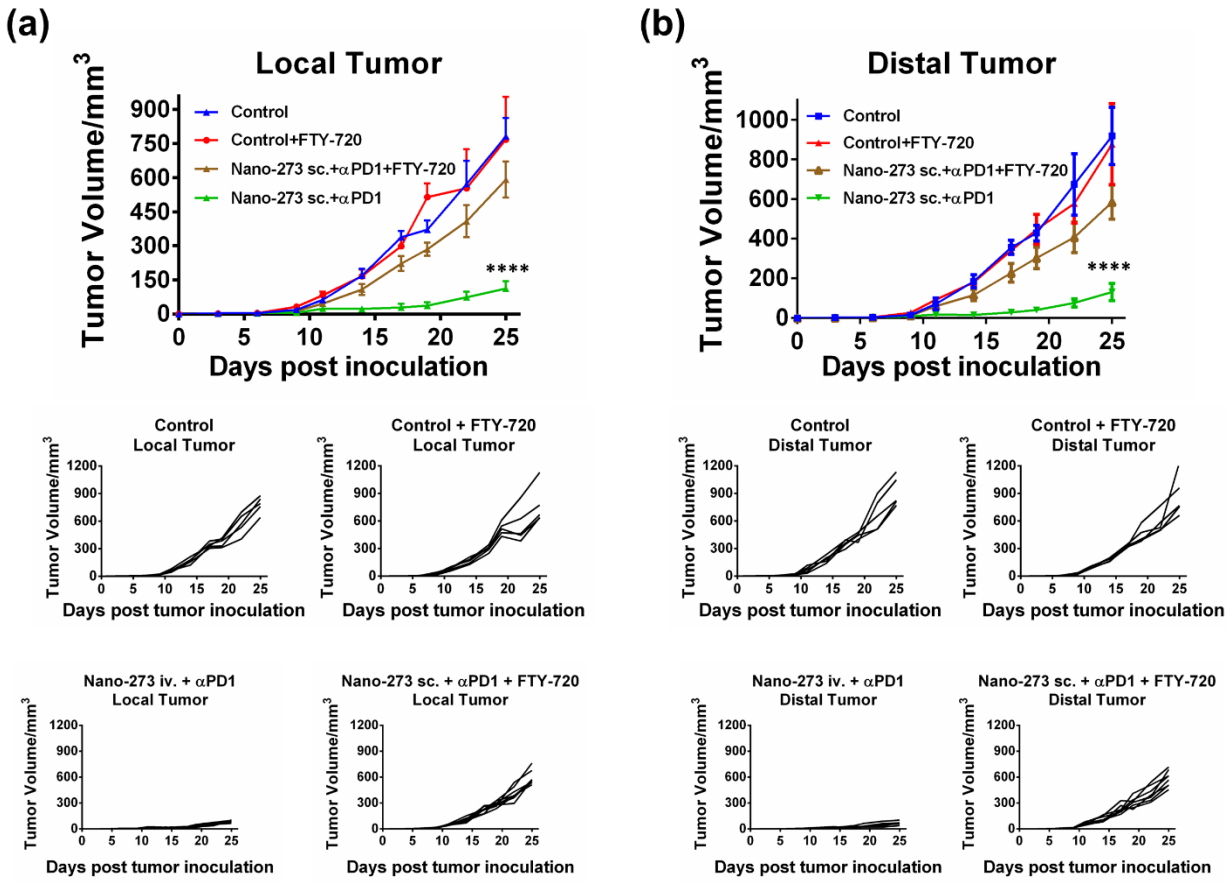


**Figure 4.S24** Antitumor efficacy for pancreatic cancer (KPC 6422 cell line) with Nano-273 treatment in subcutaneously injection. Individual tumor volume after treatment with or without Fingolimod (FTY720), or with PBS (control), Nano-273 (17.6 μmol/kg subcutaneously and intravenously injection, respectively) plus anti-PD-1 antibody (100 μg). The data represents the mean ± SD; n = 5. Statistical comparisons are based on one-way ANOVA, followed by post hoc Tukey's pairwise comparisons or by Student's unpaired T-test. The asterisks denote statistical significance at the level of **** $p < 0.0001$. ANOVA, analysis of variance; SD, standard deviation.

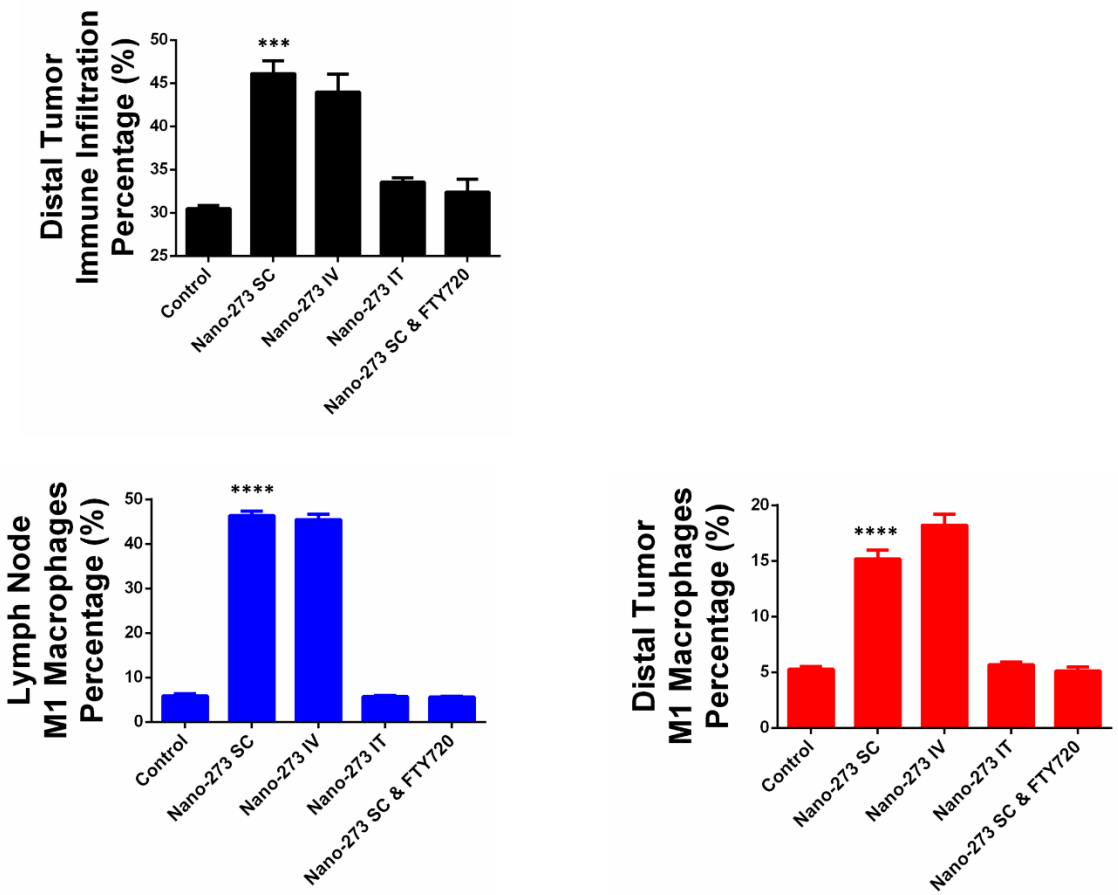


**Figure 4.S25** Quantification and representative flow cytometry analysis of tumor immune infiltration and M1 macrophage ratios in distal tumor and lymph node after treatments from efficacy study from **Figure 4c and S21**. Statistical comparisons are based on one-way ANOVA, followed by post hoc Tukey's pairwise comparisons or by Student's unpaired T-test. The asterisks denote statistical significance at the level of *** $p < 0.001$, **** $p < 0.0001$. ANOVA, analysis of variance; SD, standard deviation. statistical comparisons are conducted between Nano-273 (sc) with Nano-273 (it), Nano-273 (sc) + FTY720 and control groups.

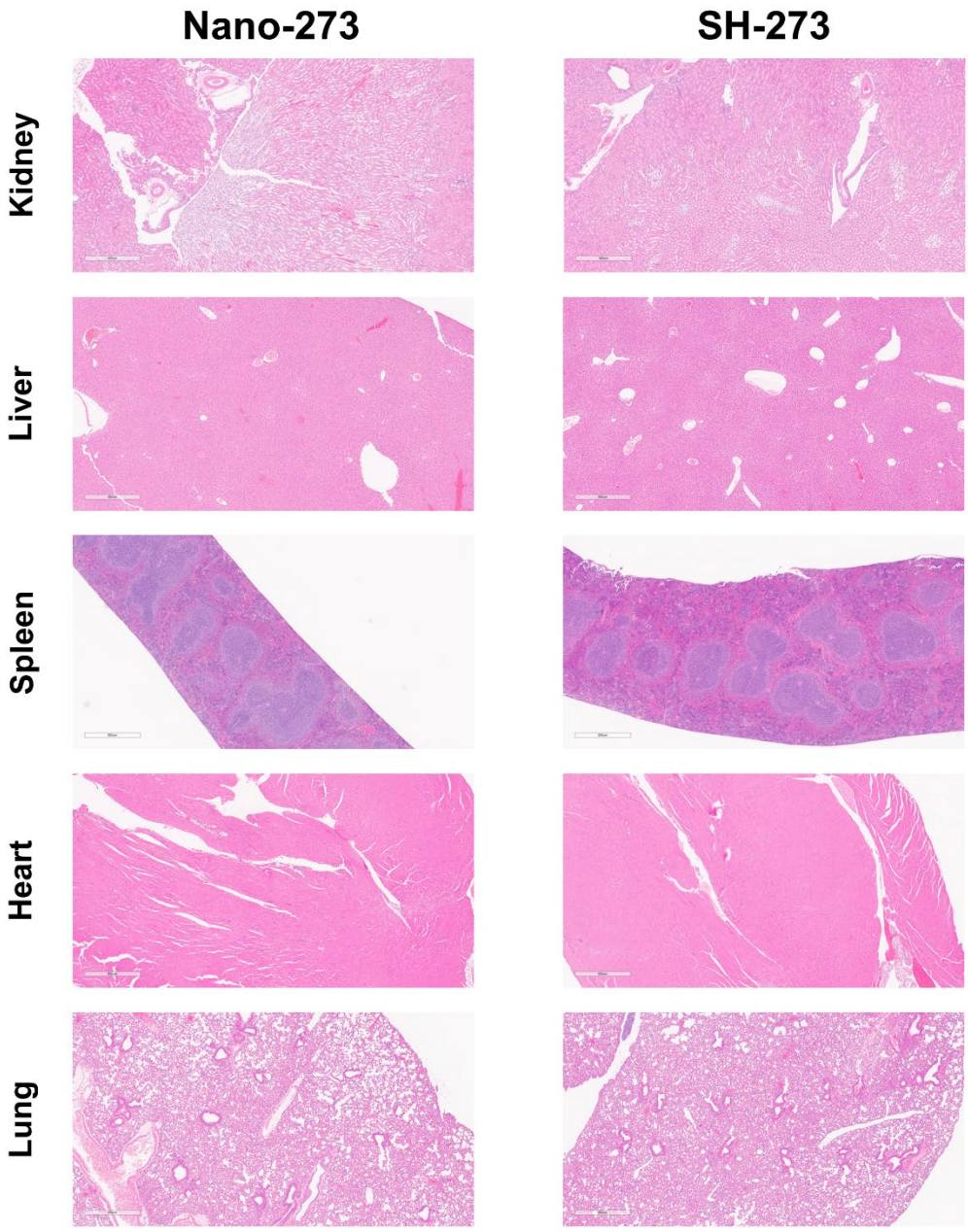


**Figure 4.S26** H&E staining of major organs in CD1 mice after treatments with SH-273 and Nano-273 every 3 days for 5 doses (17.6 μmol/kg) through intravenous injection.

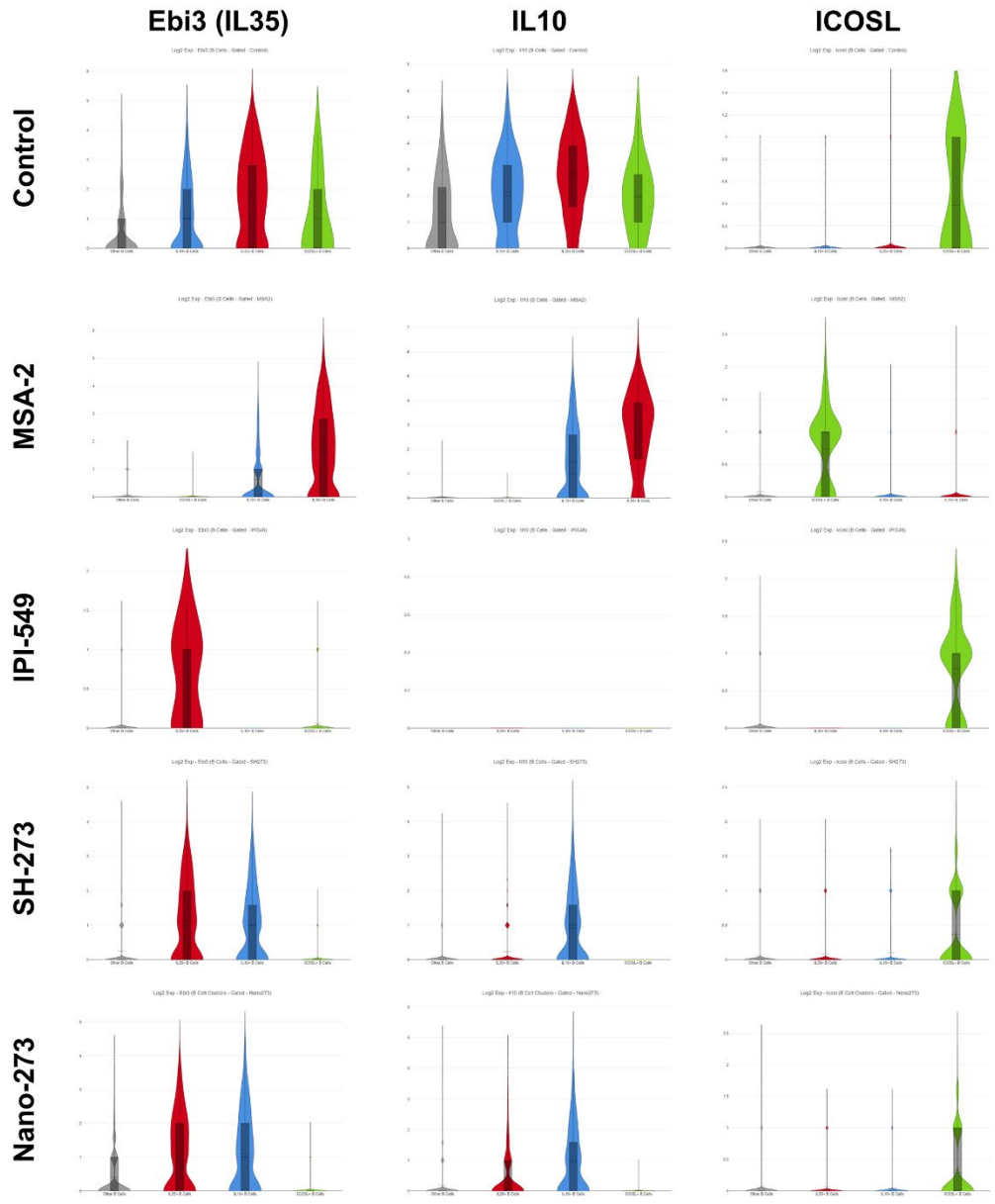


**Figure 4.S27** Ebi3, IL10 and ICOSL genes expression at B cells by single cell RNA-seq analysis for mice from anti-tumor efficacy study at **Figure 4c**

**Supporting Methods**

***Pancreatic Organoid culture***

1. Euthanize the mice, and then remove the pancreatic tumor by standard surgical procedures.
2. Mince the tissue into pieces of roughly 0.5 mm3 using fine scissors.
3. Transfer minced tissue to the 15-mL centrifuge tube and add 10 mL ice-cold wash medium.
4. Pipette the sample up and down with a 10-ml pipette to remove red blood cells and fat (which will float to the top of the solution).
5. Allow tissue pieces to settle, and discard ~7.5 ml of the supernatant, including any floating pieces of fat.
6. Repeat this wash step once.

**Tumor cell dissociation**

1. Remove any remaining wash medium, and add ~10 mL of the digestion solution.
2. Pipette the digestion solution up and down with a 10-mL pipette, and digest for 45 min at 37 °C, with shaking (500 r.p.m.).
3. When the ductal structures appear, transfer the supernatant to a fresh 15-ml centrifuge tube, add ice-cold wash medium to increase the volume to 15 ml and pellet the material at 100–300g for 5 min at 8 °C.
4. Discard the supernatant and add cold wash medium to a volume of 15 ml; repeat the pelleting procedure again to wash out any remaining digestion solution.
5. Add 10 ml of basal medium to the 15-ml centrifuge tube, and pellet the material by centrifuging at 100–200g for 5 min at 8 °C.
6. Remove and discard the supernatant before washing the pellet again with 10 ml of basal medium, and pellet the material again by centrifuging at 100–200g for 5 min at 8 °C.

**Cell seeding**

1. Remove the supernatant, and resuspend the desired number of cells (1,000 cells per well of a 24-well plate) into expansion solution (cell count = 4 * $10^5$ cell/mL) and add 50 uL (20000 cells) of the cell suspension into 1 mL matrigel matrix for seeding.
2. Add 50 (protocol reference) / 200 (Matrigel instruction) µL of Matrigel matrix into each well of a pre-chilled 24-well plate, spread evenly with a pipet tip.
3. Incubate the cells for 5–10 min at 37 °C or until the basement matrix is solidified.
4. Overlay the droplet with isolation medium (500 / 1000 µl per well for a 24-well plate).
5. Incubate the material under standard tissue culture conditions (37 °C, 5% $CO_2$).
6. Media were changed every 2 days to allow consistent growth.